

PhD thesis

# Spin-Photon Interface for Quantum Information Processing

Ming Lai Chan

Advisor: Peter Lodahl

Submitted: June 24, 2023

This thesis has been submitted to the PhD School of The Faculty of Science, University of Copenhagen



# Abstract

Hybrid integration of different quantum material platforms is probably the right path leading to eventual realizations of practical photonic quantum computing and communication. Amongst these platforms, quantum dots stand out as not only near-perfect sources emitting the purest, indistinguishable photons, but also viable spin qubits for inducing non-local correlation, i.e., entanglement, between flying photons. Entanglement generation between multiple photons is an indispensable ingredient for realizing measurement-based quantum photonic computing and loss-tolerant quantum repeaters, yet it remains to be experimentally demanding.

Self-assembled InAs quantum dots integrated on photonic-crystal waveguides are especially promising in this endeavor, since the entanglement between two guided photons can be mediated by a quantum-dot spin owing to a deterministic spin-photon interface. The same interface could also serve as a medium to swap information between flying photons and a stationary spin qubit, fulfilling DiVincenzo's sixth criteria for long-distance quantum communication.

In this thesis, we show that such a waveguide-integrated spin-photon interface enables a plethora of quantum protocols suitable for quantum information processing.

Notably, we report the on-chip generation of high-fidelity entanglement between a guided photon and the embedded quantum-dot hole spin, which lays experimental grounds for, say, two-photon entangling gates, deterministic Bell-state analyzers and spin-photon controlled-phase gate necessary for one-way quantum repeaters. The spin-photon entanglement is generated with 74% fidelity, on par with existing solid-state platforms while the generation speed is two-orders of magnitude faster.

Our second work proposes that the information carried by a flying photon can be stored in the stationary quantum dot with fidelity exceeding 95% in a realistic experimental setting. The proposal is strikingly robust to losses with performance comparable to that of the atomic platform. We therefore expect it to be useful for performing fast deterministic SWAP gates, as well as memory-assisted satellite quantum key distribution.

Finally, we demonstrate entanglement between two photons and the quantum-dot electron spin, endowed by significant improvements across most aspects of the platform. Using nuclear spin narrowing, the electron spin dephasing time is extended by fifteen-fold, with single-qubit gate fidelity of  $F_\pi \approx 98\%$ . Fidelities of spin-photon and biphoton-spin entanglement are 77% and 56%, respectively, predominantly limited by cross-excitation errors which can be mitigated in the next-generation sample. The path towards higher photons is thus straightforward, and 4-qubit entanglement should be within reach.



# Sammenfatning

Hybrid integration af forskellige kvantemateriale platforme er sandsynligvis den rigtige vej, der fører til eventuelle realiseringer af praktisk fotonisk kvanteberegning og kommunikation. Blandt disse platforme skiller kvanteprikker sig ud som ikke kun næsten perfekte kilder, der udsender de reneste, ikke-adskillelige fotoner, men også levedygtige spin-qubits til at inducere ikke-lokal korrelation, dvs. sammenfiltrering, mellem flyvende fotoner. Sammenfiltringsgenerering mellem flere fotoner er en uundværlig ingrediens for at realisere målebaseret kvantefotonisk databehandling og tabstolerante kvanterepeatere, men det er stadig eksperimentelt krævende.

Selvmonterede InAs kvanteprikker integreret på fotoniske krystalbølgeledere er særligt lovende i denne bestræbelse, da sammenfiltreringen mellem to guidede fotoner kan medieres af et kvantepunktspin på grund af en deterministisk spin-foton-grænseflade. Den samme grænseflade kunne også tjene som et medium til at udveksle information mellem flyvende fotoner og en stationær spin-qubit, hvilket opfylder DiVincenzos sjette kriterier for langdistance-kvantekommunikation.

I denne afhandling viser vi, at en sådan bølgeleder-integreret spin-foton-grænseflade muliggør et væld af kvanteprotokoller, der er egnede til kvanteinformationsbehandling.

Navnlig rapporterer vi on-chip-genereringen af high-fidelity-sammenfiltrering mellem en guidet foton og det indlejrede kvanteprikhulspin, som lægger eksperimentel grund til f.eks. to-foton-entangling-porte, deterministiske Bell-state-analysatorer og spin-foton kontrolleret fase-gate nødvendig for envejs kvanterepeatere. Spin-foton-sammenfiltreringen genereres med 74%-fidelity, på niveau med eksisterende solid-state platforme, mens generationshastigheden er to størrelsesordener hurtigere.

Vores andet arbejde foreslår, at informationen båret af en flyvende foton kan lagres i den stationære kvanteprik med en nøjagtighed, der overstiger 95% i en realistisk eksperimentel indstilling. Forslaget er slående robust over for tab med en ydeevne, der kan sammenlignes med den atomare platforms. Vi forventer derfor, at det vil være nyttigt til at udføre hurtige deterministiske SWAP-gates, såvel som hukommelsesassisteret satelitkvantenøgledistribution.

Endelig demonstrerer vi sammenfiltrering mellem to fotoner og kvantepunktelektronspindet, udstyret med betydelige forbedringer påtværs af de fleste aspekter af platformen. Ved at bruge nuklear spin-indsnævring forlænges elektronspin-affasningstiden med femten gange med en enkelt-qubit-gate-fidelity på  $F_{\pi} \approx 98\%$ . Fidelities af spin-foton og biphotonspin entanglement er henholdsvis 77% og 56%, overvejende begrænset af krydsexcitationsfejl, som kan afbødes i næste generations prøve. Vejen mod højere fotoner er således

ligetil, og 4-qubit sammenfiltrering burde være inden for rækkevidde.

# Acknowledgements

The research described in this thesis was carried out in the Quantum Photonics Group at the Niels Bohr Institute, under the supervision of Peter Lodahl. The projects presented have received funding from the European Union's Horizon 2020 research and innovation programme under the Marie Skłodowska-Curie grant agreement 861097 (project name QUDOT-TECH).

I would like to give my earnest, sincere gratitude to my supervisor Peter Lodahl, for inviting me to Copenhagen to give a talk after first knowing me for merely 23 minutes on Skype, for bringing me to the wonderful Quantum Photonics group/family and the QUDOT-tech network, and for granting me a lot of research freedom. Despite Peter is often too busy to get to the nitty gritty of experiments, his laser-sharp insights during our brief conversations would always guide me to the right track (see the introduction of Chapter 3). He is the ideal group leader who is extremely skilled at selling our platform, reigniting my passion for quantum dots every time before I start losing hope.

Alexey Tiranov is the person I am wholly indebted to. He is simultaneously my (unofficial) supervisor, mentor, good friend, colleague, programmer and technician. He transformed me from being a pure theorist, to someone who knows how to design and lead experiments. He is someone I aspire to be one day, if I decide to stay in academia starting my own group.

Another person that I am deeply admired for is Martin Hayhurst Appel. His meticulous, extensive, detailed-oriented, perfectionistic and aesthetic style of research thoroughly resonates with me. As you are reading this thesis you might notice plenty of familiar figures and descriptions which are inspired from his PhD thesis.

I could not have reached the level of research maturity I need without the consistent guidance from Yijian Meng, as he helped shape the later part of my PhD work and pushed me beyond my comfort zone. It is due to his diligent and tenacious questioning on all aspects of the experiment that the results in Chapter 6 become possible. I very much look forward to more collaborations with him in the coming months.

Anders Søndberg Sørensen is my (unofficial second) supervisor who is probably the smartest person I know. There is simply no end to his knowledge reserve. He is the ideal theorist who has unparalleled levels of physical intuition. He is a sage whose words are difficult to grasp at first, but when you finally get them your understanding ascends to a higher level. Although he is extremely attentive to every detail in the projects we have worked together, he will almost always miss a factor of 2, or one half, in his estimation.

I dare to say that the colleagues mentioned above have great tolerance on my mistakes, as they tend to go easy on me without much criticism. Nir Rotenberg, on the other hand, has left a very strong impression during my first group presentation. He constructively criticized my theory work at the time and demanded intuitive understanding at the heart of each equation in which I was severely lacking. It was a truly defining moment for me and has since moulded my way of doing research. The many annotations and intuitive

explanations you will read throughout this thesis reflect this.

At this point I think I have gabbled for too much so I will cut it short. I want to particularly thank Arne Ludwig, Peter Zajac, Andreas Dirk Wieck and Nikolai Bart for being so approachable and accommodating during my secondment in Bochum. Arne is extremely knowledgeable in solid-state physics and especially supportive of my research, whom I am profoundly grateful for. I want to also thank Richard Warburton, Giang Nam Ba Nguyen, Clemens Spinnler, Liang Zhai, Mark Hogg, Marcel Erbe and the rest of the Basel team for constructing such a hospitable, family-like environment for my stay and also for the many intriguing discussions. Urs Haeusler and Bruno Ortega Goes from the QUDOT-tech network are also good friends of mine whom I have shared some funny memories with. I sincerely thank Ziv Aqua and Barak Dayan for our wonderful collaborative work in Chapter 2.

My PhD studies have been very enjoyable thanks to the sociable, heartwarming work environment constructed by my colleagues in the Center for Hybrid Quantum Networks. My heartfelt thanks to the best office mates: Ying Wang, Vasiliki Angelopoulou (Vasso), Eva Maria González Ruiz, Cecilie Toftdahl Olesen, Evangelia Asproptomiti (Evi) and Johann Sebastian Kollath-Bönig; to young bloods of the spin team: Rasmus Bruhn Nielsen and Pratyush Anand; to my 7 guitar teachers: Carlos Fernando Duarte Faurby, Rodrigo Adriano Thomas, Patrik Isene Sund, Kasper Hede Nielsen, Leonardo Midolo (for the guitar pick, too), Vasso and Evi. I want to also thank Camille Papon, Asli Dilara Ugurlu, Hanna Le Jeannic, Ying, Beatrice Da Lio, Vasso, Freja Thilde Østfeldt, Xiaoyan Zhou and Arianne Brooks for being so excellent at organizing social activities for the group. I vividly remember the inspiring and friendly conversations during coffee breaks and meals with (in no particular order): Cornelis Jacobus Van Diepen (Sjaak), Mikkel Thorbjørn Mikkelsen, Xiao-Liu Chu, Shikai Liu, Nils Valentin Hauff, Atefeh Shadmani, Clara Celeste Qvotrup, Zhe Liu, Stefano Paesani, Ravitej Uppu, Sho Tamaki, Yu Meng, Matthias Christian Löbl, Xiang Xi, Love Alexander Mandla Pettersson, Konstantin Tiurev, Björn Schriniski, Yuxiang Zhang, and Oliver August Dall’Alba Sandberg.

I highly appreciate Yijian, Martin, Carlos and Nils for constructive feedback on this thesis.

Special gratitude goes to the unsung heroes in the administration: Lisbeth Andreassen, Frederik Uldall, Leah Strauss (from DTU), and Dorte Christiane Garde Nielsen for their support and assistance in smoothing out the administrative load during my study.

Lastly, I want to thank my parents, grandmother and brother for sending me emergency supplies (i.e., snacks) to fuel my nostalgia for my home country, and for their unconditional, entangling love and support on what I do despite the 8600-kilometer distance. This journey would have been unbearably painful without my wife Haimi Qiu, who took care of me and improved my personal hygiene and culinary skills. Haimi, I am very fortunate to share this life with you (and submit our theses around the same time), and this only marks the start of our many adventures together. Since meeting you I have become a better man.

# List of Publications

## Journal Publications

- **Ming Lai Chan\***, Alexey Tiranov\*, Martin Hayhurst Appel, Ying Wang, Leonardo Midolo, Sven Scholz, Andreas D. Wieck, Arne Ludwig, Anders S. Sørensen, and Peter Lodahl, “On-chip spin-photon entanglement based on photon-scattering of a quantum dot”, *npj Quantum Inf* 9, 49 (2023).
- **Ming Lai Chan\***, Ziv Aqua\*, Alexey Tiranov, Barak Dayan, Peter Lodahl, and Anders S. Sørensen, “Quantum state transfer between a frequency-encoded photonic qubit and a quantum dot spin in a nanophotonic waveguide”, *Phys. Rev. A*. 105.062445 (2022).
- Martin Hayhurst Appel, Alexey Tiranov, Simon Pabst, **Ming Lai Chan**, Christian Starup, Ying Wang, Konstantin Tiurev, Sven Scholz, Andreas D. Wieck, Arne Ludwig, Anders S. Sørensen, and Peter Lodahl, “Entangling a Hole Spin with a Time-Bin Photon: A Waveguide Approach for Quantum Dot Sources of Multiphoton Entanglement”, *Phys. Rev. Lett.* 128, 233602 (2022).

## In preparation

- Yijian Meng, **Ming Lai Chan**, Rasmus B. Nielsen, Zhe Liu, Nikolai Bart, Andreas D. Wieck, Arne Ludwig, Alexey Tiranov, Anders S. Sørensen, and Peter Lodahl, “On-chip genuine three-qubit entanglement from a deterministic source”.

## Results not included in this thesis

- Beatrice Da Lio, Carlos Faurby, Xiaoyan Zhou, **Ming Lai Chan**, Ravitej Uppu, Henri Thyrrerstrup, Sven Scholz, Andreas D. Wieck, Arne Ludwig, Peter Lodahl, Leonardo Midolo, “A Pure and Indistinguishable Single-Photon Source at Telecommunication Wavelength”. *Adv. Quantum Technol.* 2200006 (2022).
- Shikai Liu, Oliver August Dall’Alba Sandberg, **Ming Lai Chan**, Bjørn Schrinski, Yiouli Anyfantaki, Rasmus B. Nielsen, Robert G. Larsen, Andrei Skalkin, Ying Wang, Leonardo Midolo, Sven Scholz, Andreas D. Wieck, Arne Ludwig, Anders S. Sørensen, Alexey Tiranov, and Peter Lodahl, “Violation of Bell inequality by photon scattering on a two-level emitter”, *submitted*.

# Contents

<b>Abstract</b>	<b>i</b>
<b>Acknowledgements</b>	<b>vi</b>
<b>List of Publications</b>	<b>vii</b>
<b>Contents</b>	<b>viii</b>
<b>1 Introduction</b>	<b>1</b>
1.1 Thesis Structure . . . . .	3
1.2 Self-assembled Quantum Dots . . . . .	4
1.2.1 Band Diagram and Optical Excitations . . . . .	5
1.2.2 Charge-tunable Wafers . . . . .	6
1.3 Optical Selection Rules . . . . .	9
1.3.1 Neutral Exciton . . . . .	9
1.3.2 Negatively-charged Exciton . . . . .	11
1.4 Nanophotonic Waveguides . . . . .	15
1.5 Photon Emission and Single-photon Scattering . . . . .	18
<b>2 Quantum State Transfer from Photon to Spin</b>	<b>21</b>
2.1 Summary of Results . . . . .	22
2.2 Photon Scattering Formalism . . . . .	25
2.2.1 Photon Scattering in One-sided Waveguides . . . . .	25
2.2.2 Ideal Protocol . . . . .	26
2.3 Fidelity under Various Noises . . . . .	28
2.3.1 Resonant Scattering in QD-waveguide Systems . . . . .	28
2.3.2 Off-resonant Scattering in QD-waveguide Systems . . . . .	32
2.3.3 State Transfer of an Equatorial Photonic State to a QD spin . . . . .	33
2.3.4 Choi-Jamiolkowski Fidelity . . . . .	38
2.3.5 Error Sanity Check . . . . .	39
2.4 Additional Imperfections . . . . .	40
2.5 Comparison with Numerical Simulation . . . . .	41
2.6 Experimental Considerations . . . . .	43
2.6.1 Realization on a QD-waveguide platform . . . . .	43
2.6.2 Comparison with Rb-cavity platform . . . . .	45
2.7 Conclusion . . . . .	46
<b>3 Spin-Photon Entanglement using Photon-scattering</b>	<b>47</b>
3.1 Motivations . . . . .	48

3.2	Photon-scattering Gate Protocols . . . . .	49
3.2.1	Deterministic Photon-scattering gates . . . . .	49
3.2.2	Heralded Photon-scattering gates . . . . .	54
3.3	Experimental Setup . . . . .	56
3.3.1	Laser Paths . . . . .	56
3.3.2	Time-bin Interferometer . . . . .	58
3.3.3	Cross-polarization Scheme . . . . .	60
3.4	Hole Spin Spectroscopy . . . . .	63
3.4.1	Resonance Fluorescence . . . . .	63
3.4.2	Two-color Resonant Transmission . . . . .	64
3.4.3	Optical Cyclicity . . . . .	68
3.4.4	Spin-dependent Reflection . . . . .	71
3.4.5	Photon Visibility . . . . .	73
3.5	Hole Spin Control . . . . .	77
3.5.1	Principle of Optical Spin Control . . . . .	77
3.5.2	Measured Rabi flops . . . . .	78
3.5.3	Hahn-echo Visibility . . . . .	81
3.6	Parameter Summary . . . . .	83
3.7	Entanglement Measurement . . . . .	84
3.8	Gate Performance Metrics . . . . .	88
3.9	Conclusion . . . . .	91
<b>4</b>	<b>Theory of Spin-photon Entanglement with Photon-scattering</b>	<b>93</b>
4.1	State Evolution under the Photon-scattering Entanglement Protocol . . . . .	94
4.2	Photon Scattering Formalism and Fidelity Expression . . . . .	96
4.2.1	Scattering Coefficients in Two-sided Waveguides . . . . .	96
4.2.2	Projection Operators for Time-bin Photons . . . . .	97
4.2.3	Formula for Operational Fidelity . . . . .	97
4.3	Fidelity under Realistic Noises . . . . .	99
4.3.1	Spectral Mode Mismatch . . . . .	99
4.3.2	Finite Cyclicity and Coupling Loss . . . . .	100
4.3.3	Phonon-induced Pure Dephasing . . . . .	101
4.3.4	Spin Dephasing . . . . .	102
4.3.5	Incoherent Spin-flip Error and Finite $T_2^*$ . . . . .	104
4.3.6	Spin Readout Error . . . . .	107
4.3.7	Driving-induced Dephasing . . . . .	107
4.4	Comparison between Theoretical and Experimental Fidelity Estimates . . . . .	109
<b>5</b>	<b>Theoretical Model of Photon Visibility</b>	<b>111</b>
5.1	Input and Output states . . . . .	112
5.2	Reflection and Transmission Visibility . . . . .	114
5.3	Visibility Comparison between Theory and Simulation . . . . .	117
5.3.1	Visibility with Additional Errors . . . . .	119
5.4	Visibility Comparison with Data . . . . .	121
5.5	Comparison with Hong-Ou-Mandel Visibility . . . . .	122
<b>6</b>	<b>Multi-photon Entanglement with Photon Emission</b>	<b>125</b>
6.1	Protocol for Multi-photon Entanglement Generation . . . . .	125
6.1.1	The Lindner-Rudolph Protocol . . . . .	126

6.1.2	Time-bin Protocol . . . . .	127
6.2	Experimental Setup . . . . .	130
6.2.1	Wafer Composition . . . . .	130
6.2.2	Optical and Spin Control Setup . . . . .	131
6.3	Electron Spin Spectroscopy . . . . .	135
6.3.1	Quantum Dot Search . . . . .	135
6.3.2	Optical Cyclicality . . . . .	137
6.4	Electron Spin Control . . . . .	139
6.4.1	Spin Rabi Oscillations . . . . .	139
6.4.2	Ramsey Interferometry . . . . .	140
6.4.3	Hahn-echo Visibility . . . . .	142
6.5	Optical Pulsed Excitations . . . . .	146
6.5.1	Purity and Indistinguishability . . . . .	147
6.6	Parameter Summary . . . . .	150
6.7	Two-Qubit Entanglement . . . . .	151
6.7.1	Measurement Results . . . . .	151
6.7.2	Preliminary Infidelity Analysis . . . . .	152
6.8	Three-Qubit Entanglement . . . . .	155
6.8.1	Timing Restrictions . . . . .	155
6.8.2	Measurement Settings . . . . .	156
6.8.3	Measurement Results . . . . .	158
6.9	Summary and Outlook . . . . .	159
6.9.1	Outlook . . . . .	160
<b>7</b>	<b>Proposal for Deterministic Bell state Analyzers</b>	<b>163</b>
7.1	Basic Principle of Bell State Analyzers . . . . .	164
7.2	Gate Sequence tailored to Time-bin Photons . . . . .	165
7.3	Verification of Bell states . . . . .	166
7.4	Protocol Analysis . . . . .	167
7.4.1	Input-Output Relation for Photon-Scattering . . . . .	167
7.4.2	Fidelity for Bell state Analyzer . . . . .	168
7.4.3	Spin Control Errors . . . . .	169
7.4.4	Excitation Errors . . . . .	169
7.4.5	Systematic Errors . . . . .	170
7.4.6	Spectral Diffusion . . . . .	171
7.5	Experimental Hardware . . . . .	172
7.6	Conclusion . . . . .	173
<b>8</b>	<b>Summary with Outlook</b>	<b>175</b>
<b>A</b>	<b>Formula of the Average Gate Fidelity in Heralded Operations</b>	<b>177</b>
<b>B</b>	<b>Normalization of the Two-photon Output State</b>	<b>181</b>
<b>C</b>	<b>Speculations on the Origin of Power-dependent Spin-flips</b>	<b>185</b>
<b>D</b>	<b>Effect of Laser-induced Spin Flips on n-photon GHZ Fidelity</b>	<b>187</b>
D.1	1-photon case: A spin-photon Bell state . . . . .	187
D.2	2-photon case: A GHZ state . . . . .	188

---

D.3 Induction to $n$ -photon GHZ state . . . . .	189
<b>Bibliography</b>	<b>191</b>



# Chapter 1

## Introduction

On a semiconductor integrated chip found ubiquitously in modern electronic devices, there are thousands of tiny electronic components like transistors, resistors and capacitors, which are interconnected forming a circuit to implement logic gates, amplifiers, microprocessors and many more functions. All these components are called *electronics*, since they manipulate the flow of electrical currents, or quanta of electricity called *electrons* for information processing on the chip.

A quantum analog of this would be a quantum *photonic* chip that uses the quanta of light, called *photons*, to transmit and process information. Photons are prime candidates for quantum bit (qubit) carriers as they are naturally robust to environmental noises, travel in the speed of light, and are easy to manipulate with simple linear optical elements like beam-splitters and phase shifters [1]. In addition, these optical elements can be miniaturized and compactly integrated on the same semiconductor substrate for electronics [2]. By virtue of these merits, fully integrated quantum photonic computing is no longer fantasy in a wet dream. It can realistically be implemented using the Knill-Laflamme-Milburn (KLM) scheme [3] with linear optical elements, indistinguishable photons and photo-detectors. The field of quantum computing has now flourished in both academia and industry, attracting wide government and media attention with an accumulated global investment of \$ 35.5 billions by 2022<sup>1</sup> [4], which promises to transform existing technologies.

On the flip side of the immense hype, the fact that photons are resilient to decoherence also implies two photons rarely interact, i.e., a photon is like a lone wolf, thus making operations between pairs of photonic qubits experimentally challenging. The KLM scheme circumvents this problem by utilizing the Hong-Ou-Mandel (HOM) effect [5] to implement a controlled two-photon gate with projective measurements on two ancillary photons [6]; however this measurement-induced nonlinearity is inherently probabilistic and thus this approach might not be scalable in the long run.

An alternative architecture is to have quantum emitters fabricated on the semiconductor wafer to mediate nonlinear interaction between photons, as an integral part of the photonic circuit [7]. Quantum emitter is an atom-like object which shoots out one photon per excitation like a photon pistol. One prominent example of this is self-assembled Indium Arsenide (InAs) quantum dots in Gallium Arsenide (GaAs) semiconductor wafers, which not only produce bright single photon streams of > 99% purity and > 98% indis-

---

<sup>1</sup>It is also fitting that in the same year the Nobel Prize in Physics was awarded to Alain Aspect, John F. Clauser and Anton Zeilinger “for experiments with entangled photons, establishing the violation of Bell inequalities and pioneering quantum information science”.

tinguishability [8], but also offer a spin degree of freedom allowing on-chip spin-mediated nonlinearity [9] which is in principle deterministic. Although these quantum dots do complete the missing puzzle pieces in the original KLM scheme, they come with their own sets of challenges such as spectral inhomogeneity<sup>2</sup> and susceptibility to environment noises<sup>3</sup> [7]. Nevertheless, there is yet to be a singular quantum platform that simultaneously satisfies all five of DiVincenzo's criteria [10] necessary for a fully fledged quantum computer, thus a hybrid integration of different material platforms leveraging the strengths of each platform seems to be the future [11].

Apart from being near-perfect single-photon sources, what quantum dots could add to this quantum computing toolbox is perhaps their ability to deterministically induce non-local correlation between a photon and a spin, i.e., spin-photon entanglement [12, 13, 14, 15, 16, 17, 18]. The ability to entangle photonic qubits and auxiliary spin states is not only crucial for realizing deterministic two-photon gates *locally* within the photonic chip, but also beneficial for connecting photonic circuits over distant networks [19]. The latter is intimately related to DiVincenzo's sixth and seventh criteria for quantum communication, referring to abilities for the platform to convert between stationary and flying qubits (photons), and to faithfully transmit photons between specified locations.

This thesis aims to show that self-assembled InAs quantum dots (QD) interfaced with nanophotonic waveguides on a GaAs chip, could be a viable quantum platform which is capable of entanglement generation between a stationary QD spin and a flying photon, coherent exchange between their states, as well as the creation of multi-photon entanglement. The proof-of-principle experiments and theories performed in this thesis are built upon a *waveguide-induced spin-photon interface*<sup>4</sup> developed recently [20, 21]. The presented results establish a solid foundation for an abundance of quantum information protocols implemented on the QD-waveguide platform, laying the experimental grounds for one-way quantum repeaters [22] in quantum communication, on-chip deterministic Bell-state analyzers, photonic quantum non-demolition detector with ancillary spin qubits [23, 24] and the generation of time-bin photonic cluster states for measurement-based quantum computing [25, 18], among others.

From a pedagogical perspective, this thesis documents some valuable insights and intuitions I have learnt during the period of study, which should hopefully be helpful to future members in the group and scholars from a relevant community.

---

<sup>2</sup>This refers to the emission wavelengths of quantum dots being randomly distributed, so it remains difficult to scale up to many quantum dots.

<sup>3</sup>This includes nuclear spin, phononic and charge noises etc.

<sup>4</sup>In Layman's terms, this means the nanophotonic waveguide provides an efficient interface for flying photons to interact with a quantum-dot spin. By time-reversal symmetry, a photon emitted from exciting the quantum-dot spin state can also be efficiently collected through the waveguide.

## 1.1 Thesis Structure

The structure of this thesis resembles a 5-course meal, divided into five parts:

**Part I** includes remaining sections of Chapter 1. For starters, we introduce our experimental quantum photonic platform, which is established on self-assembled quantum-dot spins interfaced with nanophotonic waveguides. We also highlight two optical excitation schemes that are adopted in this thesis.

**Part II** presents a theory work (like a bowl of cold, dry salad<sup>5</sup>). In Chapter 2, we propose a passive scheme to transfer the quantum state of a photon onto a waveguide-integrated quantum-dot spin. To investigate the feasibility of our proposal, we analyze the effect of various imperfections in an experimental setting.

**Part III** is the first main course with a healthy mix of experiments (white meat) and theory (vegetables). More precisely, we report our experimental pursuit to generate entanglement between a photon and the quantum-dot hole spin. In Chapter 3 we present a photon-scattering protocol to achieve this, and follow up by performing a series of measurements to characterize the quantum system and estimate the entanglement fidelity. To understand errors limiting the fidelity, in Chapter 4 we analyze our protocol in depth using the theory developed in Part II, to compare with the experimental estimate. To refresh taste buds, a palate cleanser like Chapter 5 presents an interesting theory side project sprang up from one particular measurement in Chapter 3.

**Part IV** is like the second main course which is often quite heavy (red meat), as in Chapter 6 we show a multitude of experiments and device improvements, leading up to the generation of genuine entanglement between a quantum-dot electron spin and two photons.

In **Part V** we wrap up the meal with a cheese course (Chapter 7) and a dessert (Chapter 8). The former discusses the possible implementation of a Bell-state analyzer protocol that can classify Bell states with unity success rate, which is a natural extension of the photon-scattering experiment demonstrated in Part III. The latter concludes the thesis with a summary of main results and an optimistic outlook.

All experimental raw data, analysis scripts and figures have been uploaded to a frozen data archive on Ref. [26].

Results in Chapters 2-4 have been published. Chapters 5-7 contain unpublished work.

---

<sup>5</sup>Not necessarily unpleasant.

## 1.2 Self-assembled Quantum Dots

The substrate, or wafer on which a typical integrated circuit is built, is a semiconductor material, such as crystalline Silicon or Gallium Arsenide (GaAs) with a thickness of hundreds of microns. All circuit elements can be manufactured on the wafer by etching away certain areas of the wafer surface, followed by deposition of  $n$ -type (accepting electrons, negatively charged [27]) and  $p$ -type (donating electrons, positively-charged) materials.

A quantum photonic circuit can be fabricated in a similar way. The quantum device used in this thesis is made by implanting Indium Arsenide (InAs) on top of a GaAs substrate, followed by depositing a capping layer of GaAs to form self-assembled quantum dots (QD). Surrounded these QDs are micron-scaled waveguide structures that are sculpted by etching trenches and holes on the GaAs wafer [28].

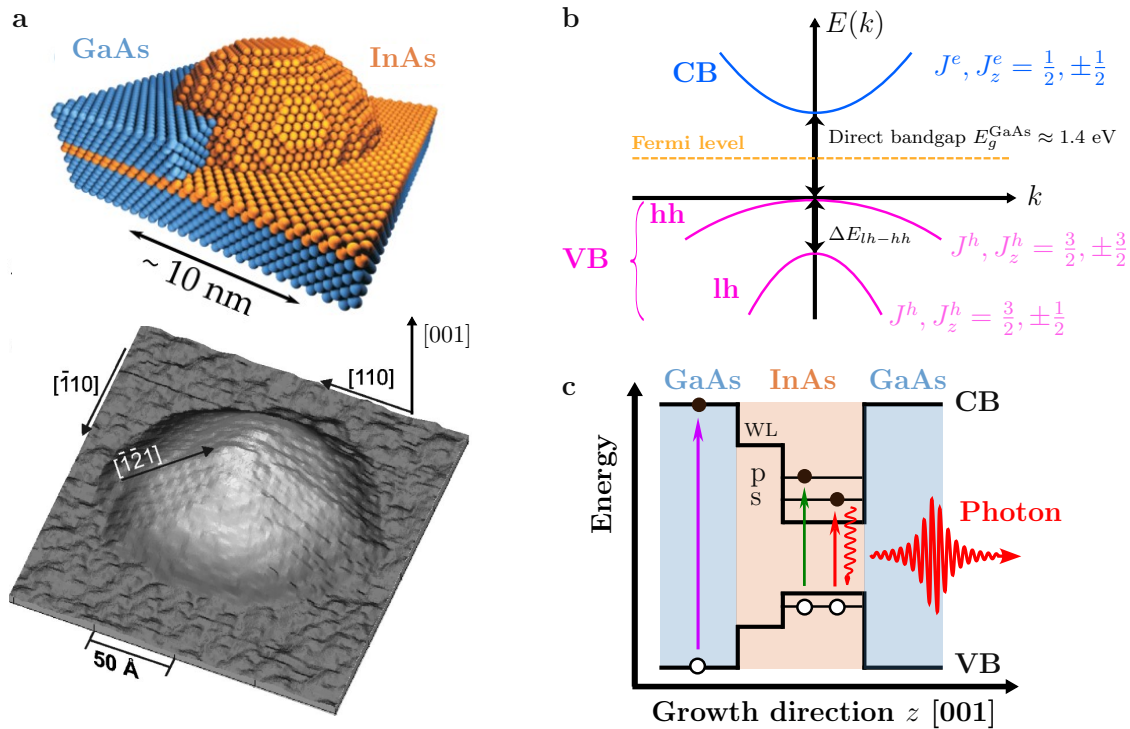


Figure 1.1: **Self-assembled Quantum Dot.** (a) Top: Schematics of a self-assembled single quantum dot, formed by submerging a dome of InAs atoms in GaAs atoms. Bottom: Scanning Tunneling Microscope (STM) image of an uncapped InAs quantum dot on a GaAs substrate grown along [001], from Ref. [29]. Arrows indicate the crystallographic axes defined by Miller index  $[xyz]$ . (b) Electronic band structure for a bulk GaAs crystal near the  $\Gamma$  point, under the effect of uniaxial strain. The split-off band  $J^h = 1/2$  is not shown. Adapted from Ref. [30]. (c) Optical excitation schemes of QDs, including above-bandgap (purple), quasi-resonant  $p$ -shell (green), and resonant  $s$ -shell (red) excitations of an electron (black dot), which then recombines with a hole (white) emitting a photon.

Self-assembled InAs/GaAs QDs are nanometer-sized dome-like objects (Fig. 1.1a) with a radius of 5-15 nm, and are 5-10 nm tall [30]. The method to synthesize these QDs is known as the Stranski-Krastanov growth mode [30], which enables InAs to nucleate randomly into small domes, through strain induced by lattice mismatch<sup>6</sup> between InAs

<sup>6</sup>Lattice mismatch means a difference in lattice constant between InAs and GaAs. InAs has 0.606 nm, while GaAs has 0.565 nm at 300 K [31].

and GaAs. Since InAs has a lower energy bandgap<sup>7</sup> than GaAs, this 1 eV<sup>8</sup> bandgap difference provides the necessary three-dimensional energy confinement to trap electrons and holes inside a QD, forming discrete electronic states (Fig. 1.1c) that resemble the energy levels of a single atom<sup>9</sup>.

### 1.2.1 Band Diagram and Optical Excitations

The merit of having access to multiple atomic energy levels is the coupling to discrete amount of light, called light quanta or a photon. This facilitates resonant excitation and spontaneous photon emission of a semiconductor QD, which are essential for interfacing a QD with flying photons. To understand the physical mechanism behind, it is useful to look at the electronic energy bands of GaAs and InAs that constitute the QD. Both are III-V semiconductor compounds with a zinc-blende crystalline structure [27]. Their energy bands share similar features so it suffices to just consider GaAs.

Since the GaAs crystal lattice is jointed compactly by a large number of atoms ( $10^{23}$  atoms in the crystal), their atomic orbitals become very close in energy and overlap to form energy bands, which are ranges of energy levels in which electrons can occupy in the material. Fig. 1.1b shows the energy  $E(k)$  of an electron at wavevector  $k$  in different bands of bulk GaAs. Of particular interests are bands closest to the Fermi level, and an energy-forbidden region called bandgap where no electronic states exist. The bottom bands belong to the valence band (VB) which is filled with electrons, while the one above is the conduction band (CB) which is in general empty.

At the Brillouin zone<sup>10</sup> center (the so-called  $\Gamma$  point where  $k = 0$ ), the energy bands are approximated by parabolic dispersion  $E(k) \approx \frac{\hbar^2 k^2}{2m^*}$ , with their curvatures  $\hbar^2 (\frac{d^2 E}{dk^2})^{-1} \equiv m^*$  [27] representing the effective masses  $m^*$  of different types of quasi-particles moving under the periodic lattice potential. For an electron promoted to the conduction band, it has the smallest effective mass<sup>11</sup> and an orbital angular momentum  $L = 0$  owing to  $s$ -orbital symmetry of its Bloch state. This means the conduction-band electron has a total angular momentum of  $J^e = S^e + L = 1/2$  with  $z$ -angular momentum projection  $J_z^e = \pm 1/2$ . Similarly, when an electron is removed from the valence band, the absence of the electron leaves a positively charged ‘‘hole’’. This valence-band hole has  $p$ -orbital Bloch states ( $L = 1$ ) and behaves like a particle of pseudo spin 1/2, thus having a total angular momentum of  $J^h = S^e + L = 3/2$ . The two valence sub-bands shown in Fig. 1.1b correspond to the heavy hole  $J_z^h = \pm 3/2$  and light hole  $J_z^h = \pm 1/2$ , with  $m_{\text{hh}}^* > m_{\text{lh}}^*$  hence their names. They become non-degenerate with minimum energy difference  $\Delta E_{\text{lh-hh}}$  thanks to uniaxial strain in the GaAs crystal [30].

It is crucial to note that both GaAs and InAs have direct bandgap (Fig. 1.1b), meaning the excitation and annihilation of a conduction-band electron requires only a quanta of energy at the same wavevector  $k$  (or momentum  $p = \hbar k$ ). In other words, only a photon is needed to access dipole transitions between the valence and conduction bands. This has profound impact on how light interacts efficiently with InAs quantum dots.

<sup>7</sup>Energy difference between valence (VB) and conduction band (CB) of a semiconductor.

<sup>8</sup>The bandgap energies for InAs (infused with Ga) and bulk GaAs are  $E_g^{\text{InGaAs}} \approx 0.477$  eV and  $E_g^{\text{GaAs}} \approx 1.519$  eV [32].

<sup>9</sup>This is why self-assembled QDs are often called artificial atoms.

<sup>10</sup>Primitive cell of the lattice expressed in the  $k$ -space [27].

<sup>11</sup>The conduction-band electron has  $m_e^* = 0.067m_e$  where  $m_e$  is the electron rest mass, whereas valence-band heavy (light) hole has  $m_{\text{hh}}^* = 0.45m_e$  ( $m_{\text{lh}}^* = 0.082m_e$ ).

For such an optically active QD, a photon is sufficient to resonantly excite an electron to  $s$ -shell (lowest energy level) of the conduction band (Fig. 1.1c), forming an electron-hole bound state called an exciton. The inverse process is also possible, where after some nanoseconds (around 1 ns lifetime for QDs in bulk [33]), the exciton decays by recombining the electron and hole, radiating a photon of same frequency as the excitation. These two processes are known as optical absorption and photo-luminescence [30].

Exciting the QD with photon energy higher than GaAs bandgap energy  $E_g^{\text{GaAs}} \approx 1.4$  eV (called above-bandgap excitation, purple arrow in Fig. 1.1c), drives the electron to the GaAs conduction band, which subsequently diffuses to the  $s$ -shell by releasing the excess energy through thermal lattice vibrations called phonons. This is frequently used as a preliminary technique to reveal QD transitions for screening. A similar off-resonant method is to excite the electron to the  $p$ -shell, which is useful for filtering out the excitation laser in a confocal microscopy setup [34].

## 1.2.2 Charge-tunable Wafers

To shield against electrical charge noises, quantum dots are grown<sup>12</sup> within layers of different materials and sandwiched between doped layers (Fig. 1.2), where the top and bottom GaAs layers are  $p$ -doped (positively charged) and  $n$ -doped (filled with electrons, negatively charged). This constitutes a  $p$ - $i$ - $n$  diode which allows a static bias voltage  $V_{\text{bias}}$  to be swept across one direction and stabilizes the charge environment around the quantum dot (QD) [28].

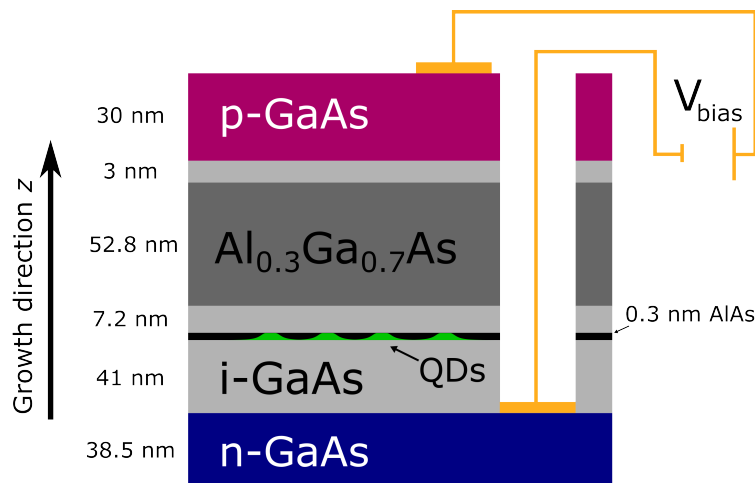


Figure 1.2: **Typical diode heterostructure of quantum-dot wafers.** Applying a bias voltage across the diode isolates QDs from fluctuating charge noises and loads them with different charge states.

The diode membrane shown in Fig. 1.2 is designed to be around 180 nm thick to support the single waveguide mode [36]. At the diode center lies the self-assembled InAs QDs. They are sandwiched between layers of 41 nm intrinsic ( $i$ ) or undoped GaAs and 52.8 nm tunnel barrier  $\text{Al}_{0.3}\text{Ga}_{0.7}\text{As}$ . This is categorized as an  $n$ -type device [37, 30] since it is more probable for an electron to be trapped into the QD via quantum tunneling

<sup>12</sup>See Ref. [35] for fabrication details of this wafer. The wafers used in this thesis were grown by our collaborators: Scholz, S., Bart, N., Ludwig, A. and Wieck, A. D. from Lehrstuhl für Angewandte Festkörperphysik, Ruhr Universität Bochum, Germany.

than a hole when an external bias voltage is applied. Due to a heavier effective mass, the probability for the heavy hole to tunnel through the  $\text{Al}_{0.3}\text{Ga}_{0.7}\text{As}$  barrier can be shown to be at least ten orders of magnitude lower than that of the electron through the *i*-GaAs layer<sup>13</sup>, using the Wentzel-Kramers-Brillouin (WKB) approximation [38].

### 1.2.2.1 Tuning Quantum dots by Electric fields

Apart from stabilizing the charge environment, the applied bias voltage is used to modulate the frequencies of QD optical transitions via the quantum-confined DC Stark effect [39, 40, 41]. The *n*- and *p*-doped layers shown in Fig. 1.2 result in a built-in energy difference  $E_i$ . Applying a forward bias voltage  $V_{\text{bias}}$  pulls the conduction-band electron and valence-band hole apart, effectively shifting the excitonic emission energy by  $\Delta E_{\text{Stark}}$ :

$$\Delta E_{\text{Stark}} = E(F_z) - E_i = -p_0 F_z - \beta_{\text{pol}} F_z^2, \quad (1.1)$$

where  $p_0 = es_0$  is the excitonic dipole moment between the center of electron (of charge  $e$ ) and hole wavefunctions displaced by distance  $s_0$  at zero bias.  $F_z$  is the amplitude of applied static electric field along the growth direction  $z$ , where  $F_z = (V_i - V_{\text{bias}})/d_{\text{intrinsic}}$  [30, 41].  $V_i \approx 1.54$  V at 4 K is the built-in voltage [33] from the diode, and  $d_{\text{intrinsic}} = 104$  nm is thickness of the intrinsic region between doped layers. The polarizability  $\beta_{\text{pol}}$  measures how easily the dipole can be pulled apart, or polarized.

### 1.2.2.2 Charging Quantum dots

Different quantum dot charged states [42] can be initialized with voltage tuning. This is achieved by either removing (adding) an electron from the valence band (into the conduction band). The quantum tunneling picture is useful to understand this.

Fig. 1.3 schematically shows the band energy levels at different layers of the diode, which prepares different QD charged states. Top (bottom) black line represents the conduction (valence) band. Applying a bias voltage effectively tilts the band structure downwards like a lever arm where the Fermi level  $E_f$  is fixated at a pivot point (*n*-layer) [43].

At a small forward bias, the tilted band structure has a large slope (Fig. 1.3a). When the QD is now illuminated by a laser of frequency resonant to<sup>14</sup> the  $X_0$  transition frequency, upon absorption of the photon energy an electron from the valence band is promoted to the conduction band *s*-shell, leaving behind a hole. At this voltage, the effective width of the *i*-GaAs layer (colored arrow in deep red) is short. Hence, the electron tunnels out to the Fermi contact without recombining with the hole<sup>15</sup>. As a result, a hole is trapped forming the ground state for  $X^+$ .

At a higher forward bias (Fig. 1.3b), however, the barrier width is sufficiently long such that the electron tunneling rate is slower than the neutral exciton  $X^0$  recombination/decay rate. Therefore, electron recombines with the hole via Coulomb interaction

<sup>13</sup>The hole effective mass in  $\text{Al}_x\text{Ga}_{1-x}\text{As}$  is given by  $(0.51 + 0.25x) m_e$  at 300 K [31] for electron rest mass  $m_e$  and Al concentration of  $x$ , while for electron it is  $(0.063 + 0.083x) m_e$ . A heavier particle means it is more localized and harder to penetrate the barrier.

<sup>14</sup>This also applies to above-bandgap excitation where the electron decays non-radiatively to the conduction band *s*-shell, which is the method we used in Chapter 3 to initialize a hole.

<sup>15</sup>Since the diode is in principle symmetric, a hole can also tunnel out to the *p*-layer [28]. However, this is highly suppressed for an *n*-type device used in this thesis.

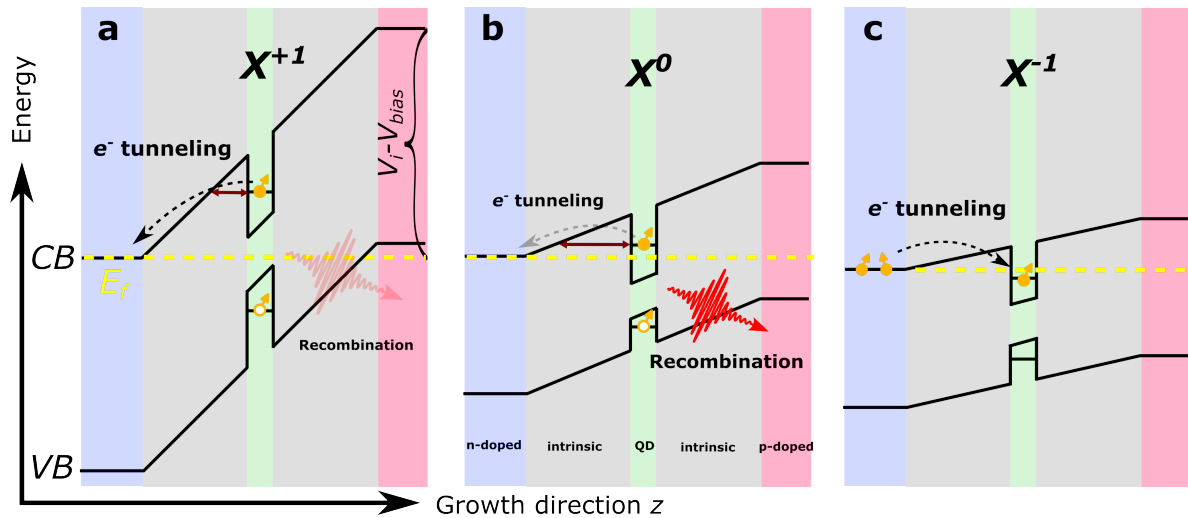


Figure 1.3: **Energy band structure of a  $p$ - $i$ - $n$  diode at different bias voltages.** The diode is shown in Fig. 1.2. A higher forward bias lowers the energy difference between doped layers, increasing the number of electrons in the exciton state. Orange filled (empty) dots are electron (hole) spins.  $V_i$  is the built-in potential difference in quasi Fermi levels between  $n$ - and  $p$ -layers at zero bias [30]. CB (VB) is the conduction (valence) band. Adapted from Fig. 4.1 of Ref. [30]. (a) Preparation of the ground state for a positively charge exciton  $X^+$ . Upon photon absorption, the electron tunnels out without radiative recombination. (b) Emission from a neutral exciton  $X^0$ . Recombination occurs as the tunneling rate is slower. (c) Preparing the ground state of a negatively charged exciton  $X^-$ .

emitting a photon<sup>16</sup>. Note that the crystal ground state for  $X^0$  does not have charges [28]. It shall now be clear that these processes are governed by the interplay between electron tunneling to the back contact and electron-hole recombination [44].

At an even larger forward bias, the Fermi level has higher energy than the QD  $s$ -shell (Fig. 1.3c). Therefore, it is energetically favourable for an electron to tunnel from the  $n$ -doped back contact into the QD, resulting in the ground state for  $X^-$ . As one may notice, there exists a small region of voltages where the Fermi sea is more or less degenerate with the QD  $s$ -shells, allowing co-tunneling of electrons in and out of the QD confinement. This range of voltages is called the co-tunneling regime and is useful for randomizing the electron spin state (Sec. 6.3.1).

The takeaway message here is that embedding the QD in a diode structure helps reduce electrical charge noise, and gives access to different charged states. The flexibility to apply bias voltages also allows the QD to be tuned by 0.5-0.75 GHz/mV<sup>17</sup> to be resonant with e.g., a cavity or another QD [45, 46].

<sup>16</sup>The valence-band hole can also recombine with an electron in the back contact. This is known as Mahan excitons [44] which have a wider linewidth than typical excitons.

<sup>17</sup>This depends on the lever-arm factor of a specific wafer [43], and is known by measuring the QD photo-luminescence at different bias voltages and frequencies, which is called a plateau map (Fig. 3.11a).

## 1.3 Optical Selection Rules

Previously we introduced different exciton states and their preparation from the perspective of energy band structures. For charged excitons, the charge in their ground states offers an extra controllable spin degree of freedom for quantum operations. Under an external magnetic field, each charge gains access to two non-degenerate spin states due to the Zeeman effect, acting as the logical  $|0\rangle$  and  $|1\rangle$  of a qubit. It can also be optically excited to form a trion emitting a single photon. Depending on the direction of magnetic field, different level structures arise according to the optical selection rules.

In this section, we describe the optical selection rules for different exciton states.

### 1.3.1 Neutral Exciton

The neutral exciton  $X^0$  has a crystal ground state  $|g_c\rangle$ . Optical excitation at a certain bias voltage creates an electron-hole pair where the electron out-tunneling is slower than the radiative recombination (Fig. 1.3b). The conduction-band electron (total angular momentum of  $J^e = 1/2$ ) and valence-band hole (total angular momentum  $J^h = 3/2$ ) is bound by Coulomb interaction [28], forming the excited state of  $X^0$ . With an equal number of electron and hole,  $X^0$  is therefore electrically neutral.

The electron (hole) spin has two eigenstates:  $|\uparrow\rangle$  and  $|\downarrow\rangle$  ( $|\uparrow\rangle$  and  $|\downarrow\rangle$ ), where  $|\uparrow\rangle$  ( $|\downarrow\rangle$ ) is the  $z$ -projection of the spin with angular momentum  $J_z^e = +1/2$  ( $J_z^h = -3/2$ <sup>18</sup>). Depending on the net angular momentum projection  $m_z = J_z^e + J_z^h$  in the excited state, two types of  $X^0$  are possible. An exciton with opposite spin orientations, i.e.,  $|\uparrow\downarrow\rangle$  or  $|\downarrow\uparrow\rangle$ , which can absorb or emit a photon<sup>19</sup> of angular momentum  $m_z = \pm 1$ , is called a bright exciton. The emitted light is therefore circularly polarized (denoted by  $\sigma^\pm$ ) as it is an eigenstate of spin-angular momentum  $\pm 1$ . Hence, the optical selection rules are

$$\begin{aligned} |g_c\rangle &\xleftrightarrow{\sigma^+} |\uparrow\downarrow\rangle; \\ |g_c\rangle &\xleftrightarrow{\sigma^-} |\downarrow\uparrow\rangle, \end{aligned} \quad (1.2)$$

with degenerate excited states. In reality, the bright exciton is not a perfect two-level system. Due to breaking of the in-plane circular symmetry of strained QDs [47], exchange interaction between the electron and hole gives rise to a fine structure splitting  $\Delta_{\text{FSS}}$  between two eigenstates  $|\uparrow\downarrow\rangle \pm |\downarrow\uparrow\rangle$ . These eigenstates now have a net angular momentum of  $m_z = 0$ , as a result of the linear combination of states with spin-angular momentum  $+1$  and  $-1$ . Therefore, the associated optical dipoles are superpositions of circular polarizations too, becoming linearly polarized<sup>20</sup>:

$$\begin{aligned} |g_c\rangle &\xleftrightarrow{Y} \frac{1}{\sqrt{2}}(|\uparrow\downarrow\rangle + |\downarrow\uparrow\rangle); \\ |g_c\rangle &\xleftrightarrow{X} \frac{1}{\sqrt{2}}(|\uparrow\downarrow\rangle - |\downarrow\uparrow\rangle), \end{aligned} \quad (1.3)$$

A dark exciton with parallel spin orientations ( $|\uparrow\uparrow\rangle$ ,  $|\downarrow\downarrow\rangle$ ) has  $m_z = \pm 2$  units of angular momentum, thus cannot be optically accessed directly from the crystal ground state.

<sup>18</sup>For brevity, here we consider only the heavy hole  $J_z^h = \pm 3/2$  and ignore the light hole  $J_z^h = \pm 1/2$ .

<sup>19</sup>A photon is a spin-1 boson with spin-angular momentum of  $\pm 1$  along  $z$ .

<sup>20</sup>The general rule is the difference in net angular momentum between the excited and ground eigenstates determines the photon polarizations.

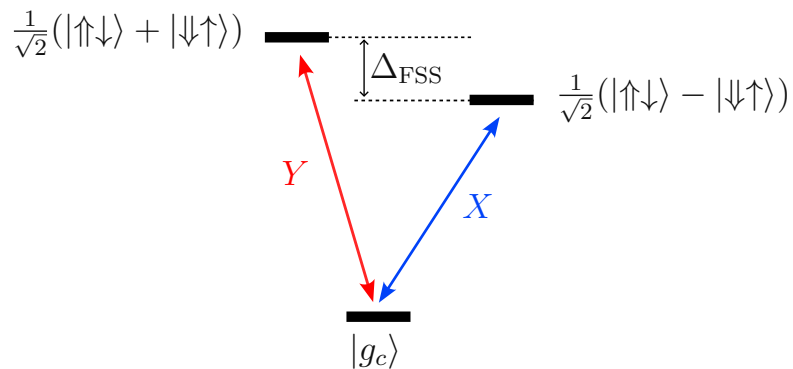


Figure 1.4: **Energy levels of neutral exciton  $X^0$ .** Strain-induced quantum dot asymmetry results in fine structure splitting  $\Delta_{\text{FSS}}$  between two excited states of a bright exciton, which couple to linearly polarized light, according to selection rules. Dark exciton states are not shown.

The transfer between the bright and dark excitons is possible via spin flips of either the electron or hole, which is primarily responsible for blinking [48] observed when measuring the intensity correlation  $g^{(2)}(\tau)$  between emitted photons from a bright exciton.

### 1.3.2 Negatively-charged Exciton

For a negatively charged exciton  $X^-$ , the ground state is an electron. Upon photo-absorption, an electron-hole pair is generated in addition to the electron, thus the excited state is a trion consisting of one hole and two electrons. The two trion electrons in the conduction band form a singlet<sup>21</sup> which has zero angular momentum, thus only the trion hole in the valence band couples to a magnetic field. The excited (ground) state therefore has a net angular momentum  $J_z^h = \pm 3/2, \pm 1/2$  ( $J_z^e = \pm 1/2$ ). For  $X^-$ , the optical transitions between a trion hole and the ground-state electron are illustrated in Fig. 1.5a. Here we define the quantization axis to be  $z$ , so all states are expressed by the  $z$ -projection of spin-angular momentum.

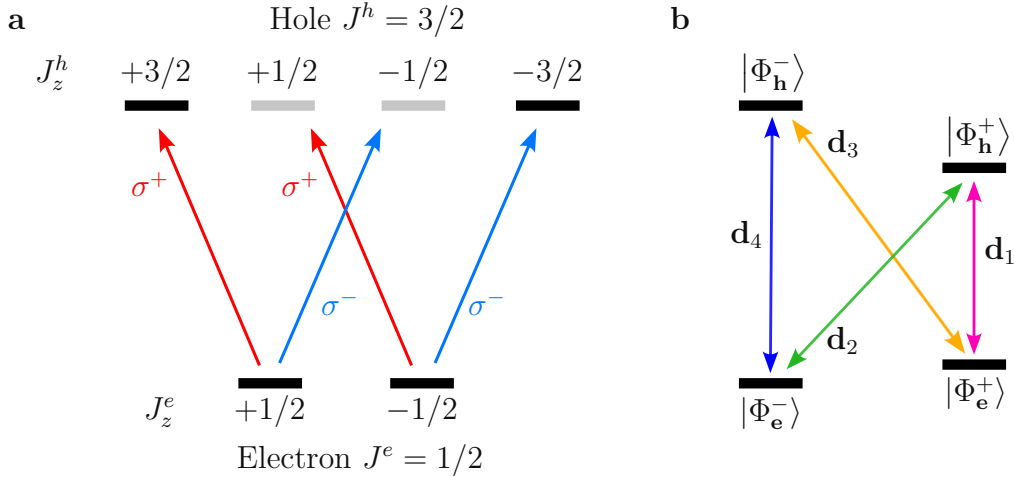


Figure 1.5: **Optical selection rules for  $X^-$ .** (a) Interband optical transitions between a trion hole and ground-state electron in the  $z$ -basis. A heavy (light) hole has  $z$ -angular momentum of  $J_z^h = \pm 3/2$  ( $J_z^h = \pm 1/2$ ) which couples to the electron  $J_z^e = \pm 1/2$  by circularly polarized light. Adapted from Fig. 9.6 of Ref. [49]. (b) Same as (a), but the eigenstates are modified according to the Hamiltonians in Eq. (1.5).

We can also describe the optical dipoles (Fig. 1.5a) mathematically below [50], which is useful for determining the selection rules at different magnetic field orientations:

$$\begin{aligned} \mathbf{d} \propto (\mathbf{e}_x - i\mathbf{e}_y) & \left( \underbrace{|+3/2\rangle\langle+1/2|}_{e^- \rightarrow \text{trion hh}} - k \underbrace{|+1/2\rangle\langle-1/2|}_{e^- \rightarrow \text{trion lh}} \right) \\ & + (\mathbf{e}_x + i\mathbf{e}_y) \left( |-3/2\rangle\langle-1/2| - k|-1/2\rangle\langle+1/2| \right), \end{aligned} \quad (1.4)$$

where  $\mathbf{e}_x$  ( $\mathbf{e}_y$ ) is a unit vector along  $x$  ( $y$ ).  $\mathbf{e}_x - i\mathbf{e}_y \equiv \sigma^+$  ( $\mathbf{e}_x + i\mathbf{e}_y \equiv \sigma^-$ ) denotes the right-hand (left-hand) circular polarization.  $|J_z^h\rangle\langle J_z^e|$  is the projection operator coupling the ground-state electron with spin projection  $J_z^e$  to the trion heavy hole (hh) or light hole (lh) state with total angular momentum  $J_z^h$ .  $k$  measures the difference in radiative coupling strength between heavy and light holes.

Under a general magnetic field  $\mathbf{B} \equiv (B_x, B_y, B_z)$ , the ground-state electron (e) and trion hole (h) are subject to the Hamiltonians [50]

$$\begin{aligned} \hat{H}_B^e &= \hat{H}_{B,Z}^e = g_e \mu_B \mathbf{B} \cdot \hat{S}; \\ \hat{H}_B^h &= \hat{H}_{B,Z}^h + \hat{H}_{B,NZ}^h = g_0 \mu_B \kappa \mathbf{B} \cdot \hat{J} + g_0 \mu_B q (B_x \hat{J}_x^3 + B_y \hat{J}_y^3 + B_z \hat{J}_z^3), \end{aligned} \quad (1.5)$$

<sup>21</sup>Electrons with equal spin states cannot occupy the s-shell due to the Pauli exclusion principle [30].

where  $g_e$  ( $g_0$ ) is the (free) electron  $g$ -factor,  $\mu_B$  is the Bohr magneton.  $\hat{S} \equiv \frac{1}{2}\hat{\sigma}$  ( $\hat{J}$ ) is the vector of spin-angular momentum matrices for a spin-1/2 (spin-3/2) particle.  $\hat{\sigma}$  are Pauli matrices. The magnetic coupling of the hole is given by the Zeeman  $\hat{H}_{B,Z}^h$  and non-Zeeman  $\hat{H}_{B,NZ}^h$  terms.  $\kappa^{22}$  and  $q$  are the Luttinger parameters dependent on the quantum dot material<sup>23</sup>.  $J_i^3$  is given by Table 3.5 of Ref. [49].

Eq. (1.5) introduces coupling between the spin basis states (i.e.,  $|\pm 1/2\rangle$ ), and modifies the energy eigenstates into  $|\Phi_p^\pm\rangle$ ,  $p \in \{e, h\}$  accordingly (Fig. 1.5b). The corresponding optical dipoles can therefore be deduced from the difference in net angular momentum between the new ground and excited eigenstates.

### 1.3.2.1 Zero Field

At zero magnetic field  $\mathbf{B} = 0$ , the basis states of the ground-state electron, as well as the trion heavy hole, have vanishing matrix elements<sup>24</sup>, i.e.,

$$\langle +1/2 | \hat{H}_B^e | -1/2 \rangle = 0; \quad \langle +3/2 | \hat{H}_B^h | -3/2 \rangle = 0, \quad (1.6)$$

which implies the ground (excited) states are degenerate. The zero-field negatively charged exciton therefore manifests as a double two-level system, with its eigenstates identical to the basis states:  $|\Phi_e^\pm\rangle = |\pm 1/2\rangle$  and  $|\Phi_h^\pm\rangle = |\pm 3/2\rangle$ . Ignoring the trion light hole in Eq. (1.4), the optical dipoles of this system (Fig. 1.5b) can then be found using [52]

$$\begin{aligned} \mathbf{d}_1 &= \langle \Phi_h^+ | \mathbf{d} | \Phi_e^+ \rangle = \mathbf{e}_x - i\mathbf{e}_y = \mathbf{d}_4^*; \\ \mathbf{d}_2 &= \langle \Phi_h^+ | \mathbf{d} | \Phi_e^- \rangle = 0 = \mathbf{d}_3^*, \end{aligned} \quad (1.7)$$

where the outer transitions  $\mathbf{d}_1, \mathbf{d}_4$  have orthogonal<sup>25</sup> circularly-polarized dipoles, while the inner transitions  $\mathbf{d}_2, \mathbf{d}_3$  are forbidden by the selection rules<sup>26</sup>.

### 1.3.2.2 Voigt Field

The degeneracy in Eq. (1.6) can be lifted by applying an external magnetic field. For a magnetic field oriented orthogonal to the QD growth direction (also called the in-plane or Voigt geometry), which is the field direction used throughout this thesis,  $\mathbf{B} \equiv (B_x, B_y, B_z) = (B \cos \phi, B \sin \phi, 0)$ . Thanks to the Zeeman term in Eq. (1.5), the electron basis states are now coupled by

$$\langle +1/2 | \hat{H}_B^e | -1/2 \rangle = \frac{1}{2} g_e \mu_B B e^{-i\phi}. \quad (1.8)$$

The new eigenstates for the ground-state electron become superposition of the  $z$ -basis states, which align with  $\mathbf{B}$ :

$$|\Phi_e^\pm\rangle = \frac{1}{\sqrt{2}} (\pm | +1/2 \rangle + e^{i\phi} | -1/2 \rangle) = \frac{1}{\sqrt{2}} (\pm |\uparrow_z\rangle + e^{i\phi} |\downarrow_z\rangle), \quad (1.9)$$

<sup>22</sup>Not to be confused with  $k$  in Eq. (1.4).

<sup>23</sup> $\kappa$  depends on Indium concentration [51].

<sup>24</sup>This can be understood as the transition element between spin states enabled by Zeeman interaction.

<sup>25</sup>Orthogonal since  $\mathbf{d}_1 \cdot \mathbf{d}_4 = 0$ .

<sup>26</sup>In fact, weak cross-transitions can be allowed via the light hole component [37].

with their energies shifted by  $\langle \Phi_e^\pm | \hat{H}_B^e | \Phi_e^\pm \rangle = \pm \frac{1}{2} g_e \mu_B B$  relative to their zero-field case.

For the trion hole, the story is different. In the simplest case where we consider only the heavy hole subspace ( $J_z^h = \pm 3/2$ ), one could show that using Eq. (1.5)<sup>27</sup>, only the non-Zeeman term  $\hat{H}_{B,NZ}^h$  couples the heavy hole basis states:

$$\langle +3/2 | \hat{H}_B^h | -3/2 \rangle = \langle +3/2 | \hat{H}_{B,NZ}^h | -3/2 \rangle = -\frac{3}{4} g_0 \mu_B q B e^{i\phi} \equiv \frac{3}{4} g_0 \mu_B q B e^{-i\phi_h}, \quad (1.10)$$

giving rise to new eigenstates for the heavy hole spin

$$|\Phi_h^\pm\rangle = \frac{1}{\sqrt{2}} (\pm | +3/2 \rangle + e^{i\phi_h} | -3/2 \rangle) = \frac{1}{\sqrt{2}} (\pm |\uparrow_z\rangle + e^{i\phi_h} |\downarrow_z\rangle), \quad (1.11)$$

which again rotate with  $\mathbf{B}$  via  $\phi_h = \pi - \phi$ . The optical transitions are therefore linearly-polarized:

$$\begin{aligned} \mathbf{d}_1 &= \langle \Phi_h^+ | \mathbf{d} | \Phi_e^+ \rangle \propto \cos\left(\frac{\phi_h - \phi}{2}\right) \mathbf{e}_x + \sin\left(\frac{\phi_h - \phi}{2}\right) \mathbf{e}_y = \sin\phi \mathbf{e}_x + \cos\phi \mathbf{e}_y = \mathbf{d}_4; \\ \mathbf{d}_2 &= \langle \Phi_h^+ | \mathbf{d} | \Phi_e^- \rangle \propto -\sin\left(\frac{\phi_h - \phi}{2}\right) \mathbf{e}_x + \cos\left(\frac{\phi_h - \phi}{2}\right) \mathbf{e}_y = -\cos\phi \mathbf{e}_x + \sin\phi \mathbf{e}_y = \mathbf{d}_3. \end{aligned} \quad (1.12)$$

This implies the optical dipoles should rotate according to orientation of the in-plane magnetic field<sup>28</sup>. However, this is not what experimentally observed in our device<sup>29</sup>. The optical dipoles can in fact be influenced by the built-in strain during quantum dot growth via heavy hole-light hole mixing. To illustrate this, we consider the trion hole basis states in the presence of light hole admixture [50]

$$|\psi_h^\pm\rangle = |\pm 3/2\rangle - \frac{\gamma e^{\pm i2\theta}}{\Delta E_{lh-hh}} |\mp 1/2\rangle, \quad (1.13)$$

which in the first order is a superposition between the heavy hole ( $J_z^h = \pm 3/2$ ) and light hole states ( $J_z^h = \mp 1/2$ ).  $\gamma$  is the hole-mixing coefficient and  $\theta$  determines the strain direction relative to the  $x$ -axis<sup>30</sup>.  $\Delta E_{lh-hh}$  is the energy splitting between the heavy and light hole ground states (Fig. 1.1b). With the new basis states, both the Zeeman and non-Zeeman terms have non-vanishing matrix elements. To highlight the coupling with  $\hat{H}_{B,Z}^h$ , we assume  $q \ll \kappa$ <sup>31</sup> thus

$$\langle \psi_h^+ | \hat{H}_B^h | \psi_h^- \rangle \approx \langle \psi_h^+ | \hat{H}_{B,Z}^h | \psi_h^- \rangle = \frac{\sqrt{3} g_0 \kappa \gamma \mu_B B}{\Delta E_{lh-hh}} e^{-i(\phi+2\theta)} \equiv \frac{\sqrt{3} g_0 \kappa \gamma \mu_B B}{\Delta E_{lh-hh}} e^{-i\phi_h}, \quad (1.14)$$

which has the same form as Eq. (1.10). The light hole components give rise to the coupling between the trion hole states via Zeeman effect. Comparing with Eq. (1.11), the new hole

<sup>27</sup>This is done mathematically by removing the light hole components and simplifying  $\hat{J}_x^3, \hat{J}_y^3$  and  $\hat{J}_z^3$  into  $2 \times 2$  matrices.

<sup>28</sup>As an additional remark, for an ideal heavy hole with perfect  $D_{2d}$  symmetry ( $q = 0$ ) [53], Eq. (1.10) should vanish, thus the in-plane pure heavy hole  $g$ -factor would be 0 [54].

<sup>29</sup>See Sec. 5.4 of Ref. [52]: From resonant transmission experiment the optical dipoles do not rotate with the in-plane magnetic field angle  $\phi$ .

<sup>30</sup>See Fig. 1 in Ref. [50].

<sup>31</sup>For InAs and GaAs,  $\kappa \gg q$  [54].

eigenstates now have a relative phase  $\phi_h = \phi + 2\theta$  between  $|\psi_h^\pm\rangle$ . Substituting this into Eq. (1.12) yields a set of dipoles which is independent of the in-plane field orientation  $\phi$ :

$$\begin{aligned}\mathbf{d}_1 &= \langle \Phi_h^+ | \mathbf{d} | \Phi_e^+ \rangle \propto \cos \theta \mathbf{e}_x + \sin \theta \mathbf{e}_y = \mathbf{d}_4; \\ \mathbf{d}_2 &= \langle \Phi_h^+ | \mathbf{d} | \Phi_e^- \rangle \propto -\sin \theta \mathbf{e}_x + \cos \theta \mathbf{e}_y = \mathbf{d}_3.\end{aligned}\quad (1.15)$$

It is now apparent that when the trion hole coupling is dominated by the light hole mixing, the resulting eigenstates are superpositions of  $|\psi_h^\pm\rangle$  that can be effectively treated as hole pseudo spin states in the equatorial basis. Under an in-plane magnetic field, the negatively charged exciton exhibits a four-level system with linear dipoles fixated by the strain angle  $\theta$ . For shear strain,  $\theta \approx \pm\pi/4$  thus the linear dipoles are locked towards  $[110]$  or  $[\bar{1}\bar{1}0]$  [50]. In this thesis, we define these linear dipoles  $\mathbf{d}_1, \mathbf{d}_4 = [\bar{1}\bar{1}0]$  ( $\mathbf{d}_2, \mathbf{d}_3 = [110]$ ) to be Y- (X-) polarized (Fig. 1.6b).

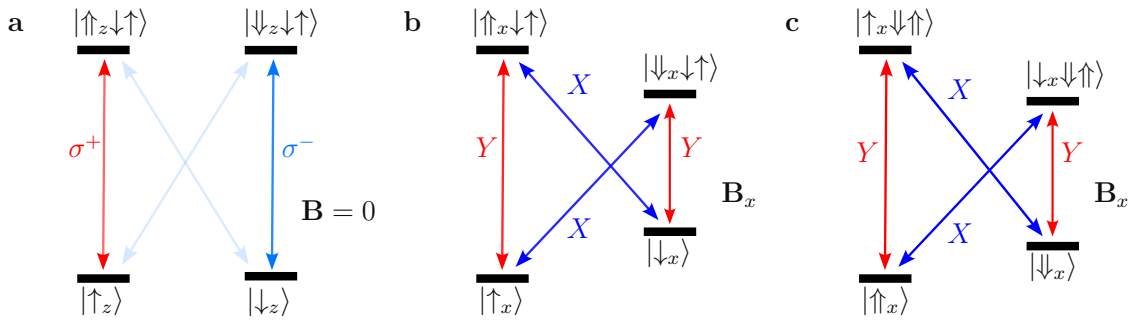


Figure 1.6: **Selection rules for charged excitons under a magnetic field.** (a) Without a magnetic field,  $X^-$  has degenerate ground and excited states.  $\mathbf{B}_z$  lifts the degeneracy but results in the same eigenstates and optical dipoles. (b) With  $\mathbf{B}_x$ , electron eigenstates are  $|\uparrow_x\rangle = (|\uparrow_z\rangle + |\downarrow_z\rangle)/\sqrt{2}$  and  $|\downarrow_x\rangle = (-|\uparrow_z\rangle + |\downarrow_z\rangle)/\sqrt{2}$ , while the hole eigenstates are defined by the strain (Eq. (1.15)). The optical dipoles also align with the strain angle  $\theta$  with equal strengths. (c) For  $X^+$  the ground and excited states are flipped, as the two holes in the trion form a singlet, leading to dipole transitions between a trion electron and the ground-state hole.

For QDs with less strain and shape anisotropy, i.e., GaAs/AlGaAs QDs grown by local droplet-etching [55], the trion heavy hole states are coupled by the non-Zeeman term, hence the linearly polarized optical dipoles following Eq. (1.12) should align with the external magnetic field  $\mathbf{B}$ .

## 1.4 Nanophotonic Waveguides

So far we have discussed the band structure and optical selection rules of self-assembled quantum dots (QD). For this section, we introduce ways to couple the dipole radiation to a guided mode.

In general, when electron-hole recombination occurs, the radiation propagates in all directions<sup>32</sup> due to energy conservation; as a result, only a small fraction of emitted light can be captured. To improve collection efficiency, the typical approach is to embed the QDs in nanostructures. The enclosure modifies the local photonic environment around the QD, thus preferentially guiding the emitted light to a single, well-defined optical mode. Inversely, when an incoming photon is coupled to the same optical mode, its interaction with the QD becomes deterministic.

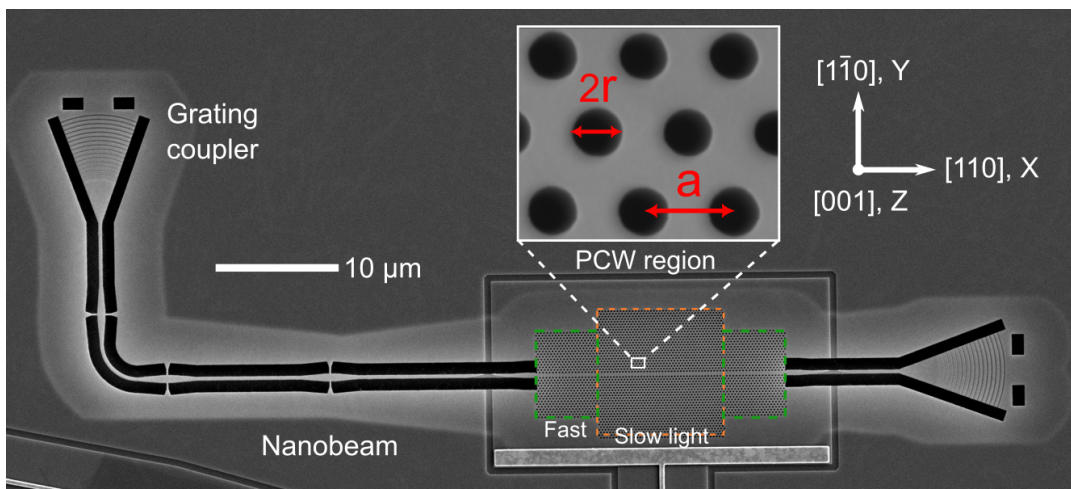


Figure 1.7: **Scanning Electron Micrograph (SEM) of a two-sided photonic-crystal waveguide (PCW).** The absence of air holes in the middle of the PCW region defines the waveguide. The device is fabricated along QD crystallographic axes, where we assume  $[1\bar{1}0]$  ( $[110]$ ) is parallel with the waveguide Y-axis (X-axis), thus for a QD at the waveguide center the coupling of Y-dipole (X-dipole) to the fundamental waveguide mode is enhanced (suppressed). Emission from a QD located in the slow light region is guided to the shallow-etched grating couplers [56] which have orthogonal linear polarizations. The couplers behave as diffraction gratings which scatter the guided light out-of-plane at an  $8.4^\circ$  angle, with  $> 82\%$  transmission efficiency [33].

In this thesis, a type of nanophotonic waveguides called photonic-crystal waveguide (PCW) is used to manifest the coupling between light and the embedded QDs. Figure 1.7 shows the Scanning Electron Micrograph (SEM) of a PCW with two outcoupling ports. The PCW is fabricated on the GaAs wafer along the QD crystallographic axes, where we take the waveguide Y-axis to be  $[1\bar{1}0]$ , to be consistent with notations in Sec. 1.3. At the center of the nanostructure, there is a periodic triangular lattice of air holes with hole radius  $r$  and lattice constant  $a$ , which are fabricated<sup>33</sup> by etching through the *p-i-n* diode shown in Fig. 1.2.

These periodic patterns alternating between air holes and GaAs cause modulation of the refractive index between  $n_{\text{air}} = 1$  and  $n_{\text{GaAs}} = 3.5$ , which leads to optical interference

<sup>32</sup>Assuming these QDs are not embedded in nanostructures, i.e., in bulk, and without distributed Bragg Reflectors underneath.

<sup>33</sup>See Ref. [57] for detailed fabrication details.

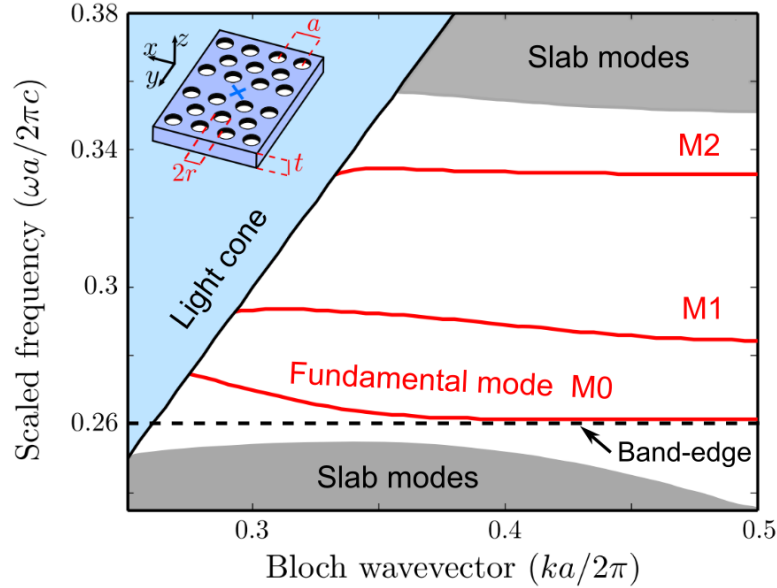


Figure 1.8: **Dispersion relation of photonic bands of a PCW.** The PCW comprises a periodic array of air holes forming a photonic bandgap (white region). One row of air holes is left out as a defect to allow coupling to a few optical modes (red lines) within the bandgap. The lattice constant  $a$  and hole radius  $r$  determine the dispersion relation. Light cone region includes unconfined modes with incident angles below the critical angle [58]. Slab modes refer to optical modes that are coupled to free space and the GaAs membrane. Adapted from Ref. [28].

between scattering waves that is highly dispersive (Bragg scattering [28]). At certain frequencies of light, its propagation through successive layers of air holes is inhibited due to destructive interference. This forbidden region of frequencies is called a photonic bandgap of photonic crystals [58], in direct analogy with the electronic bandgap arisen from periodic crystalline structure of semiconductors like GaAs (see Sec. 1.2.1).

Now, removing a single row of holes from the photonic crystal lattice creates a defect, in which a few optical modes are permitted within the photonic bandgap (Fig. 1.8). Here the bandgap lies between  $\omega a/2\pi c = [0.254, 0.361]$  [28], where  $c$  is the speed of light and  $\omega$  is frequency of the optical mode. Of relevance is the lowest-frequency mode M0 (also called the fundamental mode). For a lattice constant of  $a = 250$  nm, M0 hosts a range of allowed frequencies spanning  $\sim 313$ - $329$  THz, which is sufficiently broadband catering to the typical emission wavelength of our self-assembled QDs ( $\sim 950$  nm).

For a dipole placed at the center of the defect (blue cross in Fig. 1.8), M0<sup>34</sup> ideally couples only to the Y-dipole  $[1\bar{1}0]$  while X-dipole  $[110]$  does not<sup>35</sup>. Light travelling along the defect is thus confined in the plane of the lattice by photonic crystals, whereas the out-of-plane coupling is restricted by total internal reflection from the interface with air<sup>36</sup>,

<sup>34</sup>M0 is an even waveguide mode which has only the electric-field component  $E_y$  at the defect center, while M1 is odd meaning  $E_x$  is maximized at the center [33].

<sup>35</sup>In general M0 couples to both dipoles, with coupling strength dependent on the QD position and dipole orientations. Here we assume the dipole is perfectly centered and the fabricated waveguide aligns with the QD crystallographic axes.

<sup>36</sup>An  $\text{Al}_{0.3}\text{Ga}_{0.7}\text{As}$  sacrificial layer beneath the diode (Fig. 6.3) is etched away making the  $t \approx 180$  nm thick waveguide suspended in air. Therefore, the waveguide is interfaced with air from both the top and bottom.

comprising a photonic-crystal waveguide.

The radiative decay rate  $\Gamma_{\text{rad}}$  of an embedded dipole emitter largely depends on its spatial position in the defect as well as the orientation of the dipole relative to the waveguide.  $\Gamma_{\text{rad}}$  is given by [28]

$$\Gamma_{\text{rad}} = \frac{\pi\omega}{\hbar\epsilon_0} |\mathbf{d}|^2 \rho_{\text{LDOS}}(\omega, \mathbf{r}_0, \mathbf{e}_d), \quad (1.16)$$

where  $\epsilon_0$  is the vacuum permittivity.  $|\mathbf{d}|$  is magnitude of the dipole moment.  $\rho_{\text{LDOS}}(\omega, \mathbf{r}_0, \mathbf{e}_d)$  is the linear optical density of states (LDOS) experienced by the emitter at position  $\mathbf{r}_0$  and frequency  $\omega$ , which depends on the projection of the transition dipoles  $\mathbf{e}_d$  (introduced in Sec. 1.3) onto the normalized mode functions of the local electric field  $\mathbf{u}_{\mathbf{k}}(\mathbf{r})$  (waveguide modes), i.e.,

$$\rho_{\text{LDOS}}(\omega, \mathbf{r}_0, \mathbf{e}_d) \propto |\mathbf{e}_d \cdot \mathbf{u}_{\mathbf{k}}^*(\mathbf{r})|^2. \quad (1.17)$$

Eq. (1.16) is applicable for describing the decay rate of different dipole transitions for an emitter with a multi-level energy structure. Eq. (1.17) indicates that  $\Gamma_{\text{rad}}$  of different dipoles can be engineered by varying the emitter's spatial position in the waveguide, modifying the dipole polarizations via optical selection rules, or rotating the waveguide relative to the dipoles. In particular, this tunability realizes  $\Lambda$ -level emitters with equal decay rates (Sec. 2.6), or with one dominating transition (Secs. 3.4.3 and 6.3.2). The enhancement or suppression of the radiative decay rate is quantified by the waveguide-induced Purcell factor

$$F_{\text{P}} = \frac{\Gamma_{\text{rad}}(\omega, \mathbf{r}_0, \mathbf{e}_d)}{\Gamma_{\text{homo}}(\omega)} \propto n_g(\omega), \quad (1.18)$$

which is the ratio in radiative decay rates between a waveguide-embedded dipole emitter and the same emitter placed in a homogeneous medium (i.e., in bulk GaAs). For dipoles emitting light at frequencies very close to bottom edge of the waveguide band M0 (or band-edge in Fig. 1.8), the group velocity ( $v_g = d\omega/dk = c/n_g$ , slope of the M0 band) vanishes and light propagation begins to halt,  $\rho_{\text{LDOS}} \propto n_g(\omega)$  diverges leading to significant Purcell enhancement. A group index of  $n_g > 50$  [59] has been observed corresponding to  $F_{\text{P}} = 10$ . This also motivates the search for QDs emitting near the band-edge during initial sample characterization (see Sec. 6.3.1).

An important parameter to benchmark the coupling of the dipole emission to the guided mode is the  $\beta$ -factor, or the so-called single-photon coupling efficiency:

$$\beta = \frac{\Gamma_{\text{wg}}}{\Gamma_{\text{wg}} + \gamma_{\text{ng}} + \gamma_{\text{nr}}}, \quad (1.19)$$

where  $\Gamma_{\text{wg}} = \Gamma_{\text{rad}}^X + \Gamma_{\text{rad}}^Y$  includes radiative decay rates from both dipoles.  $\gamma_{\text{ng}}$  is the radiative decay rate into the non-guided mode<sup>37</sup>, and  $\gamma_{\text{nr}}$  is the non-radiative decay rate<sup>38</sup>. A near-unity  $\beta = 98.4\%$  [59] is measured for photonic-crystal waveguides thanks to the Purcell-enhanced  $\Gamma_{\text{wg}}$  on the waveguide mode and partial suppression of  $\gamma_{\text{ng}}$  from the photonic crystal bandgap.

<sup>37</sup>This includes coupling to higher-order TE-like modes M1 and M2, and out-of-plane TM modes.

<sup>38</sup>For instance, due to phonons, or non-radiative Auger processes for charged excitons [60].

## 1.5 Photon Emission and Single-photon Scattering

In this thesis, two different optical techniques are implemented to drive the quantum dot (QD) dipole transitions. Both are applicable to other quantum emitters. The differences between two techniques are summarized in Table 1.1 and explained in depth below.

The first method involves single-photon emission of a QD by pulsed excitations. A pulsed laser of duration  $T_{\text{pulse}}$  orders of magnitude shorter than the QD lifetime  $\tau_{\text{QD}}$  is typically adopted, which allows the QD to be ideally excited only once during the laser pulse. However, by Fourier transform this means the laser is spectrally a lot broader than the QD linewidth, a majority of the laser is thus off-resonant with the QD. To reach full population inversion of the QD ground state, sufficient optical power is thus needed. A pulse capable of populating the QD excited state is referred to as an optical  $\pi$ -pulse [61], and is used for single-photon emission. For a photon emitted following the decay of the excited state, its emission spectrum is ideally an Lorentzian broadened by the QD linewidth  $\Gamma$ , but in practice has a Voigt profile – a convolution between Lorentzian (homogeneous lifetime broadening) and Gaussian (inhomogeneous broadening due to spectral wandering, etc.) line shapes [28].

Schemes	Emission	Photon Scattering
Duration-lifetime ratio $T_{\text{pulse}}/\tau_{\text{QD}}$	$\ll 1$	$\gg 1$
Spectral width-linewidth ratio $\sigma_o/\Gamma$	$\gg 1$	$\ll 1$
Effective pulse area	$\pi$	$\ll \pi$
Ideal spectral line shape of the output photon	Lorentzian (given by the emitter)	Gaussian (given by the input pulse)
Waveguide implementation	Excite on top	Excite through waveguide

Table 1.1: Differences between two optical driving schemes used in the thesis. These are ideal general conditions considering a perfect two-level system for the emitter.

A second approach to optically address the QD state, is through scattering by single photons. Here the QD is treated as a coherent photon-scatterer instead of an emitter. For efficient scattering, the spectral width  $\sigma_o$  of the driving pulse needs to be narrower than the QD linewidth  $\Gamma$  such that the input photon appears to be monochromatic to the QD transition frequency [62, 63]. This however means the pulse is now longer than the QD lifetime where  $T_{\text{pulse}} = 1/\sigma_o \gg \tau_{\text{QD}} = 1/\Gamma$ , thus the QD could be repeatedly driven during the long pulse. To minimize the probability of over-driving (or re-excitation), it is therefore essential to drive the QD at a very low optical power<sup>39</sup>, such that ideally only a single photon interacts with the QD during the pulse. This means the mean photon number per pulse needs to be truncated to below the single-photon level ( $\bar{n} \ll 1$ ) [64]. Since the interaction is weak, the line shape of the scattered photon (assumed to be a Gaussian in Table 1.1) is ideally slightly perturbed [65] by the emitter's spectral response function (Lorentzian).

<sup>39</sup>This is why in a resonant waveguide-transmission experiment using a continuous-wave (the pulse is infinitely long) probe laser, the laser power needs to be set at only a fraction of the saturation power.

For a perfect two-level atom placed in a two-sided waveguide, we expect an incident field (single-photon state, resonant with the atomic transition) to be fully reflected, thus leading to full suppression of the incident field in the transmission due to destructive interference with the dipole emission, i.e., the so-called transmission dip in a typical resonant-transmission experiment. The origin of this destructive interference can be intuitively understood by invoking the elegant argument of energy conservation.

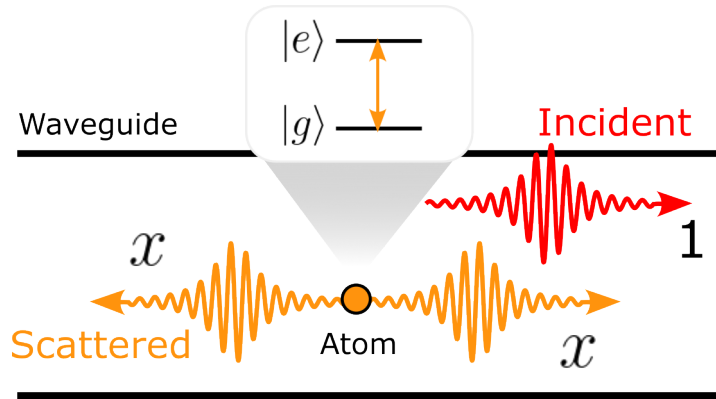


Figure 1.9: Scattering dynamics of a two-level atom.

Before scattering, we assume the weak incident field has a normalized amplitude of 1. There is no assumption on the resonant condition of the input field. Upon scattering with the two-level atom, due to symmetry of a non-chiral waveguide, we expect the dipole radiates fields equally in both backward and forward directions with scattering coefficient  $x$  (Fig. 1.9). In the forward direction, the transmitted field is a superposition of the incident and scattered fields. Since the energy before and after scattering is conserved, the total intensity from both the reflection ( $\mathcal{R}$ ) and transmission ( $\mathcal{T}$ ) should also be normalized, adding up to 1, hence

$$\mathcal{R} + \mathcal{T} = |x|^2 + |1 + x|^2 = 1. \quad (1.20)$$

Solving Eq. (1.20) gives  $x = 0, -1$  where  $x = 0$  ( $x = -1$ ) corresponds to off-resonant (resonant) scattering. For  $x = -1$ , the incident and forward scattered fields destructively interfere due to the  $\pi$ -phase shift, resulting in  $\mathcal{T} = 0$ . When  $x = 0$  there is no atomic response thus the off-resonant incident field transmits. As such, the atom behaves as a narrowband dichroic mirror: reflecting resonant light governed by the atomic linewidth while transmitting off-resonant frequencies.



## Chapter 2

# Quantum State Transfer from Photon to Spin

We kick off by presenting a theory to implement a two-qubit SWAP gate between a flying photon and a single quantum dot (QD) spin hosted on a nanophotonic chip. A SWAP gate is a quantum operation which coherently exchanges the quantum states between two qubits. In the context of long-range quantum networks, such gates could play an instrumental role in interfacing a flying qubit—an optical photon with a stationary quantum emitter, thus allowing fast information exchange between different nodes spread across the network. In this work, we provide the blueprint to transfer the state of a flying photon to a local QD spin embedded in a photonic-crystal waveguide (PCW). We present a perturbative analytical theory to describe the state-transfer fidelity, under all relevant experimental imperfections, as well as a complete numerical analysis applicable also beyond the perturbative approximation.

Although this work is a purely theoretical pursuit, it lays out a solid foundation for analyzing experimental limitations in a general quantum protocol, and provides helpful intuition to understand the influence of different errors prevalent on solid-state platforms (e.g., spectral diffusion, pure dephasing and spin dephasing). The developed theoretical tools are used throughout Chapters 3-7.

The basic principle of our photon-QD state-transfer protocol relies on single-photon Raman interaction (SPRINT) [66, 67, 68], which exploits passive Raman spin flip of the emitter’s initial state by virtue of the destructive interference between the incident and scattered fields in a waveguide geometry. While SPRINT have been experimentally applied on various platforms to realize photon-atom SWAP gate [68], single-photon router [69] and deterministic frequency down-conversion [70], the theoretical and experimental implementation of SPRINT on a QD platform has not been considered. The main purpose of this work is therefore to provide a complete theory of SPRINT under practical limitations of the QD-waveguide platform, which would guide future experiments.

The numerical simulation is performed by Ziv Aqua.

## 2.1 Summary of Results

Before diving into technicalities of the theory, it is instructive to first give a short summary of all important results in this work.

The quantum-state transfer protocol presented here is designed for a QD embedded in a one-sided nanophotonic waveguide, but can be extended to other solid-state emitters. The QD features a  $\Lambda$ -type level structure (Fig. 2.1a), where an excited state  $|e\rangle$  decays to two meta-stable spin states  $|g_1\rangle$  and  $|g_2\rangle$  with decay rates  $\Gamma_1$  and  $\Gamma_2$ , respectively. State transfer proceeds by launching a frequency-encoded photon (encoded in a superposition of two frequency states  $|\omega\rangle_1$  and  $|\omega\rangle_2$ ) into the waveguide, where  $\omega_1$  and  $\omega_2$  are different frequencies of a photon. The frequency  $\omega_i$  is resonant with the QD optical transition between  $|g_i\rangle$  and  $|e\rangle$ .

The QD is initially prepared in state  $|g_1\rangle$  and scatters either of the two optical frequencies. For optimum operation, the decay rates for the two QD transitions should be equal ( $\Gamma_1 = \Gamma_2$ ), which is naturally the case for a QD in a bulk sample subject to an in-plane magnetic field [42]. Photonic nanostructures, however, generally introduce a decay rate asymmetry as controlled by the projected local density of optical states [20]. Proper spatial positioning of the QD in the waveguide [71] would therefore be required to meet the symmetry condition, but this is still compatible with the near-unity coupling efficiency [28]. The dynamics of the state-transfer is most easily understood by considering two separate *cases*, corresponding to each of the two possible incoming frequencies:

*Case 1:* an incoming photon at frequency  $\omega_1$  resonantly drives the initial spin state  $|g_1\rangle$  to the excited state  $|e\rangle$ . For  $\Gamma_1 = \Gamma_2$ , the excited state has an equal probability to decay on either of the transitions to the two spin ground states. In the ideal limit of a deterministic and coherent photon-emitter interface (i.e., high single-photon coupling efficiency  $\beta$  and low decoherence [35]), the incident and scattered fields interfere destructively [62]. As a consequence, only a photon at frequency  $\omega_2$  is emitted and the spin state will be deterministically toggled to the state  $|g_2\rangle$  [63], cf. left illustration of Fig. 2.1b. This is a Raman process driven by a single photon, i.e., the SPRINT interaction.

*Case 2:* the incoming photon of frequency  $\omega_2$  is detuned from the QD transition by the ground-state splitting  $\omega_2 - \omega_1 = \Delta$ , which leads to only a small probability to excite the QD and therefore to drive the Raman transition. Ideally, i.e., for a large detuning, the incident photon does not interact with the QD and is thus fully reflected back from the one-sided waveguide, cf. the right box of Fig. 2.1b.

By combining the two processes, i.e., for an input photon pulse prepared in a superposition of the two frequencies  $|\psi_p\rangle = c_a|\omega_1\rangle + c_b|\omega_2\rangle$  (Fig. 2.1a), a separable frequency-spin state is generated, as described by the input-output relation

$$|\psi_p\rangle \otimes |g_1\rangle \xrightarrow{\text{ideal}} |\omega_2\rangle \otimes |\psi_s\rangle, \quad (2.1)$$

where the output spin qubit  $|\psi_s\rangle = i\hat{Y}(c_a|g_1\rangle + c_b|g_2\rangle)$  is equivalent to the input quantum state up to a local Pauli-Y rotation. Effectively this operation maps the initial photonic state onto the QD spin. This process is passive as no active control fields are required to trigger the scattering process. Moreover, by heralding the gate upon the detection of an output photon, our scheme becomes very robust to the considered imperfections. Since the outgoing photon is always supposed to have a frequency  $\omega_2$  this robustness can be further enhanced by adding a frequency filter which removes photons of the wrong frequency before the heralding.

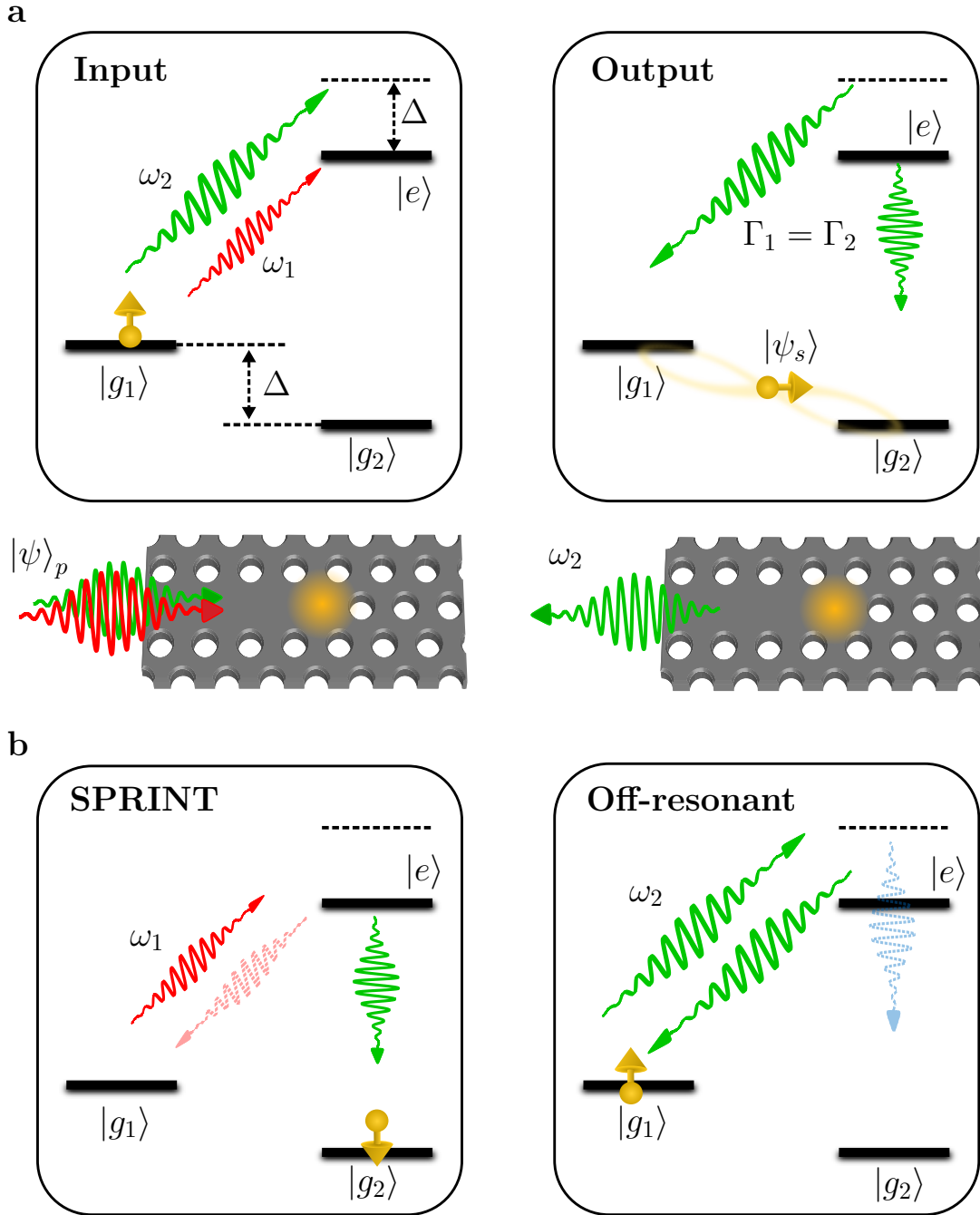


Figure 2.1: **Schematics of the photon-to-spin state transfer in a  $\Lambda$ -level emitter coupled to a one-sided nanophotonic waveguide.** (a) **Left:** Initial state of the spin-photon system, where the superposition state  $|\psi_p\rangle$  is encoded in frequency bins  $|\omega_1\rangle$  and  $|\omega_2\rangle$  separated by the ground-state splitting  $\Delta$ . The photonic qubit scatters off an emitter (orange dot) initialized in state  $|g_1\rangle$ . **Right:** the photonic state  $|\psi_p\rangle$  is deterministically transferred to the spin carrier  $|\psi_s\rangle$ . With symmetric decay rates  $\Gamma_1 = \Gamma_2$  the final spin state corresponds to the incoming photonic state due to the superposition of SPRINT and off-resonant scattering. (b) **Left:** SPRINT, where a resonant photon flips the spin state from  $|g_1\rangle$  to  $|g_2\rangle$  (solid green arrow). Imperfections induce a small probability to decay to the original spin state (dotted pink arrow). **Right:** Off-resonant scattering, where the photon is almost unaffected (solid green arrow). There is a small probability to flip the spin (dotted light blue arrow) due to finite  $\Delta$ .

To characterize the performance of the state transfer we consider the Choi-Jamiolkowski fidelity  $\mathcal{F}_{\text{transfer}}^{\text{CJ}}$  [72, 73, 74]. In Sec. 2.3 we derive that in the presence of experimental imperfections of the QD-waveguide system, the infidelity is given by

$$1 - \mathcal{F}_{\text{transfer}}^{\text{CJ}} = \frac{3\sigma_o^2}{\Gamma^2} + \frac{3\sigma_e^2}{\Gamma^2} + \frac{3\gamma_d}{2\Gamma} + \frac{(\varepsilon - \gamma)^2}{2\Gamma^2} + \frac{3\Gamma^2}{16\Delta^2} + \frac{1}{8} \frac{1}{\sigma_o^2 T_2^{*2}}, \quad (2.2)$$

where the physical meaning of each variable is provided in Table 2.1.

Variable	Description
$\Gamma$	Total decay rate of the QD ( $\text{ns}^{-1}$ )
$\Gamma_i$	Radiative decay rate of the QD transition $ e\rangle \rightarrow  g_i\rangle$ into the waveguide ( $\text{ns}^{-1}$ )
$\sigma_o$	Standard deviation of the spectral width of the incident Gaussian optical pulse ( $\text{ns}^{-1}$ )
$\sigma_e$	Standard deviation of the optical frequency fluctuation due to spectral diffusion ( $\text{ns}^{-1}$ )
$\gamma_d$	Pure dephasing rate ( $\text{ns}^{-1}$ )
$\gamma$	Coupling rate to modes outside the waveguide ( $\text{ns}^{-1}$ )
$\varepsilon$	Asymmetry in decay rates: $\varepsilon = \Gamma_1 - \Gamma_2$ ( $\text{ns}^{-1}$ )
$\Delta$	Ground-state splitting: $\Delta = \omega_2 - \omega_1$ ( $\text{ns}^{-1}$ )
$T_2^*$	Spin dephasing time (ns)

Table 2.1: Description of each variable in Eq. (2.2).

Eq. (2.2) holds in the perturbative limit, corresponding to the condition set by the inequalities:  $(\sigma_o, \sigma_e, \gamma_d, \gamma, \varepsilon) \ll \Gamma \ll \Delta$  and  $1/T_2^* \ll \sigma_o$ . This result assumes the protocol is conditioned on a heralding a photon in the output but without frequency filtering. The physical meaning of these inequalities are summarized as follows:

1. The incident photon should have a narrow bandwidth ( $\sigma_o \ll \Gamma$ ) and couple strongly to the waveguide ( $\gamma \ll \Gamma$ ) for efficient photon-emitter interaction;
2. The spin dephasing time of the emitter needs to be longer than the duration of the incoming pulse ( $T_2^* \gg 1/\sigma_o$ );
3. The emitter should have a symmetric  $\Lambda$ -system ( $\varepsilon \ll \Gamma$ ) with low coupling to its external environment ( $\sigma_e, \gamma_d \ll \Gamma$ );
4. Finally  $\Delta \gg \Gamma$  ensures that off-resonant spin-flip process is highly suppressed.

Remarkably, the fidelity in Eq. (2.2) scales quadratically with almost all of the considered imperfections. Only the third term, which describes pure dephasing on the optical transitions, is linear. For QDs, such dephasing arises from elastic phonon scattering that broadens the zero-phonon line [75, 76] leading to incoherent scrambling of the phase of the mapped state. In contrast, inelastic phonon sidebands can readily be removed with optical filtering and thereby be absorbed in the loss rate  $\gamma$ , which has a much weaker effect (to the second order) on the fidelity.

In the subsequent sections, we first revisit the formalism for photon-scattering in a waveguide, and describe the ideal state transfer scheme in Sec. 2.2. With the theoretical basis established, we will evaluate how imperfections affect the state-transfer fidelity (Eq. (2.2)) and give physical intuition of their roles in Sec. 2.3. To explore the experimental feasibility of the scheme, in Sec. 2.6 we estimate the fidelity under realistic conditions and compare with the atom-cavity setup in Ref. [67].

## 2.2 Photon Scattering Formalism

We begin this section by revisiting the photon scattering formalism in Ref. [63, 77] for an emitter embedded in a one-sided waveguide. The formalism here is the skeleton for most of the theoretical work done throughout this thesis (i.e., Chapter 4). Next, we proceed to describe the ideal protocol for the photon-to-emitter state transfer.

### 2.2.1 Photon Scattering in One-sided Waveguides

We consider an emitter consisting of three energy levels with a  $\Lambda$  configuration shown schematically in Fig. 2.1. The emitter is located at a position  $z_0 = 0$  inside a one-sided waveguide. The Hamiltonian describing such a system ( $\hbar = 1$ ) under the rotating-wave approximation is

$$\begin{aligned}\hat{\mathcal{H}} &= \hat{\mathcal{H}}_{\text{emitter}} + \hat{\mathcal{H}}_{\text{field}} + \hat{\mathcal{H}}_{\text{int}} \\ &= \sum_{i=1,2} (\omega_e - \omega_i) \hat{\sigma}_{ii} + \omega_e \hat{\sigma}_{ee} - i \int dz \hat{a}_e^\dagger(z) \frac{\partial}{\partial z} \hat{a}_e(z) \\ &\quad + \sum_{j=1,2} \int dz \delta(z - z_0) \sqrt{\Gamma_j} \hat{a}_e^\dagger(z) \hat{\sigma}_{ej} + \text{H.c.},\end{aligned}\tag{2.3}$$

where  $\omega_e$  is the frequency of the excited state  $|e\rangle$ ;  $\omega_i$  is the transition frequency from  $|g_i\rangle \rightarrow |e\rangle$ ;  $\hat{a}_e^\dagger$  is the photon creation operator of the even waveguided mode, which is a superposition of the right and left-propagating modes in a two-sided waveguide [63], and obeys the commutator relation  $[\hat{a}_e(z), \hat{a}_e^\dagger(z')] = v_g \delta(z - z')$ ;  $v_g$  is the group velocity of the waveguided mode;  $\hat{\sigma}_{ij} = |j\rangle\langle i|$  is the atomic operator;  $\Gamma_j$  is the radiative decay rate of the transition  $|e\rangle \rightarrow |g_j\rangle$  into the waveguide.

The scattering problem of a  $\Lambda$ -level emitter for weak input fields has been solved in Ref. [77]. From the non-Hermitian Hamiltonian  $\hat{\mathcal{H}}_{\text{nh}}$  that describes the dynamics of the excited-state manifold, we can directly express the output field-mode operator of the waveguide  $\hat{a}_{\text{out}}$  in terms of the incident field and dynamical response of the emitter. This allows us to easily derive the scattering matrix and spectra of the scattered fields. Assuming the emitter is initialized in the state  $|g_1\rangle$ , the non-Hermitian Hamiltonian describing the dynamics of the emitter is [77]

$$\hat{\mathcal{H}}_{\text{nh}} = \left( \delta_1 - \frac{i\Gamma}{2} \right) \hat{\sigma}_{ee} \equiv \tilde{\delta}_1 \hat{\sigma}_{ee},\tag{2.4}$$

where  $\delta_1 = \omega_1 - \omega$  is the detuning of the transition  $|g_1\rangle \rightarrow |e\rangle$  with respect to a driving field of frequency  $\omega$ .  $\Gamma = \sum_{j=1,2} [\Gamma_j + \gamma_j]$  is the total decay rate of the excited state  $|e\rangle$  and  $\gamma_j$  the radiative loss for photons emitted in the transition  $|e\rangle \rightarrow |j\rangle$  that do not couple to the waveguided mode.

For a weak incident field  $\hat{a}_{\text{in},e}$  propagating in the waveguide, the output field operator  $\hat{a}_{\text{out},e}$  at an observation point  $z > 0$  is found to be

$$\hat{a}_{\text{out},e}(z, t) = \left[ 1 - \frac{2\Gamma_1}{\Gamma + 2i\delta_1} \hat{\sigma}_{11} - \frac{2\sqrt{\Gamma_1\Gamma_2}}{\Gamma + 2i\delta_1} \hat{\sigma}_{12} \right] \hat{a}_{\text{in},e}(z - v_g t). \quad (2.5)$$

The origin of destructive interference that governs SPRINT can be inferred from Eq. (2.5): The first and second terms represent the transmitted field and the Rayleigh-scattered field respectively. When the  $\Lambda$ -level system has symmetric decay rates with no loss ( $\Gamma_1 = \Gamma_2, \gamma = 0$ ) and the incident field is resonant with the transition  $|g_1\rangle \rightarrow |e\rangle$  ( $\delta_1 = 0$ ), the transmitted and scattered  $\omega_1$  fields exhibit complete destructive interference, which leaves only the output at frequency  $\omega_2$  (the third term) in the waveguide and simultaneously flips the emitter's spin state (due to energy conservation).

## 2.2.2 Ideal Protocol

In this section, we derive the ideal input-output relation (Eq. (2.1)) for the photon-to-spin state transfer based on Eq. (2.5). This input-output relation allows us to compute the state-transfer fidelity in Sec. 2.3.

Initially, the emitter in the one-sided waveguide is in the state  $|g_1\rangle$ . We send a frequency-encoded qubit in the superposition state  $|\psi_p\rangle_G = c_a|\omega_1\rangle_G + c_b|\omega_2\rangle_G$  into the waveguide, where  $|\omega_i\rangle_G$  describes a Gaussian electric field profile  $\Phi_i(\omega)$  with central frequency  $\omega_i$ :

$$|\omega_i\rangle_G = \int_{-\infty}^{\infty} \Phi_i(\omega) |\omega\rangle d\omega = \int_{-\infty}^{\infty} (2\pi\sigma_o^2)^{-\frac{1}{4}} \exp\left(-\frac{(\omega - \omega_i)^2}{4\sigma_o^2}\right) \hat{a}^\dagger(\omega) |\emptyset\rangle d\omega. \quad (2.6)$$

Note that in the definition of the input qubit state  $|\psi_p\rangle_G$  we implicitly assume that the two frequency states  $|\omega_1\rangle_G$  and  $|\omega_2\rangle_G$  are orthogonal  ${}_G\langle\omega_1|\omega_2\rangle_G \approx 0$ . Due to the finite width of the Gaussian  $\sigma_o$ , this is a valid approximation since the overlap decreases exponentially with  $\Delta/\sigma_o$  leading to an error that is negligible compared to the other infidelity terms in Eq. (2.2), which are only polynomially small.

For an arbitrary frequency qubit on the Bloch sphere,  $|c_a|^2 + |c_b|^2 = 1$  for  $c_a, c_b \in \mathbb{C}$ . We then set  $c_a = \cos(\theta/2)$ ,  $c_b = e^{i\phi} \sin(\theta/2)$ , where  $\phi \in [0, 2\pi]$  and  $\theta \in [0, \pi]$ .

The frequency qubit subsequently interacts with the emitter spin in the waveguide, and the final state evolves according to

$$\begin{aligned} |\psi_p\rangle \otimes |g_1\rangle &= c_a |\omega_1\rangle_G |g_1\rangle + c_b |\omega_2\rangle_G |g_1\rangle \\ &\rightarrow c_a \hat{t}_1^a |\omega_1\rangle_G |g_1\rangle + c_a \hat{t}_2^a |\omega_2\rangle_G |g_2\rangle + c_b \hat{t}_1^b |\omega_2\rangle_G |g_1\rangle + c_b \hat{t}_2^b |\omega_2 + \Delta\rangle_G |g_2\rangle, \end{aligned} \quad (2.7)$$

where  $\hat{t}_m^i$  is the scattering operator acting on the photon-spin state  $|\omega\rangle_G |g_m\rangle$  for  $m \in \{1, 2\}$ ;  $i \in \{a, b\}$  indicates the type of scattering process occurred: “a” denotes resonant scattering (SPRINT), corresponding to an input state  $|\omega_1\rangle_G$ , while “b” means off-resonant scattering, corresponding to an input state  $|\omega_2\rangle_G$ . We note that the scattering amplitudes should be convoluted with the Gaussian photonic profile  $\Phi(\omega)$  and integrated within the same integral. For ease of notation we simply represent this as a frequency dependent operator  $\hat{t}_m^i$  acting on the state.  $c_i$  are normalized probability amplitudes before scattering.

The scattering amplitudes can be directly read from Eq. (2.5):

$$\begin{aligned} t_1^a &= 1 - \frac{2\Gamma_1}{\Gamma + 2i\delta_1}, & t_2^a &= \frac{-2\sqrt{\Gamma_1\Gamma_2}}{\Gamma + 2i\delta_1}, \\ t_1^b &= 1 - \frac{2\Gamma_1}{\Gamma + 2i(\delta_2 - \Delta)}, & t_2^b &= \frac{-2\sqrt{\Gamma_1\Gamma_2}}{\Gamma + 2i(\delta_2 - \Delta)}, \end{aligned} \quad (2.8)$$

and are consistent with Eq. (22) in Ref. [63].  $\delta_1 = \omega_1 - \omega = \delta_2 - \Delta$  is the laser detuning from the transition  $|g_1\rangle \rightarrow |e\rangle$  for an emitter initialized in  $|g_1\rangle$ .

In the ideal limit, where  $\gamma = \gamma_1 + \gamma_2 = 0$  (all emitted photons couple to the even waveguided mode),  $\Gamma_1 = \Gamma_2 = \Gamma/2$  (equal decay rates),  $\delta_1 = \delta_2 = 0$  (zero detuning),  $\Delta \gg \Gamma$  (no off-resonant spin flip),  $\sigma_o = 0$  (so  $\Phi_i(\omega) = \delta(\omega - \omega_i)$  for monochromatic incident field) and assuming a perfect emitter with no dephasing, the input-output relation in Eq. (2.7) becomes

$$|\psi_p\rangle \otimes |g_1\rangle \xrightarrow{\text{ideal}} -c_a|\omega_2, g_2\rangle + c_b|\omega_2, g_1\rangle = |\omega_2\rangle \otimes i\hat{Y}(c_a|g_1\rangle + c_b|g_2\rangle) = |\omega_2\rangle \otimes |\psi_s\rangle,$$

which is Eq. (2.1). It describes the ideal protocol for transferring the quantum state of an input photonic qubit  $|\psi_p\rangle$  to the spin carrier  $|\psi_s\rangle$ , as depicted in Fig. 2.1. In this case, there is perfect destructive interference between the incident and scattered fields at frequency  $\omega_1$  ( $t_1^a \rightarrow 0, t_2^a \rightarrow -1$ ). Furthermore, ( $t_1^b \rightarrow 1, t_2^b \rightarrow 0$ ) means that the off-resonant field  $\omega_2$  is fully transmitted. In reality, sources of errors will affect the scattering amplitudes and thus fidelity of the protocol. In the next section we will evaluate the influence of such errors on the fidelity.

## 2.3 Fidelity under Various Noises

Next, we analyze the fidelity of the quantum state transfer process. The general strategy that we take is to evaluate the fidelity to lowest order in perturbation theory for each of the possible errors independently. In the end the full fidelity can then be found by adding all errors. Cross terms between different errors will only appear as higher order terms (product of errors) and thus do not appear to lowest order. This allows us to treat each imperfection separately, assuming all other parameters to have their ideal values.

For clarity, we first divide the protocol into three different parts: resonant scattering (Sec. 2.3.1), off-resonant scattering (Sec. 2.3.2), and scattering of a superposition of frequency states (Sec. 2.3.3). Finally the fidelity of the whole state transfer is presented in Sec. 2.3.4.

### 2.3.1 Resonant Scattering in QD-waveguide Systems

When the incident frequency qubit is  $|\omega_1\rangle_G$  corresponding to  $\theta = 0$  or  $c_a = 1$ , the incoming field is resonant with the QD transition  $|g_1\rangle \rightarrow |e\rangle$ . In this case the dynamics is given by

$$|\omega_1\rangle_G |g_1\rangle \rightarrow \hat{t}_1^a |\omega_1\rangle_G |g_1\rangle + \hat{t}_2^a |\omega_2\rangle_G |g_2\rangle, \quad (2.9)$$

In the case of ideal SPRINT,  $t_1^a = 0$  and  $t_2^a = -1$  result in the state  $-|\omega_2\rangle_G |g_2\rangle$ . Throughout this chapter we consider the protocol to be conditioned on the detection of a photon in the output, since this allows us to reduce the effect of several kinds of errors. Demanding a photon in the output, we can express the fidelity of the process by

$$\mathcal{F}_{\omega_1}^{(c)} = \frac{\langle g_2 | \text{Tr}_{\omega} \rho | g_2 \rangle}{\text{Tr} \rho} \quad (2.10)$$

$$= \frac{\eta_{\omega_2} P_{g_2}}{\eta_{\omega_1} P_{g_1} + \eta_{\omega_2} P_{g_2}} = \begin{cases} \frac{P_{g_2}}{P_{g_1} + P_{g_2}} & \text{(no filter);} \\ 1 & \text{(filter at } \omega_2), \end{cases} \quad (2.11)$$

where  $\rho$  is the density matrix of the output state in Eq. (2.9). In the first line the index  $\omega$  on the trace indicates that we only trace over the detection of photons of frequency  $\omega$ . The photon detection can be frequency selective, e.g., by inserting a frequency filter before the detection of the heralding photon, so that the trace over detected photons may depend on the frequency. If a filter is present we assume the filter bandwidth to be wider than the photon bandwidth but not wider than the ground-state splitting. As such, any spectral detuning is preserved in the infidelity while different frequency components corresponding to undesired transitions are filtered out. Less than perfect filtering can be represented by the efficiency  $\eta_{\omega_i}$  of the filter at frequency  $\omega_i$ , but for simplicity we mainly consider no filter  $\eta_{\omega_i} = 1$  or perfect filtering of photons  $\eta_{\omega_2} = 1$ ,  $\eta_{\omega_i} = 0$  for  $i \neq 2$ . Since we consider an incoming photon of frequency  $\omega_1$  which has the scattering amplitude  $t_m^a$ , the probability of the emitter to be in the state  $|g_m\rangle$  after the scattering is

$$P_{g_m} = \int_{-\infty}^{\infty} |t_m^a(\omega) \Phi_1(\omega)|^2 d\omega, \quad (2.12)$$

where the integrand is the convolution of the frequency distribution of the incoming photon  $|\Phi_i(\omega)|^2$  with the frequency dependent scattering probability  $|t_m^a(\omega)|^2$ . The success

probability  $P^s \equiv \text{Tr } \rho$  of SPRINT is the probability of detecting a photon regardless of the final spin state:

$$P^s = \eta_{\omega_1} P_{g_1} + \eta_{\omega_2} P_{g_2} = \begin{cases} P_{g_1} + P_{g_2} & \text{(no filter);} \\ P_{g_2} & \text{(filter at } \omega_2\text{)}. \end{cases} \quad (2.13)$$

### 2.3.1.1 Spectral Mismatch Errors

The bandwidth of the pulse  $\sigma_o$  described in (2.6) will affect the state transfer quality since the scattering probability depends on the frequency of the photons. In addition, residual inhomogeneous broadening of the emitter may also hinder the performance via slow (compared to the emission lifetime) spectral diffusion of the QD parameterized by  $\sigma_e$ . Relevant slow spectral diffusion processes include Overhauser fluctuations from the QD nuclear spin bath [78, 79, 80] or electric noise from localized charged defects giving rise to Stark tuning [81]. To model these effects, we introduce a small spectral shift  $\delta_1 \rightarrow \delta_1 + \delta_e$ , where  $\delta_e$  follows a Gaussian stochastic profile  $N(0, \sigma_e)$  with root-mean-square fluctuations  $\sigma_e$ .

Using (2.8), (2.12) and the above formalism, the individual probabilities of each output state in Eq. (2.11) are

$$\begin{aligned} P_{g_1} &= \int_{-\infty}^{\infty} \frac{1}{\sqrt{2\pi\sigma_o^2}} e^{-\frac{\delta_1^2}{2\sigma_o^2}} \left| 1 - \frac{\Gamma}{\Gamma + 2i(\delta_1 + \delta_e)} \right|^2 d\omega \\ &\approx \frac{4\sigma_o^2}{\Gamma^2} + \frac{4\delta_e^2}{\Gamma^2} = 1 - P_{g_2}. \end{aligned} \quad (2.14)$$

Averaging the fidelity  $\mathcal{F}_{\omega_1}^{(c)}(\delta_e)$  over  $N(0, \sigma_e)$  results in

$$\mathcal{F}_{\omega_1}^{(c)} = 1 - \frac{4\sigma_o^2}{\Gamma^2} - \frac{4\sigma_e^2}{\Gamma^2} \quad \text{(no filter)}, \quad (2.15)$$

and  $\mathcal{F}_{\omega_1}^{(c)} = 1$  with filtering. The success probability is  $P^s = 1$  for the unfiltered case, while  $P^s = 1 - 4\sigma_o^2/\Gamma^2 - 4\sigma_e^2/\Gamma^2$  with filtering. Note that for the lowest-order approximation in (2.14), the spectral fluctuations are assumed to be small compared to the QD linewidth, i.e.,  $\sigma_o, \sigma_e \ll \Gamma$ .

### 2.3.1.2 Coupling Errors

Errors arising from imperfections in the QD-waveguide coupling include loss of the emitted photons at a rate  $\gamma = \gamma_1 + \gamma_2 \neq 0$  and asymmetric decay rates  $\varepsilon = \Gamma_1 - \Gamma_2 \neq 0$ , which create an imbalance in population between basis states  $|\omega_2\rangle_G |g_2\rangle$  and  $|\omega_2\rangle_G |g_1\rangle$  after the state transfer (2.7), reducing the transfer fidelity. The potential causes of such errors are residual coupling of the QD dipole transition to modes outside the waveguide and unequal Purcell factors of the two orthogonal dipole transitions.

To take these errors into consideration, we introduce additional loss terms in Eq. (2.4) to represent couplings to modes outside the waveguide where the total decay rate is  $\Gamma = \Gamma_1 + \Gamma_2 + \gamma$ . Including these effects yields

$$\begin{aligned} P_{g_1} &\approx \left| 1 - \frac{2\Gamma_1}{\Gamma} \right|^2 = \frac{(\varepsilon - \gamma)^2}{\Gamma^2}, \\ P_{g_2} &\approx \left| -\frac{2\sqrt{\Gamma_1\Gamma_2}}{\Gamma} \right|^2 = 1 - \frac{2\gamma}{\Gamma} - \frac{(\varepsilon^2 - \gamma^2)}{\Gamma^2}, \end{aligned} \quad (2.16)$$

where  $\Gamma_{1/2} = (\Gamma - \gamma \pm \varepsilon)/2$ . We note that since these probabilities include the probability to have a photon coming out of the waveguide they do not add up to unity when a photon is lost  $\gamma \neq 0$ . In particular, the transfer probability  $P_{g_2}$  has a first-order dependence on the coupling loss  $\gamma/\Gamma$ , which reflects the probability for the scattered photon to be lost. Here we are, however, interested in the fidelity heralded on detection of a photon in the outgoing mode. In this case events where the photon is lost do not contribute to the fidelity, which is thus only affected by the probability for the system ending up in the wrong state  $|g_1\rangle$  while having a photon in the waveguide. This results in the fidelity

$$\mathcal{F}_{\omega_1}^{(c)} = 1 - \frac{(\varepsilon - \gamma)^2}{\Gamma^2} \quad (\text{no filter}), \quad (2.17)$$

whereas  $\mathcal{F}_{\omega_1}^{(c)} = 1$  with filtering.

The reduction in fidelity is thus second order in the errors whereas the first order term only influences the success probability:

$$P^s = \begin{cases} 1 - \frac{2\gamma}{\Gamma} - \frac{2\gamma(\varepsilon - \gamma)}{\Gamma^2} & (\text{no filter}); \\ 1 - \frac{2\gamma}{\Gamma} - \frac{(\varepsilon^2 - \gamma^2)}{\Gamma^2} & (\text{filter at } \omega_2). \end{cases} \quad (2.18)$$

### 2.3.1.3 Phonon-induced Pure Dephasing

The interaction of the QD with phonons in the semiconductor material leads to decoherence of optical transitions. This decoherence results in both broad phonon sidebands and a broadening of the zero-phonon line. The phonon sideband can be filtered away with spectral filters and its contribution is included in the loss  $\gamma$  considered above, whereas the broadening of the zero-phonon line due to elastic phonon scattering is the main source of pure dephasing in the current protocol [82, 83, 76, 75].

The elastic scattering with a single phonon imprints random phases onto the excited state. We model this fast (compared to the emission lifetime) incoherent process as pure Markovian dephasing with a rate  $\gamma_d$  and the Lindblad operator  $\sqrt{2\gamma_d}\hat{\sigma}_{ee}$ . In the quantum jump approach [84], which is reminiscent of the approach with a non-Hermitian Hamiltonian that we consider here, this dephasing leads to a quantum jump to the excited state  $|e\rangle$  followed by decay to either of the two ground states with probabilities set by the branching ratio. This leads to the density matrix

$$\rho' = \rho + P_{\gamma_d}^{\omega_1} \rho_{\gamma_d}^{\omega_1} \otimes |g_1\rangle\langle g_1| + P_{\gamma_d}^{\omega_2} \rho_{\gamma_d}^{\omega_2} \otimes |g_2\rangle\langle g_2|. \quad (2.19)$$

Here  $\rho$  is the density matrix in the absence of a dephasing quantum jump, and  $\rho_{\gamma_d}^{\omega_i} \otimes |g_i\rangle\langle g_i|$  are density matrices resulting from the incoherent dephasing with probabilities given by

$$P_{\gamma_d}^{\omega_i} = \frac{\Gamma_i}{\Gamma} P_{\gamma_d} \approx \frac{\Gamma_i}{\Gamma} \left| \frac{-2\sqrt{2\gamma_d\Gamma_1}}{\Gamma} \right|^2. \quad (2.20)$$

Eq. (2.20) is derived by adding a decay channel described by the dephasing operator  $\hat{t}_{\gamma_d}$  to the scattering dynamics and evaluating the probability for the decay to happen through this channel. After the decay the system performs a quantum jump to the excited state (with a dephasing probability  $P_{\gamma_d}$ ) after which it can decay to the ground state  $|g_i\rangle$  with a probability  $\Gamma_i/\Gamma$  by emitting a photon into the waveguide with a normalized photon density matrix  $\rho_{\gamma_d}^{\omega_i}$ .

We here ignore any coherences between the ground states, which is justified for  $\Gamma \ll \Delta$ , where the emitted photons are distinguishable for the two transitions. In principle the photons emitted after the incoherent dephasing will be broader in frequency than the coherently scattered photons [85] which may lead to a different filtering efficiency. For simplicity we shall, however, ignore this difference and assume the filter bandwidth to be wide enough to preserve the broadened photon bandwidth but narrow enough to filter out phonon sidebands.

In expanding  $P_{\gamma_d}$  and the output state probabilities  $P_{g_i}$ , we substitute  $\Gamma'_{1/2} = (\Gamma - 2\gamma_d - \gamma \pm \varepsilon)/2$  as the additional dephasing channel  $\hat{t}_{\gamma_d}$  appends an imaginary term  $-i\gamma_d$  to Eq. (2.4) [77]. The probability for the incoherent excited state to decay is governed only by the branching ratio  $\Gamma_{1/2} = (\Gamma - \gamma \pm \varepsilon)/2$ . This gives

$$\begin{aligned} P_{\gamma_d}^{\omega_{1/2}} &= \frac{2\gamma_d}{\Gamma} \left( 1 - \frac{2\gamma}{\Gamma} + (1 \pm 1) \frac{\varepsilon}{\Gamma} - \frac{2\gamma_d}{\Gamma} \right), \\ P_{g_1} &\approx \left| 1 - \frac{2\Gamma'_1}{\Gamma} \right|^2 \approx \frac{4\gamma_d^2}{\Gamma^2} - \frac{4\gamma_d(\varepsilon - \gamma)}{\Gamma^2}, \\ P_{g_2} &\approx \left| -\frac{2\sqrt{\Gamma'_1\Gamma'_2}}{\Gamma} \right|^2 \approx 1 - \frac{4\gamma_d}{\Gamma} + \frac{4\gamma_d^2}{\Gamma^2} + \frac{4\gamma_d\gamma}{\Gamma^2}. \end{aligned} \quad (2.21)$$

Eq. (2.21) is simplified by considering terms only to lowest order in  $\gamma_d$  and ignoring other errors. Replacing  $\rho$  in (2.10) by the new spin-photon density matrix  $\rho'$  (2.19), the fidelity under phonon-induced pure dephasing is

$$\mathcal{F}_{\omega_1}^{(c)} = 1 - \frac{2\gamma_d}{\Gamma} \quad (\text{no filter}), \quad (2.22)$$

while  $\mathcal{F}_{\omega_1}^{(c)} = 1$  with filtering. In the latter case the infidelity is converted into inefficiency as evident from the success probability

$$P^s = \sum_{i=\{1,2\}} \eta_{\omega_i} (P_{g_i} + P_{\gamma_d}^{\omega_i}) = \begin{cases} 1 & (\text{no filter}); \\ 1 - \frac{2\gamma_d}{\Gamma} & (\text{filter at } \omega_2). \end{cases} \quad (2.23)$$

### 2.3.1.4 SPRINT Fidelity

Taking all the above errors into account, the SPRINT fidelity is found to be

$$\mathcal{F}_{\omega_1}^{(c)} \approx 1 - \frac{4\sigma_o^2}{\Gamma^2} - \frac{4\sigma_e^2}{\Gamma^2} - \frac{(\varepsilon - \gamma)^2}{\Gamma^2} - \frac{2\gamma_d}{\Gamma} \quad (\text{no filter}), \quad (2.24)$$

and  $\mathcal{F}_{\omega_1}^{(c)} = 1$  with filtering. The corresponding success probabilities are

$$\begin{aligned} P_{\text{unfiltered}}^s &= 1 - \frac{2\gamma}{\Gamma} - \frac{2\gamma(\varepsilon - \gamma)}{\Gamma^2}, \\ P_{\text{filtered}}^s &= 1 - \frac{4\sigma_o^2}{\Gamma^2} - \frac{4\sigma_e^2}{\Gamma^2} - \frac{2\gamma}{\Gamma} - \frac{(\varepsilon^2 - \gamma^2)}{\Gamma^2} - \frac{2\gamma_d}{\Gamma}. \end{aligned} \quad (2.25)$$

Eq. (2.24) shows that SPRINT can be highly effective. First of all, once we filter the output, the protocol simply cannot produce wrong results for an incoming photon of

frequency  $\omega_1$  since the only way to produce a photon at a frequency  $\omega_2$  is to decay to the desired states  $|g_2\rangle$ . Even without filtering SPRINT is very resilient to spectral effects like finite bandwidth  $\sigma_o$  of the input photon, spectral diffusion  $\sigma_e$  of the QD resonance and decay asymmetry  $\varepsilon$  of the  $\Lambda$  system, as all these effects enter to second order. A first order dependence is however found for the pure dephasing rate  $\gamma_d$ , owing to the fact that SPRINT relies on quantum interference between the incident and the scattered fields. This makes the protocol sensitive to non phase-preserving effects which reduce this interference. While the state transfer is conditioned on detecting a photon at the output, it is noteworthy that the success probability can be arbitrarily close to unity (2.25), if all emitted photons are collected by the waveguide. This is because a photon is always emitted regardless of the branching ratio and frequency bandwidth. The protocol is thus near deterministic. Compared to a fully deterministic protocol not relying on the detection of a photon, the quality of the imprinted state (2.24) is higher for the conditional protocol since we remove the dominant contribution from photon loss.

### 2.3.2 Off-resonant Scattering in QD-waveguide Systems

When the incident photon is in the state  $|\omega_2\rangle_G$  ( $\theta = \pi$ ), it is off-resonant from the QD transition  $|g_1\rangle \rightarrow |e\rangle$  by the ground-state splitting  $\Delta$ . The corresponding input-output relation is

$$|\omega_2\rangle_G|g_1\rangle \rightarrow \hat{t}_1^b|\omega_2\rangle_G|g_1\rangle + \hat{t}_2^b|\omega_2 + \Delta\rangle_G|g_2\rangle. \quad (2.26)$$

In the ideal scenario where  $\Delta \gg \Gamma$ , there is no interaction between the QD and the far-detuned incident field. Hence the transmission probability approaches unity resulting in the output state  $|\omega_2\rangle_G|g_1\rangle$ . The fidelity conditioned on detection of a photon is therefore

$$\mathcal{F}_{\omega_2}^{(c)} = \frac{\langle g_1 | \text{Tr}_\omega \rho | g_1 \rangle}{\text{Tr} \rho} = \begin{cases} \frac{P_{g_1}}{P_{g_1} + P_{g_2}} & \text{(no filter);} \\ 1 & \text{(filter at } \omega_2 \text{).} \end{cases} \quad (2.27)$$

#### 2.3.2.1 Off-resonant Raman Spin-flip Error

Unlike resonant scattering (Sec. 2.3.1), the incident field is now highly detuned so it does not drive the QD transition. This means the excited state will ideally not be populated. For any finite  $\Delta$  there will, however, always be a chance that the QD becomes excited and undergoes a Raman transition, resulting in the undesired spin state. Nonetheless, errors associated with imperfections in the QD transitions (as considered previously) become negligible compared to this dominant error since these errors will be perturbations on top of a perturbation, thus only entering to higher order. We therefore only need to evaluate the effect of having a finite  $\Delta$ .

The individual probabilities for the relevant output states are given by

$$P_{g_1} = \int_{-\infty}^{\infty} |t_1^b \Phi_2(\omega)|^2 d\omega \approx 1 - \frac{\Gamma^2}{4\Delta^2} = 1 - P_{g_2}, \quad (2.28)$$

where  $P_{g_2}$  is the probability of undesired Raman spin-flip and  $P_{g_1}$  is the transmission probability. It is apparent that without filtering the conditional fidelity for off-resonant scattering is

$$\mathcal{F}_{\omega_2}^{(c)} = 1 - \frac{\Gamma^2}{4\Delta^2} \quad (\text{no filter}), \quad (2.29)$$

with  $P^s = 1$ . Similarly we again have  $\mathcal{F}_{\omega_2}^{(c)} = 1$  for the filtered case since a decay to the wrong state will always be associated with a frequency shift. The corresponding success probability for the filtered case is  $1 - \Gamma^2/4\Delta^2$ . It is important to emphasize that the off-resonant spin-flip error  $\Gamma^2/4\Delta^2$  is different from the error coming from the frequency overlap of the two incoming states  $|\omega_1\rangle_G$  and  $|\omega_2\rangle_G$ . Assuming a Gaussian input field, the outgoing scattered field will also be a Gaussian with equal spectral width  $\sigma_o$  as the input. This overlap error scales exponentially  ${}_G\langle\omega_1|\omega_2\rangle_G = \exp(-\Delta^2/8\sigma_o^2)$ . Since a high fidelity for both scattering cases require  $\sigma_o^2 \ll \Gamma^2 \ll \Delta^2$ , this error is negligible compared to the terms we consider.

### 2.3.3 State Transfer of an Equatorial Photonic State to a QD spin

So far we have considered extreme cases where the photon is initialized in one of the two frequency basis states. More generally, we now consider an input state in which the incoming photon is in an equal superposition of two frequencies  $(|\omega_1\rangle_G + e^{i\phi}|\omega_2\rangle_G)/\sqrt{2}$  (corresponding to  $\theta = \pi/2$ ). The spin-photon scattering process is then described by Eq. (2.7):

$$\begin{aligned} \frac{1}{\sqrt{2}} \left( |\omega_1\rangle_G + e^{i\phi}|\omega_2\rangle_G \right) \otimes |g_1\rangle &\rightarrow \frac{1}{\sqrt{2}} \left( \hat{t}_1^a |\omega_1\rangle_G |g_1\rangle + \hat{t}_2^a |\omega_2\rangle_G |g_2\rangle \right. \\ &\left. + e^{i\phi} \hat{t}_1^b |\omega_2\rangle_G |g_1\rangle + e^{i\phi} \hat{t}_2^b |\omega_2 + \Delta\rangle_G |g_2\rangle \right) = |\Psi\rangle. \end{aligned} \quad (2.30)$$

Here  $|\Psi\rangle$  denotes the spin-photon output state. The conditional fidelity of the produced state is then

$$\mathcal{F}_\phi^{(c)} = \langle \Psi_{\text{ideal}}^s | \rho^{(s)} | \Psi_{\text{ideal}}^s \rangle, \quad (2.31)$$

where  $|\Psi_{\text{ideal}}^s\rangle = i\hat{Y}(|g_1\rangle + e^{i\phi}|g_2\rangle)/\sqrt{2}$  is the ideal spin state. Here  $\rho^{(s)}$  is the reduced density matrix of the spin system given by partial trace of the output density matrix  $|\Psi\rangle\langle\Psi|$  over the frequency of the outgoing photon in the waveguide

$$\rho^{(s)} = \frac{\text{Tr}_\omega(|\Psi\rangle\langle\Psi|\hat{P}_\omega)}{\text{Tr}(|\Psi\rangle\langle\Psi|\hat{P}_\omega)}, \quad (2.32)$$

where  $\hat{P}_\omega$  is a projection operator representing filtering: For a filter at  $\omega_j$ ,  $\hat{P}_\omega|\omega_i\rangle = \delta_{ij}|\omega_i\rangle$ ; if there is no filter, the projector is just the identity operator  $\hat{P}_\omega = \mathcal{I}$ . The denominator in (2.32) gives the success probability  $P^s$ .

### 2.3.3.1 Spin Dephasing Error

For a faithful photon-to-spin state transfer, it is essential that the phase of the photonic qubit is preserved in the mapped spin state. This means the spin qubit must remain coherent before being read out. However, being confined in an atom-rich environment, the QD spin is typically coupled to a neighboring nuclear spin bath via hyperfine interaction, causing it to precess with a fluctuating frequency  $\delta_g$ . This is referred to as the Overhauser noise [78, 79, 80], which is one of the external sources that limit the QD spin coherence time. This dephasing effect can be empirically modelled with the frozen fluctuation model [86], where the quasi-static Overhauser field slowly drifts the resonance of the QD spin.

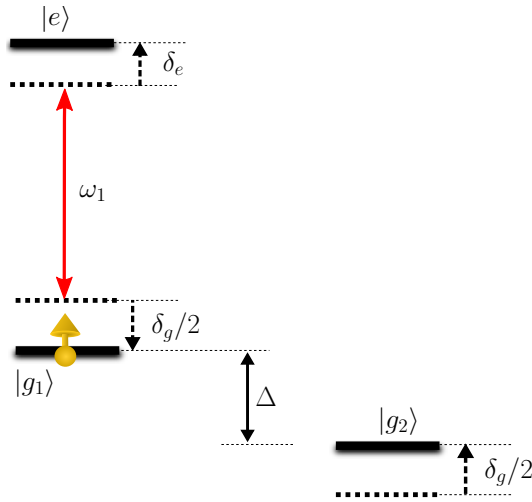


Figure 2.2: Energy levels of the  $\Lambda$ -system under spin dephasing noise and spectral diffusion.

As illustrated in Fig. 2.2 this spin dephasing noise effectively shifts the energy levels of the QD spin ground states such that  $\omega_1 \rightarrow \omega_1 + \delta_g/2$ , likened to the frequency shift  $\delta_e$  due to spectral diffusion considered above.

Now we evaluate the fidelity for the unfiltered case. The ground-state populations after state transfer are given by

$$\begin{aligned} \rho_{11}^{(s)} &= \frac{1}{2P^s} \left[ \int_{-\infty}^{\infty} |t_1^a \Phi_1(\omega)|^2 d\omega + \int_{-\infty}^{\infty} |t_1^b \Phi_1(\omega)|^2 d\omega \right] \\ &= \frac{1}{2P^s} \left( 1 + \frac{4\sigma_o^2}{\Gamma^2} + \frac{\delta_g^2}{\Gamma^2} \right) = 1 - \rho_{22}^{(s)}, \end{aligned} \quad (2.33)$$

where we assume  $\Delta \gg \delta_g$  for small fluctuations. The success probability for the unfiltered case is unity ( $P^s = \rho_{11}^{(s)} + \rho_{22}^{(s)} = 1$ ) in the absence of coupling loss. For now we ignore the dephasing of the excited state  $\delta_e \rightarrow 0$  and focus only on the ground-state coherence. In general the Overhauser field and other noise sources will shift  $\delta_e$  and  $\delta_g$  in a possibly correlated manner depending on the system investigated. For simplicity we assume the fluctuations to be uncorrelated with independent Gaussian noise distributions. This means the linear cross error  $\delta_e \delta_g$  will be averaged out, leaving only second-order dependence on  $\delta_e$  in the final fidelity. This will be considered below and for now we focus on the ground state coherence.

For the off-diagonal spin coherence terms we find

$$\rho_{12}^{(s)} = \frac{1}{2P_s} \int_{-\infty}^{\infty} t_2^{a*} t_1^b e^{i\phi} |\Phi_1 \Phi_2| d\omega \approx \frac{e^{i\phi}}{2P_s} \left( 1 - \frac{4\sigma_o^2}{\Gamma^2} - \frac{\delta_g^2}{\Gamma^2} + i \frac{\delta_g}{\Gamma} \right) = \rho_{21}^{(s)*}. \quad (2.34)$$

Note that  $\rho^{(s)}$  is time-independent as it has been derived in a rotating frame with respect to a fixed ground-state splitting  $\Delta + \delta_g$  (Fig. 2.2). Since the ground-state splitting may vary from shot to shot of the experiments, the rotating frame now depends on the splitting and we need to take this variation into account. To do this we assume the evolution before the emission of the photon is independent of the splitting since there is no superposition of the ground states before this time. Here we consider heralded operation where the photon is detected in the output. It is therefore convenient to analyze what happens for a specific photon detection time.

Let  $t_c$  be the time of detecting a photon in the output (or equivalently the creation time of the spin qubit). The spin precession induced by the Overhauser noise is then denoted by the time evolution operator  $\hat{T}(t - t_c) = \exp(-i\delta_g \hat{S}_z(t - t_c))$ , with  $\hat{S}_z = \hat{\sigma}_z/2$ .

Since the protocol outputs a superposition of two spin ground states which are subject to Overhauser noise, it is beneficial to incorporate a spin-echo sequence into the protocol to extend the spin coherence time. In the echo sequence a spin  $\pi$ -rotation pulse is applied at some time  $t_\pi$ . Ideally the time interval between the detection of the photon and the  $\pi$ -pulse will be equal to the time interval between the  $\pi$ -pulse and the final readout time  $t_R$ , i.e.,  $t_R - t_\pi = t_\pi - t_c = T$ . This ensures refocusing of the spin state at  $t_R$  such that the spin decoherence is reduced [87, 88, 89].

In practice, however, the time of the photon detection  $t_c$  cannot be determined exactly due to time jittering of the photodetector, and it is complicated to make the time of the readout or  $\pi$ -pulse be dependent on the detection time. For this reason we consider a simpler experimental procedure, where the spin-echo sequence begins at a predetermined time  $t_0$  given by the peak of the outgoing pulse (Fig. 2.3). Since in general this implies  $t_c \neq t_0$ ,  $t_R - t_\pi \neq t_\pi - t_c$  this means the echo would become imperfect, leading to dephasing of the spin qubit.

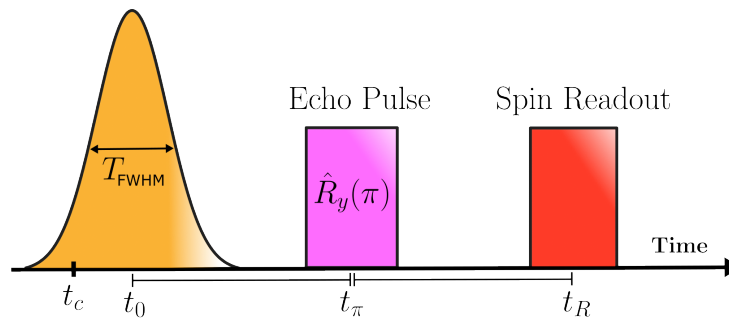


Figure 2.3: **Pulse sequence with spin echo.** The spin echo sequence assumes that the state transfer occurs at  $t_0$ , and the  $\pi$ -pulse and spin readout are applied at  $t_\pi$  and  $t_R$  respectively such that  $t_R - t_\pi = t_\pi - t_0$ .  $t_c$  follows the probability distribution of the scattered pulse.  $T_{\text{FWHM}} = 2\sqrt{2 \ln 2} T_{\text{pulse}}$  is the full-width full maximum (FWHM) pulse duration in time.

The evolution of the spin system under spin echo is described by the unitary operator

$$\hat{\mathcal{U}}_{\text{echo}} = \hat{T}(t_R - t_\pi) \hat{R}_y(\pi) \hat{T}(t_\pi - t_c), \quad (2.35)$$

where  $\hat{R}_y(\pi) = e^{i\pi\hat{\sigma}_y/2}$  is the spin echo  $\pi$ -pulse applied at  $t_\pi$ . Using Eq. (2.35) and the echo condition  $t_R - t_\pi = t_\pi - t_0 = T$ , the spin reduced density matrix becomes

$$\rho_{\text{echo}}^{(s)} = \hat{\mathcal{U}}_{\text{echo}} \rho^{(s)} \hat{\mathcal{U}}_{\text{echo}}^\dagger = \begin{bmatrix} \rho_{22}^{(s)} & -\rho_{21}^{(s)} e^{-i\delta_g(t_c - t_0)} \\ -\rho_{12}^{(s)} e^{i\delta_g(t_c - t_0)} & \rho_{11}^{(s)} \end{bmatrix}. \quad (2.36)$$

From Eq. (2.36) one can infer that for perfect spin echo ( $t_c = t_0$ ) the coherence of the mapped spin state is preserved. Using Eq. (2.31), the conditional fidelity is

$$\begin{aligned} \mathcal{F}_\phi^{(c)}(\delta_g, t_c) &= \langle \Psi_{\text{ideal}}^s | \hat{R}_y^\dagger(\pi) \rho_{\text{echo}}^{(s)} \hat{R}_y(\pi) | \Psi_{\text{ideal}}^s \rangle \\ &= \frac{1}{2P^s} \left[ 1 + \left( 1 - \frac{4\sigma_o^2}{\Gamma^2} - \frac{\delta_g^2}{\Gamma^2} + i\frac{\delta_g}{\Gamma} \right) \cos(\delta_g(t_c - t_0)) \right], \end{aligned} \quad (2.37)$$

where the ideal spin state is now  $\hat{R}_y(\pi) | \Psi_{\text{ideal}}^s \rangle$  due to the  $\pi$ -rotation refocusing pulse. The mean fidelity is calculated by averaging (2.37) with respect to the noise distributions. Averaging over the dephasing profile  $N(0, \sigma_g)$  with  $\sigma_g = \sqrt{2}/T_2^*$  gives the (unfiltered) fidelity

$$\begin{aligned} \bar{\mathcal{F}}_\phi^{(c)}(t_c) &= \int_{-\infty}^{\infty} \int_{-\infty}^{\infty} \mathcal{F}_\phi^{(c)}(\delta_g, t_c, \delta_e) N(0, \sigma_g) d\delta_g \\ &= \frac{1}{2P^s} \left[ 1 + e^{-\frac{1}{2}\sigma_g^2(t_c - t_0)^2} \left( 1 - \frac{4\sigma_o^2}{\Gamma^2} - \frac{\sigma_g^2}{\Gamma^2} \right) \right]. \end{aligned} \quad (2.38)$$

Recall that the detector click occurs at  $t_c$  within the time window of the scattering pulse, and the echo starts at  $t_0$ . Since we do not condition on the exact time of the detector click we need to average over the probability distribution of the outgoing photons. In principle, due to scattering this distribution deviates from the distribution of the incoming photon. However, in the narrowband regime where  $T_{\text{pulse}} \gg 1/\Gamma$  with  $T_{\text{pulse}} = 1/(2\sigma_o)$  as the standard deviation of the transform-limited pulse duration, the temporal profile of the scattering pulse is only slightly perturbed, thus the probability distribution of the outgoing pulse can be approximated by the Gaussian profile  $N(t_0, T_{\text{pulse}})$  of the incoming pulse. Averaging Eq. (2.38) over  $N(t_0, T_{\text{pulse}})$  gives

$$\begin{aligned} \bar{\mathcal{F}}_\phi^{(c)} &= \int_{-\infty}^{\infty} \bar{\mathcal{F}}_\phi^{(c)}(t_c) N(t_0, T_{\text{pulse}}) dt_c \\ &= \frac{1}{2P^s} \left[ 1 + \frac{1}{\sqrt{1 + \sigma_g^2 T_{\text{pulse}}^2}} \left( 1 - \frac{4\sigma_o^2}{\Gamma^2} - \frac{\sigma_g^2}{\Gamma^2} \right) \right] \\ &\approx 1 - \frac{2\sigma_o^2}{\Gamma^2} - \frac{1}{8} \frac{1}{\sigma_o^2 T_2^{*2}} - \frac{1}{T_2^{*2} \Gamma^2} \quad (\text{no filter}). \end{aligned} \quad (2.39)$$

From here we see there is an optimal bandwidth  $\sigma_{o,\text{optimal}} = 2\sqrt{\Gamma/T_2^*}$  for the incident photon as dictated by the trade-off between the first and second error terms: For incident photons with larger bandwidth  $\sigma_o$  (or shorter  $T_{\text{pulse}}$ ), the frequency mismatch between

the photon and the QD linewidth  $\Gamma$  is higher, which lowers the probability of driving the Raman transition, and eventually the state-transfer fidelity.

On the other hand, for narrow photons (or long  $T_{\text{pulse}}$ ), the transfer becomes more prone to spin dephasing. The reason for this is that a longer transfer duration  $T_{\text{pulse}}$  implies a larger uncertainty in the creation time  $t_c$  of the spin qubit, which renders the spin echo ineffective. We therefore require  $T_{\text{pulse}} \ll T_2^*$  in order for the spin qubit to remain coherent.

The third infidelity term in Eq. (2.39) originates from the energy shift in the ground states due to the Overhauser noise, which shifts the QD resonance similar to spectral diffusion. This error is always smaller than the combination of the first and third terms since these require  $1/T_2^{*2} \ll \sigma_o^2 \ll \Gamma^2$ . Furthermore experimental values confirm that this term is small for realistic systems, e.g.  $T_2^*\Gamma \approx 50$  [20].

In the case of filtering photons at the frequency  $\omega_2$ , the spin populations (2.33) are reduced due to the filter. Apart from that the calculation proceeds along the same lines and leads to a lower success probability but enhanced fidelity

$$P^s = \frac{1}{2} \int \left( |t_2^a|^2 + |t_1^b|^2 \right) |\Phi_1(\omega)|^2 d\omega \approx 1 - \frac{2\sigma_o^2}{\Gamma^2},$$

$$\bar{\mathcal{F}}_\phi^{(c)} \approx 1 - \frac{\sigma_o^2}{\Gamma^2} - \frac{1}{8} \frac{1}{\sigma_o^2 T_2^{*2}} \quad (\text{filter at } \omega_2). \quad (2.40)$$

### 2.3.3.2 Equatorial Fidelity

We conclude this section by including all the relevant errors in addition to spin dephasing. The spectral mismatch, coupling and off-resonant spin-flip infidelities are calculated straightforwardly similar to Secs. 2.3.1 and 2.3.2, whereas the phonon-induced pure dephasing transforms the output density matrix  $\rho = |\Psi\rangle\langle\Psi|$  into

$$\rho' = \rho + \frac{1}{2} \left( P_{\gamma_d}^{\omega_1} \rho_{\gamma_d}^{\omega_1} \otimes |g_1\rangle\langle g_1| + P_{\gamma_d}^{\omega_2} \rho_{\gamma_d}^{\omega_2} \otimes |g_2\rangle\langle g_2| \right),$$

since only half of the incoming qubit resonantly drives the QD to the excited state. As such, the effect from phonon scattering is halved compared to Eq. (2.19).

Including all effects, the corresponding fidelity is

$$\bar{\mathcal{F}}_\phi^{(c)} = \begin{cases} 1 - \frac{2\sigma_o^2}{\Gamma^2} - \frac{2\sigma_e^2}{\Gamma^2} - \frac{\gamma_d}{\Gamma} - \frac{(\varepsilon - \gamma)^2}{4\Gamma^2} \\ \quad - \frac{1}{8} \frac{1}{\sigma_o^2 T_2^{*2}} - \frac{\Gamma^2}{8\Delta^2} & (\text{no filter}); \\ 1 - \frac{\sigma_o^2}{\Gamma^2} - \frac{\sigma_e^2}{\Gamma^2} - \frac{\gamma_d}{2\Gamma} - \frac{1}{8} \frac{1}{\sigma_o^2 T_2^{*2}} \\ \quad - \frac{\Gamma^2}{16\Delta^2} & (\text{filtered at } \omega_2), \end{cases} \quad (2.41)$$

with the success probability

$$P_{\text{unfiltered}}^s = 1 - \frac{\gamma}{\Gamma} - \frac{\gamma(\varepsilon - \gamma)}{\Gamma^2}; \quad (2.42)$$

$$P_{\text{filtered}}^s = 1 - \frac{2\sigma_o^2}{\Gamma^2} - \frac{2\sigma_e^2}{\Gamma^2} - \frac{\gamma}{\Gamma} - \frac{(\varepsilon^2 - \gamma^2)}{2\Gamma^2} - \frac{\gamma_d}{\Gamma} - \frac{\Gamma^2}{8\Delta^2}.$$

### 2.3.4 Choi-Jamiolkowski Fidelity

Above we have characterized the performance of the state transfer for specific states. To quantify the overall performance for an unknown state, it is however, crucial to average the transfer fidelity over different input states on the Bloch sphere. The Choi-Jamiolkowski fidelity  $\mathcal{F}^{\text{CJ}}$  is an example of such a metric [72, 73, 74] which is useful for characterizing noisy quantum gates and channels. For instance  $\mathcal{F}^{\text{CJ}} \geq 50\%$  guarantees that an operation is entanglement-preserving.

In essence, if  $\mathcal{E}$  denotes a noisy operation acting on the spin-photon system  $S$ , the input state  $|\psi_{\text{in}}\rangle$  is thought to be a maximally entangled state between  $S$  and an ancillary system  $A$ . Then the Choi-Jamiolkowski fidelity  $\mathcal{F}^{\text{CJ}} \equiv \langle \psi_{\text{ideal}} | (\mathcal{I}_A \otimes \mathcal{E}_S) (|\psi_{\text{in}}\rangle\langle\psi_{\text{in}}|) | \psi_{\text{ideal}} \rangle$  measures the fidelity of the entangled state after applying  $\mathcal{E}$  to half of the input state, where  $\mathcal{I}_A$  is the identity operation on system  $A$  and  $|\psi_{\text{ideal}}\rangle$  is the ideal state.

In our case we consider a gate operation heralded on the detection of a photon in the output mode. The success probability for the gate depends on which input state we consider and this needs to be taken into account when assessing its performance. In Appendix A we generalize the formula for average gate fidelity to heralded operation in a qubit system [74]. Specifically we show that for non-trace preserving gate operations  $\mathcal{E}$  (i.e., our heralded state-transfer protocol), there is a linear relationship between the Choi-Jamiolkowski fidelity and the weighted average fidelity  $\bar{\mathcal{F}}_{\text{weighted}}^{(c)}$ :

$$\bar{\mathcal{F}}_{\text{weighted}}^{(c)} \equiv \frac{\sum_i P_i^s \mathcal{F}_i^{(c)}}{\sum_i P_i^s} = \frac{2}{3} \mathcal{F}^{\text{CJ}} + \frac{1}{3}, \quad (2.43)$$

where the index  $i$  refers to different input photonic states on 6 cardinal points of the Bloch sphere:  $i \in \{1, 2\}$  correspond to conditional fidelities of SPRINT and off-resonant scattering in Eqs. (2.24) and (2.29) respectively, whereas  $i \in [3, 6]$  represent fidelities for 4 superposition states on the equator of the Bloch sphere.  $P_i^s$  is the success probability for each transfer characterized by the number of detected photons.

Eq. (2.43) enables us to extract  $\mathcal{F}^{\text{CJ}}$  by covering only 6 cardinal input states on the Bloch sphere and measuring their conditional fidelities. Here we use this formula to evaluate the Choi-Jamiolkowski fidelity for our protocol, but this also represents a recipe for how to construct a suitable average in experiments. For instance the performance of single qubit storage is often evaluated by averaging the fidelity over the Bloch sphere and demanding that the fidelity exceeds a classical threshold of  $2/3$  [90, 91]. Our result indicates that this condition is equivalent to having an entanglement-preserving operation  $\mathcal{F}^{\text{CJ}} \geq 1/2$ , if the experimental results are weighed with the success probability as in Eq. (2.43).

Additionally, we note that Eq. (2.43) is also applicable to evaluating the averaged fidelity with filtering: Heralding on the arrival of photons with or without a filter at  $\omega_2$  results in

$$\begin{aligned}
\mathcal{F}_{\text{unfiltered}}^{\text{CJ}} &= 1 - \frac{3\sigma_o^2}{\Gamma^2} - \frac{3\sigma_e^2}{\Gamma^2} - \frac{3\gamma_d}{2\Gamma} - \frac{(\varepsilon - \gamma)^2}{2\Gamma^2} \\
&\quad - \frac{1}{8} \frac{1}{\sigma_o^2 T_2^{*2}} - \frac{3\Gamma^2}{16\Delta^2}, \\
\mathcal{F}_{\text{filtered}}^{\text{CJ}} &= 1 - \frac{\sigma_o^2}{\Gamma^2} - \frac{\sigma_e^2}{\Gamma^2} - \frac{\gamma_d}{2\Gamma} - \frac{1}{8} \frac{1}{\sigma_o^2 T_2^{*2}} - \frac{\Gamma^2}{16\Delta^2}.
\end{aligned} \tag{2.44}$$

The corresponding success probabilities are computed as a direct average over the Bloch sphere:

$$\begin{aligned}
P_{\text{unfiltered}}^s &= 1 - \frac{\gamma}{\Gamma} - \frac{\gamma(\varepsilon - \gamma)}{\Gamma^2}, \\
P_{\text{filtered}}^s &= 1 - \frac{2\sigma_o^2}{\Gamma^2} - \frac{2\sigma_e^2}{\Gamma^2} - \frac{\gamma}{\Gamma} - \frac{(\varepsilon^2 - \gamma^2)}{2\Gamma^2} - \frac{\gamma_d}{\Gamma} - \frac{\Gamma^2}{8\Delta^2}.
\end{aligned} \tag{2.45}$$

Here we again see that the filter increases the fidelity although at the expense of lowering the success probability of state transfer.

### 2.3.5 Error Sanity Check

A fast way to perform sanity tests on the perturbative expressions is to check how errors propagate between the unfiltered and filtered cases. For instance, in the case of SPRINT, when applying the frequency filter the infidelities are effectively propagated into inefficiencies, rather than being removed. This means one could check if the errors in Eqs. (2.24)-(2.25) are conserved before and after filtering:

$$\begin{aligned}
(1 - \mathcal{F}_{\omega_1, \text{unfiltered}}^{(c)}) + (1 - P_{\text{unfiltered}}^s) &= \frac{2\gamma}{\Gamma} + \frac{2\gamma_d}{\Gamma} + \frac{\varepsilon^2 - \gamma^2}{\Gamma^2} + \frac{4\sigma_o^2}{\Gamma^2} + \frac{4\sigma_e^2}{\Gamma^2} \\
&= (1 - \mathcal{F}_{\omega_1, \text{filtered}}^{(c)}) + (1 - P_{\text{filtered}}^s).
\end{aligned} \tag{2.46}$$

Similarly, one can show that  $(1 - \mathcal{F}_{\omega_1, \text{unfiltered}}^{\text{CJ}}) + (1 - P_{\text{unfiltered}}^s) = (1 - \mathcal{F}_{\omega_1, \text{filtered}}^{\text{CJ}}) + (1 - P_{\text{filtered}}^s)$ . Note that although this method works for the SPRINT, off-resonant and Choi-Jamilkowski fidelities, it is not suitable for checking the equatorial fidelity (Eq. (2.41)). To explain this further, we shall invoke each of their fidelity definitions:

$$\bar{\mathcal{F}}_{\phi}^{(c)} = \frac{\int [ |t_2^a|^2 + |t_1^b|^2 + \eta(|t_1^a|^2 + |t_2^b|^2) - t_2^a t_1^{b*} - t_2^{a*} t_1^b ] |\Phi_1(\omega)|^2 d\omega}{2 \int [ |t_2^a|^2 + |t_1^b|^2 + \eta(|t_1^a|^2 + |t_2^b|^2) ] |\Phi_1(\omega)|^2 d\omega}; \tag{2.47}$$

$$\mathcal{F}^{\text{CJ}} = \frac{\int ( |t_2^a|^2 + |t_1^b|^2 - t_2^a t_1^{b*} - t_2^{a*} t_1^b ) |\Phi_1(\omega)|^2 d\omega}{2 \int [ |t_2^a|^2 + |t_1^b|^2 + \eta(|t_1^a|^2 + |t_2^b|^2) ] |\Phi_1(\omega)|^2 d\omega}, \tag{2.48}$$

where we assume the same transmission efficiency  $\eta$  for both  $\omega_1$  and  $\omega_2 + \Delta$  photons given a sufficiently narrow filter. Now, for simplicity we consider only the spectral mismatch error and take  $\epsilon \equiv 4\sigma_o^2/\Gamma^2$ . This allows us to simplify the above equations as

$$\bar{\mathcal{F}}_{\phi}^{(c)} = \frac{1 - \frac{(1-\eta)\epsilon}{2} + (1-\epsilon)}{2[1 - \frac{(1-\eta)\epsilon}{2}]} \approx 1 - \frac{(1+\eta)\epsilon}{4} = \begin{cases} 1 - \frac{\epsilon}{2} & \text{(no filter);} \\ 1 - \frac{\epsilon}{4} & \text{(filtered at } \omega_2), \end{cases} \tag{2.49}$$

$$\mathcal{F}^{\text{CJ}} = \frac{\frac{1}{2} + \frac{1-\epsilon}{2} + (1-\epsilon)}{2[1 - \frac{(1-\eta)\epsilon}{2}]} \approx 1 - \frac{\epsilon}{4} - \frac{\eta\epsilon}{2} = \begin{cases} 1 - \frac{3\epsilon}{4} & \text{(no filter);} \\ 1 - \frac{\epsilon}{4} & \text{(filtered at } \omega_2), \end{cases} \quad (2.50)$$

with the success probability in both cases to be  $P^s = 1 - \frac{(1-\eta)\epsilon}{2}$ . One could see that the total error in  $\epsilon$  for  $\mathcal{F}^{\text{CJ}}$  is conserved before and after filtering, and is consistent with Eq. (2.44).

As for  $\bar{\mathcal{F}}_\phi^{(c)}$ , due to the extra terms  $|t_1^a|^2$  and  $|t_2^b|^2$  in the numerator of Eq. (2.47), there is an  $\epsilon/4$  term contributing to the fidelity which gets filtered out, thus the filtered and unfiltered errors do not add up. Physically, these terms spring from the output states ( $|\omega_1\rangle_G|g_1\rangle$  and  $|\omega_2 + \Delta\rangle_G|g_2\rangle$ ) in which the spin is correctly projected but resulting in an outgoing photon of different frequencies. In other words, they represent “false positives” that erroneously boost the state-transfer fidelity despite having the wrong photons.  $\bar{\mathcal{F}}_\phi^{(c)}$  does not discriminate the output photons as long as the spin state is successfully mapped. In this regard,  $\mathcal{F}^{\text{CJ}}$  is therefore a more accurate fidelity measure of the ideal process (Eq. (2.1)) with practical relevance as it requires not only the correct spin projection but also the correct output photon frequency.

## 2.4 Additional Imperfections

While the theory in Sec. 2.3 is pretty complete in describing various imperfections, to fully capture errors in an actual experiment, there are in fact several additional sources of errors that should be accounted for. Amongst them, driving-induced dephasing and imperfect spin rotation are two of the most dominant errors that linearly contribute to the state-transfer infidelity.

Driving-induced dephasing originates from multi-photon components in the scattering pulse that interact with the QD. The more mean photon number per pulse, the higher the probability of multi-photon scattering in succession with the QD during the pulse, which leads to effective damping of the phase coherence. As explained in Sec. 1.5, for scattering schemes, the driving pulse is ideally orders of magnitude longer than the QD lifetime, which implies the QD could be driven repeatedly during the pulse. To reduce the probability of over-driving<sup>1</sup>, it is therefore required for scattering schemes to minimize the mean photon number per pulse to the single-photon level.

Similar to phonon-induced pure dephasing which directly impacts the interference between incident and scattered fields, this driving error would also lead to first-order infidelity. Interested readers can refer to Sec. 4.3.7 in which this error has been treated to justify entanglement fidelity in the experiment.

Another notable error arises from infidelity of the spin-echo  $\pi$ -pulse in Sec. 2.3.3.1. An imperfect  $\pi$ -pulse directly affects the mapped superposition spin state, where the scaling of the state-transfer infidelity will depend on origins of imperfections. For instance, as we will cover in Chapter 3, when optically implementing the spin  $\pi$ -pulse there is a small probability of incoherently driving the spin transition, leading to a spin mixture. This photo-induced spin-flip error, modelled in Sec. 4.3.5, will reduce the state-transfer fidelity to the first order.

---

<sup>1</sup>This is similar to the re-excitation error in pulsed excitations, but here the multi-photon components originate from the input scattering pulse alone.

## 2.5 Comparison with Numerical Simulation

So far all results have been derived analytically with perturbation theory in order to obtain a solid understanding of the errors. To verify our results and to be able to go beyond perturbation theory we have also simulated the protocol numerically.

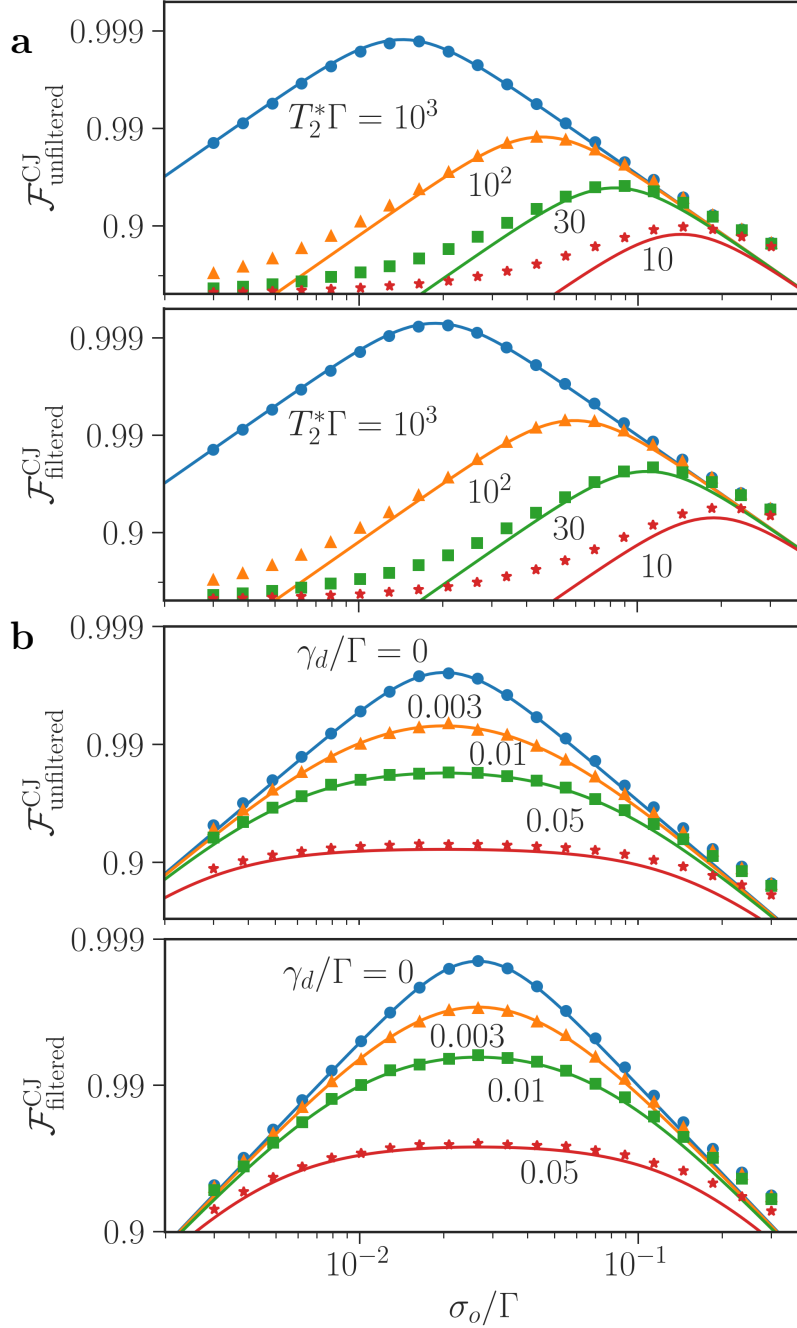


Figure 2.4: **Choi-Jamiolkowski fidelities of the photon-to-spin state transfer with/without filtering as a function of the bandwidth of the input field  $\sigma_o$ .** Solid lines correspond to theoretical values from Eq. (2.44). Symbols are simulated results. **(a)** Varying spin dephasing time  $T_2^*$ . All other errors are ignored, i.e.,  $\gamma_d = 0$ ,  $\varepsilon = 0$ ,  $\sigma_e = 0$ ,  $\Gamma/\Delta \approx 0$  and  $\gamma = 0$ . **(b)** Varying pure dephasing rate  $\gamma_d$  with  $T_2^*\Gamma = 500$ .  $\varepsilon = 0$ ,  $\sigma_e = 0$ ,  $\Gamma/\Delta \approx 0$  and  $\gamma = 0$ .

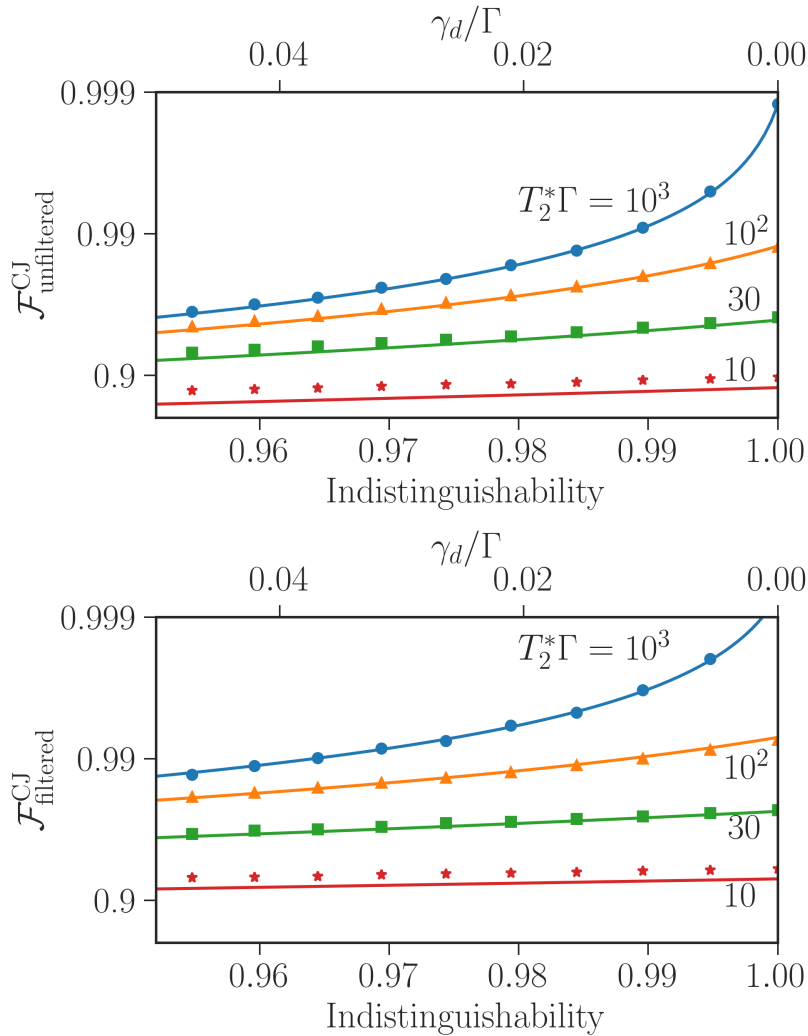


Figure 2.5: **Choi-Jamiolkowski fidelities with/without filtering as a function of pure dephasing rate  $\gamma_d$  or the photon indistinguishability  $I = \frac{\Gamma}{\Gamma+2\gamma_d}$  for various spin dephasing times  $T_2^*$  with optimal bandwidth of the input field.** Solid lines correspond to the analytical result in Eq. (2.44). Symbols are simulated results. All other errors are neglected, i.e.,  $\varepsilon = 0$ ,  $\sigma_e = 0$ ,  $\Gamma/\Delta \approx 0$  and  $\gamma = 0$ .

For this purpose, we model the interaction between an incident photon and a waveguide-embedded QD using the quantum trajectory theory of cascaded open systems [92]. The evolution of the state according to the effective non-Hermitian Hamiltonian is computed by applying the Monte-Carlo wave-function procedure [84, 93, 94] with over  $10^5$  stochastic wave-functions per simulated point. The scattering probabilities are then extracted from the simulated wave-functions to evaluate the averaged fidelities. Figs. 2.4 and 2.5 show an excellent agreement between the analytical expressions obtained in Sec. 2.3 and numerical results in the limit of  $1 - \mathcal{F}^{\text{CJ}} \ll 1$ , which is the regime where we expect perturbation theory to hold.

## 2.6 Experimental Considerations

We now discuss the possible implementation of the photon-to-spin state transfer using a QD coupled to nanophotonic waveguides. In particular, we estimate the maximum attainable fidelity using experimentally demonstrated parameters. We then compare the performance of a waveguide-QD system to that of a single atom coupled to an optical cavity, a platform previously used to demonstrate a quantum SWAP gate [67, 68].

### 2.6.1 Realization on a QD-waveguide platform

A QD coupled to a photonic crystal waveguide involving a positive (or positively charged exciton  $X^+$ ) or negative ( $X^-$ ) charge under a Voigt magnetic field could be used to realize the optical  $\Lambda$ -level system. So far we have considered a one-sided (i.e., terminated) waveguide, while in principle a two-sided configuration is also feasible. In the latter case, however, optimal performance requires excitation and collection from both sides of the waveguide with mutual interferometric stability, which would be an experimental overhead to implement [23]. As such, we here consider a one-sided waveguide.

For strong radiative coupling, the essential efficiencies include the ratio of the emission into the coherent zero-phonon line where an efficiency of 95% has been reported [95, 96], and the coupling efficiency into the waveguided mode which has been found to be exceedingly high with  $\beta = 98\%$  [59]. These two efficiencies indicate that  $\gamma/\Gamma < 7\%$  is achievable, only limiting  $\mathcal{F}_{\text{unfiltered}}^{\text{CJ}}$  and  $P_{\text{unfiltered}}^s$  to 99.5% and 93%, respectively.

To minimize spin-related errors, we consider an optically excited positively charged exciton state ( $X^+$ ). Hole spins are shown to have significantly longer spin dephasing times  $T_2^*$  than electrons [42], without additional cooling of the nuclear spin ensemble [97], thus are suitable for our protocol<sup>2</sup>. Recently,  $T_2^* = 21.4$  ns was reported for a hole spin in a photonic crystal waveguide along with a  $X^+$  radiative decay rate of  $\Gamma = 2.48$  ns<sup>-1</sup> [20]. This translates into  $T_2^*\Gamma \approx 54$  and a corresponding  $\mathcal{F}_{\text{unfiltered}}^{\text{CJ}}$  of 97.7% when the photon bandwidth is optimally engineered ( $\sigma_{o,\text{optimal}} = 24^{-\frac{1}{4}}\sqrt{\Gamma/T_2^*} \approx 0.15$  ns<sup>-1</sup> with FWHM in pulse duration  $T_{\text{FWHM}} = \sqrt{2 \ln 2}/\sigma_{o,\text{optimal}} \approx 7.85$  ns).

As noted previously, the most prominent infidelity results from the linear scaling with the pure dephasing rate  $\gamma_d$ . The pure dephasing rate is typically measured in a Hong-Ou-Mandel (HOM) interference experiment where the degree of indistinguishability between two emitted photons is recorded and expressed as  $I = \Gamma/(\Gamma + 2\gamma_d)$ .  $I > 98\%$  (corrected for finite  $g^{(2)}(0)$ ) has been reported for two subsequently emitted photons [98], which translates into  $\gamma_d/\Gamma \approx 1\%$  corresponding to a maximum  $\mathcal{F}_{\text{unfiltered}}^{\text{CJ}}$  of 98.5%.

The decay rate asymmetry  $\varepsilon$  could in principle be reduced by properly positioning the QD in an one-sided photonic-crystal waveguide (PCW) or adopting the nanobeam waveguide<sup>3</sup>. From what we know in Sec. 1.4, two PCW orientations are possible for experimental implementation:

1. For a QD located at the waveguide center, the PCW needs to be 45°-rotated relative to the QD crystallographic axis to ensure equal coupling of both orthogonally-polarized linear dipoles into the same waveguide mode M0;

<sup>2</sup>More suitable due to simplicity of the protocol without nuclear spin cooling sequences.

<sup>3</sup>Similar to photonic-crystal waveguides, nanobeam waveguides also have position-dependent Purcell enhancement; however, it is weaker thus it might be easier to find QDs there with symmetric decay rates.

2. For an off-centered QD where the decay rate symmetry condition is already satisfied, the PCW needs to be fabricated along the crystal axes similar to Fig. 1.7.

For both orientations, a cross-polarized excitation scheme is required (Sec. 3.3.3). In any case, this error only enters to the second order and is not expected to pose a fundamental limitation.

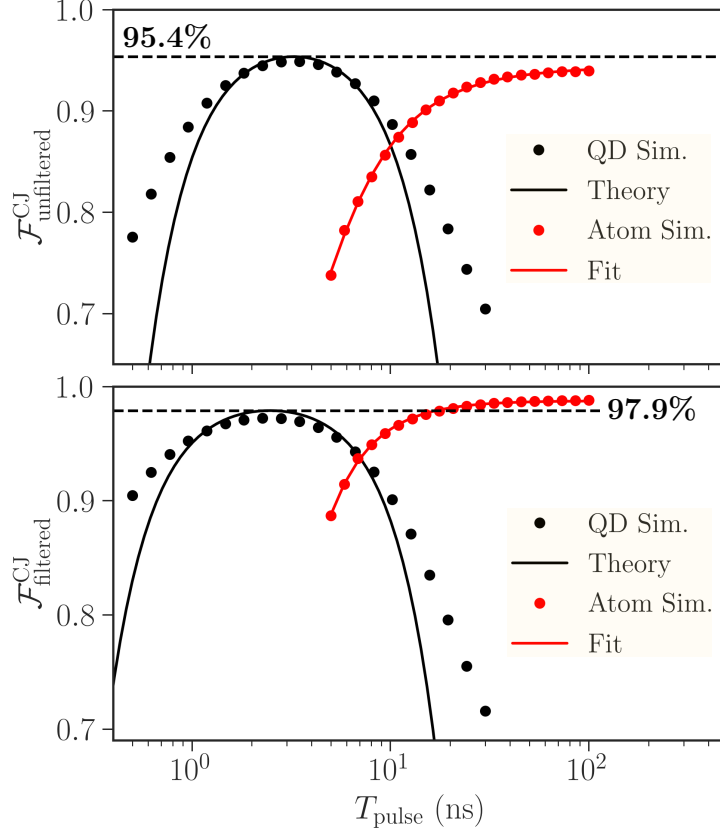


Figure 2.6: **Comparison of average fidelities between QD (black) and Rb-atom systems (red) as a function of the input pulse duration  $T_{\text{pulse}}$ .** Symbols denote numerical results. The full lines show the analytical results for the QDs and a simple fit for the Rb data. Dashed lines indicate the maximum achievable fidelity for the QD system predicted by Eq. (2.44). The parameters of the simulation are provided in the main text.

Finally, in order to reduce the probability of off-resonant spin flip  $\Gamma^2/\Delta^2$ , a strong external magnetic field could be applied to increase the ground-state splitting. In Ref. [20], a low in-plane  $g$ -factor of 0.26 for  $X^+$  was observed, leading to a sufficiently large splitting of  $\Delta/2\pi = 7.3$  GHz at 2T while preserving good spin coherence properties. This ensures  $\Delta/\Gamma \approx 20$  with  $\mathcal{F}_{\text{unfiltered}}^{\text{CJ}}$  approaching 99.9%.

To gauge the full performance of the protocol we now combine all imperfections of the protocol with realistic parameters in the QD-waveguide system:  $\sigma_e = 0.1 \text{ ns}^{-1}$ ,  $\Gamma = 2.48 \text{ ns}^{-1}$ ,  $\gamma = 0.05 \text{ ns}^{-1}$ ,  $\gamma_d = 0.03 \text{ ns}^{-1}$ ,  $\Delta/2\pi = 7.3$  GHz,  $T_2^* = 21.4 \text{ ns}$  [20] and assume  $\varepsilon = 0$ . With these parameters  $\mathcal{F}_{\text{unfiltered}}^{\text{CJ}}$  ( $\mathcal{F}_{\text{filtered}}^{\text{CJ}}$ ) reaches 95.4% (97.9%) with a success probability of 98% (95.1%) (Fig. 2.6).

## 2.6.2 Comparison with Rb-cavity platform

Finally, we compare the performance of a waveguide-embedded QD to that of a  $^{87}\text{Rb}$ -atom trapped next to a fiber-coupled ultrahigh-Q microtoroid whispering-gallery-mode (WGM) resonator.

A transverse magnetic (TM) mode of the resonator is tuned to be resonant with the  $F = 1 \rightarrow F' = 1$  transition of the D1 line of  $^{87}\text{Rb}$ . The  $\Lambda$ -system is comprised by the two ground states  $F = 1, m_F = \pm 1$ , defining the atomic qubit, and the excited state  $F' = 1, m_{F'} = 0$ . The evanescent field of the clockwise (counterclockwise) TM mode, associated with left-(right-) propagating light in the fiber, is coupled primarily to the  $\sigma^+$  ( $\sigma^-$ ) transition of the atom [99, 100, 7], allowing to independently address each transition in the  $\Lambda$ -system. By applying a weak external magnetic field of 20 G, we induce a Zeeman energy shift to the ground states that lifts the degeneracy in frequency between the two transitions, making the photonic qubit both polarization- and frequency-encoded.

We simulate numerically the photon-to-atom state-transfer fidelity using the following realistic parameters [69, 101, 68]: coherent atom-cavity coupling rate of  $g = 2\pi \times 16$  MHz, fiber-cavity coupling rate of  $\kappa_{ex} = 2\pi \times 30$  MHz, intrinsic cavity loss rate of  $\kappa_i = 2\pi \times 2$  MHz (corresponding to  $Q_{\text{cav}} \approx 10^8$ ), atomic free-space amplitude decay rate of  $\gamma = 2\pi \times 3$  MHz, parasitic coupling rate between the two modes of the cavity of  $h = 2\pi \times 1$  MHz, and an undesired polarization component  $r_\sigma = 0.19$  (see Ref. [67]). The simulation also takes into account atomic transitions outside of the  $\Lambda$ -system that affect the ideal operation of the scheme. Dephasing processes in trapped single atoms are reported to be on the order of 100  $\mu\text{s}$  [102, 103] and thus have a negligible impact on the fidelity when  $T_{\text{pulse}} < 100$  ns.

When comparing between the two platforms, one must keep in mind that the waveguide-QD system is stationary whereas trapping and cooling of a single atom next to a WGM resonator remains a challenging task [104, 105]. Simulations show that both systems have a similar maximum fidelity, yet their respective optimal pulse durations differ by about two orders of magnitude (Fig. 2.6). The fidelity in the atom-cavity system approaches its maximum at a pulse duration of around 100 ns, as opposed to an optimal pulse duration of 3.49 ns for the QD-waveguide platform, which is dictated by the ratio between the emitter's spin dephasing time and its decay rate,  $T_{\text{optimal}} \propto \sqrt{T_2^*/\Gamma}$ .

A shorter pulse duration ( $T_{\text{pulse}} \leq 10$  ns) is advantageous for increasing the repetition rate of protocols, e.g. boosting the rate of memory-assisted measurement-device-independent quantum key distribution [106, 107]. In this regime, the QD-waveguide platform is favorable but care should be taken to preserve the spin coherence. On the other hand, a longer pulse duration ( $T_{\text{pulse}} > 10$  ns), suitable to the atom-cavity platform, is favorable for interfacing with low-bandwidth emitters. Besides, the atomic system is advantageous for applications requiring long storage times thanks to its significantly lower dephasing rates.

## 2.7 Conclusion

We have proposed and theoretically analyzed a passive scheme to perform deterministic quantum state transfer from a frequency-encoded photon to a quantum-dot spin mediated by a nanophotonic waveguide. Strikingly, with the exception of pure dephasing, we find that the state-transfer fidelity is insensitive to first order in the small parameters for the considered spectral, coupling and spin dephasing errors. This demonstrates robustness of the scheme.

The thorough fidelity analysis unravels the influence of various physical processes governing the quality of quantum state transfer and hence offers an important intuitive guideline for similar experiments with QDs, i.e., in Chapters 3 and 6, as well as other solid-state emitters. The experimental realization of this scheme would require the search for QD charged excitons with symmetric decay rates under the in-plane magnetic field. Nevertheless, an estimated state-transfer fidelity exceeding 95% should be within experimental reach using the QD-waveguide platform.

The photon-spin transfer protocol will find its applications in quantum-information processing with frequency-encoded qubits. Specifically, the coherent exchange of arbitrary states between the photon and the emitter enables deterministic SWAP gates [68], quantum non-demolition detection and memory-assisted satellite quantum key distribution [107, 108].

## Chapter 3

# Spin-Photon Entanglement using Photon-scattering

In this chapter, we transition from pure theory to a healthy mix of experimental and theoretical work. Specifically, we showcase the experimental realization of an essential ingredient for non-local quantum information processing— quantum entanglement between a flying photon with a quantum-dot (QD) spin. The chapter begins by discussing motivations and proposals for quantum entangling gates, and adapting them to the QD-waveguide system in a realistic experimental setting. We then describe a series of spectroscopy measurements to characterize the physical system, as well as the generation of spin-photon entanglement by photon-scattering. Finally, this chapter concludes by benchmarking the systematic performance of our entanglement protocol.

### 3.1 Motivations

In a future quantum network [109], remote quantum nodes could be connected by a large web of entangled photons. The advent of a deterministic quantum interface between light and solid-state emitters holds great promise in realizing this vision [110]. For such systems, a flying photon is funneled into a nanophotonic structure and weakly scatters on a quantum emitter that hosts a single spin [111]. Coherent manipulation of the spin state entangles it with the photon, constituting the underlying principles for realizing deterministic quantum gates between flying photons [112] which help connect different nodes in the network, and additionally, the generation of photonic repeater graph states for long-distance one-way quantum repeaters [22]. Towards this direction, we realize spin-photon entanglement by interfacing a time-bin encoded flying photon with a local QD hole spin stationed in a photonic-crystal waveguide. We highlight a high 74% entanglement fidelity which is comparable to other solid-state platforms, but with two orders of magnitude improvement on the protocol speed. These results demonstrated the feasibility of the photon-scattering approach to induce light-matter entanglement, and serve as the experimental foundation for implementing spin-photon and spin-mediated photon-photon gates on the QD-waveguide platform.

As noble as this may sound, this was not the core motivation of the project at its initial phase. The idea of the project was first conceived as a solution to an engineering challenge in the laboratory—my supervisor Peter Lodahl, met me at the corridor one day and asked whether it is possible to run a quantum gate experiment with the existing experimental setup. The question was about saving lab resources and utilizing the current setup with minimal changes for other projects (i.e., Ref. [18]), as the spin team commonly shares one cryostat and optical setups due to limited space and funding. It has then led me to consider the compatibility of each component<sup>1</sup> with the theoretical gate protocol, eventually coming up with a minimalistic and experimentally feasible gate sequence (introduced in the next section) that becomes the basis for a deterministic entangling gate.

The experiments in this work are conducted together with Alexey Tiranov.

---

<sup>1</sup>i.e., the time-bin interferometer that defines the photon basis, the limited axis of spin rotations using the microwave setup, the number of lasers and the amount of breadboard space available.

## 3.2 Photon-scattering Gate Protocols

In this section, we briefly introduce a few landmark deterministic gate protocols that operate upon weak scattering of photons from an emitter. We estimate the scattering-induced phase shift required to implement these gates, using realistic parameters, and use it as an argument to motivate the design for heralded gate protocols. Readers who are interested in the actual implementation of the heralded entangling gate could directly navigate to Sec. 3.2.2.

### 3.2.1 Deterministic Photon-scattering gates

In the early 2000s, a new prototype of quantum controlled-phase gate between two photonic qubits based on cavity reflection has been proposed by Duan and Kimble [65]. The gate operates by reflecting two polarization-encoded photonic qubits consecutively from a single-sided optical cavity that traps a single atom. An atom is initially prepared in a superposition state  $|\Phi_a\rangle = (|0_a\rangle + |1_a\rangle)/\sqrt{2}$  where only the transition between the ground state  $|1_a\rangle$  and excited state  $|e\rangle$  is resonant with the cavity (Fig. 3.1a). Each photonic pulse with frequency resonant with the cavity is sent to a polarizing beamsplitter (PBS) (Fig. 3.1b). The  $h$  polarization component of the pulse transmits through and is subsequently reflected by the cavity, while its  $v$  component is reflected by both the PBS and a mirror.

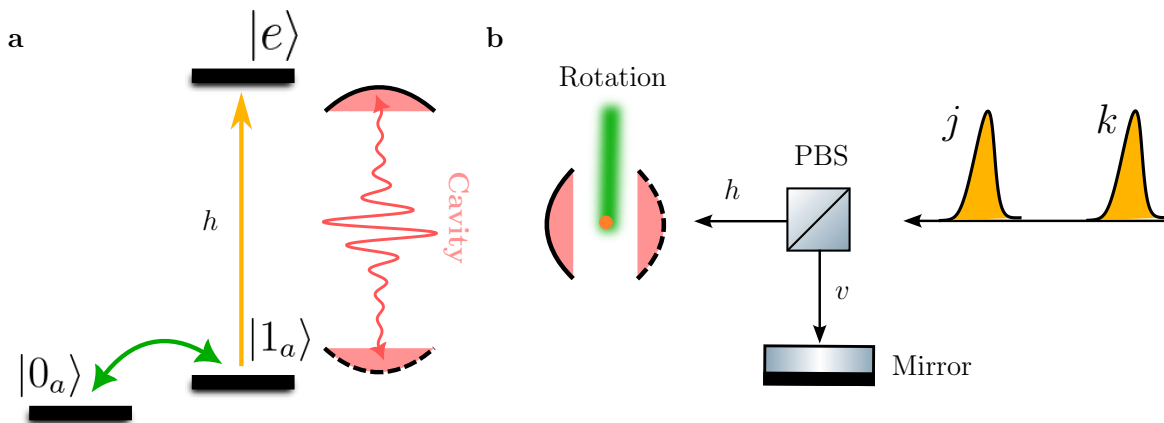


Figure 3.1: **Setup for the deterministic photon-photon gate in Ref. [65].** (a) Level scheme for the atom.  $|e\rangle$  is the atomic excited state. The  $|1_a\rangle \leftrightarrow |e\rangle$  transition couples to the one-sided cavity, and is resonantly driven by the  $h$ -polarized light (orange). The atomic ground states are coherently coupled by the green laser. (b) Experimental setup. Two photons labelled  $j$  and  $k$  resonant with the  $|1_a\rangle \leftrightarrow |e\rangle$  transition are sent through a polarizing beamsplitter (PBS) into the one-sided cavity. The  $h$ -polarized light is reflected with a  $\pi$ -phase shift when the atom is in  $|0_a\rangle$  state, while the  $v$  component is reflected by the mirror without any phase shift. Here the atomic state rotation is performed by a Raman beam (green). Figures adapted from Ref. [65].

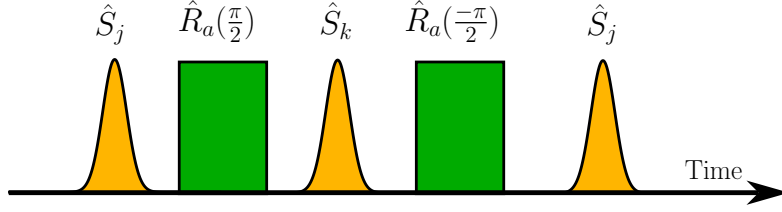


Figure 3.2: **Pulse sequence for the photon-photon CPF gate.** The protocol consists of three photon-scattering events (orange) interleaved with atomic state rotation (green). After the  $\hat{R}_a(-\pi/2)$  pulse, photon  $j$  is redirected to the cavity and scattered twice.

The interaction between the  $h$ -polarized light and the atom is described by a controlled-phase flip (CPF) gate, where the output reflected field  $\hat{a}_h^{\text{out}}$  is given by multiplying the reflection coefficient  $r$  with the incident field  $\hat{a}_h^{\text{in}}$ :

$$\hat{a}_h^{\text{out}} \approx r\hat{a}_h^{\text{in}} \equiv -\frac{\kappa_{\text{cav}} - 2i\Delta}{\kappa_{\text{cav}} + 2i\Delta}\hat{a}_h^{\text{in}}, \quad (3.1)$$

for a frequency detuning  $\Delta$  with respect to the cavity resonance and  $\kappa_{\text{cav}}$  is the cavity decay rate. When the atom is in the  $|0_a\rangle$  state, the incident pulse is resonant with the bare cavity thus  $\Delta = 0$  which gives  $r \rightarrow -1$  (corresponds to a  $\pi$ -phase shift as  $e^{i\pi} = -1$ ). When the atom is in  $|1_a\rangle$ , however, the coupling between the atom and the cavity mode (described by the interaction Hamiltonian  $\hbar g[|e\rangle\langle 1_a|\hat{a}_h + |1_a\rangle\langle e|\hat{a}_h^\dagger]$ ) effectively splits the cavity resonance into two sidebands, which are detuned from the pulse by  $\Delta = \pm g$ . Consequently, there is no phase shift as  $r \rightarrow 1$  in the strong coupling regime where  $g \gg \kappa_{\text{cav}}$ .

The protocol for a CPF gate between two photonic pulses  $j$  and  $k$ , as illustrated in Fig. 3.2, is composed of alternating scattering events  $\hat{S}_j$ ,  $\hat{S}_k$  and rotation of the atomic state  $\hat{R}_a(\theta)$ , where  $\hat{R}_a(\theta)$  is defined as the rotation around the  $-y$  axis of the Bloch sphere:

$$\hat{R}_a(\theta) = \begin{bmatrix} \cos \frac{\theta}{2} & -\sin \frac{\theta}{2} \\ \sin \frac{\theta}{2} & \cos \frac{\theta}{2} \end{bmatrix}, \quad (3.2)$$

and  $\hat{S}_j$  is a  $2^3 \times 2^3$  diagonal matrix with basis states formed by the orthogonal polarizations of the two photons and the atomic ground states. The entries of  $\hat{S}_j$  are  $r$  only for inner products  $|h_j h_k 0_a\rangle\langle h_j h_k 0_a|$  and  $|h_j v_k 0_a\rangle\langle h_j v_k 0_a|$ <sup>2</sup> but 1 otherwise. It is thus easy to show that for  $r \rightarrow -1$ , given the incident pulses  $|\Psi_j\rangle = a|h_j\rangle + b|v_j\rangle$  and  $|\Psi_k\rangle = c|h_k\rangle + d|v_k\rangle$ , the photon-photon CPF gate is mathematically described by  $\hat{S}_k[\mathcal{I} \otimes \mathcal{I} \otimes \hat{R}_a(-\pi/2)]\hat{S}_j[\mathcal{I} \otimes \mathcal{I} \otimes \hat{R}_a(\pi/2)]\hat{S}_j$ <sup>3</sup> and transforms the input state into

$$\begin{aligned} |\Phi_a\rangle \otimes |\Psi_j\rangle \otimes |\Psi_k\rangle &= |\Phi_a\rangle \otimes [ac|h_j h_k\rangle + bc|v_j h_k\rangle + ad|h_j v_k\rangle + bd|v_j v_k\rangle] \\ &\xrightarrow{\text{CPF}_{j,k}} |\Phi_a\rangle \otimes [-ac|h_j h_k\rangle + bc|v_j h_k\rangle + ad|h_j v_k\rangle + bd|v_j v_k\rangle], \end{aligned} \quad (3.3)$$

<sup>2</sup>Basically a reflection coefficient  $r$  is induced only when photon  $j$  is  $h$ -polarized and scatters on the atomic  $|0_a\rangle$  state.

<sup>3</sup>Here  $\mathcal{I}$  is a  $2 \times 2$  identity matrix. The computation is verified in the Mathematica notebook titled ‘‘GateCircuitComputationv2.nb’’ [26].

which induces a  $\pi$ -phase shift only when both photons are  $h$ -polarized. Therefore, this constitutes a controlled-phase gate between two polarization-encoded photons.

What is now interesting to us is that, firstly, Eq. (3.1) is identical to Eq. (2.5) in one-sided waveguides when taking  $\Gamma_1 = \Gamma \gg \Gamma_2$ . This equivalence is not at all surprising as one-sided cavities and waveguides share the same configuration. However, this condition implies one can realize the same CPF gate on the QD-waveguide platform when one of the optical transitions of a  $\Lambda$ -level atom has a dominating decay rate  $\Gamma_1 \gg \Gamma_2$ . This can in fact be fulfilled by having a high optical cyclicity of the QD spin state, as we will discuss later.

Secondly, one might realize that removing the first scattering event not only reduces the experimental overhead of re-routing photon  $j$ , but also results in a 3-qubit linear cluster state between the atom and photons ( $j$  and  $k$ ). This is due to the strong similarity between the gate protocol (Fig. 3.1b) and the definition of cluster states [113], namely, each scattering event operates as an entangling controlled-phase (CZ) gate between the atom and one of the photons. A succession of two atom-photon CZ gates then “knits” the nearby nodes (photons) into a linear cluster state.

### 3.2.1.1 Deterministic gate protocols for Time-bin photons

In fact, the close resemblance of the above reduced gate protocol with cluster-state generation motivates the design for a deterministic atom-photon CNOT gate in time-bin encoding. To clarify this, we swap the two single-photon pulses  $k$  and  $j$  into the time-bins of a single photon, as depicted in Fig. 3.3a. This in essence truncates the 3-qubit cluster state into a Bell state between the atom and the time-bins of a photon. Mathematically this is described by the input-output relation:

$$\begin{aligned}
|\Psi_p\rangle \otimes |1_a\rangle &\xrightarrow{\hat{R}_y(\frac{\pi}{2})} \frac{1}{\sqrt{2}}(-\alpha|e 0_a\rangle + \alpha|e 1_a\rangle - \beta|l 0_a\rangle + \beta|l 1_a\rangle) \\
&\xrightarrow{\hat{S}_e} \frac{1}{\sqrt{2}}(\alpha|e 0_a\rangle + \alpha|e 1_a\rangle - \beta|l 0_a\rangle + \beta|l 1_a\rangle) \\
&\xrightarrow{\hat{R}_y(\frac{-\pi}{2})} \alpha|e 0_a\rangle + \beta|l 1_a\rangle \\
&\xrightarrow{\hat{S}_l} \alpha|e 0_a\rangle + \beta|l 1_a\rangle,
\end{aligned} \tag{3.4}$$

which is a spin-photon Bell state with  $|\Psi_p\rangle = \alpha|e\rangle + \beta|l\rangle$  as the input photonic state encoded in early ( $e$ ) and late ( $l$ ) time-bin bases. Here for scattering event  $\hat{S}_i$  in the time-bin  $i \in \{e, l\}$ , we assume a  $\pi$ -phase shift is only induced when the scattered atom is in  $|0_a\rangle$ .  $\hat{R}_y(\theta)$  rotates the atomic ground states along the  $+y$ -axis. The gate protocol in Fig. 3.3a can therefore be straightforwardly applied to one-sided waveguides, with QD as the atom possessing the necessary cyclicity ( $\Gamma_1 \gg \Gamma_2$ ) interacting with a single photon in the time-bin bases. In practice, however, unlike a single neutral atom, the QD spin dephasing time is typically in the order of nanoseconds due to Overhauser noises arisen from neighboring nuclear spins, necessitating a spin-echo sequence built into the protocol.

Fig. 3.3b shows the modified spin-photon CNOT gate including the spin-echo  $\pi$ -pulse and the interferometer delay. Here we assume the incident photonic qubit is generated by a time-bin interferometer with delay  $\tau_{\text{int}}$ . Since the echo pulse needs to be sandwiched between two  $\pi/2$  pulses, ideally with a short  $\tau_{\text{echo}}$  to diminish effects from imperfect spin rephasing (finite  $T_2$ ), the  $\pi$  and the last  $\pi/2$  pulses should be confined between two scattering pulses. In which case, the optimal condition is to set  $\tau_{\text{echo}} = \tau_{\text{int}}$  where the

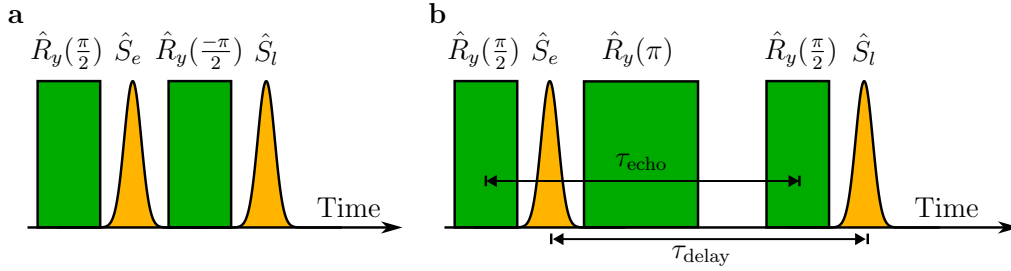


Figure 3.3: **Deterministic spin-photon CNOT protocols for time-bin photons.** (a) Minimalistic version of the gate in Fig. 3.1b by removing the first scattering pulse  $j$  and replacing the photonic qubits by single-photon pulses in different time-bins. (b) Modified version of (a) with inclusion of spin-echo refocusing pulse and time-bin interferometer delay  $\tau_{\text{int}}$ .

delay between  $\pi/2$  and  $\pi$ -pulses  $\Delta t = \tau_{\text{echo}}/2 < \tau_{\text{int}}$  is only bounded by interferometric delay, as sketched in Fig. 3.3b. Note that postponing the last  $\pi/2$  pulse until after  $\hat{S}_l$  would lead to a separable state.

While these gate protocols are in principle deterministic, they have stringent experimental requirements which are non-trivial to satisfy. Notably, the scattered field is ideally out of phase with the incident field such that they destructively interfere. To estimate the harmful effect of detuning on the imparted phase, we rewrite the reflection coefficient in Eq. (3.1) using Eq. (2.5), and obtain its average over the Gaussian pulse bandwidth and spectral diffusion distributions:

$$\bar{r} = \int_{-\infty}^{\infty} \int_{-\infty}^{\infty} \left[ 1 - \frac{2\Gamma_1}{\Gamma + 2i(\delta_e + \delta_1)} \right] N(0, \sigma_o) N(0, \sigma_e) d\delta_e d\delta_1, \quad (3.5)$$

where  $\sigma_e$  ( $\sigma_o$ ) is the standard deviation of frequency detuning  $\delta_e$  ( $\delta_1$ ) due to spectral diffusion (finite pulse bandwidth), as discussed in Sec. 2.3.1.1. In one-sided waveguides, all scattered photons ideally couple to the even waveguide mode thus  $\Gamma_1 = \Gamma$ . The first term in Eq. (3.5) represents the incident field, while the latter denotes the scattered field that carries the  $\pi$ -phase shift. The factor of 2 accounts for the overall contribution from spatially overlapping the scattered field from forward and backward modes in a two-sided waveguide<sup>4</sup>.

Figure 3.4 plots the average reflection coefficient against spectral diffusion error, at a fixed pulse bandwidth. As  $\sigma_e$  reduces, the scattered field dominates thus the overall phase shift  $\phi$  approaches  $\pi$  (as  $\bar{r} \rightarrow -1$ ); When  $\sigma_e$  grows,  $\bar{r} \rightarrow 1$  since the incident field overwhelms the scattered field: The QD resonance becomes broadened by  $\sigma_e$  such that most incident photons are reflected by the mirror in a single-sided waveguide without interaction. To see this effect, we estimated  $\bar{r} \approx 0.2$  using experimental parameters (Sec. 3.6), indicating that as the scattered field weakens, the resultant output field would mostly contain only the incident field in one-sided waveguides<sup>5</sup>.

<sup>4</sup>This is known from the fact that the even waveguide mode is the only non-vanishing mode in one-sided waveguides due to constructive interference between the backward and forward modes, i.e.,  $\hat{a}_e \equiv (\hat{a}_L + \hat{a}_R)/\sqrt{2}$  [63]. Intuitively a single-sided waveguide is viewed as folding up the two-sided waveguide [114], so the scattered fields in both  $\hat{a}_L$  and  $\hat{a}_R$  add up constructively.

<sup>5</sup>Here we assume  $\beta = 0.865$  extracted from one sample of two-sided waveguides.  $\beta$  could be higher [59]. The point is to show  $\sigma_e < 200$  MHz together with an improved  $\beta$  would make this feasible.

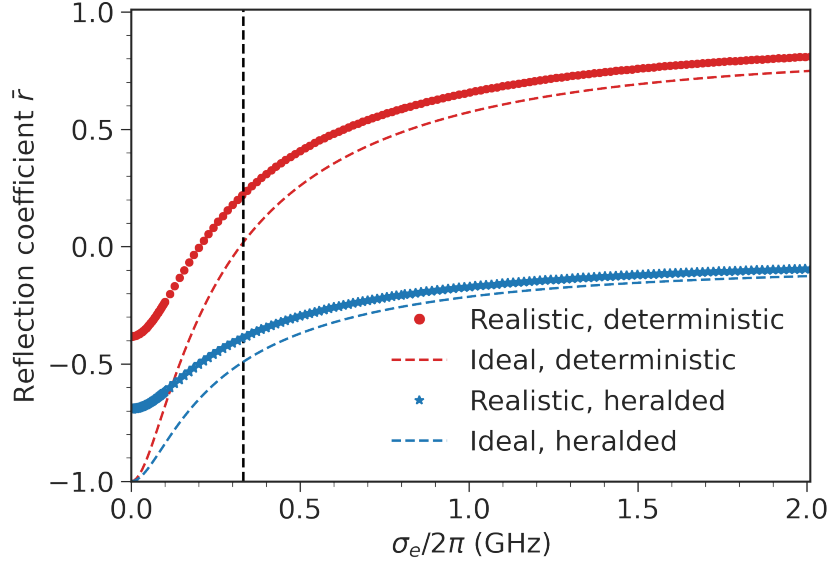


Figure 3.4: **Average reflection coefficient plotted against spectral diffusion noise**  $\sigma_e$ . For one-sided waveguides (deterministic gate), the ideal curves are computed using Eq. (3.5) with  $\Gamma_1 \rightarrow \Gamma$  and  $\sigma_o \rightarrow 0$ . The dashed curves are obtained taking  $\Gamma_1 = \frac{C}{C+1}\beta\Gamma$  (Sec. 4.3.2) and  $\sigma_o \approx 0.59 \text{ ns}^{-1}$  without pure dephasing  $\gamma_d = 0$ . For a heralded gate using two-sided waveguides, Eq. (3.6) is used to compute the curves with  $\Gamma_1 = \frac{1}{2}\frac{C}{C+1}\beta\Gamma$ .  $\Gamma = 2.48 \text{ ns}^{-1}$  is the total decay rate. Black dashed line corresponds to realistic value of  $\sigma_e/2\pi = 332 \text{ MHz}$ .

An alternative approach is to only collect the scattered photons from the backward-propagating mode in a two-sided waveguide (shown in Fig. 1.7). Although this sacrifices half of scattered photons, it avoids detecting not only the incident photons but also photons that do not interact with the spectrally broadened QD. Essentially this becomes a heralded gate that conditions on detecting the reflected photons. As such, a large  $\sigma_e$  would exclusively lower the reflectivity ( $\bar{r} \rightarrow 0$ ) but not the overall phase shift of the reflected field. In particular, the average reflection coefficient is described by

$$\bar{r}_{\text{heralded}} = \int_{-\infty}^{\infty} \int_{-\infty}^{\infty} \left[ -\frac{2\Gamma_1}{\Gamma + 2i(\delta_e + \delta_1)} \right] N(0, \sigma_o) N(0, \sigma_e) d\delta_e d\delta_1, \quad (3.6)$$

with  $\Gamma_1 = \Gamma/2$  in the ideal case. Eq. (3.6) is plotted in Fig. 3.4. In contrast to the deterministic gate, since only the backward mode is collected, there is no requirement on the interference between the incident and scattered modes. In any case, the reflection coefficient becomes more robust and increases slower with  $\sigma_e$ . There is therefore a strong motivation to opt for the heralded scheme due to its resilience to  $\sigma_e$ .

### 3.2.2 Heralded Photon-scattering gates

To implement such a heralded spin-photon gate, we need to modify the gate protocol slightly. Apart from coupling the detectors to the backward port, we also remove the last  $\pi/2$  pulse. To understand how this protocol works, we again resort to the input-output relation, but with a sole focus on the QD embedded in a two-sided waveguide.

We first substitute the atomic ground states by the QD hole spin states, where  $|0_a\rangle \rightarrow |\uparrow\rangle$  and  $|1_a\rangle \rightarrow |\downarrow\rangle$ . Following Eq. (3.4), the QD hole spin is initially prepared in the ground state  $|\downarrow\rangle$ . The ideal state evolution of the spin-photon system proceeds as

$$\begin{aligned}
(\alpha|e\rangle + \beta|l\rangle) \otimes |\downarrow\rangle &\xrightarrow{\hat{R}_y(\frac{\pi}{2})} \frac{1}{\sqrt{2}}(\alpha|e\rangle + \beta|l\rangle) \otimes (|\uparrow\rangle + |\downarrow\rangle) \\
&\xrightarrow{\hat{S}_e} \frac{1}{\sqrt{2}} \left[ \alpha(-|e\uparrow\rangle_{\mathbf{r}} + |e\downarrow\rangle_{\mathbf{t}}) + \beta(|l\uparrow\rangle + |l\downarrow\rangle) \right] \\
&\xrightarrow{\hat{R}_y(\pi)} \frac{1}{\sqrt{2}} \left[ \alpha(|e\downarrow\rangle_{\mathbf{r}} + |e\uparrow\rangle_{\mathbf{t}}) + \beta(-|l\downarrow\rangle + |l\uparrow\rangle) \right] \\
&\xrightarrow{\hat{S}_l} \frac{1}{\sqrt{2}} \left[ \alpha(|e\downarrow\rangle_{\mathbf{r}} + |e\uparrow\rangle_{\mathbf{t}}) + \beta(-|l\downarrow\rangle_{\mathbf{t}} - |l\uparrow\rangle_{\mathbf{r}}) \right] \\
&= [\alpha|e\downarrow\rangle - \beta|l\uparrow\rangle]_{\mathbf{r}} + [\alpha|e\uparrow\rangle - \beta|l\downarrow\rangle]_{\mathbf{t}}, \tag{3.7}
\end{aligned}$$

where the subscript  $\mathbf{t}$  ( $\mathbf{r}$ ) indicates the state with a transmitted (reflected) photon. The spin rotation operator  $\hat{R}_y(t) \equiv \exp(-i\hat{\sigma}_y t/2)$ , where  $\hat{R}_y(\pi)$  rotates  $|\uparrow\rangle$  to  $-|\downarrow\rangle$  ( $|\downarrow\rangle$  to  $|\uparrow\rangle$ ). From Eq. (3.7) we see that conditioning on either the reflection or transmission of a scattered photon projects the system into a different spin-photon Bell state. By varying the phase  $\theta_p$  of the photonic qubit where  $\beta/\alpha = e^{i\theta_p}$  and  $|\alpha|^2 + |\beta|^2 = 1$ , all 4 Bell states<sup>6</sup> can be generated by the gate.

---

<sup>6</sup> $|\phi^\pm\rangle_{\mathbf{r}}$  ( $|\psi^\pm\rangle_{\mathbf{t}}$ ) is obtained when conditioned on reflection (transmission), respectively.

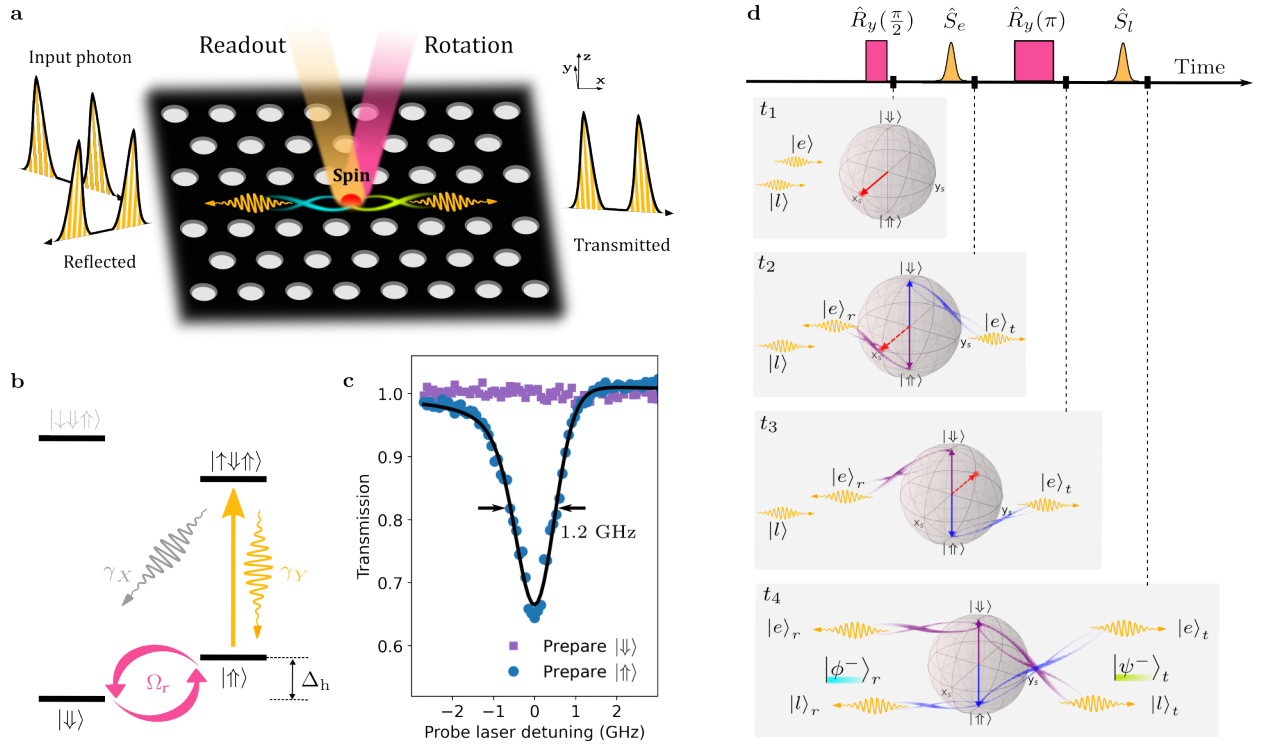


**Figure 3.5: Operational principle of the photon-scattering gate generating spin-photon entanglement.** (a) A coherently controlled spin in a QD (red) inside a photonic-crystal waveguide, where a Bell state (cyan lines) is generated upon conditional detection of a reflected photon. (b) QD level diagram. The excited state  $|\uparrow\downarrow\uparrow\rangle$  predominantly decays into  $|\uparrow\uparrow\rangle$  with rate  $\gamma_Y$  as  $\gamma_Y \gg \gamma_X$ . The wavelength of the main transition is 945 nm. Coherent control of the metastable hole spin ground states (magenta arrows, Rabi frequency  $\Omega$ ) is realized via two-photon Raman processes by a detuned laser. (c) Single-photon transmission spectra of the QD at  $\mathbf{B}_x = 2$  T when preparing the spin state in either  $|\uparrow\rangle$  or  $|\downarrow\rangle$ . (d) State evolution at different points in time during gate operation. At  $t_1$ , the QD spin (red) is prepared in a superposition state. At  $t_2$ , spin-dependent QD scattering occurs for the early time-bin  $|e\rangle$ . A  $\pi$ -rotation of the spin at  $t_3$  is followed by scattering of the late time-bin  $|l\rangle$  photon pulse at  $t_4$ . The two distinct Bell states  $|\phi^-\rangle$  ( $|\psi^-\rangle$ ) are generated conditioned on the detection of a reflected (transmitted) photon.

Figure 3.5a depicts schematics of the heralded gate in the real experimental setting, where the two-sided photonic-crystal waveguide hosts a QD. The QD is occupied by a single hole spin which exhibits a suitable  $\Lambda$ -level system with sufficiently high optical cyclicity  $\Gamma_1 \equiv \gamma_Y \gg \Gamma_2 \equiv \gamma_X$  (Sec. 3.4.1). The state evolution of the spin-photon system at different stages is illustrated in Fig. 3.5d. Here  $\hat{R}_y(\pi)$  serves two purposes: (1) to invert the spin in-between the two scattering events to create entanglement, and; (2) to prolong the spin coherence time by acting as a spin-echo pulse between the two equally long time-bins, when the spin is projected in the equatorial basis [115]. Note that the heralded photon-scattering gate protocol has previously been proposed and experimentally demonstrated on the SiV-waveguide system [116]. The novelty is therefore not on the protocol itself, but on how it is applied to the QD-waveguide platform.

### 3.3 Experimental Setup

Starting from this section, we dive into the experimental aspects of the entanglement protocol. We first introduce the optical laser setup used for spectroscopic and entanglement measurement.

#### 3.3.1 Laser Paths

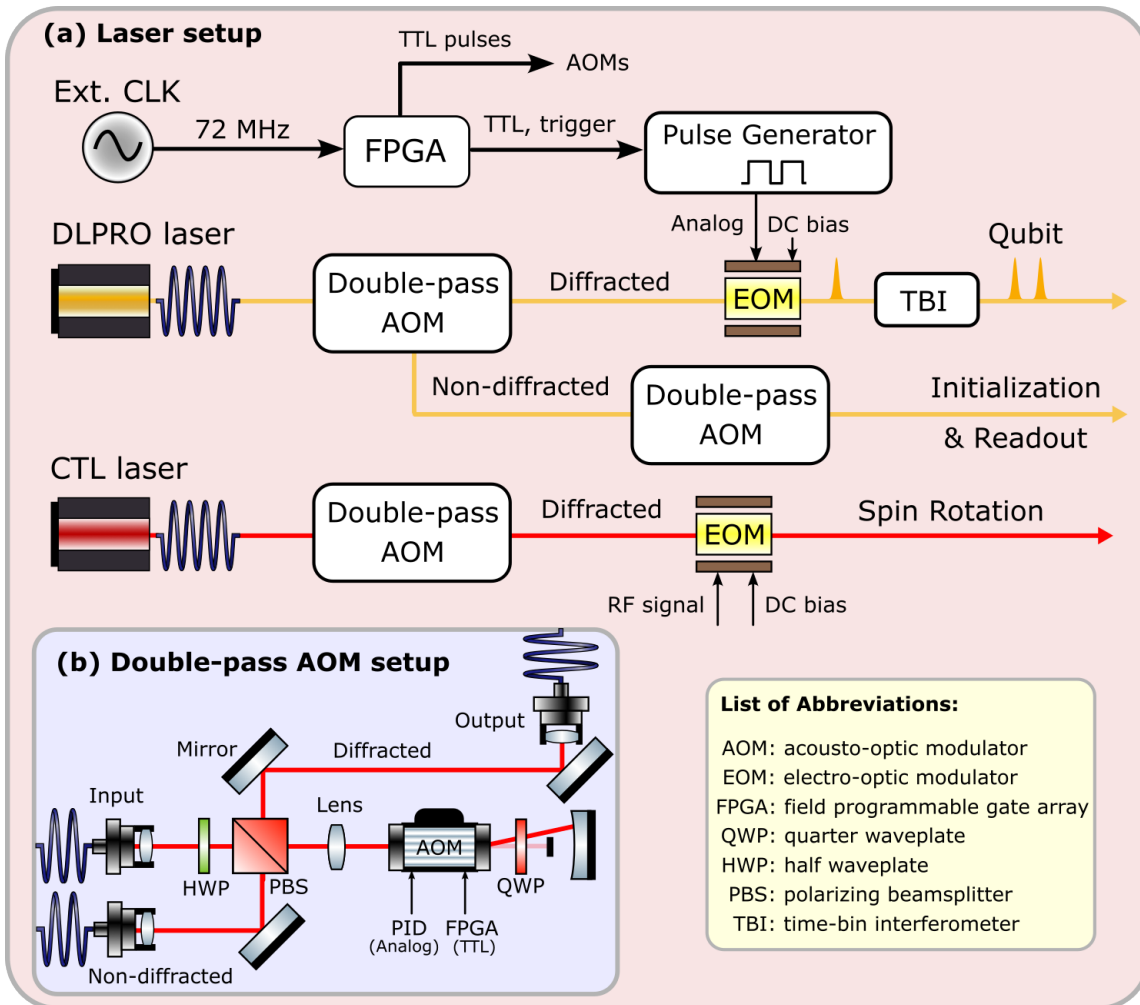


Figure 3.6: **Laser setup schematics.** (a) Two CW lasers are modulated by AOM setups and EOMs to create pulses for photonic qubits, spin initialization and rotation. An FPGA synchronized with an external clock provides TTL signals to a pulse generator and AOMs for pulse shaping. (b) Optical components for a double-pass AOM setup.

To implement the gate protocol in Sec. 3.2.2, the QD spin needs to be first optically prepared in one of its ground states. In addition, the incoming photonic qubit should be resonant with the cycling transition, such that the scattered photons in the early and late time-bins have the same polarization and frequency. Both can be achieved<sup>7</sup> by driving the same optical transition  $|\uparrow\rangle \leftrightarrow |\uparrow\downarrow\rangle$  (Fig. 3.5b).

<sup>7</sup>Spin preparation needs not to be driving the same transition as the qubit. We do this because they can be realized with a single laser.

Fig. 3.6a shows the laser setup for the experiment. For both the photonic qubit and spin preparation pulses, a continuous-wave laser (DL pro from Toptica) is used and first sent into a double-pass acousto-optic modulator (AOM) setup (Fig. 3.6b). The doubly-diffracted light from the AOM setup is then modulated by an electro-optical modulator (EOM; iXBlue NIR-MX800-LN-20), which is driven by microwave square pulses generated from a pulse generator (Agilent/HP 8131A), resulting in 2 ns (FWHM) pulses for the photonic qubit. The non-diffracted light is then directed to a second AOM setup to create spin initialization and readout pulses (200 ns each) of the same laser frequency.

Another continuous-wave laser (CTL from Toptica) is used for coherent spin control. The laser propagates through a third AOM setup, and another EOM which is amplitude-modulated by a microwave setup to generate bi-chromatic pulses for spin rotation<sup>8</sup>. All lasers are routed to an optical breadboard directly on top of the cryostat and coupled downwards to the sample chip via a 50:50 beamsplitter, as schematically shown in Fig. 3.4 of Ref. [52].

To synchronize the qubit, spin rotation and readout pulses, a sinusoidal signal with repetition frequency of 72.6 MHz<sup>9</sup> is used as an external clock for a custom-made field programmable gate array (Cyclone V FPGA from Intel), which then outputs TTL signals to produce trigger signals to the pulse generator, and square pulses for other AOMs.

The QD sample chip (Fig. 3.9) is cooled down to 4.2 K inside a closed-cycle cryostat to reduce phonon scattering processes. Inside the cryostat, a superconducting vector magnet provides a  $\mathbf{B}_x = 2$  T in-plane magnetic field enabling Zeeman splitting between two hole ground states. The sample is imaged with a 0.81 NA objective and brought to focus by translating 3 piezo positioners mounted beneath the sample [18]. A DC voltage source supplies a bias voltage at 1.148 V across the sample to populate QD charge states via tunnel coupling to a Fermi reservoir and control the charge environment (Sec. 1.2.2).

---

<sup>8</sup>More details on the spin control setup is explained in Sec. 3.5, see Figure 6.4 in Ref. [52] for the setup schematics.

<sup>9</sup>The clock signal is provided by the DG4162 function generator from RIGOL. The clock frequency is chosen to match the MIRA laser repetition rate in Ref. [18], thus only minimal changes to the timing of the pulse sequence are needed.

### 3.3.2 Time-bin Interferometer

To prepare and detect time-bin encoded photons, an unbalanced interferometer is used. The EOM-modulated pulse (orange pulse in Fig. 3.6a) enters an unbalanced time-bin interferometer (TBI) through the excitation input fiber coupler (Fig. 3.7), and splits into the short and long paths after the first beamsplitter, constituting the early and late time-bins of the photonic qubit with time delay  $\tau_{\text{int}} = 11.83$  ns.

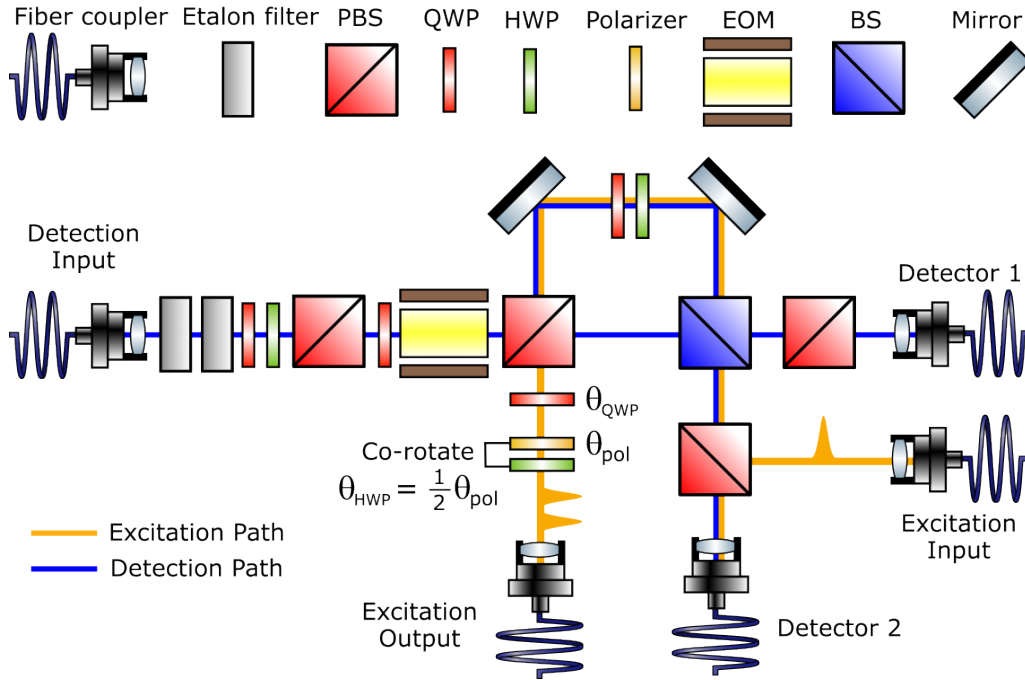


Figure 3.7: **Self-stabilizing time-bin interferometer.** The EOM-modulated pulses from DLPRO laser (Fig. 3.6a) pass through the excitation path (orange line) and divide into early and late time-bins. Photon detection (blue line) utilizes the same paths in the interferometer thus any slow drift in the phase difference between paths is cancelled out.

The photonic state can be prepared in different time-bin bases by controlling a stack of quarter-waveplate (QWP), linear polarizer and half-waveplate (HWP). Specifically, the relative amplitude between two time-bins can be tuned by the QWP: Setting  $\theta_{\text{QWP}} = 0$  ( $\theta_{\text{QWP}} = \pi/4$ ) corresponds to Z-basis (equatorial) basis state, whereas their relative phase is controlled by the combined rotation of a linear polarizer and HWP. The HWP angle  $\theta_{\text{HWP}} = \theta_{\text{pol}}/2$  with respect to the transmission axis of the polarizer is fixated at half of the polarizer angle [52], to ensure the resulting polarization state always matches the fiber polarization mode. At  $\theta_{\text{QWP}} = \pi/4$ , scanning  $\theta_{\text{pol}}$  is equivalent to creating a photonic state  $|\psi_p\rangle = |e\rangle + e^{2i\theta_{\text{pol}}}|l\rangle \equiv |e\rangle + e^{i\theta_p}|l\rangle$ , where  $\theta_p$  is the qubit phase.

Fig. 3.8a shows the pulse shape of the generated photonic qubit measured with an avalanche-photodiode detector (APD). A fit of the data using a double logistic function [117] gives a FWHM pulse duration of 1.98 ns.

For photonic state readout, the scattered time-bin photons are reinjected into the same interferometer via the detection path (orange), and pass through two narrowband (3 GHz FWHM) etalon filters [52] to remove background from the rotation laser as well as phonon sidebands. The filtered signal then traverses through a QWP and a free space polarizing-modulating EOM<sup>10</sup> which sets a 50/50 splitting ratio on the polarizing beam-

<sup>10</sup>The EOM was originally mounted for active switching of measurement basis [52]. Here it is turned

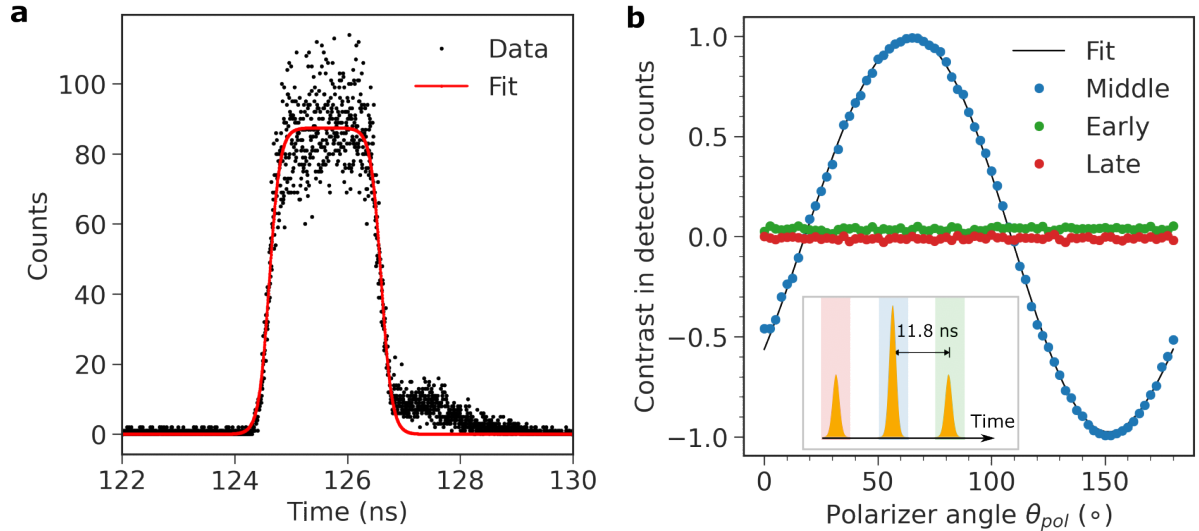


Figure 3.8: **Preparation and detection of time-bin photonic qubits.** (a) Fit of the photon pulse using the double logistic function. Recorded by APD. (b) Sweep of the linear polarizer angle  $\theta_{\text{pol}}$  at  $\theta_{\text{QWP}} = \pi/4$ . Performed by preparing a photonic qubit with the excitation path of the interferometer and reinjecting it into the detection path. The time-gated signal is measured with two superconducting nanowire single-photon detectors (SNSPDs). Inset is a schematic of the histogram recorded at one of the detectors.

splitter (PBS), allowing each time-bin to navigate through both short and long paths. For each detector, three peaks can ideally be observed from the time-resolved histogram (see inset of Fig. 3.8b). The red (green) side peak stands for an early (late) photon travelling the short (long) path of the detection interferometer, while the middle peak (blue) refers to the case when an early photon in the long path is delayed and coincides/interferes in time with a late photon travelling in the short path. Time-gating on the side (middle) peaks gives the total number of photon clicks in the Z- (X-) basis.

The advantage of combining qubit creation and readout through the same paths is that the interferometer becomes self-stabilizing [18]. By time-gating on the middle peak and varying  $\theta_{\text{pol}}$ , the classical interferometric visibility is measured to be 99.66% (Fig. 3.8b). By virtue of this, the interferometer alignment<sup>11</sup> is also robust against any slow mechanical or thermal drift<sup>12</sup> and remains stable on a week-long timescale.

off but will introduce birefringence acting similarly as a QWP. When combined with another QWP, the signal polarization is converted into diagonally polarized light.

<sup>11</sup>Details on the alignment procedures can be found in Refs. [52, 118].

<sup>12</sup>Slow compared to the interferometric delay 11.8 ns, so the noise affects both time-bins equally.

### 3.3.3 Cross-polarization Scheme

To perform reflectivity measurements and the entangling gate conditioned on reflected photons, a cross-polarized excitation scheme is adopted, where laser leakage is suppressed with polarization control, allowing a sufficiently high signal-to-noise ratio.

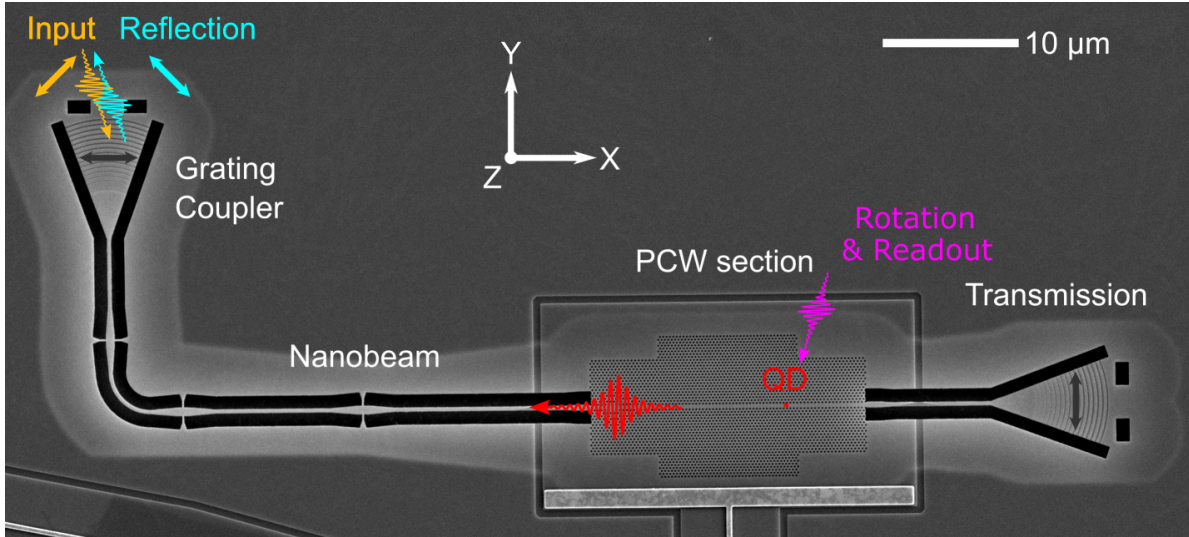


Figure 3.9: **Scanning Electron Micrograph (SEM) of a two-sided photonic-crystal waveguide (PCW), with polarizations of the input and reflected light.** It is the waveguide shown in Fig. 1.7 with identical orientations. Dark grey arrows denote the predefined polarizations of the grating couplers.

In a typical resonance-fluorescence experiment where the excitation laser (Y-polarized  $\updownarrow$ , for instance) is illuminated on top (along  $+z$ -axis in Fig. 3.9) of the QD (red dot) in a planar waveguide, laser extinction is achieved by collecting the guided dipole emission through a shallow-etched grating outcoupler [56] with its predefined polarization (X-polarized,  $\leftrightarrow$ ) to be orthogonal to the excitation. As such, the excitation and collection beams are not only spatially separated but also polarization-selective, allowing a high extinction without trading off excitation and extraction efficiencies<sup>13</sup> in a confocal microscopy setup.

For reflectivity measurements on a waveguide device, it is necessary to excite and collect through the same grating coupler. One might consider collecting from the same beam spot where the QD is excited on top; however the efficiency of the QD emission that couples out of plane will be very low due to the high waveguide-coupling efficiency  $\beta$ , and for the same reason more optical power is needed to couple into the waveguide. Therefore, it is natural to couple the out-of-plane input laser (orange arrow in Fig. 3.9) directly to the grating but collect the in-plane QD signal (red arrow) through the same beam spot, utilizing the high  $\beta$ . Table 3.1 shows the principle of the cross-polarized scheme in such a setting.

Before coupling to the grating, the polarization of the input light is optimized with a pair of excitation waveplates (half-waveplate followed by a quarter-waveplate) such that it is orthogonal to the polarization of the collected path (set by another pair of waveplates: quarter-waveplate followed by a half-waveplate). The excitation is diagonally polarized

<sup>13</sup>For implementing cross-polarized schemes in confocal microscopy, the excitation and collection modes only have a maximum of 50% overlap with the dipole polarization, see Sec. 3.1 in Ref. [119].

Exc. Pol.		Laser Leakage				GC
		$\odot$	$\ominus$	$\nearrow$	$\nwarrow$	$\leftrightarrow$
Col. $(\frac{\lambda}{2}, \frac{\lambda}{4})$						
$(0, 0) :$	$\leftrightarrow$	50%	50%	50%	50%	100%
$(\frac{\pi}{8}, 0) :$	$\odot$	100%	0%	50%	50%	50%
$(-\frac{\pi}{8}, 0) :$	$\ominus$	0%	100%	50%	50%	50%
$(\frac{\pi}{8}, \frac{\pi}{4}) :$	$\nearrow$	50%	50%	100%	0%	50%
$(-\frac{\pi}{8}, \frac{\pi}{4}) :$	$\nwarrow$	50%	50%	0%	100%	50%

Table 3.1: Overlap of polarization states between laser leakage from the excitation (Exc.) and signal through the grating coupler (GC) with the collection (Col.) at various configurations of waveplate angles.  $\lambda/2$ : Half-waveplate.  $\lambda/4$ : Quarter-waveplate. The input polarization state prior to the excitation waveplates is assumed to be horizontal ( $\leftrightarrow$ ) due to a polarizer. The waveplate settings chosen for the experiment is indicated in red, where the back-scattered light (laser leakage) is completely suppressed. The trade-off is only 50% of the QD signal through the coupler is collected.

(which can also be circularly polarized according to Table 3.1), thus only 50% of the light couples to the grating coupler which has a predefined polarization along X [56]. The X-polarized light is then converted into Y-polarization via the bend in the waveguide and subsequently interacts with the QD. Due to the non-chiral coupling of the waveguide, 50% of the scattered signal thus returns to the same grating coupler, and further passes through the polarization control on the collection path resulting in another 50% loss.

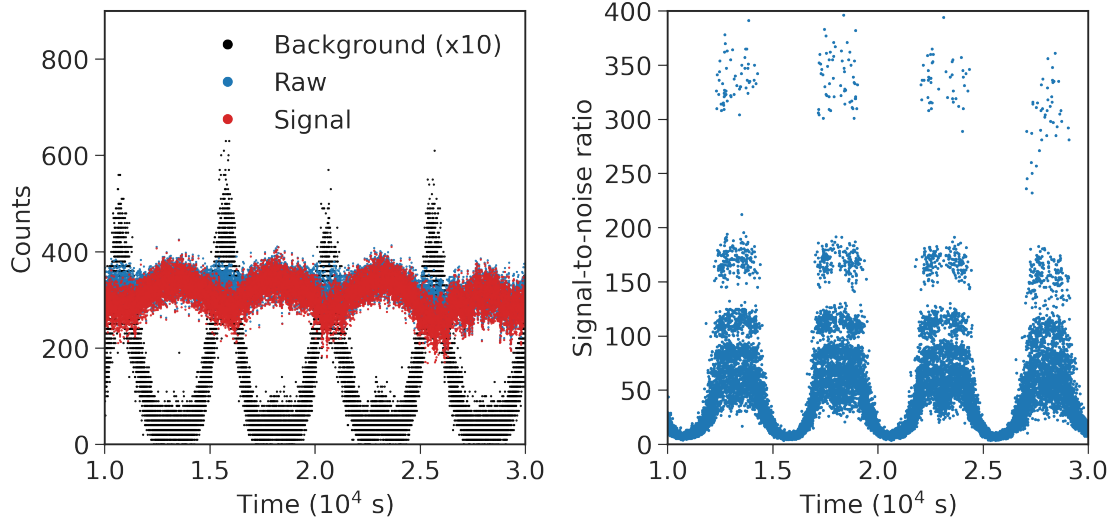


Figure 3.10: Time trace of gated counts (and signal-to-noise ratio) from photons resonantly reflected by the QD. The background counts oscillate in roughly every 75 minutes, which is attributed to the cooling cycle of an air-conditioner directly above the optical breadboard. Small temperature change of the breadboard periodically drifts the laser spot. The signal-to-noise ratio maintains a value of over 100 for 33 minutes during each crest.

Despite the loss in efficiency, the signal-to-noise ratio achieved in this setup reaches  $\sim 100$ -400 (Fig. 3.10) depending on mechanical stability of the optical setup. The trans-

mission port constitutes a second collection path which is used for probing resonant transmission. In reference to the laser setup depicted in Fig. 3.6a, both the spin rotation and readout laser pulses couple to the QD from the top (purple arrow in Fig. 3.9), while the input qubit pulses couple to the grating and interact with the QD in-plane.

## 3.4 Hole Spin Spectroscopy

With a basic understanding of the experimental setup, we are in a position to describe individual components leading up to an actual experiment. In this section, we begin by describing the physical qubit, and the optical cyclicity required for spin-dependent reflection in the gate.

### 3.4.1 Resonance Fluorescence

The physical qubit we consider here is a hole pseudo spin trapped in an InGaAs quantum dot (referred to as a positively charged exciton  $X^{1+}$  or simply  $X^+$ ). As the quantum dot is embedded in a  $p$ - $i$ - $n$  diode structure shown in Fig. 1.2, applying a bias voltage across the diode enables flexible control of the QD charged state. Figure 3.11a plots the fluorescence from a QD at different applied bias voltages and wavelengths, which reveals different QD charged states. Here the QD is excited with a pulsed broadband laser resonant with the  $p$ -shell (925 nm) [52], leading to fluorescence from electron-hole recombination of the  $s$ -shell.

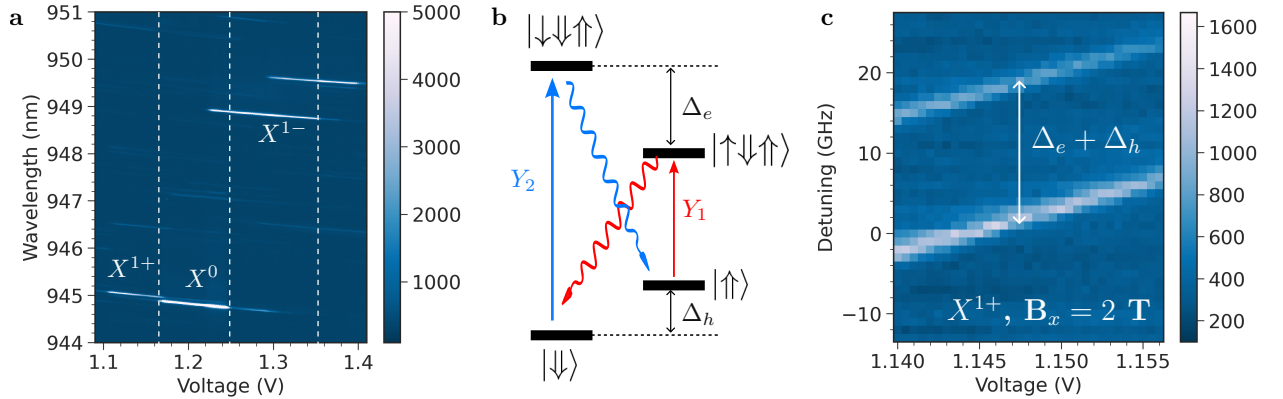


Figure 3.11: **Quantum dot photoluminescence.** (a) Emissions from different QD charged states using  $p$ -shell pulsed excitation. Figure reproduced from Ref. [52]. (b) Level structure of a QD hole pseudo spin under an in-plane magnetic field  $\mathbf{B}_x$ , following Fig. 1.6c but with the subscripts omitted. The total Zeeman splitting  $\Delta_e + \Delta_h$  is probed by continuously pumping both Y-polarized transitions and recording the photoluminescence. (c) Two-color  $X^+$  spin pumping experiment performed at around 1.145 V to measure  $\Delta_e + \Delta_h$  at  $\mathbf{B}_x = 2$  T.

Since the diode heterostructure used in this work is designed such that the GaAs tunnel barrier next to the  $n$ -doped back contact is considerably thinner than that with the  $p$ -doped region (Sec. 1.2.2), the tunneling of electrons from the back contact becomes much more probable than that of holes from  $p$ -layers [43]. Therefore, for such a design, the QD can be deterministically charged with an electron just by applying a bias and hence such a diode is referred to as an  $n$ -type device [37]. For the same reason, injecting a hole to the QD in an  $n$ -type device is probabilistic. In practice, this requires applying a blue-detuned laser (830 nm) to create an electron-hole pair in the QD, where the electron is subsequently tunneled out, leaving a hole behind (Sec. 1.2.2).

For the photon-scattering entanglement experiment, we are interested in a QD having a  $\Lambda$ -level energy scheme. This is possible by applying an external magnetic field to a single hole or electron spin of the QD. Due to Zeeman effect four non-degenerate energy

levels become optically accessible (Fig. 3.11b). To identify these transitions for  $X^+$ , two-color continuous-wave spin pumping is usually implemented where one laser is locked on resonance with one of the transitions exciting the QD on top (i.e.,  $Y_2$  in Fig. 3.11b), followed by a frequency scan of a second laser (i.e.,  $Y_1$ ). The combination of both lasers reshuffles the spin population via optical spin pumping, allowing resonance fluorescence from each transition to be detected.

Figure 3.11c scans the frequency of the second laser as a function of bias voltage at a magnetic field of  $\mathbf{B}_x = 2$  T, indicating a total frequency splitting of  $\Delta_e + \Delta_h \approx 16.9$  GHz. Here we observe only two plateau lines as both pump lasers are Y-polarized. Repeating the same scan with the polarization of one (or both) laser(s) flipped to X enables  $\Delta_e$  and  $\Delta_h$  to be determined separately [52].

### 3.4.2 Two-color Resonant Transmission

There are numerous important figures of merits that benchmark the quality of any QD-waveguide device. These include the efficiency  $\beta$  of emitted photons coupled to the waveguide mode, commonly known to as the  $\beta$ -factor, the QD total decay rate  $\Gamma$ , phonon-induced pure dephasing rate  $\gamma_d$  and standard deviation in spectral diffusion fluctuation  $\sigma_e$ . In this section, we perform resonant transmission experiments to extract  $\beta$  and  $\sigma_e$ .

For a two-level atom in a waveguide, one could extract  $\beta$  and  $\sigma_e$  by measuring the atomic transmission spectrum, driven weakly with a single probe laser. When driven resonantly, the destructive interference between the phase-shifted scattered field and the probe in the waveguide results in a transmission dip [120] (as discussed in Sec. 1.5). The dip amplitude and width of the spectrum are therefore indicative of the relative phase between the incident and scattered field, which depends on  $\beta$  and  $\sigma_e$ . As a higher probe laser power broadens the transmission width by saturating the atom, but without affecting  $\beta$  or  $\sigma_e$ <sup>14</sup>, one could essentially tune the transmission dip by varying the probe power, allowing  $\beta$  and  $\sigma_e$  to be estimated.

For any atom with a multi-level system, however, to probe the transmission of one particular optical transition one needs to first initialize the atomic state. For  $X^+$  with a four-level system depicted in Fig. 3.12a, we first apply a 150-ns pulse (green) to initialize the hole spin in the  $|\uparrow\rangle$  state by optical spin pumping, followed by scanning the frequency of a second 150-ns pulse at various probe powers (Fig. 3.12b). Both pulses are separated in time to avoid contamination in the probed signal due to spin pumping. This measurement is usually referred to as a two-color resonant transmission experiment as the two pulses usually have distinct frequencies.

Since the duration of the probe pulse is orders of magnitude longer than the QD lifetime  $1/\Gamma \approx 403$  ps, the atom displays similar saturation behaviour as being driven by a continuous-wave (CW) laser. As such, the relevant transmission fit function describing an atom driven by a weak CW laser [36, 121] is applicable to the pulsed measurement<sup>15</sup>.

The transmission spectrum recorded by time-gating on the fluorescence during the probe pulse is shaped by a combination of phonon-induced pure dephasing  $\gamma_d$ , coupling

<sup>14</sup>This might not be true in practice if the probe laser introduces charge noises or spin dragging.

<sup>15</sup>For shorter pulses comparable to the atomic lifetime, this approximation no longer holds [122] and one needs to average the transmission spectrum with a spectral intensity profile of the pulse. See Sec. 2.3.1.1 for such treatment.

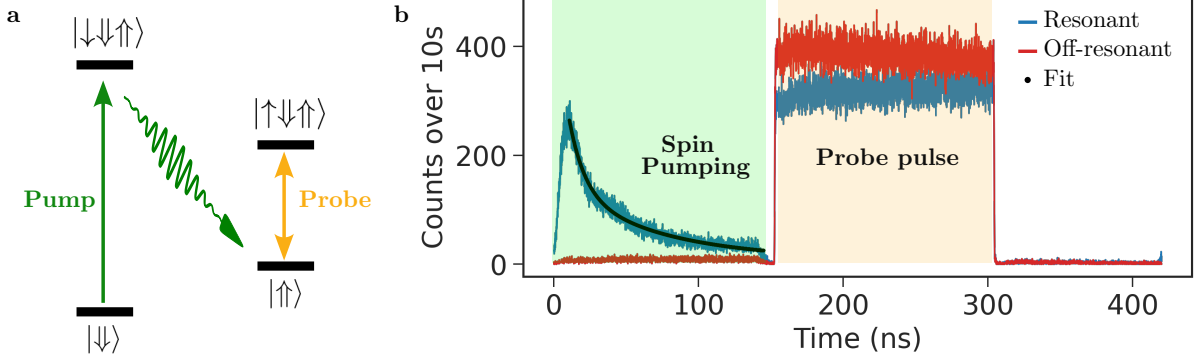


Figure 3.12: **Two-color transmission measurement on the waveguide-embedded QD hole spin.** (a) QD Level diagram. A strong pump pulse (green) prepares the spin state  $|\uparrow\rangle$ , while the frequency of the weak probe pulse (orange) is scanned to reveal the QD transmission spectrum. (b) Time-resolved histogram of the pulse sequence with resonant (1.148 V) and off-resonant (1 V) bias voltages. A bi-exponential fit is used to extract a lower bound on the spin pumping fidelity.

efficiency  $\beta$ , spectral diffusion  $\sigma_e$ , Fano parameter  $\xi$ <sup>16</sup>, spin pumping fidelity  $P_{sp}$  and optical cyclicity  $C$  (introduced in Sec. 3.4.1). To fit the spectra, the following normalized transmission function is used

$$\mathcal{I}_T(\omega - \omega_1) = 1 + P_{sp}\mathcal{R}_T(\omega - \omega_1), \quad (3.8)$$

where  $\omega - \omega_1$  is the probe laser detuning with respect to the transition frequency  $\omega_1$  of  $|\uparrow\rangle \leftrightarrow |\uparrow\downarrow\uparrow\rangle$ .  $\mathcal{R}_T(\omega - \omega_1)$  is the QD frequency response function given by

$$\mathcal{R}_T(\omega - \omega_1) = \text{Re} \left( \frac{\frac{C}{C+1}\beta\Gamma^2 [\Gamma + 2\gamma_d + 2i(\omega - \omega_1)](i + \xi) [2i + \frac{C}{C+1}\beta(-i + \xi)]}{\Gamma[(\Gamma + 2\gamma_d)^2 + 4(\omega - \omega_1)^2] + 8\eta(\Gamma + 2\gamma_d)P} \right). \quad (3.9)$$

Here  $\Omega = \sqrt{\eta P}$  is the optical Rabi frequency expressed by the setup loss factor  $\eta$  and the input laser power  $P$ <sup>17</sup>. A non-unity spin pumping fidelity  $P_{sp} \rightarrow 0$  implies the QD will go dark when its spin is prepared in the wrong state [123]. As such, the probe beam does not interact with the QD resulting in transmission  $\mathcal{I}_T(\omega - \omega_1) \rightarrow 1$ . An average value for  $P_{sp}$  is obtained by first fitting the fluorescence decay during the pumping pulse (Fig. 3.12b) then averaging over all frequencies and probe powers.

Eq. (3.8) is a phenomenological fit model that incorporates the spin pumping fidelity and cyclicity into Eq. (S33) in Ref. [121]. While this might not be a complete model<sup>18</sup>, it adequately describes the transmission spectrum. In the low power limit  $P \rightarrow 0$  with a perfectly prepared two-level system  $P_{sp} \rightarrow 1$ , the expression reduces to Eq. (S33) in Ref. [121] with  $\beta$  replaced by  $\frac{C}{C+1}\beta$ , as a finite  $C$  limits the number of resonantly reflected photons leading to diminished interference. To account for slow resonance drifts due to spectral diffusion, we obtain the average transmission intensity  $\bar{\mathcal{I}}_T(\omega_1)$  over the Gaussian distribution  $N(0, \sigma_e)$  (Sec. 2.3.1.1).

<sup>16</sup>This parameter affects the symmetry of the transmission lineshape, which is attributed to weak cavity-like interference between the scattered field and reflection from the mode adapters in the fast light photonic-crystal region [119].

<sup>17</sup>This is measured with a power meter from 10% of the input light.

<sup>18</sup>In principle, the bona fide approach for deriving the fit function is by solving the quantum Heisenberg-Langevin equations (or master equations) for a  $\Lambda$ -level atom illuminated by a coherent state  $|\alpha\rangle$ . However, this requires taking Fano resonance, pure dephasing rate, spin pumping fidelity and cyclicity into account, which is an extensive theoretical study that is out of the scope of this thesis.

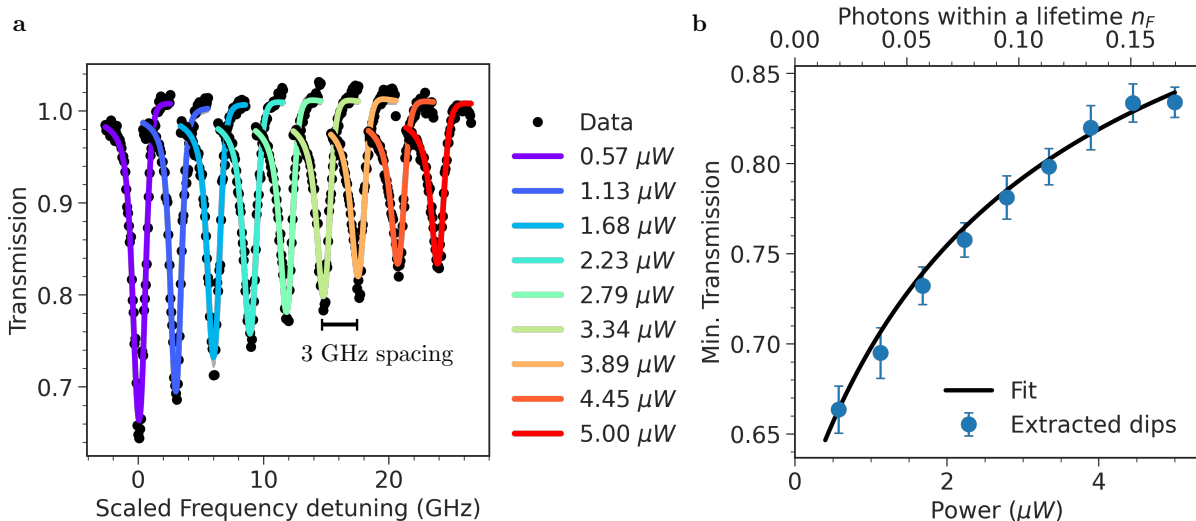


Figure 3.13: **Results from iteratively fitting transmission spectra to extract coupling efficiency  $\beta$  and spectral diffusion  $\sigma_e$ .** (a) Transmission spectra fitted at different probe powers. The frequency detuning axis has been rescaled such that each spectra is 3 GHz apart. The central frequency is 317.235 THz. The data (black circles) are fitted using Eqs. (3.8)-(3.9). (b) The transmission dips extracted from (a) are then fitted to estimate  $\beta$ . The fitting steps are described in the text.

We have developed an iterative fitting procedure for the data in Fig. 3.13 to reliably estimate  $\beta$  and  $\sigma_e$ . The general idea is to divide the data into two sub-dataset and fit both on each iteration. The first dataset is a set of transmission spectra as a function of probe powers, while the second dataset consists of only the transmission dip at various powers. The algorithm runs iteratively based on results from the previous fit and terminates when the fitted parameters from both fits converge. The convergence implies that there is a set of parameters which simultaneously holds true when using two different fit functions on the same data.

The fitting process is described as follows: (1) We fix the total decay rate  $\Gamma = 2.48 \text{ ns}^{-1}$  [18],  $P_{sp} = 0.897$ ,  $\gamma_d = 0.099^{19} \text{ ns}^{-1}$  and  $C = 14.7$  [18] as they are measured independently. For the first fit we assume  $\beta = 0.95$ ; (2) Based on these values, we take  $\sigma_e$ ,  $\xi$  and loss factor  $\eta$  as free parameters to perform a least square fit on the transmission spectrum at each power (Fig. 3.13a). This results in a list of fitted values for  $\sigma_e$ ,  $\xi$  and  $\eta$ . Their corresponding mean values are then used to fit the second dataset (transmission dips as a function of probe power) with only  $\beta$  and  $\eta$  as free parameters (Fig. 3.13b). (3) From here we obtain an updated value of  $\beta$  which is used to fit the transmission spectra again in step 2. (4) The iteration stops when  $\beta$  after loop  $i$  converges (i.e.,  $|\beta_i - \beta_{i-1}| < 0.1\%$ ).

The fit is completed in 10 iterations. The extracted parameters with  $3\sigma$ -uncertainty are presented in Table 3.2. Both  $\sigma_e = 2\pi \times (332 \pm 15) \text{ MHz}$  and  $\beta = (0.865 \pm 0.059)$  are in very good agreement with previous estimates from two-color continuous-wave spin pumping<sup>20</sup> [20] and transmission<sup>21</sup> [121] measurements, respectively, indicating that two-color pulsed transmission through photon-scattering in a waveguide, together with power-

<sup>19</sup>This is directly extracted from power-dependent photon visibility measurements, as we shall cover in Sec. 3.4.5.

<sup>20</sup>This experiment is carried out by exciting the QD on top.

<sup>21</sup>This measurement is done with a continuous-wave laser on a different QD of the same wafer.

dependent photon visibility measurements to extract  $\gamma_d$ , could be an alternative way to accurately extract these QD noise parameters. Note that due to the non-unity hole initialization efficiency, the actual value of  $\beta$  could be even higher, as the QD also blinks if the hole spin is not loaded. Additionally, since the pumping pulse is generated with a slow acousto-optical modulator with 8 ns rise time, the imperfect pump pulse shape together with residual repumping from the probe pulse might have underestimated the spin pumping fidelity. Therefore, the extracted value for  $\beta$  constitutes a lower bound.

Parameter	Value	Confidence interval (99.7%)
$\beta$	0.865	[0.806, 0.924]
$\sigma_e/2\pi$	332 MHz	[317, 347]
$\eta$	0.427	[0.406, 0.448]
$\xi$	-0.127	[-0.137, -0.117]
$P_{sp}$	0.897	[0.895, 0.899]

Table 3.2: Relevant parameters extracted from fitting the transmission spectra.  $P_{sp}$  is estimated from fitting the fluorescence decay during the spin pumping pulse.

### 3.4.3 Optical Cyclicity

Another important parameter relevant to the quality of the waveguide-integrated spin-photon interface is the optical cyclicity  $C$ . By definition, it is the ratio between radiative decay rates of an excited state that couples to multiple dipole transitions [20]. For a hole spin with the four-level system in Fig. 3.14,  $C \equiv \gamma_Y/\gamma_X$  is the decay rate ratio between the dominant and weaker transitions from either of the two trion states. When the dominant transition is fully cycling,  $C \rightarrow \infty$  meaning the spin ground state can be repeatedly excited and will eventually return to its original state without undergoing Raman spin-flip. This is equivalent to saying the QD has the highest decay rate asymmetry  $\varepsilon = \Gamma_1 - \Gamma_2 \rightarrow \Gamma$  as introduced in Chapter 2.

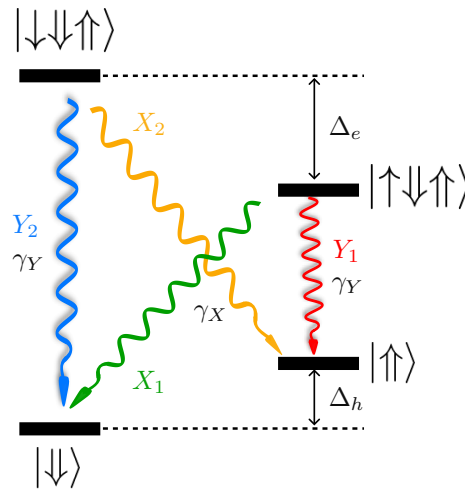


Figure 3.14: **Energy levels of  $X^+$  under an external magnetic field.** It comprises a double  $\Lambda$ -system, each consisting of an X- (cross transition) and a Y-polarized (vertical transition) linear dipoles.

By embedding a QD in a photonic-crystal waveguide (PCW), optical cyclicity can be different depending on the spatial position of the QD in the PCW. The reason being the local optical density of states around the QD varies with its position in the PCW (Eq. (1.17)), thus at certain positions (i.e., at the waveguide center) the Purcell factors for X- and Y-dipoles are different, leading to a suppression of  $\gamma_X$  and an enhancement in  $\gamma_Y$ . In unstructured bulk GaAs where Purcell enhancement is absent,  $C = 1$ .

To estimate  $C$ , the typical approach is to measure the power-dependent optical spin pumping rate  $\gamma_{\text{osp}}$  from driving the  $Y_2$  transition with a long pulse. From which the decay rate  $\gamma_X$  can be extracted and then compared with the total decay rate  $\Gamma \equiv \gamma_X + \gamma_Y$  to estimate  $C$ <sup>22</sup> [20, 52]. This measurement requires driving both Y-polarized transitions with two lasers at different frequencies, while exciting the QD from the top.

#### 3.4.3.1 Estimate Cyclicity from Spin-dependent Transmission

Here we show an alternate method to estimate  $C$  for  $X^+$ , by photon-scattering through the waveguide. Similar to the previous approach, we first excite the QD from the top to prepare the hole spin state via a 150 ns spin preparation pulse resonant with  $Y_2$  (Fig. 3.15a). A 150 ns probe pulse then propagates through the waveguide, and

<sup>22</sup>This method is later adopted in Sec. 6.3.2.

is attenuated by neutral-density filters to reduce multi-photon scattering, as well as to minimize spin pumping during the probe.

Similar to Sec. 3.4.2, we perform frequency scans of the probe pulse at different probe powers and record photon counts from the first 50 ns of each pulse at the transmission port of the two-sided waveguide. Figure 3.15b plots the total counts gated on the spin preparation pulse at different probe detunings. We observe fluorescence peaks when the probe frequency is resonant with transitions  $Y_1$  and  $X_2$ , indicating the strong presence of spin pumping by the probe pulse which transfers the spin population to  $|\downarrow\rangle$ . This is also supported by the fact that both peaks increase with probe powers.

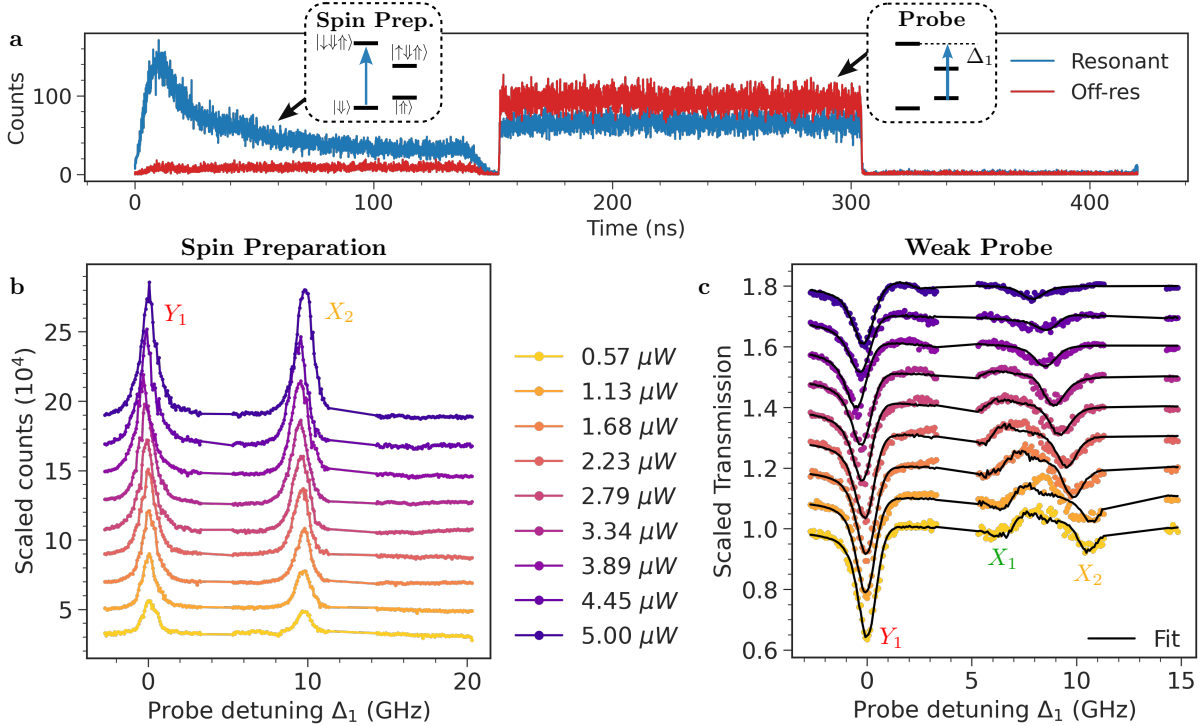


Figure 3.15: **Two-color pulsed transmission measurement to estimate cyclicity  $C$ .** (a) Time-resolved histogram of the pulse sequence at resonant (1.148 V) and off-resonant (1 V) bias voltages. The hole is probabilistically created via an above-band (ABB) pulsed laser (not shown). Photons are recorded by an APD with a 65 GHz FWHM grating filter.  $\Delta_1$  is the probe detuning with respect to the lowest energy transition. (b) Fluorescence from the spin preparation pulse as a function of probe detuning at various powers. The  $y$ -axis is rescaled so each curve differs by  $2 \times 10^4$  counts. (c) Power-dependent transmission spectra gated on the probe pulse. Each curve is vertically separated by 0.1.

Recording the photon counts from the probe pulse allows one to examine the destructive interference between the incident and scattered photons. From Fig. 3.15c, three transmission dips can be seen when the probe is resonant with  $Y_1$ ,  $X_1$  and  $X_2$ , respectively<sup>23</sup>. In addition, we note that the resonant peaks and dips shift with probe powers. This can be attributed to power tuning [52] in which the presence of photo-induced charges tunes the resonant frequency of the QD transition, a phenomenon commonly observed in the current device.

<sup>23</sup>Note that here the dip positions for  $X_1$  and  $X_2$  are swapped, when compared to Figure 5.8b in Ref. [52], owing to the flipped level structure of  $X^+$ .

To estimate  $C$ , we fit the normalized transmission spectra  $\bar{\mathcal{L}}_T$  in Fig. 3.15c at various probe powers, using the model

$$\bar{\mathcal{L}}_T = 1 + P_{sp}\bar{\mathcal{R}}_T(\omega_1) + (1 - P_{sp})\bar{\mathcal{R}}_T(\omega_1 + \Delta_h) + AP_{sp}\bar{\mathcal{R}}_T(\omega_1 + \Delta_e), \quad (3.10)$$

where  $P_{sp}$  is the spin pumping fidelity,  $\bar{\mathcal{R}}_T(\omega_j)$  is the QD response function (Eq. (3.9)) centered at  $\omega_j$  averaged over the Gaussian spectral diffusion, which takes all relevant waveguide parameters (i.e.,  $\beta$ , Fano resonance  $\xi$ ,  $\gamma_d$  etc.) into account.  $\omega_1$  ( $\omega_1 + \Delta_h$ ) is the resonant frequency of the transition  $Y_1$  ( $X_1$ ). For transitions  $X_1$  and  $X_2$ ,  $\beta$  is multiplied by the fraction  $\frac{1}{C+1}$  to represent the suppressed decay rates<sup>24</sup>. On account for the dip asymmetry between  $X_1$  and  $X_2$  observed in Fig. 3.15c, a factor  $A$  is introduced to the response function of  $X_2$ . This factor is estimated to be  $\approx 3$  by computing the average ratio between dip amplitudes of  $X_1$  and  $X_2$  at different powers, and is attributed to the difference in spin pumping rates between the two pulses.

By performing a bi-exponential fit on the spin preparation pulse at each detuning  $\Delta_1$ , we observe that  $P_{sp}$  varies by 10% due to spin pumping of the probe pulse. To account for this, instead of using an average value of  $P_{sp}$ , we adopt the list of  $P_{sp}$  as fixed parameters<sup>25</sup> in the transmission fit model (Eq. (3.10)). From fitting the spectra in Fig. 3.15c we estimated a cyclicity of  $C = 15.1 \pm 0.9$ <sup>26</sup> with an uncertainty of  $3\sigma$ , which agrees very well with the value of  $14.7 \pm 0.2$  [18] extracted from two-color spin pumping with top-excitations.

While this photon-scattering approach predicts an accurate value of  $C$ , it is generally not recommended as the fitting formula involves a lot more parameters that are subject to measurement noises. In contrast, the top-excitation method requires only measuring the total decay rate  $\Gamma$ , spectral diffusion noise  $\sigma_e$  and the power-dependent optical spin pumping rate  $\gamma_{osp}$ . Nevertheless, the close agreement between two estimated values of  $C$  demonstrates good validity of both approaches.

<sup>24</sup>For the dominant transition  $Y_1$ , this factor becomes  $\frac{C}{C+1}$  as introduced in Eq. (3.9).

<sup>25</sup>This means  $P_{sp}$  is an  $n \times m$  matrix where  $n$  is the number of scanned powers and  $m$  is the number of detunings. A row of  $m$  values of  $P_{sp}$  is inputted as fixed parameters in the fit at each power.

<sup>26</sup>When fitting the transmission spectra, we use the extracted values for the total decay rate  $\Gamma$ , pure dephasing rate  $\gamma_d$ , waveguide-coupling efficiency  $\beta$  and spectral diffusion noise  $\sigma_e$  in Sec. 3.4.2, and fix  $A$ ,  $P_{sp}$  and the dip position for  $X_2$ , while taking the loss factor  $\eta$ , the Fano resonance  $\xi_j$  for each transition  $j \in \{1, 2, 3\}$  and the dip position for  $X_1$  as free parameters. Special care is taken to ensure the dip position for  $X_1$  lies around the measured value of  $\Delta_1 = \Delta_h = 2\pi \times 7.3$  GHz.

### 3.4.4 Spin-dependent Reflection

Apart from measuring the transmission spectrum, another approach to probe the single-photon scattering process is through QD saturation measurement by analyzing the reflection spectrum, in which the QD saturation behaviour is observed by scanning the power of the input probe laser. The mean photon number per pulse  $\bar{n}$  can then be extracted at a given probe power, where  $\bar{n} \ll 1$  indicates the scattering occurs in the single-photon regime. As we shall explore in Sec. 4.3.7, this is useful for estimating the gate infidelity as a non-zero  $\bar{n}$  enters as a linear error due to driving-induced dephasing.

To accurately estimate  $\bar{n}$ , we run a pulse sequence that mimics the entangling gate experiment: A single pulse of 2 ns duration is prepared and scatters on a QD spin initialized in either  $|\uparrow\rangle$  or  $|\downarrow\rangle$ . Due to the QD spin-dependent reflectivity, the input photon which is resonant with the QD transition  $|\uparrow\rangle \rightarrow |\uparrow\downarrow\rangle$  is coherently reflected. By time-gating on the reflected signal (Fig. 3.16a; green shaded region) and increasing the input power, the QD prepared in  $|\uparrow\rangle$  becomes saturated (Fig. 3.16b). The averaged intensity in the reflected signal is fitted assuming a two-level system between  $|\uparrow\rangle \rightarrow |\uparrow\downarrow\rangle$

$$\mathcal{I}_R = b_{\max} \int_{-\infty}^{\infty} \frac{\frac{C}{C+1}\beta(1 + \frac{2\gamma_d}{\Gamma})\Omega_1^2}{(\frac{\Gamma}{2} + \gamma_d)^2 + \delta_e^2 + 2(1 + \frac{2\gamma_d}{\Gamma})\Omega_1^2} N(0, \sigma_e) d\delta_e, \quad (3.11)$$

where  $\Omega_1$  is the Rabi frequency driving the transition  $|\uparrow\rangle \rightarrow |\uparrow\downarrow\rangle$ ,  $\delta_e$  is the effective resonance drift due to spectral diffusion. A setup loss factor  $b$  is introduced to associate the Rabi frequency to the input power  $P$  where  $\Omega_1 = \sqrt{bP}$ <sup>27</sup>. Here  $b_{\max}$  and  $b$  are free parameters, whereas  $\sigma_e$  and  $\gamma_d$  are estimated in Secs. 3.4.2 and 3.4.5. Eq. (3.11) holds when  $\Gamma \gg \kappa_g$  and  $T_p \gg \Gamma^{-1}$  where  $\kappa_g$  is the effective spin-flip rate between the hole ground states and  $T_p$  is the FWHM qubit duration measured from the pulse intensity. The first condition implies that the QD decays faster than the spin can recycle, thus  $|\uparrow\rangle \rightarrow |\uparrow\downarrow\rangle$  is effectively a two-level system. This is generally true since  $\kappa_g$  is typically on the order of  $10^{-7} \text{ ns}^{-1}$  at the plateau center voltage [124], which is lower than  $\Gamma = 2.48 \text{ ns}^{-1}$ . The second condition ensures that the QD decays back to  $|\uparrow\rangle$  before the next scattering event within the pulse. When the driving pulse is sufficiently long, i.e.,  $T_p = 2 \text{ ns} > \Gamma^{-1} = 0.4 \text{ ns}$  with increasing power, the QD saturates similarly as when being driven continuously by a CW laser<sup>28</sup>. In addition, a finite cyclicity leads to a resonant spin-flip into the dark state  $|\downarrow\rangle$  reflecting a photon of frequency  $\omega_2 \neq \omega_1$  which is filtered out, thus only reducing the total intensity included in  $b_{\max}$  and not affecting the scaling of Eq. (3.11).

From fitting the data (Fig. 3.16b), we extract  $b = (3.00 \pm 0.07) \text{ ns}^{-2}/\text{nW}$ . The saturation parameter  $S$  at an input power  $P = 0.075 \text{ nW}$  used for a single pulse is estimated to be  $0.05 \pm 0.001$  using

$$S = \int_{-\infty}^{\infty} \frac{2(1 + \frac{2\gamma_d}{\Gamma})bP}{(\frac{\Gamma}{2} + \gamma_d)^2 + \delta_e^2} N(0, \sigma_e) d\delta_e. \quad (3.12)$$

<sup>27</sup> $b$  is a proportionality constant that relates the measured input power (from a power meter) to the output optical Rabi frequency, which includes optical losses, waveguide-coupling efficiency  $\beta$ , and polarization mismatch between the laser and QD dipole via  $-\hat{d} \cdot \hat{E}$ . It states how fast the QD can be driven given one unit of energy.  $\beta \rightarrow 0$  or exciting with an incorrect orthogonal polarization means the QD cannot be driven despite having sufficient optical power thus  $\eta \rightarrow 0$ .

<sup>28</sup>One could average Eqs. (3.11) and (3.12) with a Gaussian or sinc (Fourier transform of square pulse in time) spectral field profiles, but the extracted  $\bar{n}$  will not change.

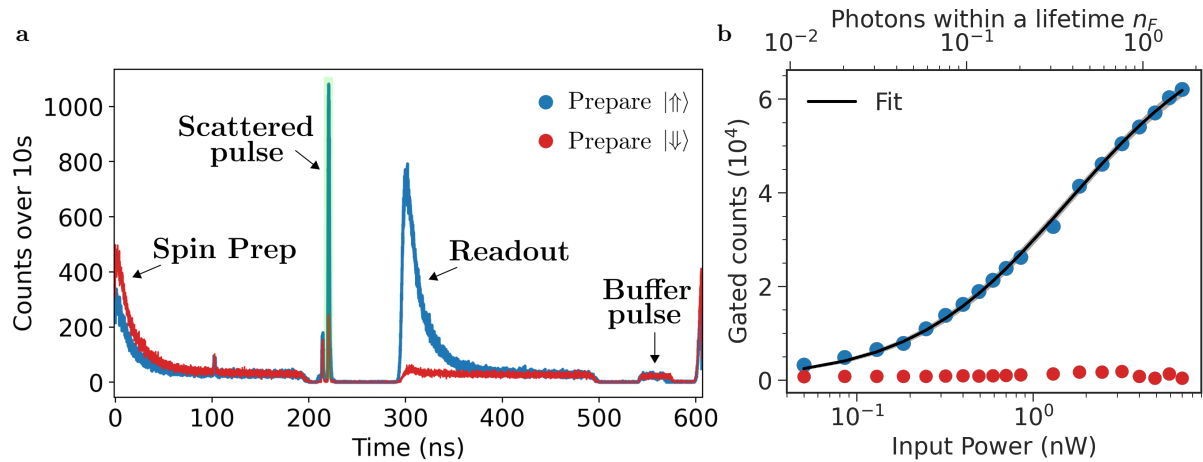


Figure 3.16: **Saturation measurement to calibrate the mean photon flux.** (a) Time-resolved histogram of the measurement sequence. A 2 ns probe pulse gets reflected from a QD prepared in  $|\uparrow\rangle$  via optical spin pumping followed by a  $\pi$ -rotation pulse. The reflected signal is time-gated (green shaded region) and recorded for each input power. Peaks at around 100 ns and 215 ns are laser scatter from the time-bin interferometer and the optical breadboard, respectively. The spin readout at 300 ns maintains the same duty cycle as the entangling gate experiment and does not affect the gated counts. (b) Gated fluorescence in the reflection as a function of the input probe power. Blue (red) circles are summed counts over a time window of 3 ns, when the QD spin is prepared in  $|\uparrow\rangle$  ( $|\downarrow\rangle$ ). Fitted (black solid line) using Eq. (3.11). Around 0.075 nW is used for a single pulse in the quantum gate experiment.

The mean photon number *within* one QD lifetime or mean photon flux in the guided mode is defined as  $n_F \equiv S n_c$  with  $n_c \equiv \frac{(1+2\gamma_d/\Gamma)}{4\beta^2}$  [36] to be the critical photon flux leading to an excited state population of 1/4. As a sanity check, in the ideal limit where  $\gamma_d, \delta_e \rightarrow 0$  and  $\beta \rightarrow 1$ ,  $n_F = \frac{2\Omega_1^2}{\Gamma^2}$ <sup>29</sup> recovers the definition in Ref. [36]. Using  $\beta \geq 0.865 \pm 0.059$ , we estimate the average number of photons in a single pulse<sup>30</sup>  $\bar{n} = n_F T_p \Gamma \leq 0.089 \pm 0.012 \ll 1$ . This will be helpful in estimating the entanglement infidelity from driving-induced dephasing error (Sec. 4.3.7).

<sup>29</sup>There has been some confusion regarding the unit of  $n_F$ . Here  $n_F$  is a dimensionless quantity that counts the average number of photons in the waveguide *within* one lifetime of the QD, as  $\Omega_1$  and  $\Gamma$  both have the same unit. It is thus misleading to describe it as “mean photon number *per* lifetime”.

<sup>30</sup>The average number of photons in the pulse is given by the average number of photons within one QD lifetime  $n_F$ , multiplied by the total number of lifetimes in the pulse  $T_p \Gamma$ . This formula assumes a square photon pulse (Fig. 3.8a).

### 3.4.5 Photon Visibility

One more essential figure of merit specific to the QD systems is the phonon-induced pure dephasing rate  $\gamma_d$ . In this section, we obtain a reliable estimate of  $\gamma_d$  by measuring the interference visibility between reflected photons in the early and late time-bins. Specifically, by interfering two scattered pulses in a time-bin interferometer with a time delay of  $\tau_{\text{int}} = 11.8$  ns, noise processes which occurred in  $< 11.8$  ns can be probed. Effectively, the interferometer acts as a high-pass frequency filter that removes the effect of slow noise (i.e., spectral diffusion), similar to the Hahn-echo pulse sequence that filters out slow nuclear noise, allowing fast dephasing processes (i.e.,  $\gamma_d$ <sup>31</sup>) to be directly observed.

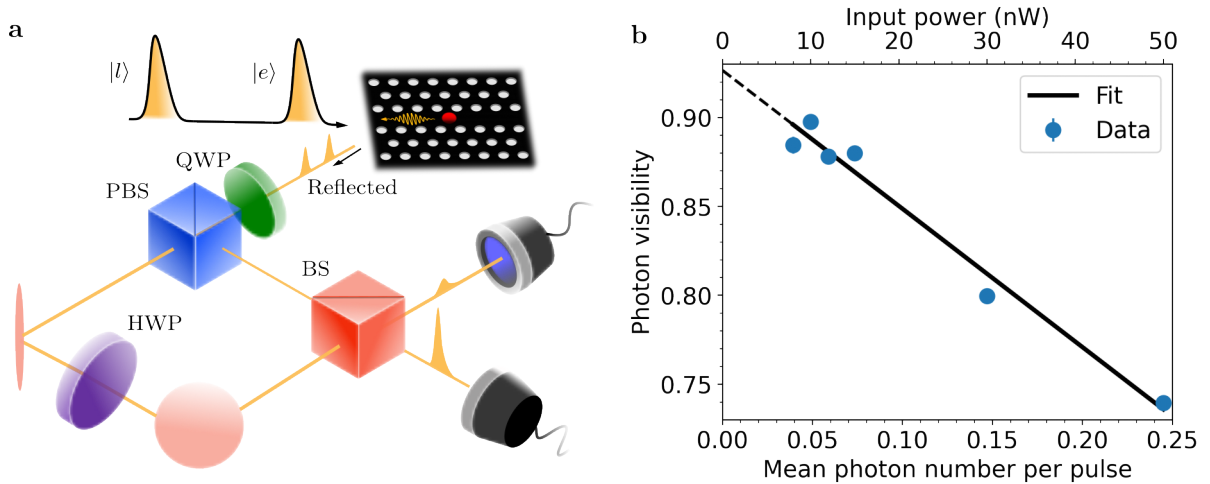


Figure 3.17: **Photon visibility measurement to extract  $\gamma_d$ .** (a) The time-bin encoded qubit is reflected off of the QD initialized in  $|\uparrow\rangle$ . Upon entering the interferometer, the early time-bin is delayed which interferes with the late time-bin, constituting a  $|\pm X\rangle = |e\rangle \pm |l\rangle$  basis measurement. PBS, polarizing beam-splitter; BS, 50:50 beam-splitter; QWP (HWP), quarter (half) wave-plate. (b) Visibility in the photonic  $|\pm X\rangle$  basis as a function of the mean photon number per pulse  $\bar{n}$ .  $\gamma_d$  is extracted from the  $y$ -intercept where  $\bar{n} = 0$ .

#### 3.4.5.1 Measurement Setup

The experiment benefits from having a self-stabilizing time-bin interferometer (Sec. 3.3.2) that prepares and reads out the photonic state, as it offers extra robustness against slow setup instability.

A coherent state generated from a CW laser is first pulsed by an AOM-EOM setup and fed into the excitation path of the interferometer (Sec. 3.3.1), creating a superposition of early and late time-bins separated in  $\tau_{\text{int}} = 11.8$  ns. Similar to the reflectivity measurement (Sec. 3.4.4), the QD spin is initialized in  $|\uparrow\rangle$  and is resonant with the laser. The time-bin qubit is then allowed to interact with the QD spin and resonantly scattered. The reflected signal is then routed to the detection path wherein the early and late time-bin interferes (Fig. 3.17a). The contrast in intensities between the two photodetectors is then recorded as a function of the laser power. This highly resembles a measurement

<sup>31</sup>The timescale for elastic phonon scattering is in the order of 100 ps [75].

of the classical visibility, or normalized first-order correlation function between the early and late time-bins.

### 3.4.5.2 Visibility Model

We now present a simple model to describe the relationship between the measured photon visibility and  $\gamma_d$ , followed by a discussion of the measurement result.

The initial state of the spin-photon system is expressed as  $|\text{in}\rangle = (|e\rangle + |l\rangle)/\sqrt{2} \otimes |\uparrow\rangle$ , where there is an one-photon Fock state in each time-bin. Here we have neglected multi-photon components from the input coherent state, but a complete modelling of the photon visibility, including nonlinear contributions from two-photon scattering [120] is extensively explored in Chapter 5.

Upon interaction with the QD hole spin with a  $\Lambda$ -system (Fig. 3.14), the output state becomes a mixture between the Rayleigh-scattered photons (where the spin is preserved in  $|\uparrow\rangle$ ) and Raman photons (with flipped spin state):

$$|\text{out}\rangle = \frac{1}{\sqrt{2}} \left[ r_1(|e\rangle_r + |l\rangle_r) + t_1(|e\rangle_t + |l\rangle_t) \right] \otimes |\uparrow\rangle + \frac{1}{\sqrt{2}} \left[ r_2(|e'\rangle_r + |l'\rangle_r) + t_2(|e'\rangle_t + |l'\rangle_t) \right] \otimes |\downarrow\rangle, \quad (3.13)$$

where the superscript prime ( $'$ ) represents a scattered photon of frequency  $\omega_2 = \omega_1 + \Delta_h \neq \omega_1$  and the subscript “r” (“t”) indicates a reflected (transmitted) photon. We then seek the photonic density matrix by tracing out the spin degree of freedom, the transmitted photons as well as the wrong frequency state  $\omega_2$ <sup>32</sup>. For ease of computation the scattering coefficients are replaced by  $C_i$  where  $i \in \{e, l\}$  refers to the time-bin, thus

$$|\text{out}\rangle_p \langle \text{out}|_p = \frac{\text{Tr}_{s,t,\omega_2}(|\text{out}\rangle \langle \text{out}|)}{\text{Tr}(|\text{out}\rangle \langle \text{out}|)} = |C_e|^2 |e\rangle_r \langle e|_r + |C_l|^2 |l\rangle_r \langle l|_r + C_e C_l^* |e\rangle_r \langle l|_r + C_l C_e^* |l\rangle_r \langle e|_r. \quad (3.14)$$

Now (3.14) is used to evaluate the intensity recorded in detector D2(D1) in the middle time window where both time-bins interfere:

$$I_{D2/D1} = \int \text{Tr} \left[ \frac{(\hat{a}_e \pm e^{i\theta_p} \hat{a}_l)}{\sqrt{2}} \left( |\text{out}\rangle_p \langle \text{out}|_p \right) \frac{(\hat{a}_e^\dagger \pm e^{-i\theta_p} \hat{a}_l^\dagger)}{\sqrt{2}} \right] dt, \quad (3.15)$$

where the output photon state is projected onto the superposition state  $\hat{a}_e(t) \pm e^{i\theta_p} \hat{a}_l(t)$  which is equivalent to adding a phase shifter on the long path of the excitation interferometer and interfering both bins. Setting  $\theta_p = 0$  implies projecting the output state into the  $p_\pm = |\pm X\rangle_p \langle \pm X|_p$  bases. The projected state is then traced out in both the early and late time-bin bases. The photon visibility is the normalized contrast of the middle-bin intensity when  $\theta_p = 0$ :

$$V_p \equiv \frac{I_{D2} - I_{D1}}{I_{D2} + I_{D1}} = \frac{\int \text{Tr} \left( \hat{a}_e |\text{out}\rangle_p \langle \text{out}|_p \hat{a}_l^\dagger + \hat{a}_l |\text{out}\rangle_p \langle \text{out}|_p \hat{a}_e^\dagger \right) dt}{\int \text{Tr} \left( \hat{a}_e |\text{out}\rangle_p \langle \text{out}|_p \hat{a}_e^\dagger + \hat{a}_l |\text{out}\rangle_p \langle \text{out}|_p \hat{a}_l^\dagger \right) dt}. \quad (3.16)$$

<sup>32</sup>This is traced out due to frequency filtering in the detection.

When the scattering events of the early and late bins are identical, i.e., with the same scattering coefficient  $C_e = C_l = r_1$ , using Eq. (3.14) the photon visibility can be shown to be unity in the single-photon regime.

To account for the effect of phonon-induced pure dephasing, we write the resulting spin-photon density matrix to be the sum of coherent and incoherent parts as described by Eqs. (2.19) and (2.20), where  $\rho_{\gamma_d, j}^{\omega_i}$  is the normalized density matrix of an incoherent photon at frequency  $\omega_i$  in the time-bin  $j$  with probability  $P_{\gamma_d}^{\omega_i}$ . The advantage of the formalism in (2.19) is that its effect can be straightforwardly included in Eq. (3.14). Accordingly, the new photonic density matrix becomes

$$|\text{out}'\rangle_p \langle \text{out}'|_p \approx |\text{out}\rangle_p \langle \text{out}|_p + \frac{1}{2} P_{\gamma_d}^{\omega_1} \rho_{\gamma_d, e}^{\omega_1} |\emptyset\rangle_l \langle \emptyset|_l + \frac{1}{2} P_{\gamma_d}^{\omega_1} \rho_{\gamma_d, l}^{\omega_1} |\emptyset\rangle_e \langle \emptyset|_e. \quad (3.17)$$

The last two terms represent dephasing occurred during the single-photon scattering of either the early or late time-bin. The effect of pure dephasing on the multi-photon component is not considered due to its polynomial dependence on the mean photon number per pulse  $\bar{n}$ , which is negligible as  $\bar{n} \ll 1$ . Note that the incoherent photon does not contribute to the interference since  $\text{Tr}(\hat{a}_e \rho_{\gamma_d, e}^{\omega_1} |\emptyset\rangle_l \langle \emptyset|_l \hat{a}_l^\dagger) = \text{Tr}(\hat{a}_e \rho_{\gamma_d, e}^{\omega_1}) \times \text{Tr}(|\emptyset\rangle_l \langle \emptyset|_l \hat{a}_l^\dagger) = 0$ <sup>33</sup>. This means only the total intensity is affected and Eq. (3.16) can be simplified as

$$V_p = \frac{\int_{-\infty}^{\infty} |\Phi_1(\omega)|^2 |r_1(\omega)|^2 d\omega}{\int_{-\infty}^{\infty} |\Phi_1(\omega)|^2 |r_1(\omega)|^2 d\omega + P_{\gamma_d}^{\omega_1}}, \quad (3.18)$$

where  $r_1(\omega)$  is the reflection coefficient<sup>34</sup> at frequency  $\omega$ , and  $\Phi_1(\omega)$  is the Gaussian pulse spectral profile center at frequency  $\omega_1$  (Eq. (2.6)). The pure dephasing probability<sup>35</sup> is

$$\begin{aligned} P_{\gamma_d}^{\omega_1} &= \frac{\Gamma_1^r}{\Gamma} P_{\gamma_d} = \frac{\Gamma_1^r}{\Gamma} \int_{-\infty}^{\infty} \left| \frac{-2\sqrt{2\gamma_d \Gamma_1^r}}{\Gamma + 2i(\omega - \omega_1)} \right|^2 N(0, \sigma_o) d\omega \\ &= \frac{2\gamma_d}{\Gamma} \int_{-\infty}^{\infty} |\Phi_1(\omega)|^2 |r_1(\omega)|^2 d\omega. \end{aligned} \quad (3.19)$$

Here  $\Gamma_1^r = \Gamma_1/2$  is the decay rate of the dominant optical transition into the reflected mode.

As an additional remark, to include slow resonance drift  $\omega \rightarrow \omega + \delta_e$  due to spectral wandering (Sec. 2.3.1.1), both the probability of reflecting a photon and  $P_{\gamma_d}^{\omega_1}$  need to be averaged over a Gaussian distribution  $N(0, \sigma_e)$ . As anticipated, the photon visibility (to the single-photon level) is resilient against detuning error  $\sigma_o$ <sup>36</sup> and slow noise  $\sigma_e$ <sup>37</sup>. This translates to

$$V_p = \frac{\int_{-\infty}^{\infty} |\Phi_1(\omega)|^2 |r_1(\omega)|^2 d\omega}{\int_{-\infty}^{\infty} |\Phi_1(\omega)|^2 |r_1(\omega)|^2 d\omega + P_{\gamma_d}^{\omega_1}} = \frac{\Gamma}{\Gamma + 2\gamma_d}, \quad (3.20)$$

<sup>33</sup>This is apparent as  $\text{Tr}(|\emptyset\rangle_l \langle \emptyset|_l \hat{a}_l^\dagger) = \sum_{i=e,l} \langle i | (|\emptyset\rangle_l \langle \emptyset|_l \hat{a}_l^\dagger) | i \rangle = 0$ .

<sup>34</sup>The expression for  $r_1$  is given by the integrand of Eq. (3.6).

<sup>35</sup>The rationale and assumptions behind this formula are described in more details in Sec. 2.3.1.3.

<sup>36</sup>This measurement is conditioned on detecting photons which are resonantly reflected.

<sup>37</sup>Essentially this is averaged out as a global phase shift on both the early and late time-bins, as the spectral diffusion noise is sufficiently slow such that it is quasi-static during scattering.

which is interestingly identical to the photon indistinguishability formula derived in Ref. [75]. In the limit  $\bar{n} \approx 0$  where only single photons interact with the QD, the  $y$ -intercept of the photon visibility curve in Fig. 3.17b is therefore given by Eq. (3.20). This provides a direct approach to measure photon indistinguishability<sup>38</sup> and allows one to extract  $\gamma_d$  given  $\Gamma$ . A linear fit followed by extrapolation of the data gives a  $y$ -intercept of  $V_p = 0.926 \pm 0.003$ , corrected for unequal intensities between early and late bins<sup>39</sup>. Substituting this into Eq. (3.20) implies  $\gamma_d \approx (0.099 \pm 0.004) \text{ ns}^{-1}$ . The corrected photon visibility  $V_p$  is intuitively understood as the mean wavepacket overlap between single photons.

---

<sup>38</sup>It turns out that  $V_p$  and the Hong-Ou-Mandel visibility  $V_{\text{HOM}}$  are intimately related, see Chapter 5.

<sup>39</sup>This is quantified by the ratio in intensities between early-short and late-long time windows averaged over two detectors, which is around 3%. The asymmetry is due to extra optical loss in the long path.

## 3.5 Hole Spin Control

The final ingredient to implement the entangling gate is high-fidelity and coherent state control of the hole spin. Naturally this refers to demonstrating Rabi flops of an effective two-level system (TLS) formed by the hole spin ground states, when driven by an oscillating field. For the current work, this oscillatory field is provided by a bi-chromatic laser as a result of linear modulation from a microwave field (Sec. 3.3.1). In this section, we first describe the working principle behind such optical spin control, followed by experimental verification of Rabi flopping between the hole ground states. The ability to coherently control the hole spin state then allows us to implement the previously discussed built-in Hahn-echo sequence in the gate protocol (Sec. 3.2.2) and measure the Hahn-echo visibility  $V_{SE}$ . By construction,  $V_{SE}$  provides an upper bound to spin-photon entanglement fidelity measured in the X-basis, thus serving as a fast pre-calibration of the QD spin device, as we shall explain later.

### 3.5.1 Principle of Optical Spin Control

Figure 3.18b depicts the level scheme of a hole spin under an external in-plane magnetic field, under the driving of a bi-chromatic laser. As described in Sec. 3.3.1, to optically drive the spin transitions, we employ a monochromatic laser (green) at a frequency  $\omega_o = \omega_1 - \Delta_r$ , detuned from the main transition  $|\uparrow\rangle \leftrightarrow |\uparrow\downarrow\rangle$ . This laser is microwave-modulated resulting in two sidebands at  $\omega_o \pm \Delta_h/2$ , where the higher-frequency (lower-frequency) band drives the  $|\downarrow\rangle$  ( $|\uparrow\rangle$ ) state. The combination of both colors drives both  $\Lambda$ -systems (labelled as “1” and “2”) via two-photon Raman transitions without populating the trions, thus creating an effective coupling between only the hole ground-state manifold.

For this two-photon Raman scheme [52, 125] to work, each frequency band must be circularly-polarized, such that firstly, it drives both vertical Y-polarized and diagonal X-polarized transitions with equal optical Rabi frequencies<sup>40</sup> ( $\Omega_y = \Omega_x$ ), and secondly,  $\Omega_x$  is  $\pi/2$  out of phase with  $\Omega_y$ , thus the optical fields constructively drive both  $\Lambda$ -systems. Intuitively, this could be visualized as reversing the direction of the arrows for diagonal transitions in Fig. 3.18b, where the  $\Lambda$ -system “1” (“2”) now transfers population from  $|\downarrow\rangle$  to  $|\uparrow\rangle$  ( $|\uparrow\rangle$  to  $|\downarrow\rangle$ ), forming a cycling drive via a virtual state.

Mathematically, the spin dynamics under the optical drive is governed by the effective spin TLS Hamiltonian [52] in the rotating frame of the drive:

$$\hat{H}_s = \frac{\Omega_r}{2}(\hat{\sigma}_x \cos \phi_s + \hat{\sigma}_y \sin \phi_s) - \frac{\Delta_{MW}}{2}\hat{\sigma}_z, \quad (3.21)$$

where  $\Omega_r$  is the effective spin Rabi frequency of the TLS.  $\phi_s$  is the azimuthal angle on the Bloch sphere with hole spin states as the poles.  $\phi_s = 0$  ( $\phi_s = \pi/2$ ) sets the axis of rotation along  $+x$  ( $+y$ )<sup>41</sup>.  $\hat{\sigma}_i$  are Pauli matrices.  $\Delta_{MW}$  is the detuning of the bi-chromatic laser with the virtual state.

<sup>40</sup>For optical spin control in a photonic-crystal waveguide, the Raman-modulated laser might not be used to excite through the waveguide, as the spatial position of the QD affects the coupling of its optical dipoles to the waveguide modes. For a QD with high cyclicity, the laser needs to be elliptically-polarized to fulfill  $\Omega_y = \Omega_x$ . Exciting on top circumvents this issue. However, the optical power required is higher due to low-coupling  $1 - \beta$  to non-guided modes.

<sup>41</sup>Not to be confused with the external magnetic field  $\mathbf{B}$  direction and the waveguide axis. Here the rotation axis is defined only by the Bloch sphere, so in this picture  $\mathbf{B}$  is oriented along  $z$ .

Now, to study the time evolution of the hole spin state under Eq. (3.21), we proceed to solve the Lindblad master equation ( $\hbar = 1$ ):

$$\dot{\rho}_s = -i[\hat{H}_s, \rho_s] + \sum_{i=1}^n D[\hat{C}_i]\rho_s, \quad (3.22)$$

for  $\rho_s$  is the spin density matrix spanning the hole spin ground states. The latter term in Eq. (3.22) represents the static Lindblad dissipator  $D[\hat{C}_i]\rho \equiv \hat{C}_i\rho\hat{C}_i^\dagger - \frac{1}{2}\{\hat{C}_i^\dagger\hat{C}_i, \rho\}$  for a list of  $n$  collapse operators  $\hat{C}_i$ . To model realistic noises in the experiment, we first consider a Markovian noise that destroys spin coherence by flipping the spin state with a rate  $\kappa$ . Specifically, we take  $\hat{C}_1 = \sqrt{\kappa}\hat{\sigma}_+$  and  $\hat{C}_2 = \sqrt{\kappa}\hat{\sigma}_-$  where  $\hat{\sigma}_+ \equiv |\downarrow\rangle\langle\uparrow| = \hat{\sigma}_-^\dagger$  is the atomic raising operator<sup>42</sup>. Eq. (3.22) can be solved analytically when there is no laser detuning  $\Delta_{\text{MW}} = 0$ . Taking  $\phi_s = 0$ , the population in  $|\uparrow\rangle$  as a function of the driving time  $T_r$  is found to be [52, 125]

$$\rho_{|\uparrow\rangle\langle\uparrow|}(T_r) = \frac{1}{2} \left[ 1 - e^{-\frac{3\kappa T_r}{2}} \cos\left(\frac{\tilde{\Omega}_r T_r}{2}\right) + \frac{\kappa}{\tilde{\Omega}_r} e^{-\frac{3\kappa T_r}{2}} \sin\left(\frac{\tilde{\Omega}_r T_r}{2}\right) \right], \quad (3.23)$$

where  $\tilde{\Omega}_r \equiv \sqrt{4\Omega_r^2 - \kappa^2}$ . Eq. (3.23) describes damped Rabi oscillations of the  $|\downarrow\rangle$  state with frequency  $\tilde{\Omega}_r$  bounded by the decay envelopes  $\frac{1}{2}(1 \pm e^{-3\kappa T_r/2})$ . As a sanity check, it is easy to show that in the limit of  $\tilde{\Omega}_r, \Delta_{\text{MW}} = 0$ , the hole spin decoheres<sup>43</sup> and becomes a completely mixed state at large  $T_r$ .

Generally, for a finite detuning  $\Delta_{\text{MW}} \neq 0$ , Eq. (3.22) can only be numerically evaluated. To elaborate further, we now include the Overhauser field noise. For a frozen nuclear bath [86] with a dominant noise from Overhauser field components parallel to the external magnetic field  $\Delta_{\text{OH}}^\parallel$ , this corresponds to introducing a fluctuating noise  $\Delta_{\text{MW}} = \Delta_{\text{OH}}^\parallel$  along  $z$ -axis of the spin Bloch sphere. This picture is consistent with the treatment in Sec. 2.3.3.1 where a non-zero  $\Delta_{\text{OH}}^\parallel$  leads to precession of the spin qubit on the equator of Bloch sphere. The  $|\downarrow\rangle$  population under the Overhauser noise is then found by averaging  $\rho_{|\uparrow\rangle\langle\uparrow|}(T_r, \Delta_{\text{OH}}^\parallel)$  with a Gaussian spin dephasing profile  $N(\Delta_{\text{OH}}^\parallel, \sigma_{\text{OH}})$ :

$$\bar{\rho}_{|\uparrow\rangle\langle\uparrow|}(T_r) = \int_{-\infty}^{\infty} d\Delta_{\text{OH}}^\parallel \rho_{|\uparrow\rangle\langle\uparrow|}(T_r, \Delta_{\text{OH}}^\parallel) N(\Delta_{\text{OH}}^\parallel, \sigma_{\text{OH}}). \quad (3.24)$$

### 3.5.2 Measured Rabi flops

Figure 3.18 shows measured and fitted Rabi oscillations between the hole spin ground states at different optical powers. To avoid populating the trion states, we set the carrier frequency  $\omega_o$  of the Raman laser to be  $\Delta_r = 2\pi \times 350$  GHz detuned from the main transition. The experiment begins by photocreating a hole spin with a 830 nm pulsed laser then optically pumping the hole spin into  $|\downarrow\rangle$ , followed by a pulse driven by the Raman laser with a varying duration  $T_r$ . The state evolution of the hole spin under the effect of Raman pulse is then probed by detecting fluorescence from  $|\uparrow\rangle$  with a readout pulse. Note that a buffer pulse from the Raman laser is added at the end of the sequence, such that the sequence duty cycle and the average optical power of the laser are kept constant when sweeping  $T_r$ .

<sup>42</sup>Here  $\kappa$  is taken to be the average spin-flip rate between two collapse operators. Setting different values of  $\kappa$  does not impact the fit results.

<sup>43</sup>Off-diagonal elements of  $\rho_s$  vanish.

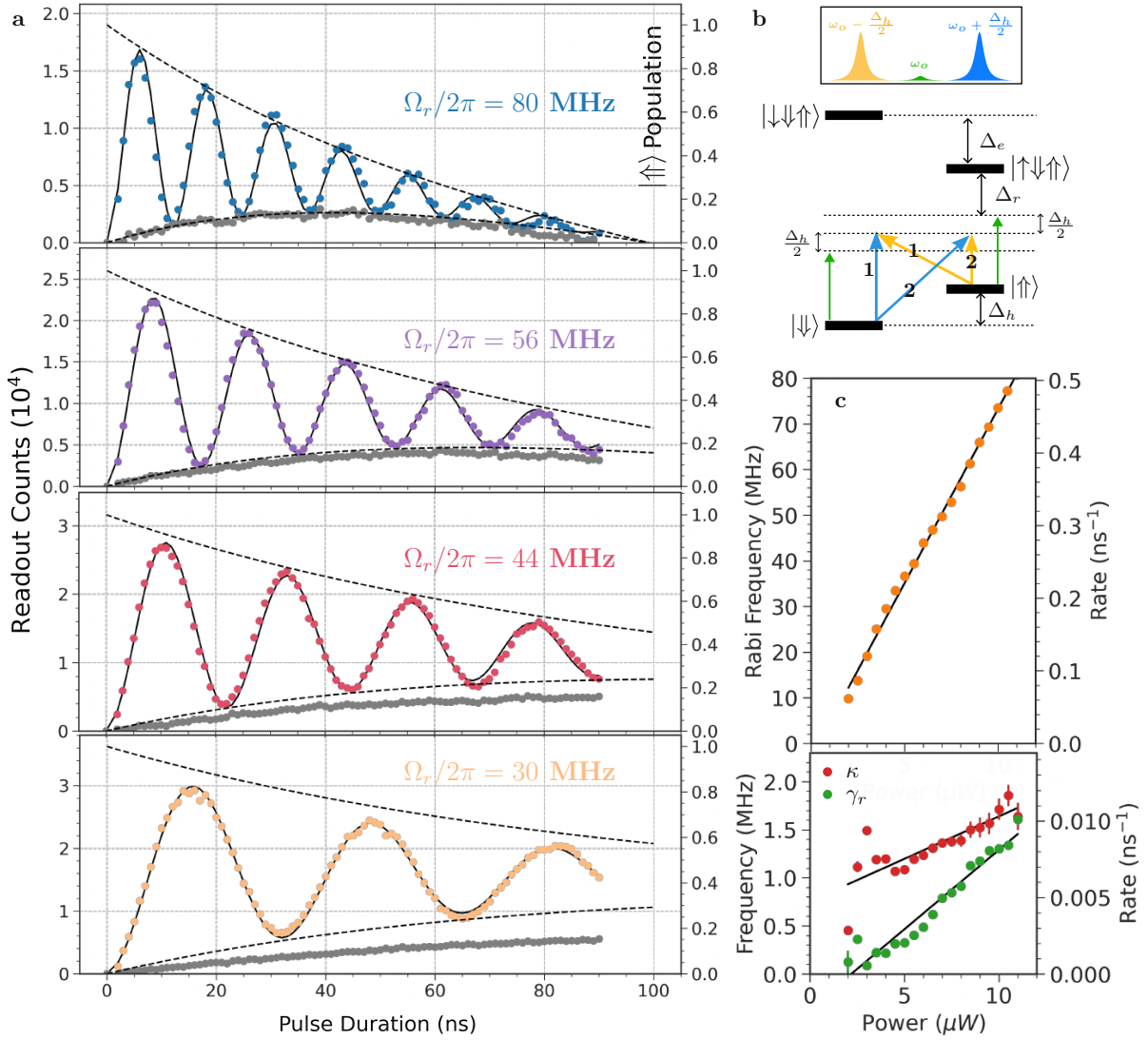


Figure 3.18: **Rabi oscillations between the hole spin states.** (a) Measured (dotted) and fitted (black lines) Rabi curves at different Raman laser powers. Dashed curves correspond to the  $\kappa$ -induced decay envelopes  $\frac{1}{2}\eta_r(1 \pm e^{-3\kappa T_r/2})$ . Grey curves are measured when the sidebands are off-resonant by  $\Delta_{\text{MW}} = 2\pi \times 245$  MHz. (b) Schematics of optical spin control using a bi-chromatic laser, generated by splitting the Raman laser carrier frequency  $\omega_o$  into two sidebands  $\omega_o \pm \Delta_h/2$ . Here  $\Delta_{\text{MW}} = 0$  is taken for resonant drive. (c) Power-dependence of the spin Rabi frequency, incoherent spin-flip rate  $\kappa$  and  $\gamma_r$ .

The fluorescence signal from the first 50 ns of the readout pulse can be fitted by the formula [52]:

$$I(T_r) = I_0 \times \eta_r \times \bar{\rho}_{|\uparrow\rangle\langle\uparrow|}(T_r), \quad (3.25)$$

where  $\eta_r \approx (1 - \gamma_r T_r)$  is an empirical model describing the reduced readout efficiency with a power-dependent rate  $\gamma_r$  [52]. Before fitting the data, the photon counts at  $T_r = 0$  ns are first subtracted to remove background fluorescence from the readout pulse. Each dataset is numerically fitted with Eq. (3.25) using  $\kappa$ ,  $\gamma_r$ ,  $I_0$  and  $\Omega_r$  as free parameters, and with the standard deviation in Overhauser field fluctuations  $\sigma_{\text{OH}}$  fixed. The fitted peak intensity  $I_0$  can then be extracted to normalize the dataset. For the fit, we take  $\sigma_{\text{OH}} = \sqrt{2}/T_2^* \approx 2\pi \times 9.7$  MHz for a measured spin dephasing time of  $T_2^* \approx 23.2$  ns [52].

Starting from  $\Omega_r \approx 5 \sigma_{\text{OH}}$ , the spin noise dynamics is dominated by  $\kappa$  as the curves in Figure 3.18a become tightly bounded by the decay envelopes  $\frac{1}{2}\eta_r(1 \pm e^{-3\kappa T_r/2})$ .

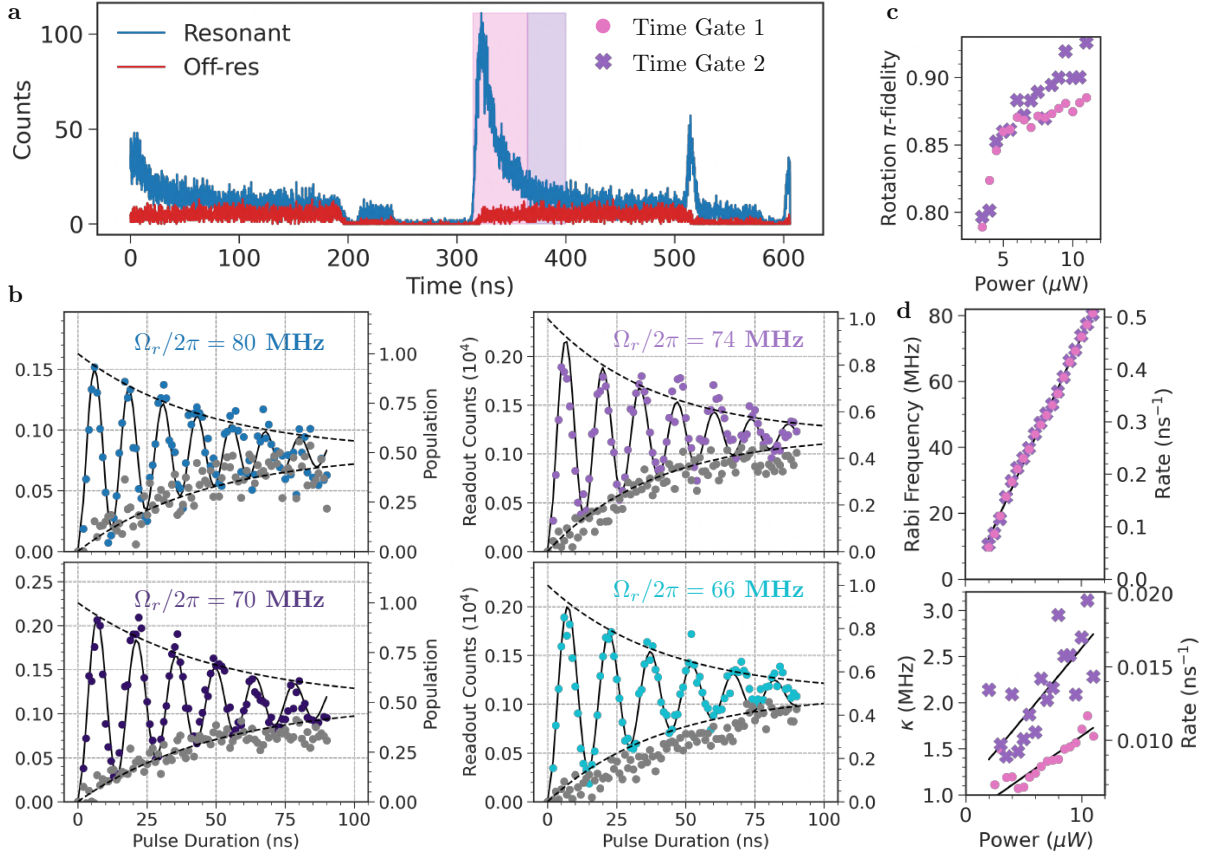


Figure 3.19: **Rabi oscillations when photon counts are gated at a later time.** (a) Pulse sequence of the Rabi flop measurement. The sequence consists of a Raman pulse of duration  $T_r$  sandwiched between two readout pulses. The first readout pulse prepares  $|\downarrow\rangle$  while the second probes the population in  $|\uparrow\rangle$ . A buffer pulse is added at 510 ns to maintain total pulse duration of 100 ns. (b) Fitted Rabi curves with data extracted within Time Gate 2. The gradual drop in fluorescence due to finite  $\gamma_r$  vanishes. (c)-(d) Power-dependence of the  $\pi$ -pulse fidelity,  $\Omega_r$  and  $\kappa$  with different time-gates. Pink dots are fit results from the same data shown in Fig. 3.18.

Figure 3.18c shows the fitted spin Rabi frequency  $\Omega_r$ <sup>44</sup>, the power-dependent spin-flip rate  $\kappa$  and  $\gamma_r$ , which all increase linearly with Raman laser power, as observed in Refs. [52, 125]. For modelling the photon-scattering gate infidelity due to imperfect spin rotations, we need to quantify the fidelity of the spin  $\pi$ -rotation  $F_\pi$ . For each normalized Rabi curve in Fig. 3.18a,  $F_\pi$  is estimated from its first peak at which the  $|\uparrow\rangle$  population is maximized.

For the gate experiment, a  $T_r = 7$  ns  $\pi$ -pulse (corresponding to  $\Omega_r \approx 71$  MHz) is used,  $F_\pi = (88.1 \pm 3.8)\%$ <sup>45</sup> with  $\kappa = (0.0098 \pm 0.0007)$  ns<sup>-1</sup> and  $\gamma_r = (0.0081 \pm 0.0002)$  ns<sup>-1</sup>. Error bounds are obtained from the fit. The estimated rotation fidelity is consistent with the one extracted previously on the same QD ( $F_\pi = (88.5 \pm 0.3)\%$ ) [52].

<sup>44</sup>As opposed to the optical Rabi frequency which scales with  $\sqrt{P}$ , here it is linearly proportional to the Raman laser power since this is a two-photon process.

<sup>45</sup>In Sec. 4.3.5 we compare this measured fidelity with an analytical expression of the  $\pi$ -fidelity derived for a given  $\kappa$  and  $\gamma_r$ .

Intriguingly, the apparent drop in fluorescence at large  $T_r$  due to high Raman laser power disappears when the photon counts are gated at a later time. Figure 3.19a displays the time-resolved histogram of the pulse sequence with different time-gating schemes. The data in Fig. 3.18 is gated on the first 50 ns of the readout pulse (as indicated in pink), whereas a different set of Rabi oscillations is obtained by gating in the next 35 ns (in purple).

As observed in Fig. 3.19b, the reduced fluorescence at large  $T_r$  is not visible, the data is thus fitted with Eq. (3.25) taking  $\eta_r = 1$ . This could indicate the presence of a fast ( $< 50$  ns) power-dependent process which uncouples the hole spin from the QD with a rate  $\gamma_r$ <sup>46</sup>. Time-gating photon counts at a subsequent time effectively acts as a temporal filter that post-selects events in which the hole spin is recovered, i.e., by re-tunneling under the constant  $X^+$  bias voltage. A two-color time-resolved  $X^0$  resonance fluorescence [126] or pulsed bias voltage measurements [127] could be useful in probing the time dynamics of  $\gamma_r$  and tunneling processes of the hole spin when subject to the Raman laser.

### 3.5.3 Hahn-echo Visibility

Analogous to the photon visibility measurement in Sec. 3.4.5 which probes the coherence of the photonic qubit, in this section we examine the coherence of the hole spin qubit by measuring the Hahn-echo visibility.

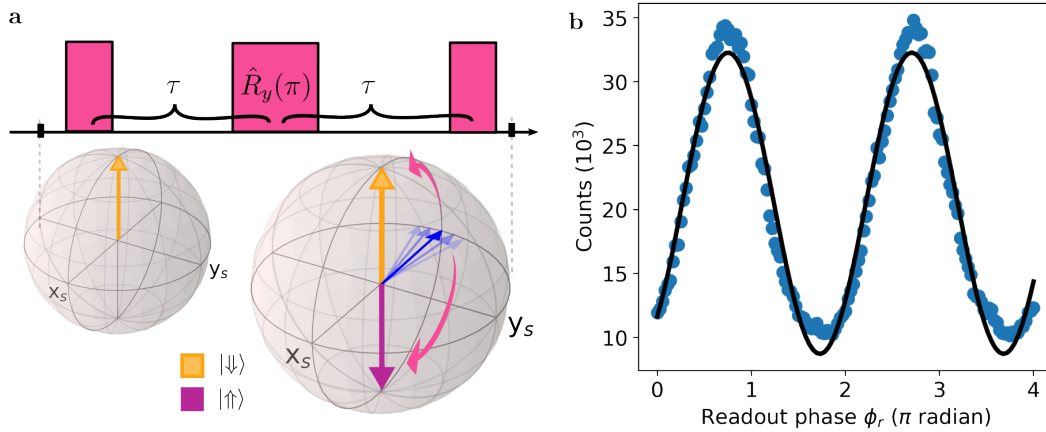


Figure 3.20: **Hahn-echo visibility measurement.** (a) Hahn-echo sequence used to probe spin coherence. The  $\pi$ -pulse is equally distant from the two  $\pi/2$  pulses by  $\tau = \tau_{\text{echo}}/2$  to eliminate inhomogeneous spin dephasing. The phase of the last  $\pi/2$  pulse  $\phi_r$  maps the equatorial state  $|\uparrow\rangle + e^{i\phi_r}|\downarrow\rangle$  to the optically bright state  $|\uparrow\rangle$  ( $\phi_r = \pi$ ) or dark state  $|\downarrow\rangle$  ( $\phi_r = 0$ ). (b) Contrast between the spin  $|\downarrow\rangle$  and  $|\uparrow\rangle$  populations as a function of  $\phi_r$ , measured at  $\tau = 13$  ns.

Specifically, we perform a spin-echo sequence [87] consisting of two  $\hat{R}_y(\pi/2)$  pulses separated by a  $\hat{R}_y(\pi)$  pulse (Fig. 3.20a), which are implemented via the two-photon Raman scheme discussed in the previous section. After the first  $\hat{R}_y(\pi/2)$  pulse, due to fluctuating Overhauser nuclear fields [128] the spin state begins to fan out over the Bloch sphere equator (denoted by blue arrows) decaying with a spin dephasing time  $T_2^* = 23.2$  ns [18]. Applying a  $\hat{R}_y(\pi)$  pulse after time  $\tau$  inverts the direction of spin

<sup>46</sup>This could be related to the photo-ionization rate of the hole spin due to intra-band excitation with a red-detuned laser, see Ref. [126] and Appendix C.

precession, thus refocusing the spin state at  $t = 2\tau$ . The spin coherence is then probed by applying a second  $\hat{R}_y(\pi/2)$  pulse, and scanning its phase  $\phi_r$ <sup>47</sup> followed by spin readout, which projects the resulting spin state onto either the optically bright or dark state. The resulting interferometric fringe is depicted in Fig. 3.20b with an extracted visibility of  $V_s = (57.5 \pm 0.4)\%$  at  $\tau = 13$  ns, which is primarily limited by photo-induced incoherent spin processes [18].  $V_s$  indicates how well the spin coherence is preserved, and benchmarks the quality of spin-photon correlations on the equatorial basis. It is crucial to note that the delay between  $\pi$  and  $\pi/2$  pulses  $\tau$  is particularly chosen at 13 ns where the Hahn-echo visibility is maximized due to echo revival<sup>48</sup> [129].

As an additional comment, despite using the same QD at the same delay  $\tau$  as in Ref. [18]<sup>49</sup>, the Hahn-echo visibility  $V_s$  measured in this work is 12% higher. This is accomplished by removing the above-bandgap<sup>50</sup> (ABB) laser that was originally used in Ref. [18] to photo-create the hole spin (Sec. 1.2.2), followed by fine optical alignment on the readout laser paths. We suspect that the strong above-bandgap laser introduces an effective spin-flip rate to the hole spin by reinitializing it during each experimental repetition, thus neutralizing the effect from polarizing nuclear spins<sup>51</sup>. In simple words, the ABB laser effectively flushes out the nuclear spin states and lowers the echo rephasing amplitude.

---

<sup>47</sup> $\phi_r$  is defined as the phase of the last  $\hat{R}_y(\pi/2)$  pulse *relative to* the previous two pulses.

<sup>48</sup>This is explained in more details in Sec. 6.4.3.

<sup>49</sup>For reference, please refer to Fig. 6.11 of Ref. [52] for echo visibility measurements on the same QD.

<sup>50</sup>This is a fiber-pigtailed diode laser fixed at 830 nm.

<sup>51</sup>This is like a weak nuclear spin narrowing effect thanks to the readout and rotational pulses.

## 3.6 Parameter Summary

Before discussing the entanglement experiment, it is helpful to first summarize all relevant parameters that characterize the current QD-waveguide device in a table:

Parameter	Value
QD qubit	Hole spin $X^+$
Emission wavelength	945 nm
External magnetic field $\mathbf{B}_x$	2 T
Total decay rate of the QD $\Gamma$	$(2.48 \pm 0.02) \text{ ns}^{-1}$ [18]
Ground-state Zeeman splitting $\Delta_h$	$2\pi \times 7.3 \text{ GHz}$ [18]
Optical cyclicity $C = \gamma_Y/\gamma_X$	$14.7 \pm 0.2$ [20]
Waveguide-coupling efficiency $\beta$	$(0.865 \pm 0.059)$ (Sec. 3.4.2)
Standard deviation in spectral diffusion fluctuation $\sigma_e$	$2\pi \times (332 \pm 15) \text{ MHz}$ (Sec. 3.4.2)
Standard deviation in pulse spectral width $\sigma_o$	$0.589 \text{ ns}^{-1}$ (Sec. 3.3.2)
Pure dephasing rate $\gamma_d$	$(0.099 \pm 0.004) \text{ ns}^{-1}$ (Sec. 3.4.5)
Spin-echo visibility $V_s$	$(57.5 \pm 0.4)\%$ (Sec. 3.5.3)
Spin $\pi$ -rotation fidelity $F_\pi$	$(88.1 \pm 3.8)\%$ (Sec. 3.5)
Spin dephasing time $T_2^*$	$(23.2 \pm 1.4) \text{ ns}$ [18]
Spin coherence time $T_2^{\text{echo}}$	$(448 \pm 37) \text{ ns}$ [52]

Table 3.3: Key properties characterizing the QD hole spin and the waveguide device.

The estimated values for these quantities will be repeatedly used throughout Chapters 4 and 5.

### 3.7 Entanglement Measurement

After characterizing the optical properties and coherences of both qubits, we are in a position to demonstrate the entangling gate. The hole spin is first loaded in the QD by a 50 ns buffer pulse from the Raman laser, which is also a part of the spin rotation sequence to maintain constant optical power (Sec. 3.5.2). The above-bandgap laser is removed to reach a higher spin-echo visibility (Sec. 3.5.3). The spin is then prepared in a superposition state  $|+X\rangle_s = (|\uparrow\rangle + |\downarrow\rangle)/\sqrt{2}$  by applying a 3.5 ns  $\hat{R}_y(\pi/2)$  pulse (Fig. 3.21a).

The time-bin qubit is attenuated to  $\bar{n} \approx 0.09$  before interacting with the QD (Sec. 3.4.4). Thanks to the high cyclicity  $C = 14.7$  (Sec. 3.4.3) of the optical transition  $|\uparrow\rangle \leftrightarrow |\uparrow\downarrow\rangle$ , the QD behaves as a dichroic mirror which reflects only the resonant component of the qubit during each scattering event (Sec. 1.5). The reflected signal is collected and measured by the interferometer. Heralding on the reflected photonic component carves out the output state [Eq. (3.7)] resulting in the spin-photon Bell state  $|\phi^-\rangle_r$ .

To determine the fidelity of the entangled state, we perform correlation measurements between the photonic modes and spin states. This involves projecting the entangled state on the  $\hat{\sigma}_i^{(p)} \otimes \hat{\sigma}_i^{(s)}$  bases, where  $i \in \{x, y, z\}$  denotes the Pauli operator, and the superscripts s (p) represent the spin and photonic qubits.

As shown in Fig. 3.21a, the detection of an early (late) photon traversing through the short (long) path of the interferometer constitutes the  $\hat{\sigma}_z^{(p)}$ -basis measurement (green). The spin readout in the  $\hat{\sigma}_z^{(s)}$ -basis is performed by applying another rotation pulse  $\hat{R}_i = \hat{R}_y(0)$  ( $\hat{R}_y(\pi)$ ) followed by optical driving of the main transition. Similarly, projection on the  $\hat{\sigma}_x^{(p)} \otimes \hat{\sigma}_x^{(s)}$  ( $\hat{\sigma}_y^{(p)} \otimes \hat{\sigma}_y^{(s)}$ ) bases is performed by detecting photons in the middle time window (blue) at  $\theta_p \approx 2\pi \equiv \theta_0$  ( $\theta_p = \theta_0 + \pi/2$ ) where the early and late time-bins between the short and long paths [18] interfere, followed by  $\hat{R}_i = \hat{R}_y(\pm\pi/2)$  ( $\hat{R}_x(\pm\pi/2)$ ) before the spin readout.

For each experimental setting<sup>52</sup>, we condition on the detection of a reflected photon and the spin readout. Concerning the thermal drift on the optical alignment in Sec. 3.3.3, we run the experiment when the SNR of the scattered signal goes above 100. The measurement time for each setting is 100 s. The entanglement fidelity is measured using [18]

$$\mathcal{F}_{\text{Bell}} = \frac{\langle \hat{\mathcal{P}}_z \rangle}{2} + \frac{\langle \hat{\mathcal{M}}_y \rangle - \langle \hat{\mathcal{M}}_x \rangle}{4}, \quad (3.26)$$

where  $\langle \hat{\mathcal{M}}_i \rangle = \langle \hat{\sigma}_i^{(p)} \otimes \hat{\sigma}_i^{(s)} \rangle$  is the normalized contrast, and  $\langle \hat{\mathcal{P}}_z \rangle \equiv (1 + \langle \hat{\mathcal{M}}_z \rangle)/2$ . For measuring  $\langle \hat{\mathcal{M}}_{x/y} \rangle$ ,  $\hat{R}_i = \hat{R}_{y/x}(\pi/2)$  is required for spin projection onto the equatorial state. Since the protocol now resembles a spin-echo sequence, the central  $\hat{R}_y(\pi)$  pulse has an added benefit of spin-refocusing, whereas for Z-basis projections, spin echo is not necessary as  $\langle \hat{\mathcal{P}}_z \rangle$  is impervious to spin dephasing. As such,  $|\langle \hat{\mathcal{M}}_{x/y} \rangle|$  is dictated by the spin-echo visibility  $V_s$ , while  $\langle \hat{\mathcal{P}}_z \rangle$  largely reflects fidelity of the  $\hat{R}_y(\pi)$  pulse  $F_\pi$ .

<sup>52</sup>To fully characterize the entanglement fidelity, the generated state needs to be projected in three measurement bases. Since we can only read out  $|\uparrow\rangle$ , in total there are 6 experimental settings [52].

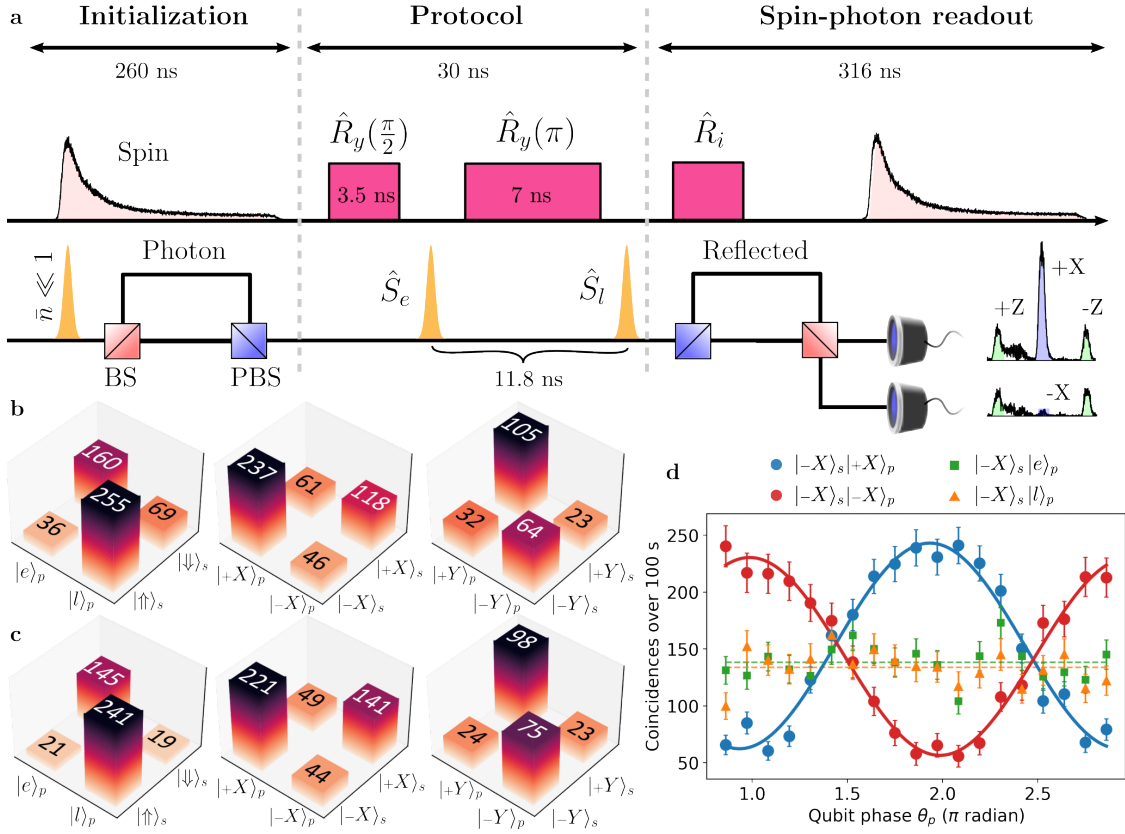


Figure 3.21: **Generation and verification of Bell states.** (a) Experimental sequence consisting of the preparation of spin and photonic qubits, the gate protocol and the readout. The spin state is initialized and read out by optically driving the  $|\uparrow\rangle \leftrightarrow |\downarrow\rangle$  transition (pale red), and  $\hat{R}_i$  controls the spin projection basis. The photonic qubit is prepared and measured by the same interferometer in either the Z-basis (green) or equatorial basis (blue) time window. (b) Raw two-photon coincidences measured during the photonic (p) readout window and spin (s) projections. (c) Measured two-photon coincidences after correcting for laser background from rotation pulses (Sec. 3.7.0.1). (d) Visibility fringes of background-corrected two-photon coincidences as a function of the qubit phase  $\theta_p$  when the spin state is projected on  $|-X\rangle_s = (|\uparrow\rangle - |\downarrow\rangle)/\sqrt{2}$ . Circles (squares/triangles) correspond to projection on the photonic X-basis ( $\pm$ Z-basis). Solid curves are fits using  $V_s \cos(\theta_p + \theta_{\text{offset}})$ , and dashed lines are horizontal line fits.

Figures 3.21b-d show the raw (background corrected) coincidence counts in various readout bases. We record

$$\begin{cases} \langle \hat{\mathcal{P}}_z \rangle = (90.7 \pm 2.2)\%; \\ \langle \hat{\mathcal{M}}_x \rangle = (-58.8 \pm 4.5)\%; \\ \langle \hat{\mathcal{M}}_y \rangle = (57.3 \pm 6.6)\%, \end{cases} \quad (3.27)$$

where residual background counts from laser rotation pulses were subtracted (Sec. 3.7.0.1). The recorded values of  $|\langle \hat{\mathcal{M}}_{x/y} \rangle|$  and  $\langle \hat{\mathcal{P}}_z \rangle$  are consistent with measured  $V_s$  and  $F_\pi$ , respectively (Sec. 3.6). Using Eq. (3.26), we obtain a corrected Bell-state fidelity of  $\mathcal{F}_{\text{Bell}} = (74.3 \pm 2.3)\%$  (raw fidelity of  $(66 \pm 2)\%$ ), which far exceeds the classical limit of 50%, clearly demonstrating the presence of entanglement in the generated quantum state. To understand various imperfections that reduce fidelity of the Bell state, in Chapter 4 we conducted a thorough theoretical analysis of each experimentally known error, and compared the predicted theoretical fidelity with the measured value.

### 3.7.0.1 Background Subtraction

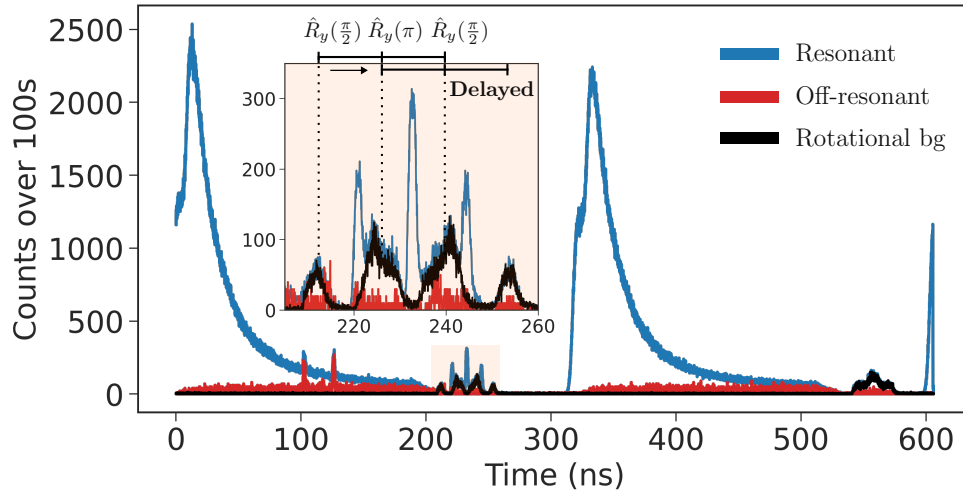


Figure 3.22: **Entanglement pulse sequence overlaid with rotational background fluorescence.** Fluorescence from the 350 GHz off-detuned rotational pulses near 200 ns can be seen in the time-resolved histogram recorded by the detectors. The inset shows a magnified view of the gate sequence, where the background fluorescence from the rotational laser partially overlaps in time with the photon detection.

Background photons in this work include leakage from the photonic qubit and readout lasers, detector dark counts, accidental coincidence counts, and fluorescence from the rotational laser. Prior to running the experiment, both optical paths for the photonic qubit and spin readout are optimized such that the signal-to-noise ratio is  $> 100$ . The photon detection uses superconducting nanowire single-photon detectors (SNSPDs) with a dark count rate of 10 Hz. False coincidence counts account for  $< 3\%$  of all detected coincidences. A majority of the background subtraction is done by removing the fluorescence during the rotational pulses which overlaps in time with the photon detection window, see inset of Fig. 3.22. The fluorescence may be due to photo-ionization by the red-detuned Raman laser [126] followed by subsequent reinjection of a hole, which leads to photon emission through the unfiltered cycling transition. This hypothesis could be supported by the fact that a 40 ns buffer pulse at 540 ns is used partly to inject a hole in the current device, and the spin Rabi oscillations with delayed time-gating discussed in Sec. 3.5.2. The fluorescence from these pulses thus enters the detection path of the TBI and half of which is then delayed in time, partially overlapping with the time-bin detection windows.

### 3.8 Gate Performance Metrics

In this section we investigate the metrics that characterize the performance of an entangling gate. A functional quantum gate should operate at high speed, with a high gate fidelity, be tolerant to noise, and have a low insertion loss. We estimate these metrics for our system to compare with the state-of-the-art scattering gates implemented on other platforms in Table 3.4.

System	Fidelity		$T_{\text{gate}}$	$\eta_{\text{gate}}$	$\mathcal{R}^*$	Ref.
	Raw	Corrected				
SiV-PCC	0.7	0.89-0.94	30 $\mu\text{s}$	0.493	11.9 Hz	[130, 64]
QD-PCW	0.66	0.74	0.29 $\mu\text{s}$	0.179	4.75 Hz	Present work
Rb-cavity	0.86 <sup>†</sup>	-	146 $\mu\text{s}$	0.39	34.5 Hz	[131]

Table 3.4: Comparison of various gate performance metrics.  $T_{\text{gate}}$ : Gate duration.  $\eta_{\text{gate}}$ : Gate efficiency.  $\mathcal{R}$ : Entanglement rate. PCC: Photonic crystal cavity. PCW: Photonic crystal waveguide. \*See Table. 3.6 for estimation details. <sup>†</sup>Not specified if raw or corrected.

From Table 3.4, several conclusions can be drawn. First, the raw (corrected) entanglement fidelity 66% (74%) in QD-PCW is comparable to those achieved in SiV-PCC [132]. It is noted that the 89% fidelity reported in Ref. [130] should be regarded as an inferred maximum fidelity after correcting for imperfect single-shot readout. In contrast our reported 74% fidelity only corrects for subtraction of background fluorescence due to time delay of rotational pulses in the long path of the interferometer (Sec. 3.7.0.1), which can be readily mitigated using shorter pulses and better pulse shaping, or longer interferometric delays.

Second, the gate duration of the QD-PCW is two-orders of magnitude shorter than that of SiV-PCC. This is primarily due to the long duration (30  $\mu\text{s}$ ) required to distinguish between the two SiV spin states during single-shot readout [64]. Similarly the gate duration is even longer in Rb-cavity system. Table 3.5 shows a breakdown of the gate duration, which is defined as the total duration of several pulses required to run the entangling gate sequence. This includes the spin initialization pulse, two optical pulses with a delay that made up the photonic qubit, and the spin rotation  $\pi/2$ - and  $\pi$ -pulses. For both systems, the emitter's lifetime is short compared to the duration of each photonic pulse, and therefore not included in the gate duration. A faster gate speed without compensating for entanglement fidelity therefore enables quantum communication at a higher clock rate.

For both schemes, the gate is heralded on detecting a reflected photon, and is therefore ideally successful 50% of the time in each run since at most half of the input photon gets reflected when the spin is initialized in a superposition state. This means that the success probability of the gate  $P_s$  depends on the spin-dependent reflectivity of the emitter, which can be expressed by Eq. (4.9):

$$P_s = \frac{1}{2} \left[ \int_{-\infty}^{\infty} |\Phi_1(\omega)|^2 |r_1(\omega)|^2 d\omega + \int_{-\infty}^{\infty} |\Phi_1(\omega)|^2 |\hat{r}_1(\omega)|^2 d\omega + P_{\gamma_d}^{\omega_1} \right]. \quad (3.28)$$

System	Init.	$2T_p$	TBI delay	$\pi/2$ -pulse	$\pi$ -pulse	Ref.
SiV-PCC	30 $\mu$ s	20 ns	142 ns	16 ns	32 ns	[64]
SiV-PCC	13 $\mu$ s	10 ns	30 ns	6 ns	12 ns	[130]
QD-PCW	0.2 $\mu$ s	4 ns	11.8 ns	3.5 ns	7 ns	Present work
Rb-cavity	140 $\mu$ s	0.6 $\mu$ s*	-	1.7 $\mu$ s	3.4 $\mu$ s	[131]

Table 3.5: Breakdown of the total gate duration in each step.  $T_p$ : duration of a photonic pulse. \*The Rb-cavity scheme uses polarization-encoding for the photonic qubit.

We find that for each incoming photon, it is reflected with a probability of 33.9% from the  $|\uparrow\rangle$  state and with a probability of 0.05% from  $|\downarrow\rangle$ . The gate efficiency is therefore  $(17.1 \pm 0.3)\%$ . The reflectivity is inferred from the two-color transmission experiment (Sec. 3.4.2), which depends on the device cooperativity and noise properties.

Another conclusion drawn from Table 3.4 is that the entanglement rates of the QD-PCW and SiV-PCC systems are of similar order of magnitude despite the difference in gate efficiency. In our work, heralded spin readout is used instead since the single-shot fidelity could only reach 52% due to limited collection efficiency  $\eta_c \approx 0.3\%$  and cyclicity  $C = 14.7$  [18]. The collection efficiency can readily be improved in next-generation devices. The low coupling rate is compensated by fast repetition rate of the system. As opposed to the 200 ms long calibration step, which includes active locking of the TBI and preselection procedures used to lock the SiV resonance, our experiment is able to be executed in 606 ns. The self-stabilizing TBI in this work does not require active locking and offers week-long stability with  $> 99\%$  interferometric visibility.

System	$P_{\text{photon}}$ (%)	$P_{\text{spin}}$ (%)	$\tau_{\text{seq}}$	$\mathcal{R}$
SiV-PCC	$2\langle n \rangle_m \eta = 0.17$	$F_{\text{ssr}} \eta = 42.3$	60 $\mu$ s	11.9 Hz
QD-PCW	0.027	1.1	0.606 $\mu$ s	4.75 Hz
Rb-cavity	$\langle n \rangle_m \eta = 3.45$	100	0.001 s	34.5 Hz

Table 3.6: Entanglement rate estimation.  $P_{\text{photon}}$  ( $P_{\text{spin}}$ ): probability of detecting a reflected photon during readout of the photonic (spin) qubit in a single run.  $\tau_{\text{seq}}$ : sequence duration including spin initialization, gate sequence and state readout.  $\mathcal{R}$ : Entanglement rate.  $\langle n \rangle_m$ : average number of photon per pulse incident on the cavity.  $\eta$ : total heralding efficiency.  $F_{\text{ssr}}$ : fidelity of single-shot readout. For QD-PCW,  $P_{\text{photon}}$  ( $P_{\text{spin}}$ ) is obtained by summing all photon clicks during the photonic (spin) detection windows, then divided by the 100 s integration time and repetition rate. For Rb-cavity,  $\eta \equiv \mathcal{R} \eta_{\text{det}} = 0.69 \times 0.56 = 0.38$  and  $\langle n \rangle_m = 0.09$ .

In Table 3.6 we estimate the entanglement rates of both systems using  $\mathcal{R} \equiv P_{\text{photon}} \times P_{\text{spin}} \times \mathcal{R}_{\text{rep}}$  where the experimental repetition rate is given by  $\mathcal{R}_{\text{rep}} = 1/\tau_{\text{seq}}$ .  $P_{\text{photon}}$  ( $P_{\text{spin}}$ ) is the probability of detecting a reflected photon in one iteration of the experiment

during the photon (spin) readout window. For a fair comparison, we define  $\tau_{\text{seq}}$  to be the time it takes to initialize, perform the gate and read out the final state, rather than the total sequence time that includes calibration steps. To validate our rate estimation of 4.75 Hz, we predict an entanglement rate of  $4.75 \text{ Hz} \times 4/(2\bar{n}) \approx 106 \pm 15 \text{ Hz}$  for Bell-state generation using optical excitations, where  $2\bar{n} = 2 \times (0.089 \pm 0.012)$  is the total number of photons scattered off the QD and the factor of 4 originates from the 50% reduction in waveguide collection efficiency due to the cross-polarized scheme (Sec. 3.3.3). This is in excellent agreement with 124 Hz extracted rate in Ref. [18]. A 25-fold improvement in the entanglement rate is possible as near-90% single-shot readout fidelity on a sub-nanosecond timescale with collection efficiency  $\eta_c = 76\%$  can be achieved [133]. To reach an even higher entanglement rate, it is necessary to improve the device reflectivity by reducing the spectral diffusion noise and increasing the QD-waveguide coupling efficiency  $\beta$ .

## 3.9 Conclusion

In this chapter, we have experimentally realized spin-photon entanglement between a guided photonic qubit and a stationary QD spin. This is made possible by the successful integration of waveguide-enabled optical cyclicity, optical spin control and coherent photon scattering. The demonstrated high entanglement fidelity (74%) is competitive with previous solid-state implementations [132, 134], while the speed is improved. Indeed, the protocol operates on a sub-microsecond timescale ( $0.6 \mu\text{s}$ ) which is at least 2 orders of magnitude faster than realized in SiV and atomic systems [116, 64, 131] as a consequence of the faster spin preparation time.

The versatility of the QD-waveguide platform is reflected by the fact that the same QD can also be operated as a source of multi-photon time-bin encoded entanglement generation [18]. Such versatile spin-photon interfaces constitute building blocks of one-way quantum repeaters [22] where spin-photon controlled-phase gates are necessary. Furthermore, the time-bin approach for scattering protocols can be extended to realize a range of new integrated quantum photonics devices and functionalities, e.g., a deterministic Bell state analyzer (BSA) or a photonic quantum non-demolition detector [23, 24] that both rely on faithful quantum state transfer from a flying photon to an emitter. As an example, in Chapter 7 we present an experimentally accessible scheme to realize a deterministic BSA for two entangled photons, based on the current QD-waveguide platform.



# Chapter 4

## Theory of Spin-photon Entanglement with Photon-scattering

In Chapter 3, we experimentally demonstrated spin-photon entanglement between a flying photon and a quantum-dot (QD) hole spin embedded in a waveguide, and measured fidelity of the entangled state. To gain an in-depth understanding of how various experimental imperfections impact the fidelity, this chapter extends the theoretical tools developed in Chapter 2 to break down each infidelity contribution, and to provide a reliable theory that accurately explains the measured value. Agreement between the measured and estimated fidelities would not only warrant validity of the proposed theory, but also shed light on the eminent error mechanisms existing in the current experimental platform, serving as an important guide for future improvements.

The chapter opens by discussing state evolution of the spin-photon system under the photon-scattering scheme in the ideal case, and introducing some theoretical basics for constructing the analytical expression of the entanglement fidelity. What immediately follows is a series of analysis performed on each known experimental imperfection, similar to the approach taken in Chapter 2, which is to evaluate the infidelity contribution for each imperfection based on realistic parameters measured in Chapter 3. In the end these individual infidelities are combined to provide a theoretical estimate, which is then compared with the fidelity measured in Sec. 3.7.

## 4.1 State Evolution under the Photon-scattering Entanglement Protocol

As described previously in Sec. 3.2.2, we consider the propagation of a time-bin photonic qubit  $\alpha|e\rangle + \beta|l\rangle$  into a two-sided waveguide where  $\alpha, \beta \in \mathbb{C}$ , and the QD hole spin is initialized in the ground state  $|\downarrow\rangle$ . The entanglement protocol is composed of scattering events of both time bins ( $\hat{S}_e$  followed by  $\hat{S}_l$ ), sandwiched between the  $\hat{R}_y(\pi/2)$  and  $\hat{R}_y(\pi)$  rotation pulses (Fig. 3.5). Here the scattering process in each time-bin follows the input-output relations [63]:

$$\begin{aligned}
 \underbrace{|\omega \uparrow\rangle}_{\text{resonant}} &\rightarrow r_1|\omega \uparrow\rangle_r + t_1|\omega \uparrow\rangle_t + r_2|\omega_2 \downarrow\rangle_r + t_2|\omega_2 \downarrow\rangle_t; \\
 \underbrace{|\omega \downarrow\rangle}_{\text{off-resonant}} &\rightarrow \underbrace{\overset{\circ}{r}_1|\omega \downarrow\rangle_r}_{\text{reflection, left-propagating}} + \underbrace{\overset{\circ}{t}_1|\omega \downarrow\rangle_t}_{\text{transmission, right-propagating}} + \underbrace{\overset{\circ}{r}_2|\omega - \Delta_h \uparrow\rangle_r}_{\text{reflection, left, spin-flip}} + \underbrace{\overset{\circ}{t}_2|\omega - \Delta_h \uparrow\rangle_t}_{\text{transmission, right, spin-flip}},
 \end{aligned} \tag{4.1}$$

where the photon in each time-bin centers around the resonant frequency  $\omega_1$  of the main optical transition ( $|\uparrow\rangle \leftrightarrow |\uparrow\downarrow\rangle$ ) with a Gaussian spectral profile, and  $r_1$  ( $t_1$ ) is the reflection (transmission) operator associated with  $|\uparrow\rangle \rightarrow |\uparrow\downarrow\rangle$  that has a decay rate  $\Gamma_1$ .  $r_2$  ( $t_2$ ) corresponds to the diagonal transition  $|\downarrow\rangle \rightarrow |\uparrow\downarrow\rangle$  with decay rate  $\Gamma_2$ .  $\omega_2 = \omega + \Delta_h$  is the frequency of the Raman photon emitted from the diagonal transition where  $\Delta_h$  is the ground-state splitting. The symbol ( $\circ$ ) denotes off-resonant scattering when the spin is in  $|\downarrow\rangle$ . Below we use the superscript prime ( $'$ ) to represent a scattered photon of frequency  $\omega_2 \neq \omega$ . By substituting Eq. (4.1), the state of the spin-photon system evolves as

$$\begin{aligned}
 & \left( \alpha|e\rangle + \beta|l\rangle \right) \otimes |\downarrow\rangle \\
 & \xrightarrow{\hat{R}_y(\pi/2)} \left( \alpha|e\rangle + \beta|l\rangle \right) \otimes \frac{1}{\sqrt{2}} \left( |\uparrow\rangle + |\downarrow\rangle \right) \\
 & \xrightarrow{\hat{S}_e} \frac{1}{\sqrt{2}} \left[ \alpha \left( r_1^e |e \uparrow\rangle_r + t_1^e |e \uparrow\rangle_t + r_2^e |e' \downarrow\rangle_r + t_2^e |e' \downarrow\rangle_t \right) \right. \\
 & \quad \left. + \alpha \left( \overset{\circ}{r}_1^e |e \downarrow\rangle_r + \overset{\circ}{t}_1^e |e \downarrow\rangle_t + \overset{\circ}{r}_2^e |e' \uparrow\rangle_r + \overset{\circ}{t}_2^e |e' \uparrow\rangle_t \right) + \beta |l \uparrow\rangle + \beta |l \downarrow\rangle \right] \\
 & \xrightarrow{\hat{R}_y(\pi)} \frac{1}{\sqrt{2}} \left[ \alpha \left( -r_1^e |e \downarrow\rangle_r - t_1^e |e \downarrow\rangle_t + r_2^e |e' \uparrow\rangle_r + t_2^e |e' \uparrow\rangle_t \right) \right. \\
 & \quad \left. + \alpha \left( \overset{\circ}{r}_1^e |e \uparrow\rangle_r + \overset{\circ}{t}_1^e |e \uparrow\rangle_t - \overset{\circ}{r}_2^e |e' \downarrow\rangle_r - \overset{\circ}{t}_2^e |e' \downarrow\rangle_t \right) - \beta |l \downarrow\rangle + \beta |l \uparrow\rangle \right] \\
 & \xrightarrow{\hat{S}_l} \frac{1}{\sqrt{2}} \left[ \alpha \left( -r_1^e |e \downarrow\rangle_r - t_1^e |e \downarrow\rangle_t + r_2^e |e' \uparrow\rangle_r + t_2^e |e' \uparrow\rangle_t \right) \right. \\
 & \quad + \alpha \left( \overset{\circ}{r}_1^e |e \uparrow\rangle_r + \overset{\circ}{t}_1^e |e \uparrow\rangle_t - \overset{\circ}{r}_2^e |e' \downarrow\rangle_r - \overset{\circ}{t}_2^e |e' \downarrow\rangle_t \right) \\
 & \quad + \beta \left( r_1^l |l \uparrow\rangle_r + t_1^l |l \uparrow\rangle_t + r_2^l |l' \downarrow\rangle_r + t_2^l |l' \downarrow\rangle_t \right) \\
 & \quad \left. - \beta \left( \overset{\circ}{r}_1^l |l \downarrow\rangle_r + \overset{\circ}{t}_1^l |l \downarrow\rangle_t + \overset{\circ}{r}_2^l |l' \uparrow\rangle_r + \overset{\circ}{t}_2^l |l' \uparrow\rangle_t \right) \right] = |\psi_{\text{out}}\rangle.
 \end{aligned} \tag{4.2}$$

Now, considering the ideal scenario where the early and late pulses are identical, monochromatic and resonant at  $\omega_1$ , and the QD optical cyclicity is infinite with no dephasing and loss, each scattering operator can be simplified (from Eq. (4.4)) into

1.  $r_1 \rightarrow -1$  (resonant photons are coherently reflected with a  $\pi$ -phase shift);
2.  $\mathring{t}_1 \rightarrow 1, \mathring{r}_1 \rightarrow 0$  (off-resonant photons are being transmitted instead of reflected);
3.  $t_1 \rightarrow 0$  (complete destructive interference in transmission);
4.  $r_2, \mathring{r}_2, t_2, \mathring{t}_2 \rightarrow 0$  (there are no Raman photons in both reflection and transmission due to infinite cyclicity).

Henceforth the ideal output state of the entanglement protocol becomes  $|\psi_{\text{out}}\rangle = [\alpha|e\downarrow\rangle - \beta|l\uparrow\rangle]_{\text{r}} + [\alpha|e\uparrow\rangle - \beta|l\downarrow\rangle]_{\text{t}}$ . Heralding on either the reflected or transmitted photon curves [135] the system into orthogonal spin-photon Bell states. Tuning the phase  $\theta_p$  of the photonic qubit where  $\beta/\alpha = e^{i\theta_p}$  and  $|\alpha|^2 + |\beta|^2 = 1$  allows all 4 maximally entangled states to be generated.

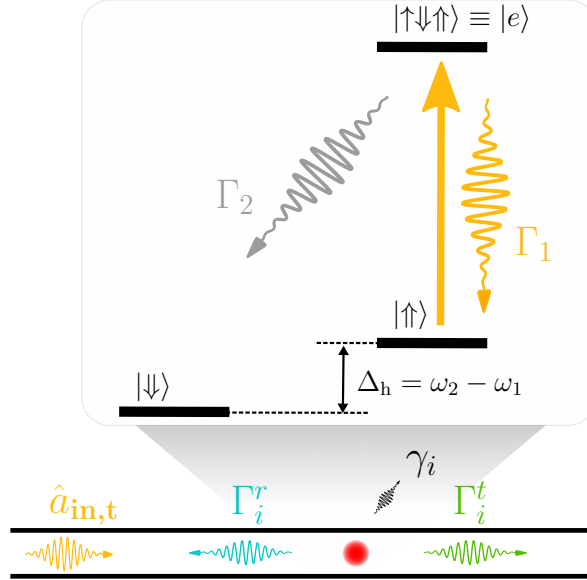


Figure 4.1: **Energy levels for a QD embedded in a two-sided waveguide under an in-plane magnetic field.**  $\Gamma_1$  ( $\Gamma_2$ ) is the radiative decay rate into the waveguide from the transition  $|e\rangle \equiv |\uparrow\downarrow\uparrow\rangle \rightarrow |\uparrow\rangle$  ( $|e\rangle \rightarrow |\downarrow\rangle$ ).  $\Gamma_i = \Gamma_i^t + \Gamma_i^r$  for  $i \in \{1, 2\}$  includes both decay rates into the transmitted (“t”) and reflected (“r”) waveguide modes. The QD is indicated in red.  $\gamma_i$  is the radiative rate into the lossy modes (Not to be confused with the radiative decay rates  $\gamma_Y \equiv \Gamma_1$  and  $\gamma_X \equiv \Gamma_2$  in Fig. 3.5).

## 4.2 Photon Scattering Formalism and Fidelity Expression

With a decent understanding of the working principle of the entanglement protocol, we are ready to formulate the gate fidelity. To do so, we shall first find the general expressions of each scattering operator starting from the system Hamiltonian.

### 4.2.1 Scattering Coefficients in Two-sided Waveguides

Similar to Sec. 2.2.1, The scattering matrix of a weak coherent state on the  $\Lambda$ -level emitter in a two-sided waveguide has been studied in Ref. [77]. The scattering coefficients in Eq. (4.1) can be inferred from the following input-output relation (Eq. (4.3)), where the output field bosonic operator of the waveguide is expressed in terms of the incident field and dynamical response of the emitter from the non-Hermitian Hamiltonian  $\hat{\mathcal{H}}_{\text{nh}}$  [77]. For two-sided waveguides, we label the field operator in the reflection port by the subscript ‘‘r’’, and the transmitted port by ‘‘t’’ (Fig. 4.1). Suppose a photon  $\hat{a}_{\text{in,t}}^\dagger$  enters the waveguide from the left, the output field operators on the transmitted (t) and reflected (r) ports are

$$|\omega \uparrow\rangle : \begin{cases} \hat{a}_{\text{out,t}} &= \left[ 1 - \frac{2\Gamma_1^t}{\Gamma + 2i\delta_1} \hat{\sigma}_{11} - \frac{2\sqrt{\Gamma_1^t \Gamma_2^t}}{\Gamma + 2i\delta_1} \hat{\sigma}_{12} \right] \hat{a}_{\text{in,t}} \\ \hat{a}_{\text{out,r}} &= \left[ -\frac{2\sqrt{\Gamma_1^t \Gamma_1^r}}{\Gamma + 2i\delta_1} \hat{\sigma}_{11} - \frac{2\sqrt{\Gamma_1^t \Gamma_2^r}}{\Gamma + 2i\delta_1} \hat{\sigma}_{12} \right] \hat{a}_{\text{in,t}} \end{cases}$$

$$|\omega \downarrow\rangle : \begin{cases} \hat{a}_{\text{out,t}} &= \left[ 1 - \frac{2\Gamma_1^t}{\Gamma + 2i(\delta_1 + \Delta_h)} \hat{\sigma}_{11} - \frac{2\sqrt{\Gamma_1^t \Gamma_2^t}}{\Gamma + 2i(\delta_1 + \Delta_h)} \hat{\sigma}_{12} \right] \hat{a}_{\text{in,t}} \\ \hat{a}_{\text{out,r}} &= \left[ -\frac{2\sqrt{\Gamma_1^t \Gamma_1^r}}{\Gamma + 2i(\delta_1 + \Delta_h)} \hat{\sigma}_{11} - \frac{2\sqrt{\Gamma_1^t \Gamma_2^r}}{\Gamma + 2i(\delta_1 + \Delta_h)} \hat{\sigma}_{12} \right] \hat{a}_{\text{in,t}}, \end{cases} \quad (4.3)$$

where  $\delta_1 = \omega_1 - \omega$  is the laser detuning from the transition  $|\uparrow\rangle \rightarrow |e\rangle \equiv |\uparrow\downarrow\rangle$  for an emitter initialized in  $|\uparrow\rangle$ . The total decay rate  $\Gamma = \Gamma_1 + \Gamma_2 + \gamma_1 + \gamma_2$  where  $\Gamma_i$  ( $\gamma_i$ ) is the radiative decay rate into (out of) the waveguide.  $\Gamma_i = \Gamma_i^t + \Gamma_i^r$  includes both decay rates into the transmitted (‘‘t’’) and reflected (‘‘r’’) waveguide modes.  $\Delta_h$  is the ground-state splitting. The output field operators have different detunings in their denominators because of different initial spin states of the QD: If the spin is initially  $|\uparrow\rangle$ , the resonant frequency is  $\omega_1$ ; If it is  $|\downarrow\rangle$  then the resonant frequency required to drive the diagonal spin transition is  $\omega_2 = \omega_1 + \Delta_h$ .  $\hat{\sigma}_{ij} = |j\rangle\langle i|$  is the atomic operator denoting a spin-flip in the atomic state when  $i \neq j$ .

When evaluating the probability of a spin-photon state, i.e.,  $|e \downarrow\rangle_r$ , the corresponding scattering coefficient  $r_1^e(\omega)$  is first convoluted with a Gaussian lineshape  $\Phi_1(\omega)$  and integrated with respect to  $\omega$  (Sec. 2.2.2). The resonant scattering coefficients in the frequency domain are read directly from Eq. (4.3):

$$t_1(\omega) = 1 - \frac{2\Gamma_1^t}{\Gamma + 2i\delta_1}, \quad t_2(\omega) = -\frac{2\sqrt{\Gamma_1^t \Gamma_2^t}}{\Gamma + 2i\delta_1},$$

$$r_1(\omega) = -\frac{2\sqrt{\Gamma_1^t \Gamma_1^r}}{\Gamma + 2i\delta_1}, \quad r_2(\omega) = -\frac{2\sqrt{\Gamma_1^t \Gamma_2^r}}{\Gamma + 2i\delta_1}, \quad (4.4)$$

where the off-resonant scattering coefficients are found similarly by replacing  $\delta_1 \rightarrow \delta_1 + \Delta_h$ .

## 4.2.2 Projection Operators for Time-bin Photons

The scattering coefficients obtained above are expressed in the (angular) frequency domain, whereas the actual fidelity measurement is done by reading out the photonic state in three different detection time windows. It is therefore necessary to define the measurement operators in different time-bins, and relate them to the photon creation operator in the frequency domain.

We first define the detection of a time-bin photon by projection operators on different photonic readout bases:

$$\begin{aligned} |e\rangle\langle e| &= \int_{-\infty}^{\infty} \hat{a}_e^\dagger(t)\hat{a}_e(t)dt, & |l\rangle\langle l| &= \int_{-\infty}^{\infty} \hat{a}_e^\dagger(t+\tau)\hat{a}_e(t+\tau)dt, \\ |e\rangle\langle l| &= \int_{-\infty}^{\infty} \hat{a}_e^\dagger(t)\hat{a}_e(t+\tau)dt = (|l\rangle\langle e|)^\dagger, \end{aligned} \quad (4.5)$$

where the bosonic creation operator  $\hat{a}_e^\dagger(t)$  represents the emission of a photon at time  $t$  in the early time-bin, and  $\tau$  is the interferometric delay. The projections  $|e\rangle\langle e|$  ( $|l\rangle\langle l|$ ) correspond to detecting photons in the side peak windows (green) (Fig. 3.21a), whereas  $|e\rangle\langle l|$  refers to projection onto the middle detection window (blue central peak) where the early and late photons interfere. Since we only resolve the time-bin, the creation operator can be expressed in either the time or frequency domain. Applying the Fourier transform  $a(t) = \frac{1}{\sqrt{2\pi}} \int_{-\infty}^{\infty} a(\omega)e^{i\omega t}d\omega$ , one can show

$$\int_{-\infty}^{\infty} \hat{a}_e^\dagger(t)a_e(t)dt = \int_{-\infty}^{\infty} \hat{a}_e^\dagger(\omega)a_e(\omega)d\omega. \quad (4.6)$$

This implies we can apply the same perturbation theory in the frequency domain to evaluate the fidelity as in Chapter 2.

## 4.2.3 Formula for Operational Fidelity

Now that the time-bin projection operators are defined, we can express the entanglement fidelity in terms of the scattering coefficients in Eq. (4.4).

The measure of the quality of generated quantum states is traditionally quantified by the fidelity, which in our case evaluates the overlap between the output and ideal Bell states:

$$\mathcal{F}_r^{\text{theory}} = \frac{\langle \psi_{\text{ideal}} | \rho_{\text{out}} | \psi_{\text{ideal}} \rangle}{\text{Tr}(|\psi_{\text{out}}\rangle\langle\psi_{\text{out}}|)}. \quad (4.7)$$

Here the output reduced density matrix is given by  $\rho_{\text{out}} = \text{Tr}_{t,\omega}(|\psi_{\text{out}}\rangle\langle\psi_{\text{out}}|)$  which is a partial trace of the output density matrix  $|\psi_{\text{out}}\rangle\langle\psi_{\text{out}}|$  over the transmitted modes and frequency states  $\omega \neq \omega_1$ , as these photons are not detected in the reflection. The total output density matrix  $\rho_{\text{out}}$  is therefore obtained by effectively tracing out the unwanted modes. Here we assume the use of perfect filters prior to detection which removes photons of frequencies other than  $\omega_1$ . The bandwidth of each etalon filter used in the experiment is  $\sim 3$  GHz with over 95% transmission. This means the filter bandwidth is much narrower than the ground-state splitting  $\Delta_h/2\pi = 7.3$  GHz but wider than the QD transform-limited linewidth  $\Gamma/2\pi = 394$  MHz (Sec. 3.6) justifying the assumption.

The fidelity in Eq. (4.7) is normalized by the success probability or gate efficiency  $P_s = \text{Tr}(|\psi_{\text{out}}\rangle\langle\psi_{\text{out}}|) \equiv \sum_i \langle i |_r (|\psi_{\text{out}}\rangle\langle\psi_{\text{out}}|) | i \rangle_r$ , since the gate is heralded by the detection

of a photon in the reflection. In such case any event contributing to the loss of the scattered photon (e.g., finite cyclicity, nonzero coupling to leaky modes of the waveguide, and the transmission of a photon, which is effectively treated as loss) does not reduce the gate fidelity.

The normalized output reduced density matrix is computed from Eq. (4.2) to be

$$\begin{aligned} \frac{\rho_{\text{out}}}{P} = \frac{1}{2P} & \left( |\alpha|^2 |r_1^e|^2 |e \downarrow\rangle \langle e \downarrow| - \alpha\beta^* r_1^e r_1^{l*} |e \downarrow\rangle \langle l \uparrow| \right. \\ & \left. - \alpha^* \beta r_1^{e*} r_1^l |l \uparrow\rangle \langle e \downarrow| + |\beta|^2 |r_1^l|^2 |l \uparrow\rangle \langle l \uparrow| + |\alpha|^2 |\tilde{r}_1^e|^2 |e \uparrow\rangle \langle e \uparrow| + \dots \right), \end{aligned}$$

where each scattering probability here (i.e.,  $|r_1^e|^2$ ) can be expressed as an integral in the frequency domain (Sec. 4.2.2). For instance we write out two of the matrix elements in  $\rho_{\text{out}}$  using Eq. (4.6):

$$\begin{aligned} \frac{1}{2} |\alpha|^2 |r_1^e|^2 |e \downarrow\rangle \langle e \downarrow| &= \frac{1}{2} |\alpha|^2 \int_{-\infty}^{\infty} \int_{-\infty}^{\infty} d\omega d\omega' r_1(\omega) r_1^*(\omega') \Phi_1(\omega) \Phi_1(\omega') \\ & \quad \times \hat{a}_e^\dagger(\omega) |\emptyset \downarrow\rangle \langle \emptyset \downarrow| \hat{a}_e(\omega'); \\ \frac{1}{2} \alpha\beta^* r_1^e r_1^{l*} |e \downarrow\rangle \langle l \uparrow| &= \frac{1}{2} \alpha\beta^* \int_{-\infty}^{\infty} \int_{-\infty}^{\infty} d\omega d\omega' r_1(\omega) r_1^*(\omega') \Phi_1(\omega) \Phi_1(\omega') \\ & \quad \times \hat{a}_e^\dagger(\omega) |\emptyset \downarrow\rangle \langle \emptyset \uparrow| \hat{a}_l(\omega'), \end{aligned}$$

where  $|\emptyset\rangle$  is the vacuum state. For simplicity we now say that the early and late scattering events are identical for any given input frequency thus  $r_1^e = r_1^l = r_1$ . The reasoning behind this is discussed in Sec. 4.3.4. Therefore, for an ideal Bell state in the reflected mode:  $|\psi_{\text{ideal}}\rangle = \alpha|e \downarrow\rangle - \beta|l \uparrow\rangle$ , the overlap of the first density matrix elements with the ideal state becomes

$$\begin{aligned} & \langle \psi_{\text{ideal}} | \left[ \frac{1}{2} |\alpha|^2 |r_1^e|^2 |e \downarrow\rangle \langle e \downarrow| \right] | \psi_{\text{ideal}} \rangle \\ &= \frac{|\alpha|^4}{2} \int_{-\infty}^{\infty} \int_{-\infty}^{\infty} \int_{-\infty}^{\infty} d\omega d\omega' d\omega'' \\ & \quad \times \langle \emptyset \downarrow | \hat{a}_e(\omega'') \left[ r_1(\omega) r_1^*(\omega') \Phi_1(\omega) \Phi_1(\omega') \hat{a}_e^\dagger(\omega) |\emptyset \downarrow\rangle \langle \emptyset \downarrow| \hat{a}_e(\omega') \right] \hat{a}_e^\dagger(\omega'') |\emptyset \downarrow\rangle \\ &= \frac{|\alpha|^4}{2} \int_{-\infty}^{\infty} \int_{-\infty}^{\infty} \int_{-\infty}^{\infty} d\omega d\omega' d\omega'' r_1(\omega) r_1^*(\omega') \Phi_1(\omega) \Phi_1(\omega') \delta(\omega - \omega'') \delta(\omega' - \omega'') \\ &= \frac{|\alpha|^4}{2} \int_{-\infty}^{\infty} |\Phi_1(\omega)|^2 |r_1(\omega)|^2 d\omega. \end{aligned}$$

Repeating for the remaining matrix elements, the conditional fidelity is found to be

$$\mathcal{F}_r^{\text{theory}} = \frac{1}{2P} \int_{-\infty}^{\infty} |\Phi_1(\omega)|^2 |r_1(\omega)|^2 d\omega, \quad (4.8)$$

where the success probability  $P_s$  is the trace of the output density matrix over the four basis states  $|i\rangle = \{|e \uparrow\rangle_r, |e \downarrow\rangle_r, |l \uparrow\rangle_r, |l \downarrow\rangle_r\}$  in the Hilbert space of the spin-photon

system. It is given by

$$\begin{aligned}
P_s &= \text{Tr}(|\psi_{\text{out}}\rangle\langle\psi_{\text{out}}|) \\
&= \sum_i \langle i|_r(|\psi_{\text{out}}\rangle\langle\psi_{\text{out}}|)|i\rangle_r \\
&= \frac{1}{2} \left[ \int_{-\infty}^{\infty} |\Phi_1(\omega)|^2 |r_1(\omega)|^2 d\omega + \int_{-\infty}^{\infty} |\Phi_1(\omega)|^2 |\hat{r}_1(\omega)|^2 d\omega \right]. \tag{4.9}
\end{aligned}$$

Combining Eqs. (4.8) and (4.9) results in the formula for the gate fidelity conditioned on reflected photons

$$\mathcal{F}_r^{\text{theory}} = \frac{\int_{-\infty}^{\infty} |\Phi_1(\omega)|^2 |r_1(\omega)|^2 d\omega}{\int_{-\infty}^{\infty} |\Phi_1(\omega)|^2 |r_1(\omega)|^2 d\omega + \int_{-\infty}^{\infty} |\Phi_1(\omega)|^2 |\hat{r}_1(\omega)|^2 d\omega}. \tag{4.10}$$

### 4.3 Fidelity under Realistic Noises

The two integrals in Eq. (4.10) are in fact probabilities of scattering a photon of frequency  $\omega_1$  from the spin state  $|\uparrow\rangle$  (resonant) and from  $|\downarrow\rangle$  (off-resonant), respectively. Substituting Eq. (4.4) further simplifies the integrals, resulting in the perturbative forms:

$$\begin{aligned}
\int_{-\infty}^{\infty} |\Phi_1(\omega)|^2 |r_1(\omega)|^2 d\omega &= \frac{1}{\sqrt{2\pi\sigma_o^2}} \int_{-\infty}^{\infty} e^{-\frac{(\omega-\omega_1)^2}{2\sigma_o^2}} \left| -\frac{2\sqrt{\Gamma_1^t \Gamma_1^r}}{\Gamma + 2i\delta_1} \right|^2 d\omega \\
&\approx 1 - \frac{4\sigma_o^2}{\Gamma^2} - \frac{\Gamma^2 - \Gamma_1^2}{\Gamma^2}, \\
\int_{-\infty}^{\infty} |\Phi_1(\omega)|^2 |\hat{r}_1(\omega)|^2 d\omega &\approx \frac{\Gamma_1^2}{\Gamma^2 + 4\Delta_h^2}, \tag{4.11}
\end{aligned}$$

where we assume that the scattered photon is equally coupled to the reflected and transmitted modes, i.e.,  $\Gamma_i^r = \Gamma_i^t = \Gamma_i/2$ .  $\sigma_o$  is the standard deviation of the spectral width (in angular frequency) of the incident Gaussian pulse. In evaluating Eq. (4.11) perturbatively we assume the frequency detuning  $\delta_1$  to be small compared to the QD total decay rate  $\Gamma$  and the ground-state splitting  $\Delta_h$  for efficient light-matter interaction. With both Eqs. (4.10) and (4.11), we are prepared to evaluate the fidelity under different realistic noises.

#### 4.3.1 Spectral Mode Mismatch

By heralding on the detection of a reflected photon of frequency  $\omega_1$  within the time-bin window, the entanglement fidelity becomes immune to the spectral error due to the nonzero bandwidth  $\sigma_o$  of the incident pulse to lowest order in perturbation theory. To understand this, we consider only finite bandwidth  $\sigma_o \neq 0$  and take other imperfections to be negligible, where  $\Gamma_1 \rightarrow \Gamma$  and  $\Delta_h \rightarrow \infty$ . Using Eqs. (4.10) and (4.11), the resultant fidelity is then

$$\mathcal{F}_r^{\text{theory}} \approx 1. \tag{4.12}$$

Simply put, photons which are not resonant with the QD transition will be transmitted instead of reflected. Since the gate is conditioned on the reflection of either an early or a late photon, the transmission of the photon only reduces the success probability. The gate will thus have unity fidelity as long as the dynamics of the early and late scattering events are identical. The same argument can be made for the broadening of the QD optical transition due to slow spectral wandering. Due to the ms-long spectral diffusion time [136], the QD resonance drift is effectively constant over its lifetime (0.4 ns) and also the interferometric delay (11.8 ns), the QD reflectivity is thus identical for both early and late scattering events, with the entanglement fidelity remains unharmed.

If the entangling gate is heralded on the presence of transmitted photon; however, the fidelity becomes susceptible to the spectral mismatch error. Following the treatment in Sec. 2.3.1.1, the fidelity heralded on transmission of a photon is

$$\mathcal{F}_t^{\text{theory}} \approx 1 - \frac{4\sigma_o^2}{\Gamma^2} - \frac{4\sigma_e^2}{\Gamma^2}, \quad (4.13)$$

as the spectral infidelity arises from incomplete destructive interference between the incident field and the resonantly scattered photon ( $t_1 \neq 0$ ). Any spectral effects reducing this interference would stain the quality of the entangled state. It is important to note that there is still a small probability of detecting undesired Raman photons of frequency  $\omega_2 = \omega_1 + \Delta_h$  in the reflection due to the finite optical cyclicity. These photons result from the imperfect QD two-level system and are filtered out.

### 4.3.2 Finite Cyclicity and Coupling Loss

On the reflection, photons could either originate from **(i)** resonant reflection on the spin-preserving transition (indicated by  $r_1$ ), **(ii)** resonant Raman spin-flip process to  $|\downarrow\rangle$  ( $r_2$ ), or **(iii)** off-resonant reflection from  $|\downarrow\rangle$  ( $r_1$ ). A high cyclicity reduces the probability of resonant spin-flip process but strengthens off-resonant reflection; however, the undesired events (ii) and (iii) can be reduced by having a larger ground-state splitting  $\Delta_h \gg \Gamma$ . In addition, coupling to lossy modes of the waveguide would imply that the reflected photons are lost without being detected; as a result these events do not affect the fidelity. To understand this, we evaluate the reflection fidelity

$$\mathcal{F}_r^{\text{theory}} \approx 1 - \frac{\Gamma^2}{4\Delta_h^2} \left( \frac{C}{C+1} \beta \right)^2. \quad (4.14)$$

From here we observe that the fidelity is indeed insensitive to coupling loss and optical cyclicity, and is primarily reduced due to the finite probability  $\sim \Gamma^2/\Delta_h^2$  of detecting Rayleigh-scattered photons from  $|\downarrow\rangle$ . Note that when deriving Eq. (4.14) we define the optical cyclicity  $C \equiv \Gamma_1/\Gamma_2$  [20], the total decay rate  $\Gamma = \Gamma_1 + \Gamma_2 + \gamma_1 + \gamma_2$  where  $\gamma_1$  ( $\gamma_2$ ) is the radiative rate from the transition  $|e\rangle \rightarrow |\uparrow\rangle$  ( $|e\rangle \rightarrow |\downarrow\rangle$ ) which couples to lossy modes. The waveguide-coupling efficiency  $\beta \equiv (\Gamma_1 + \Gamma_2)/\Gamma$ . From these conditions we obtain  $\Gamma_1 = \frac{C}{C+1}\beta\Gamma$  which is then substituted into Eq. (4.11).

### 4.3.3 Phonon-induced Pure Dephasing

The interaction of the QD with a phononic environment results in the broadening of the zero-phonon line and a broad phonon sideband [82, 83, 76, 75]. The latter can be filtered out while the former contributes to the reflection of incoherent photons which scramble the phase coherence of the spin-photon Bell state. The incoherent photons are only slightly broadened and thus cannot easily be removed by filters.

We follow the approach in Sec. 2.3.1.3 and model this incoherent process as Markovian decoherence given by a dephasing rate  $\gamma_d$  with the Lindblad operator  $\sqrt{2\gamma_d}\hat{\sigma}_{ee}$  where  $|e\rangle \equiv |\uparrow\downarrow\uparrow\rangle$  is the atomic excited state. The output density matrix is a sum of coherent and incoherent photon density matrices:

$$\rho' = \rho + P_{\gamma_d}^{\omega_1} \rho_{\gamma_d}^{\omega_1} \otimes |\uparrow\rangle\langle\uparrow|, \quad (4.15)$$

where  $\rho$  is the density matrix without a dephasing quantum jump. The normalized photon density matrix  $\rho_{\gamma_d}^{\omega_1}$  represents an incoherently scattered photon centered at frequency  $\omega_1$  into the waveguide, with dephasing probability given by Eq. (3.19):

$$\begin{aligned} P_{\gamma_d}^{\omega_1} &= \frac{\Gamma_1^r}{\Gamma} P_{\gamma_d} = \frac{\Gamma_1^r}{\Gamma} \int_{-\infty}^{\infty} \frac{e^{-\frac{(\omega-\omega_1)^2}{2\sigma_o^2}}}{\sqrt{2\pi\sigma_o^2}} \left| \frac{-2\sqrt{2\gamma_d}\Gamma_1^r}{\Gamma + 2i(\omega - \omega_1)} \right|^2 d\omega \\ &= \frac{2\gamma_d}{\Gamma} \int_{-\infty}^{\infty} |\Phi_1(\omega)|^2 |r_1(\omega)|^2 d\omega, \end{aligned} \quad (4.16)$$

where  $\Gamma_1^r = \Gamma_1/2$  is the decay rate in the reflected mode. Initially there are also incoherent photons of frequency  $\omega_2$  due to finite optical cyclicity but these are subsequently filtered out together with phonon sidebands.

To evaluate the effect of pure dephasing in the gate protocol, it is instructive to consider the propagation of the error as there are two separate scattering events which will both lead to incoherent decay. Since Eq. (4.15) depends on whether there is a quantum jump to the excited state, we can safely assume that pure dephasing occurs primarily when the incident photon is resonant with the QD state, since the excited state is unlikely to be populated via off-resonant scattering. As such, there are two additional incoherent density matrices (resulted from each time-bin) in the normalized output reduced density matrix:

$$\rho'_{\text{out}} = \frac{P_s \rho_{\text{out}} + \frac{1}{2} |\alpha|^2 P_{\gamma_d}^{\omega_1} \rho_{\gamma_d}^{\omega_1, e} \otimes \hat{R}_y(\pi) |\uparrow\rangle\langle\uparrow| \hat{R}_y^\dagger(\pi) + \frac{1}{2} |\beta|^2 P_{\gamma_d}^{\omega_1} \rho_{\gamma_d}^{\omega_1, l} \otimes |\uparrow\rangle\langle\uparrow|}{P_s + \text{Tr}\left(\frac{1}{2} |\alpha|^2 P_{\gamma_d}^{\omega_1} \rho_{\gamma_d}^{\omega_1, e} \otimes \hat{R}_y(\pi) |\uparrow\rangle\langle\uparrow| \hat{R}_y^\dagger(\pi)\right) + \text{Tr}\left(\frac{1}{2} |\beta|^2 P_{\gamma_d}^{\omega_1} \rho_{\gamma_d}^{\omega_1, l} \otimes |\uparrow\rangle\langle\uparrow|\right)}. \quad (4.17)$$

Together with Eq. (4.16) for an equatorial qubit  $|\alpha| = |\beta| = 1/\sqrt{2}$ , the entanglement fidelity under pure dephasing is

$$\begin{aligned} \mathcal{F}_r^{\text{theory}} &= \langle \psi_{\text{ideal}} | \rho'_{\text{out}} | \psi_{\text{ideal}} \rangle \\ &= \frac{\int_{-\infty}^{\infty} |\Phi_1(\omega)|^2 |r_1(\omega)|^2 d\omega + (|\alpha|^4 + |\beta|^4) P_{\gamma_d}^{\omega_1}}{\int_{-\infty}^{\infty} |\Phi_1(\omega)|^2 |r_1(\omega)|^2 d\omega + \int_{-\infty}^{\infty} |\Phi_1(\omega)|^2 |\dot{r}_1(\omega)|^2 d\omega + P_{\gamma_d}^{\omega_1}} \\ &\approx 1 - \frac{\gamma_d}{\Gamma}. \end{aligned} \quad (4.18)$$

### 4.3.4 Spin Dephasing

In this section, we investigate how the decoherence of the spin states affects the entanglement fidelity. Specifically we consider the dephasing of the QD spin ground states, due to the presence of an external Overhauser field effectively formed by a neighboring nuclear ensemble. This effect causes a superposition spin qubit to precess on the equatorial plane at a random frequency  $\delta_g$  slower than the QD decay rate, which is modelled by applying a time evolution operator  $\hat{T}(\Delta t) = \exp(-i\delta_g \hat{S}_z \Delta t)$  on the superposition spin state, where  $\hat{S}_z = \hat{\sigma}_z/2$  (Sec. 2.3.3.1). In the course of the entangling gate, a  $\pi$ -pulse is applied between two scattering events to ensure the precession of the spin is reversed and thus the spin is eventually refocused. In theory, the superposition qubit starts to precess at  $t_0$  and the  $\pi$ -rotation pulse is applied at  $t_\pi$ . The spin is then refocused and read out at  $t_r$  where  $t_r - t_\pi = t_\pi - t_0 = \Delta t$  must be satisfied for the perfect echo condition. In the experiment, a rotation pulse  $\hat{R}_i = \hat{R}_{y, \phi_s}(\pi/2)$  is applied at  $t_r$  to project the spin state onto one of its poles thus preventing further precession.

To understand how spin echo works for the gate, we introduce the spin-echo operator  $\hat{U}_{\text{echo}} \equiv \hat{T}(t_r - t_\pi) \hat{R}_y(\pi) \hat{T}(t_\pi - t_0)$  which transforms the spin states into

$$\begin{cases} \hat{U}_{\text{echo}}|\uparrow\rangle = -\exp\left(\frac{-i\delta_g(2t_\pi - t_r - t_0)}{2}\right)|\downarrow\rangle \equiv \lambda_\downarrow|\downarrow\rangle; \\ \hat{U}_{\text{echo}}|\downarrow\rangle = \exp\left(\frac{i\delta_g(2t_\pi - t_r - t_0)}{2}\right)|\uparrow\rangle \equiv \lambda_\uparrow|\uparrow\rangle. \end{cases} \quad (4.19)$$

Using Eq. (4.19), the output state in Eq. (4.2) is rewritten as

$$|\psi_{\text{out}}\rangle = -\alpha\lambda_\downarrow r_1^e |e\downarrow\rangle_r + \alpha\lambda_\uparrow \hat{r}_1^e |e\uparrow\rangle_r + \beta\lambda_\uparrow r_1^l |l\uparrow\rangle_r - \beta\lambda_\downarrow \hat{r}_1^l |l\downarrow\rangle_r + \dots \quad (4.20)$$

Eq. (4.20) implies that the phase coherence between  $|e\downarrow\rangle_r$  and  $|l\uparrow\rangle_r$  depends on **(i)** the accumulated phase from spin precession, and **(ii)** the phase acquired from the early and late single-photon scattering events which is determined by the *exact time* of scattering occurred within the optical pulse. Condition (ii) is made equal by interfering the time-bins with a matching time delay  $\tau_{\text{int}} = 11.8$  ns on the detection path. Since the time-bin qubit is created and measured using the same interferometer setup, by having an equal time delay  $\tau_e = \tau_d = \tau$  for the excitation and detection paths, the interferometer temporally picks out events in which the exact time of scattering is in the same position of the pulse, i.e.,  $r_1^e(t') = r_1^l(t')$  for some time  $t' \in \Phi_1(t)$  within the optical pulse. Therefore, the fidelity of the spin-photon Bell state is in principle impervious to spin dephasing.

Now, to study how condition **(i)** affects the entanglement fidelity, we assume perfect single-photon scattering and consider only the output state conditioned on reflected photons, thus Eq. (4.20) is simplified as

$$|\psi_{\text{out}}\rangle = \alpha\lambda_\downarrow |e\downarrow\rangle_r - \beta\lambda_\uparrow |l\uparrow\rangle_r. \quad (4.21)$$

For measuring the output state in the Z-basis, we compute the expectation value of the Z-basis projection operator  $\hat{\mathcal{P}}_z \equiv |e\downarrow\rangle_r \langle e\downarrow|_r + |l\uparrow\rangle_r \langle l\uparrow|_r$  [18, 137]

$$\langle \hat{\mathcal{P}}_z \rangle \equiv \langle \psi_{\text{out}} | \hat{\mathcal{P}}_z | \psi_{\text{out}} \rangle = |\alpha\lambda_\downarrow|^2 + |\beta\lambda_\uparrow|^2 = 1, \quad (4.22)$$

which is insensitive to spin dephasing, regardless of whether the echo condition is fulfilled. However, when measuring in the X- (Y-basis), the corresponding expectation value of  $\hat{\mathcal{M}}_x$

$\langle \hat{\mathcal{M}}_y \rangle$  averaged over  $N(\delta_g, \sigma_{\text{OH}})$  is

$$\begin{aligned}\langle \hat{\mathcal{M}}_x \rangle &= \int_{-\infty}^{\infty} \langle \psi_{\text{out}}^x | \hat{\mathcal{M}}_x | \psi_{\text{out}}^x \rangle N(\delta_g, \sigma_{\text{OH}}) d\delta_g = - \int_{-\infty}^{\infty} \cos \frac{\delta_g \Delta \tau}{2} N(\delta_g, \sigma_{\text{OH}}) d\delta_g = -e^{-(\Delta \tau / T_2^*)^2}; \\ \langle \hat{\mathcal{M}}_y \rangle &= \int_{-\infty}^{\infty} \langle \psi_{\text{out}}^y | \hat{\mathcal{M}}_y | \psi_{\text{out}}^y \rangle N(\delta_g, \sigma_{\text{OH}}) d\delta_g = e^{-(\Delta \tau / T_2^*)^2},\end{aligned}\quad (4.23)$$

with the output state (Eq. (4.21)) rewritten in the X- (Y-basis)

$$\begin{aligned}|\psi_{\text{out}}^x\rangle &= \frac{1}{2} [(\lambda_{\downarrow} - \lambda_{\uparrow})|X_p^+ X_s^+\rangle - (\lambda_{\uparrow} + \lambda_{\downarrow})|X_p^+ X_s^-\rangle + (\lambda_{\uparrow} + \lambda_{\downarrow})|X_p^- X_s^+\rangle + (\lambda_{\uparrow} - \lambda_{\downarrow})|X_p^- X_s^-\rangle]; \\ |\psi_{\text{out}}^y\rangle &= \frac{1}{2} [-i(\lambda_{\uparrow} + \lambda_{\downarrow})|Y_p^+ Y_s^+\rangle + i(\lambda_{\uparrow} - \lambda_{\downarrow})|Y_p^+ Y_s^-\rangle + (\lambda_{\downarrow} - \lambda_{\uparrow})|Y_p^- Y_s^+\rangle + (\lambda_{\downarrow} + \lambda_{\uparrow})|Y_p^- Y_s^-\rangle],\end{aligned}\quad (4.24)$$

and the respective projection operators

$$\begin{aligned}\hat{\mathcal{M}}_x &= |X_p^+ X_s^+\rangle \langle X_p^+ X_s^+| + |X_p^- X_s^-\rangle \langle X_p^- X_s^-| - |X_p^+ X_s^-\rangle \langle X_p^+ X_s^-| - |X_p^- X_s^+\rangle \langle X_p^- X_s^+|; \\ \hat{\mathcal{M}}_y &= |Y_p^+ Y_s^+\rangle \langle Y_p^+ Y_s^+| + |Y_p^- Y_s^-\rangle \langle Y_p^- Y_s^-| - |Y_p^+ Y_s^-\rangle \langle Y_p^+ Y_s^-| - |Y_p^- Y_s^+\rangle \langle Y_p^- Y_s^+|.\end{aligned}\quad (4.25)$$

Eq. (4.23) shows a Gaussian decay with spin dephasing time  $T_2^* = \sqrt{2}/\sigma_{\text{OH}}$  when the echo condition  $\Delta \tau \equiv 2t_{\pi} - t_r - t_0 \neq 0$  is not met. For that reason, to measure spin-photon correlations in the equatorial bases, a second  $\hat{R}_y(\pi/2)$  pulse is applied at  $t_r = 2t_{\pi} - t_0$  to rotate the spin state to either of its two poles to prevent subsequent precession. From here, we note that for Z-basis fidelity measurements, the second  $\hat{R}_y(\pi/2)$  pulse is not necessary as  $\langle \hat{\mathcal{P}}_z \rangle$  is tolerant to spin dephasing error. In such a case, the central  $\pi$ -rotation pulse does not play a refocusing role but is still required for inverting the spin between two scattering events. Additionally, due to having identical rotational pulse sequence, the spin-echo visibility  $V_s$  measured in Fig. 3.20b in principle establishes an upper bound for  $|\langle \hat{\mathcal{M}}_x \rangle|$  and  $|\langle \hat{\mathcal{M}}_y \rangle|$ , while  $\langle \hat{\mathcal{P}}_z \rangle$  is primarily limited by fidelity of the  $\hat{R}_y(\pi)$  pulse.

Note that Eq. (4.24) is derived from Eq. (4.21) taking  $\beta = \alpha e^{i\theta_0} = \alpha$  for  $|\psi_{\text{out}}^x\rangle$  ( $\beta = \alpha e^{i(\theta_0 + \pi/2)} = i\alpha$  for  $|\psi_{\text{out}}^y\rangle$ )<sup>1</sup>, where  $|e\rangle \equiv |X_p^+\rangle + |X_p^-\rangle = |Y_p^+\rangle + |Y_p^-\rangle$  and  $|l\rangle \equiv |X_p^+\rangle - |X_p^-\rangle = |Y_p^+\rangle - |Y_p^-\rangle$ . Taking  $\Delta \tau = 0$ , the ideal case of Eq. (4.24) has  $\langle \hat{\mathcal{M}}_x \rangle = -1$  and  $\langle \hat{\mathcal{M}}_y \rangle = 1$  which is consistent with the experimental spin-photon correlations in Figs. 3.21c-d.

<sup>1</sup>See Sec. 3.7 for projective measurement settings.

### 4.3.5 Incoherent Spin-flip Error and Finite $T_2^*$

The next error concerns spin decoherence induced by the red-detuned spin rotation laser and due to finite spin coherence time  $T_2^*$ . The former has been observed in Refs. [125, 18] which results in power-dependent spin-flips, thereby destroying the coherence of the spin qubit during spin rotations. Despite its exact origin not being fully resolved, its effect on the spin coherence and the fidelity can be approximated by modelling the spin-flip error by a depolarizing channel  $\mathcal{E}_{\text{depol}}^s$ , with the probability  $p$  of undergoing a random spin-flip dependent on the incoherent spin-flip rate  $\kappa$  and the duration of the respective rotation pulse  $T_r$ . The action of the depolarizing channel on a density matrix  $\rho$  is represented by  $\mathcal{E}_{\text{depol}}(\rho) = (1-p)\rho + p\mathcal{I}/2$ , where  $\mathcal{I}$  is the identity matrix<sup>2</sup>. As an example, after applying a  $\hat{R}_y(\pi/2)$  pulse on a spin state initialized in  $|\downarrow\rangle$ , the spin density matrix transforms according to

$$\begin{aligned}
& \mathcal{E}_{\text{depol}}^s \left( \hat{R}_y^i(\pi/2) \rho_{\downarrow} \hat{R}_y^{\dagger}(\pi/2) \right) \\
&= \mathcal{E}_{\text{depol}}^s \left( \mathcal{F}_{\frac{\pi}{2}} \hat{R}_y(\pi/2) \rho_{\downarrow} \hat{R}_y^{\dagger}(\pi/2) + (1 - \mathcal{F}_{\frac{\pi}{2}}) \rho_{-} \right) \\
&= (1 - p_{\pi/2}) \left( \mathcal{F}_{\frac{\pi}{2}} \hat{R}_y(\pi/2) \rho_{\downarrow} \hat{R}_y^{\dagger}(\pi/2) + (1 - \mathcal{F}_{\frac{\pi}{2}}) \rho_{-} \right) + \frac{p_{\pi/2}}{2} \mathcal{I} \\
&= \begin{bmatrix} \frac{1}{2} & (1 - p_{\pi/2})(\mathcal{F}_{\frac{\pi}{2}} - \frac{1}{2}) \\ (1 - p_{\pi/2})(\mathcal{F}_{\frac{\pi}{2}} - \frac{1}{2}) & \frac{1}{2} \end{bmatrix} \equiv \mathbf{E}_{\pi/2}, \tag{4.26}
\end{aligned}$$

where  $\rho_{\downarrow}$  is the initial spin density matrix and  $\rho_{-} \equiv |-\rangle_s \langle -|_s$ .  $\mathbf{E}_{\pi/2}$  is the output density matrix. In addition to the incoherent spin flip with a probability  $p_{\pi/2}$  we here include known imperfections of the rotation pulse  $\hat{R}_y^i(\pi/2)$ , which has a fidelity of  $\mathcal{F}_{\frac{\pi}{2}}$  to coherently rotate the spin to the superposition state  $|+\rangle_s$  and a probability of  $1 - \mathcal{F}_{\frac{\pi}{2}}$  to project onto  $|-\rangle_s$ . The fidelity of *coherent*  $\pi/2$ -spin rotation is determined by limitations of the two-photon Raman scheme, which is dominated by finite spin coherence time  $T_2^*$  and the power-dependent rate  $\gamma_r$  (Sec. 3.5):

$$\mathcal{F}_{\frac{\pi}{2}} \approx (1 - \gamma_r T_{\pi/2}) \times \mathcal{F}_{\frac{\pi}{2}}(T_2^*), \tag{4.27}$$

where the  $\pi/2$ -rotation fidelity under the Overhauser field noise  $\sigma_{\text{OH}} = \sqrt{2}/T_2^*$  is expressed by

$$\begin{aligned}
\mathcal{F}_{\frac{\pi}{2}}(T_2^*) &\equiv \left| \langle \downarrow | \hat{U}_{rot,ideal}^{\dagger} \hat{U}_{rot} | \downarrow \rangle \right|^2 \\
&= \int_{-\infty}^{\infty} \frac{\Delta_{\text{OH}}^2 + \Omega_r(\Omega_r + \sqrt{\Omega_r^2 + \Delta_{\text{OH}}^2})}{2(\Omega_r^2 + \Delta_{\text{OH}}^2)} N(0, \sigma_{\text{OH}}) d\Delta_{\text{OH}} \\
&\approx 1 - \frac{2}{\pi^2} \left( \frac{T_{\pi/2}}{T_2^*} \right)^2, \tag{4.28}
\end{aligned}$$

<sup>2</sup>In theory, the spin state should be described by the Boltzmann distribution instead of being a completely mixed state. For example, the hole spin has a thermal state  $0.52|\downarrow\rangle\langle\downarrow| + 0.48|\uparrow\rangle\langle\uparrow|$  at  $T = 4.2$  K,  $\Delta_h/2\pi = 7.3$  GHz and  $\mathbf{B}_x = 2$  T. However, this depends on the ground-state splitting of the spin qubit and temperature of the cryogenic setup, for simplicity we thus treat both occupations to be equal.

for a  $\pi/2$ -pulse duration of  $T_{\pi/2}$ . Eq. (4.28) is derived following Ref. [52] where  $\theta \equiv \frac{T_{\pi/2}}{2} \sqrt{\Omega_r^2 + \Delta_{\text{OH}}^2} = \frac{\pi}{4}$ , and  $\Omega_r$  is the spin Rabi frequency with  $\Omega_r T_{\pi/2} = \frac{\pi}{2}$ .  $\mathcal{F}_\pi$  can also be similarly derived. The probability of introducing a depolarizing error  $p_{\pi/2}$  during a  $\hat{R}_y(\pi/2)$  rotation is estimated by integrating the exponential distribution over the pulse duration for a given incoherent spin-flip rate  $\kappa$ :

$$p_{\pi/2} = \int_0^{T_{\pi/2}} \kappa e^{-\kappa t} dt = 1 - e^{-\kappa T_{\pi/2}}. \quad (4.29)$$

The exponential distribution describes the probability of a random spin-flip occurring in a certain time period, where the spin-flip event is assumed not to depend on how much time has passed in the protocol (i.e., it is memory-less). Similarly, for a  $\hat{R}_y(\pi)$  pulse applied on an arbitrary spin state  $\rho_s$ ,

$$\begin{aligned} & \mathcal{E}_{\text{depol}}^s \left( \hat{R}_y^i(\pi) \rho_s \hat{R}_y^{i\dagger}(\pi) \right) \\ &= (1 - p_\pi) \left( \mathcal{F}_\pi \hat{R}_y(\pi) \rho_s \hat{R}_y^\dagger(\pi) + (1 - \mathcal{F}_\pi) \rho_s \right) + \frac{p_\pi}{2} \mathcal{I} \\ &= \begin{bmatrix} (1 - p_\pi)[\mathcal{F}_\pi \rho_4 + (1 - \mathcal{F}_\pi) \rho_1] + \frac{p_\pi}{2} & (1 - p_\pi)[-\mathcal{F}_\pi \rho_3 + (1 - \mathcal{F}_\pi) \rho_2] \\ (1 - p_\pi)[-\mathcal{F}_\pi \rho_2 + (1 - \mathcal{F}_\pi) \rho_3] & (1 - p_\pi)[\mathcal{F}_\pi \rho_1 + (1 - \mathcal{F}_\pi) \rho_4] + \frac{p_\pi}{2} \end{bmatrix} \\ &\equiv \mathbf{E}_\pi, \end{aligned} \quad (4.30)$$

where the initial spin density matrix is

$$\rho_s \equiv \begin{bmatrix} \rho_1 & \rho_2 \\ \rho_3 & \rho_4 \end{bmatrix}, \quad (4.31)$$

and  $p_\pi$  is the probability of introducing the depolarizing error during a  $\hat{R}_y(\pi)$  rotation found similarly as in Eq. (4.29). To check the validity of this formalism, using Eq. (4.30) and  $\rho_1 = \rho_2 = \rho_3 = 0$ ,  $\rho_4 = 1$ , the total  $\pi$ -rotation pulse fidelity which includes the contribution from both coherent and incoherent spin-flip processes can be estimated to be

$$\begin{aligned} \mathcal{F}_{\pi, \text{total}} &= (1 - p_\pi) \mathcal{F}_\pi + \frac{p_\pi}{2} \\ &= (1 - p_\pi)(1 - \gamma_r T_\pi) \mathcal{F}_\pi(T_2^*) + \frac{p_\pi}{2} \\ &\approx 1 - \frac{1}{2}(\kappa + 2\gamma_r) T_\pi - \frac{2}{\pi^2} \left( \frac{T_\pi}{T_2^*} \right)^2. \end{aligned} \quad (4.32)$$

Using experimental values for the incoherent spin-flip rate  $\kappa = 0.0098 \text{ ns}^{-1}$  and  $\gamma_r = 0.0081 \text{ ns}^{-1}$  extracted in Sec. 3.5 with spin dephasing time  $T_2^* = 23.2 \text{ ns}$  [52], we estimate  $\mathcal{F}_{\pi, \text{total}} \approx 89.6\%$  for  $\Omega_r = 2\pi \times 69.4 \text{ MHz} = \pi/T_r$ , which is indeed consistent with the measured value of  $(88.1 \pm 3.8)\%$ . Now we again consider the evolution of the spin-photon system during the entangling gate to study propagation of the spin-flip error.

The protocol begins by preparing a time-bin photonic qubit  $\rho_p$  and a spin state in  $\rho_s$ :

$$\begin{aligned}
\rho_p \otimes \rho_s &= \begin{bmatrix} |\alpha|^2 & \alpha^* \beta \\ \alpha \beta^* & |\beta|^2 \end{bmatrix} \otimes \begin{bmatrix} 0 & 0 \\ 0 & 1 \end{bmatrix} \\
&\xrightarrow{\hat{R}_y(\pi/2)} (\mathcal{I} \otimes \mathcal{E}_{\text{depol}}^s)(\rho_p \otimes \rho_s) \\
&= \begin{bmatrix} |\alpha|^2 \mathbf{E}_{\pi/2} & \alpha^* \beta \mathbf{E}_{\pi/2} \\ \alpha \beta^* \mathbf{E}_{\pi/2} & |\beta|^2 \mathbf{E}_{\pi/2} \end{bmatrix} \equiv \begin{bmatrix} |\alpha|^2 \begin{bmatrix} E_{\pi/2}^1 & E_{\pi/2}^2 \\ E_{\pi/2}^3 & E_{\pi/2}^4 \end{bmatrix} & \alpha^* \beta \begin{bmatrix} E_{\pi/2}^1 & E_{\pi/2}^2 \\ E_{\pi/2}^3 & E_{\pi/2}^4 \end{bmatrix} \\ \alpha \beta^* \begin{bmatrix} E_{\pi/2}^1 & E_{\pi/2}^2 \\ E_{\pi/2}^3 & E_{\pi/2}^4 \end{bmatrix} & |\beta|^2 \begin{bmatrix} E_{\pi/2}^1 & E_{\pi/2}^2 \\ E_{\pi/2}^3 & E_{\pi/2}^4 \end{bmatrix} \end{bmatrix} \\
&\xrightarrow{\hat{S}_e} \begin{bmatrix} |\alpha|^2 \begin{bmatrix} |r_1^e|^2 E_{\pi/2}^1 & r_1^{e*} \hat{r}_1^e E_{\pi/2}^2 \\ r_1^e \hat{r}_1^{e*} E_{\pi/2}^3 & |\hat{r}_1^e|^2 E_{\pi/2}^4 \end{bmatrix} & \alpha^* \beta \begin{bmatrix} r_1^{e*} E_{\pi/2}^1 & r_1^{e*} E_{\pi/2}^2 \\ \hat{r}_1^{e*} E_{\pi/2}^3 & \hat{r}_1^{e*} E_{\pi/2}^4 \end{bmatrix} \\ \alpha \beta^* \begin{bmatrix} r_1^e E_{\pi/2}^1 & \hat{r}_1^e E_{\pi/2}^2 \\ r_1^e E_{\pi/2}^3 & \hat{r}_1^e E_{\pi/2}^4 \end{bmatrix} & |\beta|^2 \begin{bmatrix} E_{\pi/2}^1 & E_{\pi/2}^2 \\ E_{\pi/2}^3 & E_{\pi/2}^4 \end{bmatrix} \end{bmatrix} \\
&\equiv \begin{bmatrix} |\alpha|^2 \begin{bmatrix} \rho_1^1 & \rho_1^2 \\ \rho_1^3 & \rho_1^4 \end{bmatrix} & \alpha^* \beta \begin{bmatrix} \rho_2^1 & \rho_2^2 \\ \rho_2^3 & \rho_2^4 \end{bmatrix} \\ \alpha \beta^* \begin{bmatrix} \rho_3^1 & \rho_3^2 \\ \rho_3^3 & \rho_3^4 \end{bmatrix} & |\beta|^2 \begin{bmatrix} \rho_4^1 & \rho_4^2 \\ \rho_4^3 & \rho_4^4 \end{bmatrix} \end{bmatrix} \\
&\xrightarrow{\hat{R}_y(\pi)} \begin{bmatrix} |\alpha|^2 \begin{bmatrix} E_{\pi}^1(\rho_1^4, \rho_1^1) & E_{\pi}^2(\rho_1^3, \rho_1^2) \\ E_{\pi}^3(\rho_1^2, \rho_1^3) & E_{\pi}^4(\rho_1^1, \rho_1^4) \end{bmatrix} & \alpha^* \beta \begin{bmatrix} E_{\pi}^1(\rho_2^4, \rho_2^1) & E_{\pi}^2(\rho_2^3, \rho_2^2) \\ E_{\pi}^3(\rho_2^2, \rho_2^3) & E_{\pi}^4(\rho_2^1, \rho_2^4) \end{bmatrix} \\ \alpha \beta^* \begin{bmatrix} E_{\pi}^1(\rho_3^4, \rho_3^1) & E_{\pi}^2(\rho_3^3, \rho_3^2) \\ E_{\pi}^3(\rho_3^2, \rho_3^3) & E_{\pi}^4(\rho_3^1, \rho_3^4) \end{bmatrix} & |\beta|^2 \begin{bmatrix} E_{\pi}^1(\rho_4^4, \rho_4^1) & E_{\pi}^2(\rho_4^3, \rho_4^2) \\ E_{\pi}^3(\rho_4^2, \rho_4^3) & E_{\pi}^4(\rho_4^1, \rho_4^4) \end{bmatrix} \end{bmatrix} \\
&\xrightarrow{\hat{S}_l} \begin{bmatrix} |\alpha|^2 \begin{bmatrix} \boxed{E_{\pi}^1(\rho_1^4, \rho_1^1)} & E_{\pi}^2(\rho_1^3, \rho_1^2) \\ E_{\pi}^3(\rho_1^2, \rho_1^3) & \boxed{E_{\pi}^4(\rho_1^1, \rho_1^4)} \end{bmatrix} & \alpha^* \beta \begin{bmatrix} r_1^l E_{\pi}^1(\rho_2^4, \rho_2^1) & \hat{r}_1^l E_{\pi}^2(\rho_2^3, \rho_2^2) \\ \boxed{r_1^l E_{\pi}^3(\rho_2^2, \rho_2^3)} & \hat{r}_1^l E_{\pi}^4(\rho_2^1, \rho_2^4) \end{bmatrix} \\ \alpha \beta^* \begin{bmatrix} r_1^{l*} E_{\pi}^1(\rho_3^4, \rho_3^1) & \boxed{r_1^{l*} E_{\pi}^2(\rho_3^3, \rho_3^2)} \\ \hat{r}_1^{l*} E_{\pi}^3(\rho_3^2, \rho_3^3) & \hat{r}_1^{l*} E_{\pi}^4(\rho_3^1, \rho_3^4) \end{bmatrix} & |\beta|^2 \begin{bmatrix} |r_1^l|^2 E_{\pi}^1(\rho_4^4, \rho_4^1) & \hat{r}_1^l r_1^{l*} E_{\pi}^2(\rho_4^3, \rho_4^2) \\ \boxed{\hat{r}_1^{l*} r_1^l E_{\pi}^3(\rho_4^2, \rho_4^3)} & \boxed{|\hat{r}_1^l|^2 E_{\pi}^4(\rho_4^1, \rho_4^4)} \end{bmatrix} \end{bmatrix} \\
&\equiv \rho_{\text{out}}. \tag{4.33}
\end{aligned}$$

Here the basis states spanning  $\rho_p \otimes \rho_s$  are  $\{|e \uparrow\rangle_r, |e \downarrow\rangle_r, |l \uparrow\rangle_r, |l \downarrow\rangle_r\}$  which govern only the Hilbert space formed by the reflected photon and spin, as events in which photons are transmitted do not contribute to the fidelity. Note that when applying the  $\hat{R}_y(\pi)$  pulse, we apply Eq. (4.30) to each of the four  $2 \times 2$  blocks (which consists of spin density matrix elements  $\rho_j^i$ ). For instance, the inner product  $|e \downarrow\rangle_r \langle e \uparrow|_r$  has a matrix element  $E_{\pi}^2(\rho_1^3, \rho_1^2)$ , which corresponds to the (1, 2)-th entry of the matrix  $\mathbf{E}_{\pi}$  with  $\rho_3 \rightarrow \rho_1^3$  and  $\rho_2 \rightarrow \rho_1^2$ . Only the boxed terms at the end of Eq. (4.33) contribute to the fidelity. As an example we now evaluate the matrix element of the inner product  $|e \uparrow\rangle_r \langle e \uparrow|_r$ :

$$\begin{aligned}
|\alpha|^2 E_{\pi}^1(\rho_1^4, \rho_1^1) &= |\alpha|^2 \left[ (1 - p_{\pi}) [\mathcal{F}_{\pi} \rho_1^4 + (1 - \mathcal{F}_{\pi}) \rho_1^1] + \frac{p_{\pi}}{2} \right] \\
&= |\alpha|^2 \left[ \frac{(1 - p_{\pi})}{2} [\mathcal{F}_{\pi} |r_1^e|^2 + (1 - \mathcal{F}_{\pi}) |r_1^e|^2] + \frac{p_{\pi}}{2} \right]. \tag{4.34}
\end{aligned}$$

For an ideal state of  $|\psi_{\text{ideal}}\rangle = (\alpha|e \downarrow\rangle_r - \beta|l \uparrow\rangle_r)$  where  $|\alpha| = |\beta| = 1/\sqrt{2}$ , with  $\rho_{\text{out}}$  given by Eq. (4.33), the entanglement fidelity is found to be

$$\begin{aligned} \mathcal{F}_r^{\text{theory}} &\equiv \frac{\langle \psi_{\text{ideal}} | \rho_{\text{out}} | \psi_{\text{ideal}} \rangle}{\text{Tr}(|\psi_{\text{out}}\rangle\langle\psi_{\text{out}}|)} \\ &= \frac{|\alpha|^4 E_\pi^4(\rho_1^1, \rho_1^4) + |\beta|^4 |r_1^l|^2 E_\pi^1(\rho_4^4, \rho_4^1) - |\alpha^* \beta|^2 r_1^l E_\pi^3(\rho_2^2, \rho_2^3) - |\alpha \beta^*|^2 r_1^{l*} E_\pi^2(\rho_3^3, \rho_3^2)}{|\alpha|^2 E_\pi^4(\rho_1^1, \rho_1^4) + |\beta|^2 |r_1^l|^2 E_\pi^1(\rho_4^4, \rho_4^1) + |\alpha|^2 E_\pi^1(\rho_1^4, \rho_1^1) + |\beta|^2 |r_1^l|^2 E_\pi^4(\rho_4^1, \rho_4^4)} \\ &\stackrel{r_1^l = -1}{\underset{\hat{r}_1 = 0}{\approx}} 1 - \frac{5\pi}{4} \left( \frac{\kappa + \gamma_r}{\Omega_r} \right) - \frac{3}{2} \frac{1}{\Omega_r^2 T_2^{*2}}, \end{aligned} \quad (4.35)$$

for  $\kappa \ll \Omega_r$  where  $\Omega_r T_\pi = \pi$  for a  $\pi$ -pulse. The final expression is found by perturbative expansion for each error to the first order. Using the relevant parameters:  $T_\pi = 7$  ns,  $T_{\pi/2} = 3.5$  ns,  $\kappa = 0.0098$  ns<sup>-1</sup>,  $\gamma_r = 0.0081$  ns<sup>-1</sup> and  $T_2^* = 23.2$  ns, we find  $\mathcal{F}_\kappa^{\text{theory}} = 84.6\%$  from the analytical form in Eq. (4.35) taking  $r_1 = -1$  and  $\hat{r}_1 = 0$ .

### 4.3.6 Spin Readout Error

The non-ideal spin readout by optical pumping is also considered as one of the prevailing sources of imperfections as it directly influences the spin readout basis. Due to finite optical cyclicity, optically pumping of the main transition can unfavourably result in the opposite outcome by flipping the spin state:

$$\rho_{\text{out}} \xrightarrow{\text{Spin readout}} \mathcal{F}_R \rho_{\text{out}} + (1 - \mathcal{F}_R) \hat{\sigma}_x(\pi) \rho_{\text{out}} \hat{\sigma}_x^\dagger(\pi). \quad (4.36)$$

where the readout fidelity is estimated to be  $\mathcal{F}_R = 96.6\%$  [52]. Using Eqs. (4.33) and (4.36), the resulting entanglement fidelity under both rotation error and imperfect spin readout is  $\mathcal{F}_{\kappa, R}^{\text{theory}} = (81.8 \pm 0.6)\%$ . From here it is apparent that the dominant infidelity results from incoherent spin flips and finite  $\gamma_r$  (15.4%).

### 4.3.7 Driving-induced Dephasing

Another source of error emerges from finite multi-photon component of the input pulse, which destroys the QD ground-state spin coherence through successions of photon-scattering events within the pulse. The driving-induced dephasing probability  $p_d$  is related to the success probability of scattering  $P_{\omega_1} + P_{\omega_2}$  and the mean photon number in the driving pulse  $\bar{n}$  via  $p_d = 1 - \exp[-\bar{n}(P_{\omega_1} + P_{\omega_2})]$  [138]. This can be understood as the probability of  $\bar{n}$  disjoint successful scattering events. To describe the effect of this error, we adopt a phase-damping model  $\mathcal{E}_d$  where

$$\begin{aligned} \mathcal{E}_d \left( \text{Tr}_p \left( \hat{S}(\rho_p \otimes \rho_s) \right) \right) &\equiv (1 - \frac{p_d}{2}) \text{Tr}_p \left( \hat{S}(\rho_p \otimes \rho_s) \right) + \frac{p_d}{2} \hat{\sigma}_z \text{Tr}_p \left( \hat{S}(\rho_p \otimes \rho_s) \right) \hat{\sigma}_z^\dagger \\ &= \begin{bmatrix} s_{11} & (1 - p_d) s_{12} \\ (1 - p_d) s_{21} & s_{22} \end{bmatrix}. \end{aligned} \quad (4.37)$$

Here  $\hat{S}$  is the scattering matrix acting on the spin-photon density matrix and  $s_{ij}$  corresponds to the  $(i, j)$ -th entry of the reduced spin density matrix  $\text{Tr}_p \left( \hat{S}(\rho_p \otimes \rho_s) \right)$ .  $\mathcal{E}_d$

introduces dephasing only to the QD spin state thus the photonic component is traced out before applying the phase-damping channel.

Now we follow the same approach in Sec. 4.3.5 and consider propagation of the dephasing error in the protocol:

$$\begin{aligned}
& \rho_p \otimes \rho_s \\
& \xrightarrow{\hat{R}_y(\frac{\pi}{2})} \begin{bmatrix} |\alpha|^2 & \alpha^* \beta \\ \alpha \beta^* & |\beta|^2 \end{bmatrix} \otimes \frac{1}{2} \begin{bmatrix} 1 & 1 \\ 1 & 1 \end{bmatrix} \\
& \xrightarrow{\mathcal{E}_d(\hat{S}_e)} \frac{1}{2} \begin{bmatrix} |\alpha|^2 \mathcal{E}_d \left( \begin{bmatrix} |r_1^e|^2 & r_1^{e*} \hat{r}_1^e \\ r_1^e \hat{r}_1^{e*} & |\hat{r}_1^e|^2 \end{bmatrix} \right) & \alpha^* \beta \mathcal{E}_d \left( \begin{bmatrix} r_1^{e*} & r_1^{e*} \\ \hat{r}_1^{e*} & \hat{r}_1^{e*} \end{bmatrix} \right) \\ \alpha \beta^* \mathcal{E}_d \left( \begin{bmatrix} r_1^e & \hat{r}_1^e \\ r_1^e & \hat{r}_1^e \end{bmatrix} \right) & |\beta|^2 \mathcal{E}_d \left( \begin{bmatrix} 1 & 1 \\ 1 & 1 \end{bmatrix} \right) \end{bmatrix} \\
& \xrightarrow{\hat{R}_y(\pi)} \frac{1}{2} \begin{bmatrix} |\alpha|^2 \begin{bmatrix} |\hat{r}_1^e|^2 & -(1-p_d)r_1^e \hat{r}_1^{e*} \\ -(1-p_d)r_1^{e*} \hat{r}_1^e & |r_1^e|^2 \end{bmatrix} & \alpha^* \beta \begin{bmatrix} \hat{r}_1^{e*} & -(1-p_d)\hat{r}_1^{e*} \\ -(1-p_d)r_1^{e*} & r_1^{e*} \end{bmatrix} \\ \alpha \beta^* \begin{bmatrix} \hat{r}_1^e & -(1-p_d)r_1^e \\ -(1-p_d)\hat{r}_1^e & r_1^e \end{bmatrix} & |\beta|^2 \begin{bmatrix} 1 & -(1-p_d) \\ -(1-p_d) & 1 \end{bmatrix} \end{bmatrix} \\
& \xrightarrow{\mathcal{E}_d(\hat{S}_l)} \frac{1}{2} \begin{bmatrix} |\alpha|^2 \begin{bmatrix} \boxed{|\hat{r}_1^e|^2} & -(1-p_d)^2 r_1^e \hat{r}_1^{e*} \\ -(1-p_d)^2 r_1^{e*} \hat{r}_1^e & \boxed{|r_1^e|^2} \end{bmatrix} & \alpha^* \beta \begin{bmatrix} r_1^l \hat{r}_1^{e*} & -(1-p_d)^2 \hat{r}_1^l \hat{r}_1^{e*} \\ -(1-p_d)^2 r_1^l r_1^{e*} & \hat{r}_1^l r_1^{e*} \end{bmatrix} \\ \alpha \beta^* \begin{bmatrix} r_1^{l*} \hat{r}_1^e & \boxed{-(1-p_d)^2 r_1^{l*} r_1^e} \\ -(1-p_d)^2 \hat{r}_1^{l*} \hat{r}_1^e & \hat{r}_1^{l*} r_1^e \end{bmatrix} & |\beta|^2 \begin{bmatrix} \boxed{|r_1^l|^2} & -(1-p_d)^2 r_1^{l*} \hat{r}_1^l \\ -(1-p_d)^2 r_1^l \hat{r}_1^{l*} & \boxed{|\hat{r}_1^l|^2} \end{bmatrix} \end{bmatrix}. \tag{4.38}
\end{aligned}$$

Likewise, only the boxed matrix elements overlap with the ideal state  $|\psi_{\text{ideal}}\rangle = (\alpha|e \downarrow\rangle_r - \beta|l \uparrow\rangle_r)$  with  $|\alpha| = |\beta| = 1/\sqrt{2}$ , the entanglement fidelity under driving-induced dephasing is then found to be

$$\begin{aligned}
\mathcal{F}_r^{\text{theory}} & \equiv \frac{\langle \psi_{\text{ideal}} | \rho_{\text{out}} | \psi_{\text{ideal}} \rangle}{\text{Tr}(|\psi_{\text{out}}\rangle \langle \psi_{\text{out}}|)} = \frac{\frac{1}{2} |r_1|^2 [1 + e^{-2\bar{n}(P_{\omega_1} + P_{\omega_2})}]}{|r_1|^2 + |\hat{r}_1|^2} \\
& \xrightarrow{\substack{r_1 = -1 \\ \hat{r}_1 = 0}} \frac{1}{2} [1 + e^{-2\bar{n}(P_{\omega_1} + P_{\omega_2})}] \\
& \approx 1 - \bar{n}(P_{\omega_1} + P_{\omega_2}), \tag{4.39}
\end{aligned}$$

where the average probability of successful scattering is given by Eq. (4.4):

$$P_{\omega_1} + P_{\omega_2} = \int_{-\infty}^{\infty} \left[ |r_1(\omega)|^2 + |t_1(\omega)|^2 + |r_2(\omega)|^2 + |t_2(\omega)|^2 \right] |\Phi_1(\omega)|^2 d\omega. \tag{4.40}$$

To estimate the infidelity in the experiment, we first extract the average number of photons in the pulse  $\bar{n} \leq (0.089 \pm 0.012)$  (Sec. 3.4.4). Given that optical cyclicity  $C = 14.7$ , pulse bandwidth  $\sigma_o = \sqrt{2 \ln 2} / T_{\text{FWHM}} \approx 0.589 \text{ ns}^{-1}$ , spectral diffusion fluctuation  $\sigma_e = 2\pi \times (332 \pm 15) \text{ MHz}$  and waveguide coupling efficiency  $\beta \geq 0.865 \pm 0.059$  (Sec. 3.4.2), the experimental infidelity is estimated using the exact form in Eq. (4.39) to be  $1 - \mathcal{F}_{\bar{n}}^{\text{theory}} \leq (7.2 \pm 0.7)\%$ .

## 4.4 Comparison between Theoretical and Experimental Fidelity Estimates

Assuming perfect manipulation of the hole spin state, the fidelity of the entangling gate is expressed by:

$$\mathcal{F}_r^{\text{theory}} = 1 - \frac{\gamma_d}{\Gamma} - \frac{\Gamma^2}{4\Delta_h^2} \left( \frac{C}{C+1} \beta \right)^2, \quad (4.41)$$

which is estimated to be  $(96.2 \pm 0.1)\%$  with  $\Gamma = 2.48 \text{ ns}^{-1}$ ,  $\Delta_h = 2\pi \times 7.3 \text{ GHz}$  [20],  $C = 14.7$ ,  $\beta = (0.865 \pm 0.059)$  and  $\gamma_d = (0.099 \pm 0.004) \text{ ns}^{-1}$  (Sec. 3.4.2). This predominantly reflects the infidelity from phonon-induced pure dephasing  $1 - \mathcal{F}_{\gamma_d}^{\text{theory}}$  as the off-resonant reflection error  $\Gamma^2/\Delta_h^2$  is comparably small. Together with the incoherent spin rotations, driving-induced dephasing and the readout errors discussed above, we estimate a lower bound on the overall entanglement fidelity<sup>3</sup>  $\mathcal{F}_{\text{total}}^{\text{theory}}$  of

$$\mathcal{F}_{\text{total}}^{\text{theory}} \approx \mathcal{F}_{\gamma_d}^{\text{theory}} \times \mathcal{F}_{\kappa, R}^{\text{theory}} \times \mathcal{F}_{\bar{n}}^{\text{theory}} \approx (73.0 \pm 0.6)\%, \quad (4.42)$$

which generally agrees with the experimentally obtained value  $(74.3 \pm 2.3)\%$  including error margins. Here a lower fidelity bound is obtained as the waveguide-coupling efficiency  $\beta$  could be underestimated (Sec. 3.4.2) which leads to overestimating  $\bar{n}$  and the corresponding infidelity  $1 - \mathcal{F}_{\bar{n}}^{\text{theory}}$ . Imperfect spin initialization (1.4%) [18] is not considered in the theory but is expected to have negligible infidelity ( $< 1\%$ ).

<sup>3</sup>Here we multiply the fidelities of individual errors instead of adding them as in Sec. 2.3, to include cross-error terms that contribute to the infidelity.



# Chapter 5

## Theoretical Model of Photon Visibility

In Sec. 3.4.5, we measured the photon visibility, by interfering two photon pulses resonantly scattered from a quantum dot (QD). We observed that when the average number of photons in the incident pulse increases, the interferometric visibility reduces linearly. It turns out that explaining this phenomenon is not a trivial task: As the pulse carries more photons, the QD scattering dynamics becomes drastically different due to its nonlinear response to multi-photon scattering processes, so it is necessary to consider the effect of these multi-photon terms when modelling the photon visibility.

In this chapter, we develop a theoretical model of the photon visibility by considering nonlinear dynamics up to two-photon scattering processes. Interestingly, the connection between photon visibility and multi-photon components in the input pulse is reminiscent of the close relation between Hong-Ou-Mandel visibility and the zero-delay second-order correlation function  $g^{(2)}(0)$ . As we shall explain in later parts of the chapter, this close resemblance has an useful application in accurately determining the phonon-induced pure dephasing rate.

The project idea is conceived by Anders Søndberg Sørensen. The simulation performed in this work is done by Oliver August Dall’Alba Sandberg. The theory<sup>1</sup> is completed with assistance from Björn Schränski and Yu-Xiang Zhang.

---

<sup>1</sup>Theoretical derivations and simulation files can be found in the Mathematica notebook “AnalyticalPhotonVisibility.nb”, and Jupyter script “PhotonVisibility\_TheoryVsSimulationVsData\_Final.ipynb” respectively in Ref. [26].

## 5.1 Input and Output states

We first recapitulate the context of the measurement conducted in Sec. 3.4.5. In the experiment, a time-bin encoded qubit is scattered by a quantum-dot (QD) spin embedded in a two-sided photonic-crystal waveguide, and is subsequently measured by an unbalanced Mach-Zehnder interferometer with equal time delay as the qubit. The intensity contrast between two detectors, or the interferometric visibility is a measure of the temporal overlap between the time-bins of the scattered pulses.

Since the experiment involves two separate scattering events with a coherent state, the input photonic state  $|\text{in}\rangle_{\text{p}}$  can be expressed as the tensor product of two coherent state in each time-bin. To elucidate the effect of two-photon nonlinearity on the visibility in the low power regime, it is adequate to truncate the coherent state up to the two-photon component:

$$\begin{aligned} |\text{in}\rangle_{\text{p}} &= \frac{1}{\sqrt{2}} \left( |\alpha\rangle_{\text{e}} |\alpha\rangle_{\text{l}} \right) \\ &\approx \frac{1}{\sqrt{2}} \left[ \left( |0\rangle_{\text{e}} + \alpha |1\rangle_{\text{e}} + \frac{\alpha^2}{\sqrt{2}} |2\rangle_{\text{e}} \right) \left( |0\rangle_{\text{l}} + \alpha |1\rangle_{\text{l}} + \frac{\alpha^2}{\sqrt{2}} |2\rangle_{\text{l}} \right) \right] \\ &= \frac{1}{\sqrt{2}} |00\rangle_{\text{l,e}} + \frac{\alpha}{\sqrt{2}} \left( |10\rangle_{\text{l,e}} + |01\rangle_{\text{l,e}} \right) + \alpha^2 \left( \frac{|20\rangle_{\text{l,e}}}{2} + \frac{|11\rangle_{\text{l,e}}}{\sqrt{2}} + \frac{|02\rangle_{\text{l,e}}}{2} \right). \end{aligned} \quad (5.1)$$

Here  $|n\rangle_i$  is the  $n$ -photon Fock state in the  $i \in \{\text{e}, \text{l}\}$  time-bin. Similar to the time-bin qubit considered in Section. 3.4.5, the one-photon component in Eq. (5.1) is a superposition of Fock states in the time-bin basis. The output state is obtained by applying the scattering matrix  $\mathcal{S}$  on the initial spin-photon system, where the QD spin is prepared in  $|\uparrow\rangle$  state, resulting in

$$\begin{aligned} |\text{out}\rangle &= \frac{1}{\sqrt{2}} \mathcal{S}(|00\rangle_{\text{l,e}} |\uparrow\rangle) + \frac{\alpha}{\sqrt{2}} \left[ \mathcal{S}(|10\rangle_{\text{l,e}} |\uparrow\rangle) + \mathcal{S}(|01\rangle_{\text{l,e}} |\uparrow\rangle) \right] \\ &\quad + \alpha^2 \left[ \frac{\mathcal{S}(|20\rangle_{\text{l,e}} |\uparrow\rangle)}{2} + \frac{\mathcal{S}(|11\rangle_{\text{l,e}} |\uparrow\rangle)}{\sqrt{2}} + \frac{\mathcal{S}(|02\rangle_{\text{l,e}} |\uparrow\rangle)}{2} \right] \\ &= |\text{out}\rangle_{\text{p}} \otimes |\uparrow\rangle. \end{aligned} \quad (5.2)$$

The zero-photon term  $\mathcal{S}(|00\rangle_{\text{l,e}} |\uparrow\rangle)$  vanishes as scattering does not occur.  $\mathcal{S}(|01\rangle_{\text{l,e}} |\uparrow\rangle)$  and  $\mathcal{S}(|10\rangle_{\text{l,e}} |\uparrow\rangle)$  contain the scattering dynamics of a photon in a time-bin with the QD. Due to finite cyclicity of the optical transition, the scattering process in general leads to a mixed state between photons and different spin states (Eq. (4.1)); however experimentally we do not detect events in which Raman spin-flip occurs, as narrowband etalon filters are used to filter out photons from the off-resonant transitions. The cyclicity error thus enters as a prefactor to the waveguide coupling efficiency  $\beta$ , since the off-resonant scattered photons are effectively lost. The output state can therefore be described as a separable state as in Eq. (5.2).

The two-photon scattering results in either both photons being reflected (with operator  $S^{r,r}$ ), or one reflected and one transmitted ( $S^{r,t}$ ). The two-photon transmission ( $S^{t,t}$ ) is not detected.  $\mathcal{S}(|11\rangle_{\text{l,e}} |\uparrow\rangle)$  corresponds to consecutive single-photon scattering events in each time-bin. These cases are summarized in Fig. 5.1, which contain all possible Fock states in the scattering matrix of a two-level system in two-sided waveguides.

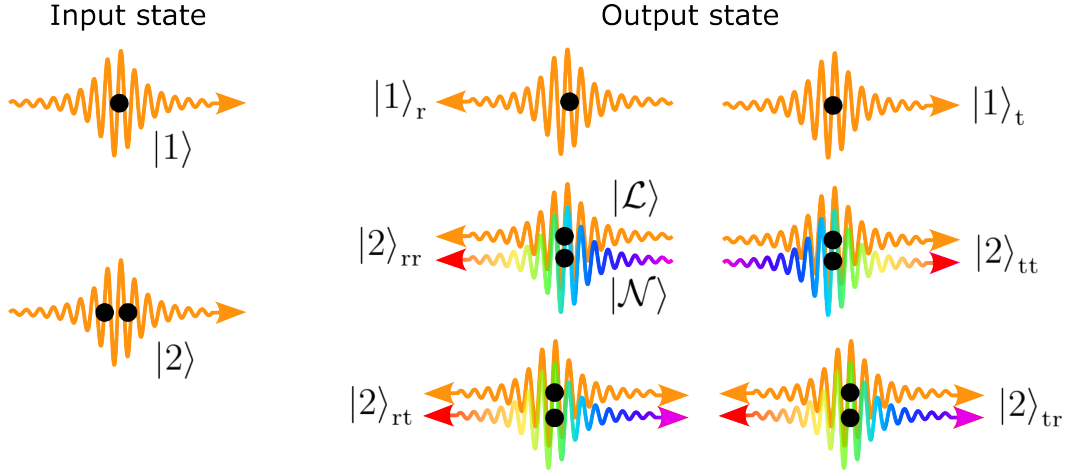


Figure 5.1: Input and output states up to two-photon scattering occurred at each time-bin. Black dots are photons. The subscript r (t) indicates the photon state is reflected (transmitted). Each two-photon state can be written as a superposition of linear  $|\mathcal{L}\rangle$  (from elastic scattering) and nonlinear (inelastic)  $|\mathcal{N}\rangle$  terms (Eq. (B.2)).  $|2\rangle_{rt}$  is a two-photon Fock state where one photon is reflected while another one is transmitted.

The scattering terms in Eq. (5.2) are given by

$$\begin{aligned}
\mathcal{S}(|10\rangle_{1,e}|\uparrow\rangle) &= r_l|10\rangle_{1,e}^r \otimes |00\rangle_{1,e}^t \otimes |\uparrow\rangle + t_l|00\rangle_{1,e}^r \otimes |10\rangle_{1,e}^t \otimes |\uparrow\rangle; \\
\mathcal{S}(|01\rangle_{1,e}|\uparrow\rangle) &= r_e|01\rangle_{1,e}^r \otimes |00\rangle_{1,e}^t \otimes |\uparrow\rangle + t_e|00\rangle_{1,e}^r \otimes |01\rangle_{1,e}^t \otimes |\uparrow\rangle; \\
\mathcal{S}(|20\rangle_{1,e}|\uparrow\rangle) &= \left(\frac{1}{\sqrt{2}}S_l^{r,t}|10\rangle_{1,e}^r \otimes |10\rangle_{1,e}^t + \frac{1}{\sqrt{2}}S_l^{t,r}|10\rangle_{1,e}^r \otimes |10\rangle_{1,e}^t \right. \\
&\quad \left. + S_l^{t,t}|00\rangle_{1,e}^r \otimes |20\rangle_{1,e}^t + S_l^{r,r}|20\rangle_{1,e}^r \otimes |00\rangle_{1,e}^t\right) \otimes |\uparrow\rangle; \\
\mathcal{S}(|02\rangle_{1,e}|\uparrow\rangle) &= \left(\frac{1}{\sqrt{2}}S_e^{r,t}|01\rangle_{1,e}^r \otimes |01\rangle_{1,e}^t + \frac{1}{\sqrt{2}}S_e^{t,r}|01\rangle_{1,e}^r \otimes |01\rangle_{1,e}^t \right. \\
&\quad \left. + S_e^{t,t}|00\rangle_{1,e}^r \otimes |02\rangle_{1,e}^t + S_e^{r,r}|02\rangle_{1,e}^r \otimes |00\rangle_{1,e}^t\right) \otimes |\uparrow\rangle; \\
\mathcal{S}(|11\rangle_{1,e}|\uparrow\rangle) &= \mathcal{S}_l(|1\rangle_1 \otimes \mathcal{S}_e(|1\rangle_e|\uparrow\rangle)) \\
&= (r_e r_l |11\rangle_{1,e}^r \otimes |00\rangle_{1,e}^t + t_l r_e |01\rangle_{1,e}^r \otimes |10\rangle_{1,e}^t \\
&\quad + r_l t_e |10\rangle_{1,e}^r \otimes |01\rangle_{1,e}^t) \otimes |\uparrow\rangle + t_l t_e |00\rangle_{1,e}^r \otimes |11\rangle_{1,e}^t \otimes |\uparrow\rangle,
\end{aligned}$$

where special care has been taken to ensure each of the above terms is normalized (See Appendix B, where the integral of each scattering operator is given). Note that  $\mathcal{S}(|11\rangle_{1,e}|\uparrow\rangle)$  will interfere with the two-mode states (i.e.,  $\mathcal{S}(|20\rangle_{1,e}|\uparrow\rangle)$ ) as the time-bin interferometer redistributes the photon number between two modes. Before we evaluate the visibility, it is important to verify that the total photon number is conserved after scattering because of energy conservation. This is confirmed by applying the number operator on the input and output states, respectively. As a quick example,  $\text{Tr}\left[a_e(\text{in})_p \langle \text{in} |_p a_e^\dagger + a_l(\text{in})_p \langle \text{in} |_p a_l^\dagger\right] = |\alpha|^2 + 2|\alpha|^4$  is the photon number in the input state<sup>2</sup>.

<sup>2</sup>A series of codes has been developed to apply raising and lowering operators (and inner products) on the output Fock state of each time-bin mode using the Mathematica notebook “AnalyticalPhoton-Visibility.nb” in Ref. [26].

## 5.2 Reflection and Transmission Visibility

Now, we are in the position to express the photon visibility in terms of the output state. Since the photon visibility is defined to be the maximum contrast between the two detectors at the middle time-bin, we are interested in the intensity of each detector D2(D1) from recording either the reflected ( $r$ ) or transmitted ( $t$ ) photons (Sec. 3.4.5):

$$I_{D2/D1}^j = \int \text{Tr} \left[ \frac{(\hat{a}_e^j \pm e^{i\theta_p} \hat{a}_l^j)}{\sqrt{2}} \left( |\text{out}\rangle_p \langle \text{out}|_p \right) \frac{(\hat{a}_e^{j\dagger} \pm e^{-i\theta_p} \hat{a}_l^{j\dagger})}{\sqrt{2}} \right] dt, \quad (5.3)$$

where the output photon state  $|\text{out}\rangle_p$  is projected onto the superposition state  $\hat{a}_e^j(t) \pm e^{i\theta_p} \hat{a}_l^j(t)$ ,  $j \in \{r, t\}$  which is equivalent to adding a phase shifter on the long path of the excitation interferometer and interfering both bins. Setting  $\theta_p = 0$  implies projecting the output state into the  $|\pm X\rangle_p \langle \pm X|_p$  bases. The projected state is then traced out in both the early and late time bases. The photon visibility is the normalized contrast of the middle-bin intensity:

$$V_p^j \equiv \frac{I_{D2}^j - I_{D1}^j}{I_{D2}^j + I_{D1}^j} = \frac{\int \text{Tr} \left[ \hat{a}_e^j |\text{out}\rangle_p \langle \text{out}|_p \hat{a}_l^{j\dagger} + \hat{a}_l^j |\text{out}\rangle_p \langle \text{out}|_p \hat{a}_e^{j\dagger} \right] dt}{\int \text{Tr} \left[ \hat{a}_e^j |\text{out}\rangle_p \langle \text{out}|_p \hat{a}_e^{j\dagger} + \hat{a}_l^j |\text{out}\rangle_p \langle \text{out}|_p \hat{a}_l^{j\dagger} \right] dt}. \quad (5.4)$$

The numerator reduces the photon number in early and late time-bins by one, and picks out the states in which both their reflected and transmitted modes overlap. For instance, for reflection  $j = r$ , the non-vanishing terms come from the following pairs of states:

$$\begin{aligned} \textcircled{1} &= \{ \quad r_l |10\rangle_{l,e}^r \otimes |00\rangle_{l,e}^t \quad , \quad r_e |01\rangle_{l,e}^r \otimes |00\rangle_{l,e}^t \quad \} \\ \textcircled{2} &= \{ \quad S_l^{r,r} |20\rangle_{l,e}^r \otimes |00\rangle_{l,e}^t \quad , \quad r_e r_l |11\rangle_{l,e}^r \otimes |00\rangle_{l,e}^t \quad \} \\ \textcircled{3} &= \{ \quad S_e^{r,r} |02\rangle_{l,e}^r \otimes |00\rangle_{l,e}^t \quad , \quad r_e r_l |11\rangle_{l,e}^r \otimes |00\rangle_{l,e}^t \quad \} \\ \textcircled{4} &= \{ \quad S_l^{r,t} |10\rangle_{l,e}^r \otimes |10\rangle_{l,e}^t \quad , \quad t_l r_e |01\rangle_{l,e}^r \otimes |10\rangle_{l,e}^t \quad \} \\ \textcircled{5} &= \{ \quad S_l^{t,r} |10\rangle_{l,e}^r \otimes |10\rangle_{l,e}^t \quad , \quad t_l r_e |01\rangle_{l,e}^r \otimes |10\rangle_{l,e}^t \quad \} \\ \textcircled{6} &= \{ \quad S_e^{r,t} |01\rangle_{l,e}^r \otimes |01\rangle_{l,e}^t \quad , \quad r_l t_e |10\rangle_{l,e}^r \otimes |01\rangle_{l,e}^t \quad \} \\ \textcircled{7} &= \{ \quad S_e^{t,r} |01\rangle_{l,e}^r \otimes |01\rangle_{l,e}^t \quad , \quad r_l t_e |10\rangle_{l,e}^r \otimes |01\rangle_{l,e}^t \quad \}, \end{aligned} \quad (5.5)$$

where  $\{A, B\} \equiv |A\rangle\langle B|$  and  $\{A\} \equiv |A\rangle\langle A|$ . For the denominator, the non-vanishing terms constitute the total intensity summed over the detectors:

$$\begin{aligned} \textcircled{a} &= \{ \quad r_l |10\rangle_{l,e}^r \otimes |00\rangle_{l,e}^t \quad \} & \textcircled{b} &= \{ \quad r_e |01\rangle_{l,e}^r \otimes |00\rangle_{l,e}^t \quad \} \\ \textcircled{c} &= \{ \quad S_l^{r,r} |20\rangle_{l,e}^r \otimes |00\rangle_{l,e}^t \quad \} & \textcircled{d} &= \{ \quad S_e^{r,r} |02\rangle_{l,e}^r \otimes |00\rangle_{l,e}^t \quad \} \\ \textcircled{e} &= \{ \quad S_l^{r,t} |10\rangle_{l,e}^r \otimes |10\rangle_{l,e}^t \quad \} & \textcircled{f} &= \{ \quad S_e^{t,r} |01\rangle_{l,e}^r \otimes |01\rangle_{l,e}^t \quad \} \\ \textcircled{g} &= \{ \quad S_l^{t,r} |10\rangle_{l,e}^r \otimes |10\rangle_{l,e}^t \quad \} & \textcircled{h} &= \{ \quad S_e^{r,t} |01\rangle_{l,e}^r \otimes |01\rangle_{l,e}^t \quad \} \\ \textcircled{i} &= \{ \quad S_l^{r,t} |10\rangle_{l,e}^r \otimes |10\rangle_{l,e}^t \quad , \quad S_l^{t,r} |10\rangle_{l,e}^r \otimes |10\rangle_{l,e}^t \quad \} \\ \textcircled{j} &= \{ \quad S_e^{r,t} |01\rangle_{l,e}^r \otimes |01\rangle_{l,e}^t \quad , \quad S_e^{t,r} |01\rangle_{l,e}^r \otimes |01\rangle_{l,e}^t \quad \} \\ \textcircled{k} &= \{ \quad r_l r_e |11\rangle_{l,e}^r \otimes |00\rangle_{l,e}^t \quad \} & \textcircled{l} &= \{ \quad r_l t_e |10\rangle_{l,e}^r \otimes |01\rangle_{l,e}^t \quad \} \\ \textcircled{m} &= \{ \quad t_l r_e |01\rangle_{l,e}^r \otimes |10\rangle_{l,e}^t \quad \}. \end{aligned} \quad (5.6)$$

Therefore,

$$\begin{aligned}
V_p^r &= \frac{\int \text{Tr} \left[ \hat{a}_e^r(|\text{out}\rangle_p \langle \text{out}|_p) \hat{a}_l^{r,\dagger} + \hat{a}_l^r(|\text{out}\rangle_p \langle \text{out}|_p) \hat{a}_e^{r,\dagger} \right] dt}{\int \text{Tr} \left[ \hat{a}_e^r(|\text{out}\rangle_p \langle \text{out}|_p) \hat{a}_e^{r,\dagger} + \hat{a}_l^r(|\text{out}\rangle_p \langle \text{out}|_p) \hat{a}_l^{r,\dagger} \right] dt} \\
&= \frac{\int \left[ \frac{1}{2} r_e r_l^* + \frac{|\alpha|^2}{2} (r_e r_l S_l^{r,r,*} + S_e^{r,r} r_e^* r_l^*) \right. \\
&\quad \left. + \frac{|\alpha|^2}{4} (t_l r_e S_l^{r,t,*} + t_l r_e S_l^{t,r,*} + S_e^{r,t} r_l^* t_e^* + S_e^{t,r} r_l^* t_e^*) + \text{h.c.} \right] dt}{\int \left[ |r|^2 + |\alpha|^2 |S^{r,r}|^2 + |\alpha|^2 |S^{t,r}|^2 + |\alpha|^2 |rr|^2 + |\alpha|^2 |tr|^2 \right] dt} \\
&= \frac{|r|^2 + 2|\alpha|^2 \text{Re}\{rr S^{r,r,*}\} + 2|\alpha|^2 \text{Re}\{tr S^{r,t,*}\}}{|r|^2 + |\alpha|^2 |S^{r,r}|^2 + |\alpha|^2 |S^{t,r}|^2 + |\alpha|^2 |rr|^2 + |\alpha|^2 |tr|^2}, \tag{5.7}
\end{aligned}$$

where we have used  $\hat{a}_e^r|02\rangle_{1,e} = \sqrt{2}|01\rangle_{1,e}$ . In the last few steps we assume the scattering dynamics for early and late time-bins to be identical, i.e.,  $r_e = r_l = r$ , and the two photons within each time-bin are identical, i.e.,  $S^{r,t} = S^{t,r}$ , with the corresponding coefficients given by

$$\begin{aligned}
|r|^2 &\approx 1 - \frac{4\sigma_o^2}{\Gamma^2} + \frac{48\sigma_o^4}{\Gamma^2}; \\
\text{Re}\{rr S^{r,r,*}\} &= \text{Re}\{\langle \mathcal{L}|\mathcal{L}\rangle_{\text{RR}} + \langle \mathcal{N}|\mathcal{L}\rangle_{\text{RR}}\} \approx 1 - \frac{4}{\sqrt{\pi}} \frac{\sigma_o}{\Gamma} - \frac{8\sigma_o^2}{\Gamma^2} + \frac{72}{\sqrt{\pi}} \frac{\sigma_o^3}{\Gamma^3} + \frac{112\sigma_o^4}{\Gamma^4}; \\
\text{Re}\{tr S^{r,t,*}\} &= \text{Re}\{\langle \mathcal{L}|\mathcal{L}\rangle_{\text{TR}} + \langle \mathcal{N}|\mathcal{L}\rangle_{\text{TR}}\} \approx \frac{4\sigma_o^2}{\Gamma^2} - \frac{8}{\sqrt{\pi}} \frac{\sigma_o^3}{\Gamma^3} - \frac{64\sigma_o^4}{\Gamma^4}; \\
|S^{r,r}|^2 &= \langle \mathcal{L}|\mathcal{L}\rangle_{\text{RR}} + \langle \mathcal{L}|\mathcal{N}\rangle_{\text{RR}} + \langle \mathcal{N}|\mathcal{L}\rangle_{\text{RR}} + \langle \mathcal{N}|\mathcal{N}\rangle \\
&\approx 1 - \frac{6}{\sqrt{\pi}} \frac{\sigma_o}{\Gamma} - \frac{8\sigma_o^2}{\Gamma^2} + \frac{120\sigma_o^3}{\Gamma^3} + \frac{112\sigma_o^4}{\Gamma^4}; \\
|S^{t,r}|^2 &= \langle \mathcal{L}|\mathcal{L}\rangle_{\text{TR}} + \langle \mathcal{L}|\mathcal{N}\rangle_{\text{TR}} + \langle \mathcal{N}|\mathcal{L}\rangle_{\text{TR}} + \langle \mathcal{N}|\mathcal{N}\rangle \\
&\approx \frac{2}{\sqrt{\pi}} \frac{\sigma_o}{\Gamma} + \frac{4\sigma_o^2}{\Gamma^2} - \frac{40}{\sqrt{\pi}} \frac{\sigma_o^3}{\Gamma^3} - \frac{64\sigma_o^4}{\Gamma^4}; \\
|rr|^2 &= \langle \mathcal{L}|\mathcal{L}\rangle_{\text{RR}} \approx 1 - \frac{8\sigma_o^2}{\Gamma^2} + \frac{112\sigma_o^4}{\Gamma^4}; \\
|tr|^2 &= \langle \mathcal{L}|\mathcal{L}\rangle_{\text{TR}} \approx \frac{4\sigma_o^2}{\Gamma^2} - \frac{64\sigma_o^4}{\Gamma^4} \tag{5.8}
\end{aligned}$$

For completeness, the transmission visibility is found similarly to be

$$V_p^t = \frac{|t|^2 + 2|\alpha|^2 \text{Re}\{tt S^{t,t,*}\} + 2|\alpha|^2 \text{Re}\{tr S^{r,t,*}\}}{|t|^2 + |\alpha|^2 |S^{t,t}|^2 + |\alpha|^2 |S^{t,r}|^2 + |\alpha|^2 |tt|^2 + |\alpha|^2 |tr|^2}. \tag{5.9}$$

A nice way to check both visibility formula is by removing the two-photon nonlinear contribution ( $\langle \mathcal{N}|\mathcal{L}\rangle, \langle \mathcal{N}|\mathcal{N}\rangle = 0$ ). As such, the photon visibility should approach unity as only the linear coherent photons interfere. Any nonlinear contribution gives rise to different frequencies between the interfering photons thus reducing the interference contrast. The scattering coefficients in Eq. (5.8) can be numerically evaluated but here they are expanded perturbatively in the limit of narrow pulse bandwidth  $\sigma_o$

(compared to the QD total decay rate  $\Gamma$ ), which is valid in the current experiment as  $\sigma_o = \sqrt{2 \ln 2}/T_{\text{FWHM}} \approx 0.589 \text{ ns}^{-1} < \Gamma = 2.48 \text{ ns}^{-1}$  for a pulse length of  $T_{\text{FWHM}} = 2 \text{ ns}$  (Sec. 3.3.2). In the narrowband regime, the scattering becomes efficient as the input Gaussian spectral profile is more monochromatic towards the QD resonant frequency, thus  $|r|^2 \rightarrow 1$  and  $|t|^2 \rightarrow 0$ . Additionally, in the time domain, as the pulse is 5 times longer than the QD lifetime, it is less likely for two photons to interact simultaneously with the QD within its lifetime (with probability proportional to the overlap between the QD nonlinear response and two Gaussian spectral profiles, as in Eq. (B.4)). As a result, the two-photon nonlinear terms vanish, leading to unity visibilities in both reflection and transmission.

It is worth noting that obtaining the perturbative expressions in Eq. (5.8) is not a trivial task. For example, in evaluating  $\langle \mathcal{N} | \mathcal{N} \rangle$ , the trick is to first apply a Taylor expansion for  $\sigma_o \ll \Gamma$  before integrating with  $K$ :

$$\begin{aligned} \langle \mathcal{N} | \mathcal{N} \rangle &= \int_{-\infty}^{\infty} \frac{e^{-\frac{2K^2 + \Gamma^2}{4\sigma_o^2}} \Gamma^3 \left[ i + \text{Erfi}\left(\frac{K - i\Gamma}{2\sqrt{2}\sigma_o}\right) \right] \left[ -i + \text{Erfi}\left(\frac{K + i\Gamma}{2\sqrt{2}\sigma_o}\right) \right]}{8(K^2 + \Gamma^2)\sigma_o^2} dK \\ &\approx \int_{-\infty}^{\infty} \frac{e^{-\frac{K^2}{4\sigma_o^2}} (-2K^2 + \Gamma^2 - 8\sigma_o^2)}{\pi\Gamma^3} dK = \frac{2}{\sqrt{\pi}} \frac{\sigma_o}{\Gamma} - \frac{24}{\sqrt{\pi}} \frac{\sigma_o^3}{\Gamma^3}. \end{aligned} \quad (5.10)$$

The perturbative forms in the broadband limit  $\sigma_o \gg \Gamma$  are obtained using the same trick, but are not included in this thesis since no measurements have yet been done in this regime<sup>3</sup>.

---

<sup>3</sup>Interested readers may refer to the attached Mathematica notebook titled ‘‘AnalyticalPhotonVisibility’’ in Ref. [26] for these expressions.

### 5.3 Visibility Comparison between Theory and Simulation

To verify these theory expressions, we compare them with the visibility and slope curves obtained from numerical simulation. Since the theory renders up to only two-photon dynamics, whereas the simulation considers an arbitrary Rabi frequency  $\Omega(t) \propto \alpha(t)$ , we expect the convergence to occur in the limit of small  $\alpha$ .

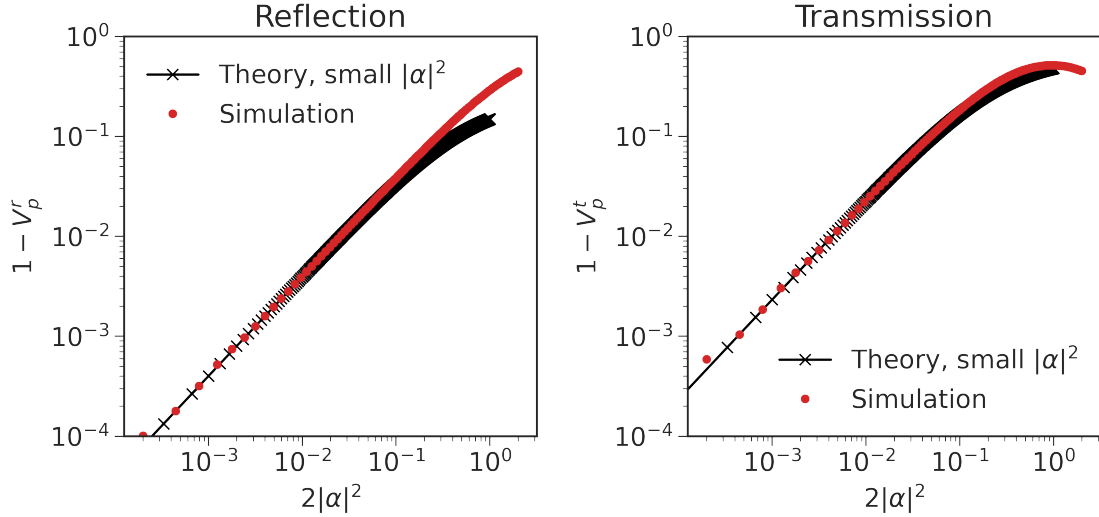


Figure 5.2: **Photon visibility as a function of mean photon number per two pulses**  $2|\alpha|^2$ . The theory curves are numerically evaluated at  $\sigma_o = \sqrt{2 \ln 2}/T_{\text{FWHM}}$  using Eqs. (5.7) and (5.9), which hold when  $\alpha \approx 0$ . Note that despite  $|t|^2 \rightarrow 0$  when  $\sigma_o \ll \Gamma$ , the transmission visibility  $V_p^t$  still approaches unity as the two-photon terms decay faster than  $|t|^2$ .

Figure 5.2 shows the plots of the photon visibility in reflection and transmission as a function of the mean photon number per two pulses  $2|\alpha|^2$ , at a given pulse bandwidth  $\sigma_o = \sqrt{2 \ln 2}/T_{\text{FWHM}}$  and pulse duration  $T_{\text{FWHM}} = 2$  ns. Here we observe an excellent agreement between the theory and the simulation. The deviation between two curves becomes noticeable once  $2|\alpha|^2$  surpasses  $\approx 10^{-1}$ , which is precisely the regime where we expect the theory to hold. The theoretical visibility is plotted by evaluating Eqs. (5.7) and (5.9) numerically with discrete sums, while the numerical simulation is performed by solving the master equations given the system Hamiltonian.

Another way to verify the theory is to plot the visibility slope at different values of pulse bandwidth  $\sigma_o$ . This step is crucial as some nonlinear terms are very small when  $\sigma_o \ll \Gamma$  or  $\sigma_o \gg \Gamma$ , thus an error in the visibility formula would be too elusive to catch. By using  $\sigma_o$  as a tuning knob, the nonlinearity contribution can be magnified, allowing the smaller terms to be probed. To understand this, we first refer to the theoretical visibility formula, which can be rewritten using the inner products in Eq. (5.8) as

$$\begin{aligned}
 V_p^j &= 1 - \frac{2|\alpha|^2 \langle \mathcal{N} | \mathcal{N} \rangle}{|j|^2 + 2|\alpha|^2 (\langle \mathcal{L} | \mathcal{L} \rangle_{\text{jj}} + \langle \mathcal{L} | \mathcal{L} \rangle_{\text{TR}} + \langle \mathcal{L} | \mathcal{N} \rangle_{\text{jj}} + \langle \mathcal{L} | \mathcal{N} \rangle_{\text{TR}} + \langle \mathcal{N} | \mathcal{N} \rangle)} \\
 &\approx V_p^0 + |\alpha|^2 \frac{dV_p^j}{d|\alpha|^2} \Big|_{|\alpha|^2=0},
 \end{aligned} \tag{5.11}$$

where  $j \in \{r, t\}$  for reflection ( $r$ ) or transmission ( $t$ ) visibility. Here it is apparent that in the limit of small  $\alpha$ , the visibility slope, or photo-sensitivity of the interference

$$\frac{dV_p^j}{d|\alpha|^2} \Big|_{|\alpha|^2=0} \equiv \frac{-2 \langle \mathcal{N} | \mathcal{N} \rangle}{|j|^2}, \quad (5.12)$$

is given by the ratio between the two-photon nonlinear  $\langle \mathcal{N} | \mathcal{N} \rangle$  and single-photon probabilities  $|j|^2$ . In the case of reflection,  $\langle \mathcal{N} | \mathcal{N} \rangle \rightarrow 0$  in both narrowband and broadband limits, the visibility is thereby insensitive to the photon number per pulse. For narrowband pulses, this can be understood as having an infinitely long pulse<sup>4</sup> whereby increasing the number of photons per pulse could not trigger nonlinear scattering of multiple photons with the QD at the same time. The QD behaves as a mirror that reflects one photon at a time, hence the visibility remains unscathed. As for pulses that are spectrally far broader than the QD linewidth, any pair of photons that come into contact with the QD are too off-resonant for nonlinear effect to take place.

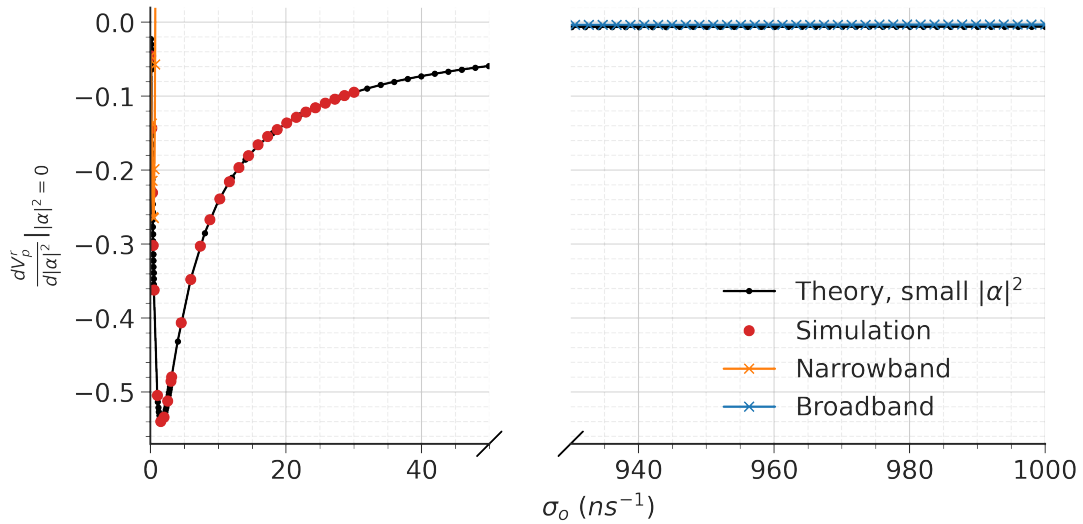


Figure 5.3: **Reflection visibility slope versus pulse bandwidth**  $\sigma_o$ . The theory (black dotted line) curve is computed numerically using Eq. (5.12), while the narrowband (orange cross) and broadband (blue cross) curves use Eq. (5.12) with perturbative expansion in the limits of  $\sigma_o \ll \Gamma$  and  $\sigma_o \gg \Gamma$ , respectively. The simulated slope (red dots) is acquired by fitting the power-dependent visibility then computing its derivative.

Figure 5.3 shows the slope of the reflection visibility as a function of  $\sigma_o$ . Excellent agreement is seen between the simulation and theory. The photo-sensitivity reaches its peak when  $\sigma_o \approx 0.6523\Gamma$ , whereas  $\langle \mathcal{N} | \mathcal{N} \rangle$  is maximized when  $\sigma_o$  is tuned to  $\approx 0.3548\Gamma$ . The closed forms of these numbers are not determined here as there is no exact form of  $\langle \mathcal{N} | \mathcal{N} \rangle$  (see the integral of Eq. (5.10)). Interestingly, Eq. (5.12) implies that the nonlinearity contribution  $\langle \mathcal{N} | \mathcal{N} \rangle$  can be experimentally measured by fitting the power-dependent visibility and extracting its slope in the weak power regime. The QD reflectivity  $|r|^2$  or transmittivity  $|t|^2$  can be directly measured from resonant fluorescence and waveguide transmission experiments (see Sec. 3.4.2, for example), accordingly.

<sup>4</sup>Note that for input pulses longer than or close to the interferometric delay  $T_{\text{pulse}} \geq \tau_{\text{int}}$ , it is experimentally difficult to define a middle-bin time window.  $T_{\text{pulse}} < \tau_{\text{int}}$  might be necessary for experimental demonstrations. Here we ignore this constraint for simplicity.

### 5.3.1 Visibility with Additional Errors

To explain the measured photon visibility in Sec. 3.4.5, several experimental imperfections need to be included in the model. In this subsection, we consider non-unity waveguide coupling efficiency  $\beta$ , finite optical cyclicity  $C$  and phonon-induced pure dephasing rate  $\gamma_d$ . Spectral diffusion is not considered here, as we are only interested in evaluating the reflection visibility, which is in principle robust to it.

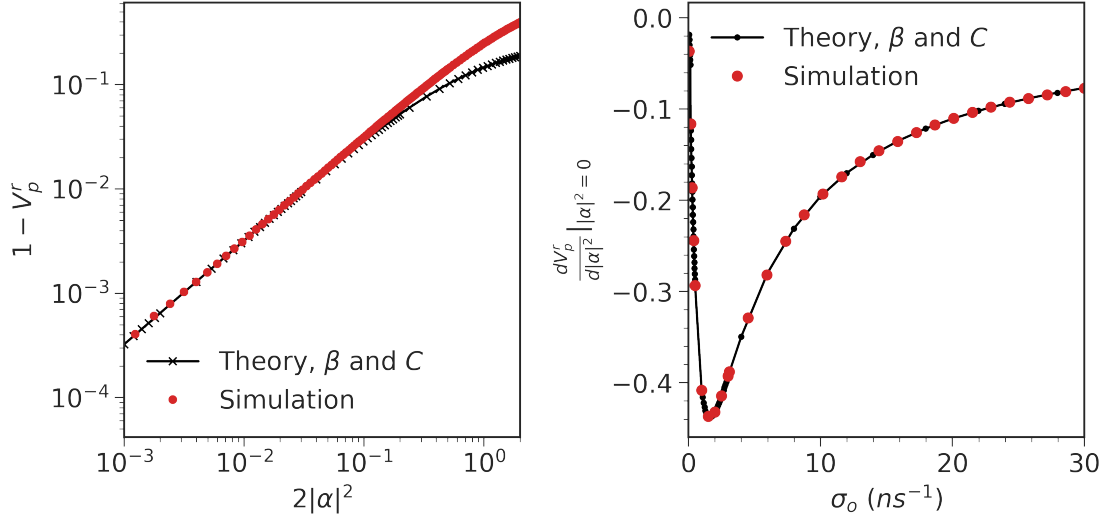


Figure 5.4: **Reflection visibility under additional errors.** Here we only considered imperfect coupling efficiency  $\beta = 0.865$  and branching error due to limited cyclicity  $C = 14.7$ . **Left:** Visibility plot versus  $2|\alpha|^2$ . **Right:** Visibility slope plotted against  $\sigma_o$ . Both errors together amount to a factor of  $\frac{C}{C+1}\beta$  to the slope in Fig. 5.3.

Both waveguide coupling loss and finite cyclicity error can be treated as dissipative loss in the two-level system, as photons scattered at a different frequency are eventually filtered out not being detected. This is achieved by replacing some  $\Gamma$  by the effective total decay rate  $\Gamma_1 = \frac{C}{C+1}\beta\Gamma$  in the inner products, for instance, in the reflection:

$$\begin{aligned} \langle \mathcal{N} | \mathcal{N} \rangle &= \int_{-\infty}^{\infty} \frac{e^{-\frac{2K^2 + \Gamma^2}{4\sigma_o^2}} \Gamma_1^3 \left[ i + \text{Erfi}\left(\frac{K - i\Gamma}{2\sqrt{2}\sigma_o}\right) \right] \left[ -i + \text{Erfi}\left(\frac{K + i\Gamma}{2\sqrt{2}\sigma_o}\right) \right]}{8(K^2 + \Gamma^2)\sigma_o^2} dK; \\ |r|^2 &= \int_{-\infty}^{\infty} \frac{e^{-\frac{(\omega - \omega_1)^2}{2\sigma_o^2}}}{\sqrt{2\pi\sigma_o^2}} \left| \frac{-\Gamma_1}{\Gamma + 2i(\omega - \omega_1)} \right|^2 d\omega, \end{aligned} \quad (5.13)$$

where  $\omega_1$  is the transition frequency of the effective two-level system ( $|\uparrow\rangle \leftrightarrow |\uparrow\downarrow\rangle$ ).  $\text{Erfi}(x)$  is the imaginary error function. The extra factor on the total decay rate implies that only the fraction of photons scattered from the dominant optical transition  $\frac{C}{C+1}$  that couples to the waveguide mode with efficiency  $\beta$  contributes to the interference. Figure 5.4 plots the reflection visibility under these errors, where the magnitude of its slope is down-scaled precisely by a factor of  $\frac{C}{C+1}\beta$ . This is easily seen from observing Eq. (5.13) and can be explained intuitively: When  $\beta$  decreases, the multi-photon terms dissipate quicker than the single-photon scattering probability (as the probability of losing at least one photons for an  $(N \geq 2)$ -photon input state scales as  $1 - (1 - \beta)^N \gg 1 - \beta$  which is greater than losing a 1-photon state). As such, the visibility becomes less responsive to

any change in the mean photon number per pulse (or more sensitive to the single-photon dynamics).

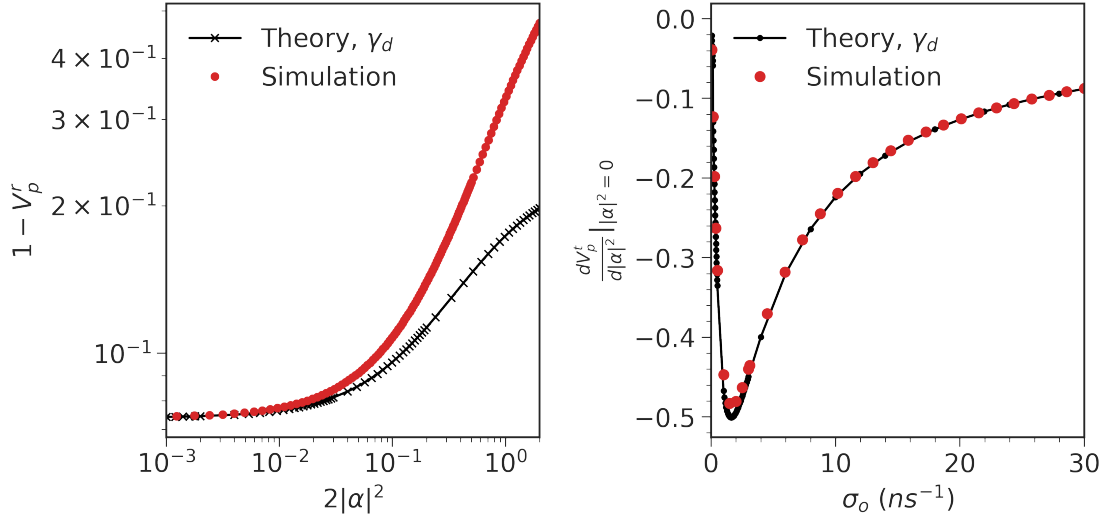


Figure 5.5: **Reflection visibility under phonon-induced pure dephasing  $\gamma_d$ .** We assumed  $\gamma_d = 0.099 \text{ ns}^{-1}$ . **Left:** Visibility plot versus  $2|\alpha|^2$ . **Right:** Visibility slope against  $\sigma_o$ .

The phonon-induced dephasing rate can be incorporated to the model using the same formalism developed in Sec. 3.4.5, where the single-photon scattering leads to a quantum jump to the excited state with a rate  $2\gamma_d$ , followed by the decay of an incoherent photon of frequency  $\omega_1$ . The output photon density matrix is then rewritten as

$$|\text{out}'\rangle_p \langle \text{out}'|_p \approx |\text{out}\rangle_p \langle \text{out}|_p + \frac{|\alpha|^2}{2} P_{\gamma_d}^{\omega_1} \rho_{\gamma_d,e}^{\omega_1} |0\rangle_1 \langle 0|_1 + \frac{|\alpha|^2}{2} P_{\gamma_d}^{\omega_1} \rho_{\gamma_d,l}^{\omega_1} |0\rangle_e \langle 0|_e \quad (5.14)$$

and the visibility formula with its slope would become

$$V_p^j = \frac{|j|^2 + 2|\alpha|^2 \text{Re}\{jjS^{j,j,*}\} + 2|\alpha|^2 \text{Re}\{trS^{r,t,*}\}}{|j|^2 + |\alpha|^2 |S^{j,j}|^2 + |\alpha|^2 |S^{t,r}|^2 + |\alpha|^2 |jj|^2 + |\alpha|^2 |tr|^2 + P_{\gamma_d}^{\omega_1}},$$

$$\frac{dV_p^j}{d|\alpha|^2} \Big|_{|\alpha|^2=0} = \frac{-2 \langle \mathcal{N} | \mathcal{N} \rangle}{|j|^2 + P_{\gamma_d}^{\omega_1}}, \quad (5.15)$$

with the pure dephasing probability (see Eq. (4.16)):

$$P_{\gamma_d}^{\omega_1} = \frac{\Gamma'_1}{\Gamma} \int_{-\infty}^{\infty} \frac{e^{-\frac{(\omega-\omega_1)^2}{2\sigma_o^2}}}{\sqrt{2\pi\sigma_o^2}} \left| \frac{-2\sqrt{2\gamma_d\Gamma'_1}}{\Gamma + 2i(\omega - \omega_1)} \right|^2 d\omega, \quad (5.16)$$

where  $\Gamma'_1 = \Gamma_1/2$  is the decay rate in either the reflected or transmitted mode.

Figure 5.5 shows the reflection visibility under the effect of  $\gamma_d$ . The theory deviates from the simulation now at a smaller value of  $\alpha$  as the theory considers only pure dephasing error from single-photon scattering. The visibility slope is generally reduced due to the extra dephasing term in the denominator (Eq. (5.15)). Note that this approach of treating the dephasing error is valid when the timescale of phonon-induced process is much faster ( $\ll \tau_{\text{int}} = 11.83 \text{ ns}$  [75]) than the interferometer delay. In the case of spectral diffusion where the timescale is in the order of ms [136], the early time-bin experiences the same scattering dynamics, or the same phase shift as the late time-bin, thus the interference between two time-bins would not be affected (Sec. 3.4.5).

## 5.4 Visibility Comparison with Data

Now that we have shown convergence between theory and simulation, we proceed to describe the experimental data in Sec. 3.4.5.

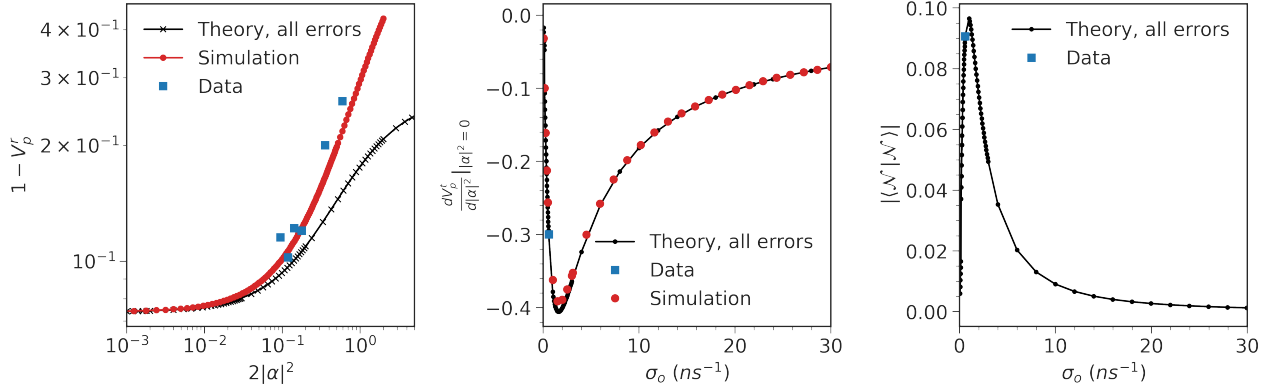


Figure 5.6: **Reflection visibility comparison with data under realistic errors.** The parameters used in the theory and simulation are identical to the previous section. Data taken in Sec. 3.4.5. **Left:** Visibility versus  $2|\alpha|^2$ . The conversion between measured powers and mean photon number is done using the fit result in Sec. 3.4.4. **Middle:** Visibility slope plotted against  $\sigma_o$ . Blue data point corresponds to the slope when  $\sigma_o = 0.589 \text{ ns}^{-1}$  in the experiment. **Right:** Plot of the nonlinear term  $|\langle \mathcal{N} | \mathcal{N} \rangle|$  against  $\sigma_o$ .

Figure 5.6 compares the measured power-dependent visibility with theory and simulation, which adopt the same set of parameters ( $\beta = 0.865$ ,  $C = 14.7$  and  $\gamma_d = 0.099 \text{ ns}^{-1}$ ) extracted from resonant transmission experiments (Sec. 3.4.2). On the left subplot, the x-axis is chosen (so as in the previous sections) to be twice the mean photon number per pulse, since the average optical power measured in the experiment corresponds to the total power from both the early and late pulses. The data in general agrees nicely with the simulation. In hindsight, a better measurement could be performed with a higher resolution and at even lower powers as it appears the theory already begins to stray off on the first data point; however, this necessitates a sufficiently stable optical path with a decent signal-to-noise ratio<sup>5</sup>.

<sup>5</sup>Note that the theory does not consider the effect of laser leakage to the visibility.

## 5.5 Comparison with Hong-Ou-Mandel Visibility

In the last section we draw a connection between the photon visibility and the Hong-Ou-Mandel visibility, another metric that benchmarks the coherence of photons emitted from the QD. While in principle they are two different measurements in terms of excitation schemes (the former uses QD as a scatterer, whereas the latter typically treats the QD as an emitter) and the measured degree of coherence (the former measures first-order coherence, the latter the second-order coherence), both can be used to measure the exact same quantity that characterizes the photon indistinguishability. We then follow up by discussing several implications that can be inferred from such a connection.

Throughout the literature, the Hong-Ou-Mandel visibility  $V_{\text{HOM}}$  is extensively used to infer the indistinguishability of photons emitted from a single-photon source. The measured  $V_{\text{HOM}}$  is in general tainted by impurity of the photon source  $g^{(2)}(0) > 0$  and laser leakage, which needs to be corrected such that it exclusively contains contribution from pure dephasing. To do so, the equation  $V_{\text{HOM}} = V^{(0)} - 2g^{(2)}(0)$  is typically adopted wherein  $V^{(0)} \equiv \frac{\Gamma}{\Gamma + 2\gamma_d}$  [28, 75] can be deduced. However, recent works [139, 140] have established a more general (and correct) relation

$$V_{\text{HOM}} = V^{(0)} - Fg^{(2)}, \quad (5.17)$$

where  $1 < F < 3$  is the slope of the visibility with respect to  $g^{(2)}(0)$ , depending on the distinguishability of the emitted one-photon and two-photon states [139]. To illustrate the connection between Eq. (5.17) and the photon visibility discussed in the previous sections, we rewrite the reflection visibility in the form of Eq. (5.11):

$$\begin{aligned} V_p^r &= 1 - \frac{2|\alpha|^2 \langle \mathcal{N} | \mathcal{N} \rangle + P_{\gamma_d}^{\omega_1}}{|r|^2 + 2|\alpha|^2 (\langle \mathcal{L} | \mathcal{L} \rangle_{\text{RR}} + \langle \mathcal{L} | \mathcal{L} \rangle_{\text{TR}} + \langle \mathcal{L} | \mathcal{N} \rangle_{\text{RR}} + \langle \mathcal{L} | \mathcal{N} \rangle_{\text{TR}} + \langle \mathcal{N} | \mathcal{N} \rangle) + P_{\gamma_d}^{\omega_1}} \\ &\approx \frac{|r|^2}{|r|^2 + P_{\gamma_d}^{\omega_1}} - |\alpha|^2 \frac{2 \langle \mathcal{N} | \mathcal{N} \rangle}{|r|^2 + P_{\gamma_d}^{\omega_1}} \equiv V_p^0 + |\alpha|^2 \frac{dV_p^j}{d|\alpha|^2} \Big|_{|\alpha|^2=0}. \end{aligned} \quad (5.18)$$

In the last step we expand the visibility to the first order of  $|\alpha|^2$ . Here we see that  $V_p^0$  is the intrinsic visibility that is only affected by the distinguishability (marked by pure dephasing rate  $\gamma_d$ ) between photons in the two time-bins, and is independent of the impurity of the scattering process (given by a non-zero  $|\alpha|^2$ ). Interestingly, it bears a striking resemblance with Eq. (5.17). The second-order correlation function  $g^{(2)}(0)$ , which at zero time delay characterizes the purity of a given single-photon source [28], also shares a somewhat similar physical meaning with the visibility slope: A vanishing slope implies the single-photon scattering probability dominates, which is equivalent to saying that the multi-photon component fades away, or  $g^{(2)}(0) \rightarrow 0$ .

One possible implication of this is that one could measure the power-dependent photon visibility in the reflection, using scattering pulses from the time-bin interferometer. From which  $V_p^0$  (the  $y$ -intercept where  $|\alpha|^2 = 0$ ) can be extrapolated from the theory fit, to determine  $\gamma_d$  (Sec. 3.4.5). This method could be very accurate in estimating  $\gamma_d$  as it requires only measuring  $V_p^r$ . The photon visibility  $V_p^r$  is essentially a measure of the first-order coherence  $g^{(1)}$  between two time-bins, which could be less sensitive to fluctuations than measuring  $g^{(2)}$ . In fact,  $V_p^0$  is mathematically equivalent to  $V^{(0)}$  in Eq. (5.17), by simplifying (5.16) into  $P_{\gamma_d}^{\omega_1} = 2\gamma_d|r|^2/\Gamma$ . This means  $V^{(0)}$  (and  $\gamma_d$  given  $\Gamma$ ) can simply be determined by measuring the power-dependent photon visibility alone, without the need to measure  $g^{(2)}(0)$ ,  $V_{\text{HOM}}$  and  $F$ .

Type	$g^{(2)}(0)$ (%)	$V_{\text{HOM}}^{\text{raw}}$ (%)	$V_{\text{HOM}}^{\text{corr}}$ (%)	$F$
Pump series	$4 \pm 0.6$	$88.8 \pm 0.6$	$89.5 \pm 0.7$	$0.788 \pm 0.15$
$\pi$ -pulse series	$4.7 \pm 0.9$	$86.5 \pm 0.7$	$87.1 \pm 0.7$	$1.16 \pm 0.15$

Table 5.1: Estimated values for the Hong-Ou-Mandel visibility slope  $F$  for two different measurement sequences, using Eq. (5.17) with  $V^{(0)} = 92.6\%$ . Data taken from Ref. [18]. Note that  $V_{\text{HOM}}^{\text{corr}}$  is the HOM visibility corrected only for interferometer imperfections but not for non-zero  $g^{(2)}(0)$  (see the main text for details), not to be confused with  $\mathcal{V}_{\text{hom}}^{\text{corr}}$  in Ref. [52].

Another interesting implication is that given  $V_{\text{HOM}}$  and  $g^{(2)}(0)$ ,  $F$  can be roughly estimated. The measured Hong-Ou-Mandel visibility is first corrected for interferometer imperfections including unequal beamsplitter splitting ratio and non-unity classical interferometer visibility, following Ref. [141] with data from Table 9.3 of Ref [52]. Thus, the corrected visibility  $V_{\text{HOM}}^{\text{corr}} = V_{\text{HOM}}$  ideally contains only contributions from single-photon impurity  $g^{(2)}(0) > 0$  and pure dephasing, which can then be substituted into Eq. (5.17) together with  $V^{(0)} = V_p^0 = 92.6\%$ , to find  $F$ . Table 5.1 shows the estimated values for  $F$  under two different measurement schemes, which are a bit lower than expected (maybe off by a factor of 2). Nevertheless, the similarity and apparent agreement between Eqs. (5.17)-(5.18) is highly promising, and thus strongly motivates for further study towards this end.



# Chapter 6

## Multi-photon Entanglement with Photon Emission

Previously on Chapters 3 to 5, we have both experimentally and theoretically investigated exclusively the photon-scattering approach to induce spin-photon entanglement. Working in the weak scattering regime implies that entanglement is generated with the highest fidelity when interfacing with a low photon number state. While this is naturally applicable to flying photons that are heavily attenuated over long distances, the scattering approach is in principle not scalable to a larger photonic Hilbert space, i.e., the generation of multi-photon resource states where the entanglement generation rate becomes a key determining factor. Fortunately, an easy fix to this issue is through time-reversal symmetry of the light-matter interaction: What if instead of sending single photons to the quantum emitter, the emitter spits out photons which are entangled with itself?

This chapter investigates the generation of multi-photon entangled states, by single-photon emission from a quantum dot (QD). This is the continuation of the time-bin multi-photon entanglement generation scheme reported in Ref. [18]. In the chapter, we first briefly summarize others and our work on the quest to create large entangled states using quantum dots, followed up by several improvements in terms of optical setup and wafer structure. Next, spectroscopic measurements of a quantum-dot electron spin and entanglement characterization are discussed in depth. In particular, a near-unity  $\mathcal{F}_\pi = 98\%$  spin  $\pi$ -rotation fidelity and a 3-qubit GHZ entanglement fidelity of  $\mathcal{F}_{\text{GHZ}} = 56\%$  are highlighted. The experiments presented in this chapter were conducted together with Yijian Meng and Rasmus Bruhn Nielsen.

### 6.1 Protocol for Multi-photon Entanglement Generation

The generation of multi-photon entanglement has been achieved on numerous atomic systems, with a monumental work using a single neutral atom in an optical cavity [142], creating a 14-photon GHZ state and 12-photon linear cluster state. These resource states will be useful since they can be probabilistically fused [143] to synthesize larger graph states, which can be utilized for measurement-based one-way quantum computing [25] or quantum repeaters [22] for long-range quantum communication.

### 6.1.1 The Lindner-Rudolph Protocol

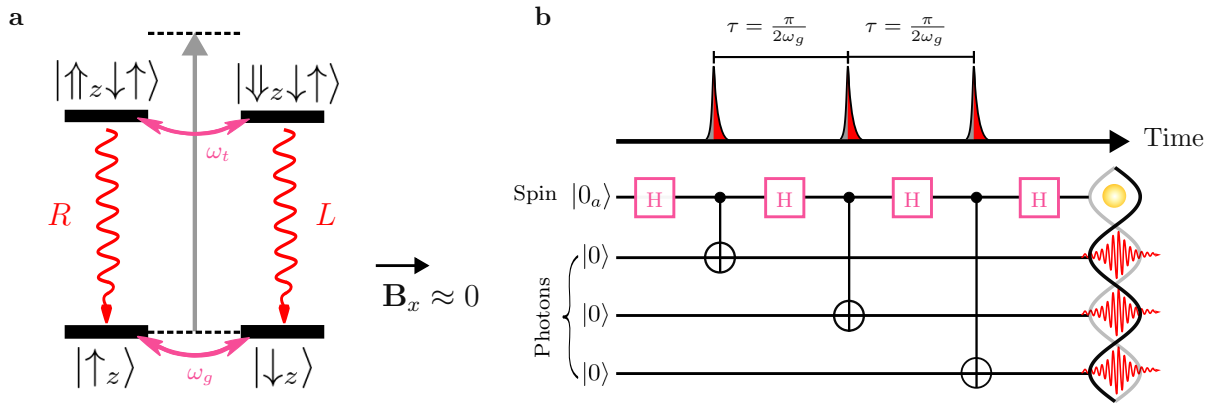


Figure 6.1: **Lindner-Rudolph protocol.** (a) Level scheme of a negatively charged QD subject to a weak in-plane magnetic field  $\mathbf{B}_x$ , described by the spin  $z$ -basis states. The ground (trion) states precess with a frequency  $\omega_g$  ( $\omega_t$ ) around  $\hat{x}$ . (b) Generation protocol for a linear cluster state between the QD electron and 3 polarization encoded photons, which composes of periodic pulsed excitations separated by precession time  $\tau$  of the electron. Each photon emission event corresponds to performing a spin-photon CNOT gate in the circuit diagram, whereas a Hadamard gate is applied by spin precession.

An elegant approach for generating these resource states with a single solid-state quantum emitter has been proposed by N. H. Lindner and T. Rudolph in 2009. The protocol considers a negatively charged QD placed in a small in-plane  $\mathbf{B}_x \approx 0$  magnetic field, where its ground states are encoded in the spin  $z$ -basis [144] (Fig. 6.1a). The optical dipoles associated with the outer transitions become circularly polarized ( $R/L$  for right/left-handed circular polarization) according to the selection rules (Sec. 1.3). Since both the ground and excited states are not energy eigenstates along  $x$ , they exhibit Larmor precessions with frequencies  $\omega_g$  and  $\omega_t$ , respectively. Therefore, controlling the free precession time  $\tau = \pi/2\omega_g$  of the electron performs a spin  $\pi/2$ -rotation, i.e., a Hadamard gate. Together with single-photon emissions from the QD, a string of photons entangled with the QD spin can be deterministically created.

To understand this, we go through the ideal protocol in steps. The QD is first initialized in  $|\downarrow_z\rangle$  and allowed to precess for  $\tau$  to end up in the superposition state  $|\psi\rangle = (|\uparrow_z\rangle + |\downarrow_z\rangle)/\sqrt{2}$ . Exciting the QD with a linear polarization drives both outer transitions equally, leading to spin-dependent emission of photons with orthogonal polarizations:  $|\psi\rangle = (|R\rangle|\uparrow_z\rangle + |L\rangle|\downarrow_z\rangle)/\sqrt{2}$ , which becomes a spin-photon Bell state. Letting the spin precess for another time  $\tau$  results in  $|\psi\rangle = (|R\rangle|\uparrow_z\rangle + |R\rangle|\downarrow_z\rangle + |L\rangle|\uparrow_z\rangle - |L\rangle|\downarrow_z\rangle)/\sqrt{2}$ , which is now a 2-qubit linear cluster state. Performing optical excitation followed by free precession for  $n$  times sequentially generates an  $n$ -photon linear cluster state entangled with the spin, equivalent to the quantum circuit in Fig. 6.1b.

Experimentally, the earliest demonstration of the Lindner-Rudolph protocol can be traced back to 2016, where a QD loaded with a dark exciton emits 2 photons entangled with itself [16], following a similar level scheme in Fig. 6.1a. Pulsed excitations of the QD dark exciton ground state are achieved with a 11 nm blue-detuned picosecond laser<sup>1</sup>, whereas the Hadamard gate is applied by natural precession of 3 ns without a magnetic

<sup>1</sup>Resonant excitation is challenging to implement for the Lindner-Rudolph protocol, since the cross-polarized scheme (commonly used for laser extinction) cannot be adopted to filter out the input light when

field thanks to the strain-induced energy splitting between  $z$ -basis states. Both the entanglement fidelity and witness are measured to be above the classical thresholds with  $1.2\sigma$  significance, certifying a genuine 3-qubit entanglement. While this is a remarkable feat, it might not be a scalable approach for fusing into large entangled states as the indistinguishability of emitted photons is low<sup>2</sup> due to finite non-radiative decay (100 ps) of the excited dark exciton state, which culminates in fast spectral broadening of the emitted photons.

Since then, numerous experiments have emerged to demonstrate multi-photon entanglement using other QD excitonic states, including hole spin [146] and electron spin [147]. Although these schemes yield an improved fidelity, indistinguishability and setup efficiency, they are conceptually identical. This means the limitations in the original Lindner-Rudolph protocol remain unresolved. For instance, the protocol requires  $\Gamma \gg \omega_g \gg 1/T_2^*$  [52], where the QD radiative decay rate  $\Gamma$  must be faster than both the ground-state precession frequency  $\omega_g$  and spin dephasing noise  $1/T_2^*$ . Here  $\omega_g \ll \Gamma$  is necessary since both outer transitions in Fig. 6.1a need to be spectrally close for emitting the polarization encoded photons ( $|R\rangle$  and  $|L\rangle$ ) of the same frequency. Moreover, the spin must remain coherent with sufficiently long  $T_2^*$  during photon emissions and Hadamard gates. While a higher Purcell factor from an improved nanostructure design [147] could enhance the emission rate and push for a few more photons, the fundamental issue with low  $T_2^*$  cannot seem to be circumvented without active spin control, i.e., implementing nuclear spin cooling<sup>3</sup> [97] or spin-echo sequences [87], thus questioning the scalability of this approach.

### 6.1.2 Time-bin Protocol

An alternative approach which might be scalable in the long run is the time-bin protocol, which is first proposed and attempted in Ref. [148], followed by a detailed theoretical analysis in Ref. [149], and is experimentally demonstrated [18].

As its name suggests, the protocol uses the emission time of photons, i.e., time-bin, to define a photonic qubit. A photon emitted at an earlier (later) time corresponds to the logical 0 (1) of the qubit. This type of encoding is especially useful for long-distance fiber transmission, since polarization drifts in the fiber do not affect the presence of a photon in the time-bin<sup>4</sup>.

The time-bin protocol follows the level scheme depicted in Fig. 6.2a, where a large in-plane magnetic field  $\mathbf{B}_x$  is applied to realize a double  $\Lambda$ -system. To be consistent with the rest of the chapter, we use an electron spin as the qubit. Here the electronic ground states are defined as  $x$ -eigenbases<sup>5</sup> (poles) but owing to selection rules the cross transitions (i.e.,  $|\uparrow_x\rangle \leftrightarrow |\downarrow_x\downarrow\uparrow\rangle$ ) are allowed (Sec. 1.3). Ideally, for time-bin encoding all emitted photons shall be generated with the same polarization and frequency<sup>6</sup>. This is

---

the output photons need to be collected with opposite polarizations. Off-resonant excitation followed by spectral filtering is thus a better solution.

<sup>2</sup>Roughly estimated to be 20% [145].

<sup>3</sup>It is uncertain whether nuclear cooling or even optical spin control can be implemented at low  $\mathbf{B}_x \approx 40$  mT for the level scheme in Lindner-Rudolph protocol.

<sup>4</sup>Rather, information is encoded in the emission time of the photons as well as a relative phase between them, thus a phase-stable unbalanced interferometer (Sec. 3.3.2) is required for detection.

<sup>5</sup>In this dressed state picture, there is no apparent precession between the two  $x$ -eigenstates around  $\mathbf{B}_x$ , thus passive spin control using free precession is not possible.

<sup>6</sup>This is to ensure indistinguishability between photons emitted at different time-bins.

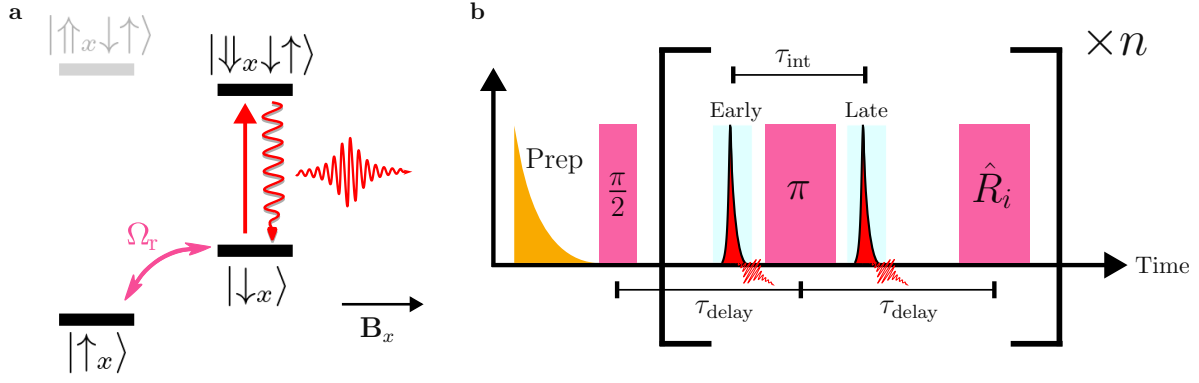


Figure 6.2: **Time-bin entanglement protocol between  $n$  photons and an electron spin.** (a) Level diagram of a negatively charged QD subject to a strong in-plane magnetic field. The qubit is encoded in the  $x$ -eigenbases. (b) Protocol consisting of spin preparation (orange), spin control pulses (magenta) and optical excitations (red). Each round (inside the square bracket) knits one photon to the initial state. Running it  $n$  times with  $\hat{R}_i = \hat{R}_y(\pi)$  ( $\hat{R}_i = \hat{R}_y(\pi/2)$ ) manifests in an  $n$ -photon GHZ (linear cluster) state entangled with the spin.

achieved by driving the QD repeatedly through a strong cycling transition (i.e.,  $|\downarrow_x\rangle \leftrightarrow |\downarrow_x\downarrow\uparrow\rangle$ <sup>7</sup>) with the same preferential decay channel  $|\downarrow_x\downarrow\uparrow\rangle \rightarrow |\downarrow_x\rangle$ . As already introduced in Sec. 3.4.1, this can be engineered by embedding the QD at the center of a photonic-crystal waveguide, thereby suppressing (enhancing) the cross (outer) transitions. Additionally, a large Zeeman splitting between the spin ground states allows coherent active spin control for realizing  $\pi$ -rotation and Hadamard gates (Sec. 3.5).

The ideal protocol begins by initializing the electron in  $|\uparrow_x\rangle$  accompanied by a Hadamard gate  $\hat{R}_y(\pi/2)$  to project it into a superposition state  $|\psi\rangle = (|\uparrow_x\rangle + |\downarrow_x\rangle)/\sqrt{2}$ . What follows is a series of optical  $\pi$ -pulses (denoted by photon creation operator  $\mathcal{A}_{i_n}^\dagger$  for  $i \in \{e, l\}$  time-bin and  $n$ -th photon) and a spin  $\pi$ -rotation  $\hat{R}_y(\pi)$ :

$$\begin{aligned}
 |\psi\rangle &= \frac{|\uparrow_x\rangle + |\downarrow_x\rangle}{\sqrt{2}} \xrightarrow{\mathcal{A}_{e_1}^\dagger} \frac{|\emptyset\rangle|\uparrow_x\rangle + |e_1\rangle|\downarrow_x\rangle}{\sqrt{2}} \\
 &\xrightarrow{\hat{R}_y(\pi)} \frac{|\emptyset\rangle|\downarrow_x\rangle - |e_1\rangle|\uparrow_x\rangle}{\sqrt{2}} \\
 &\xrightarrow{\mathcal{A}_{l_1}^\dagger} \frac{|l_1\rangle|\downarrow_x\rangle - |e_1\rangle|\uparrow_x\rangle}{\sqrt{2}}, \tag{6.1}
 \end{aligned}$$

which is a Bell state between the time-bin encoded photons and the QD spin. It is straightforward to show that applying another spin  $\pi$ -rotation pulse  $\hat{R}_i = \hat{R}_y(\pi)$  followed by another round of  $\mathcal{A}_{e_2}^\dagger - \hat{R}_y(\pi) - \mathcal{A}_{l_2}^\dagger$  winds up in a GHZ state between 2 photons and the electron spin. Similarly, a linear cluster state can be generated taking  $\hat{R}_i = \hat{R}_y(\pi/2)$ .

It is vital to emphasize that aside from being resistant to polarization drifts, the time-bin protocol in Fig. 6.2b applies a built-in Hahn-echo sequence with total echo delay  $2\tau_{\text{delay}}$  when measuring the spin in the equatorial bases. At higher number of photons, with addition of more  $\pi$ -rotation pulses this becomes a Carr-Purcell dynamical decoupling sequence [150]. The entanglement fidelity is therefore insensitive to slow nuclear  $T_2^*$  noises

<sup>7</sup>Note that this is true for the ideal case. In reality, this is not what we observed since the waveguide is oriented  $90^\circ$  relative to the QD crystallographic axis, as we explain further in Sec. 6.9.

that are filtered out by the echo. Furthermore, nuclear spin cooling techniques can be applied before the entanglement protocol to prolong  $T_2^*$ .

However, as Ref. [18] showed, the entanglement fidelity remains sensitive to the fidelity of spin control. A 67% fidelity of spin-photon Bell state using a hole spin has been measured, where a majority of the Bell-state infidelity (22.8%) is attributed to photo-induced incoherent spin-flip errors present during spin control. The 3-qubit GHZ state generation has also been attempted, but with 42.3% fidelity, just 7.7% shy of the classical threshold.

To overcome this limitation, for this work we pivot to electron spins. Notably, there are several potential benefits: First, the in-plane g-factor of electrons ( $g_{e,x} \approx 0.34 - 0.389^8$ ) is reported to be slightly higher than holes ( $g_{h,x} \approx 0.26 - 0.298$ ) in a similar sample, meaning that the ground-state splitting is 7 GHz larger when subject to the same magnetic field (at  $\mathbf{B}_x = 4$  T), leading to reduced cross-excitation error as a result of the spectrally broad excitation laser. Second, the electron  $T_2^*$  can be lengthened to orders of magnitude longer by nuclear spin cooling. A narrower Overhauser field noise spectrum  $\sigma_{\text{OH}} = \sqrt{2}/T_2^*$  means the spin noises are more easily filtered out by the echo. Third, the rotation fidelity using hole spins has been limited to  $F_\pi = 87 - 91\%^9$  [125, 18] (see also Sec. 3.5), while for the electron spin  $F_\pi = 98.8\%$  is reported [125]. Bringing  $F_\pi$  to above the 99% mark would eminently boost both spin-echo visibility and spin readout fidelity. Finally, in an  $n$ -type device, an electron spin can be deterministically injected into the QD (Sec. 1.2.2), as opposed to the hole spin which might require an additional off-resonant laser<sup>10</sup>.

For further improvements, an in-plane magnetic field larger than 2 T seems helpful in not only widening the ground-state splitting but also improving the spin coherence time  $T_2$  [151], as the Zeeman interaction dominates over the quadrupolar fields. For higher entanglement rates, layers of distributed Bragg reflectors (DBR) can be grown underneath the wafer heterostructure to increase the overall collection efficiency. There are a few more modifications to the existing optical and spin control setups in this regard, all of which will be covered in the next section.

---

<sup>8</sup>See Table 4.1 of Ref. [52].

<sup>9</sup>It remains unclear whether this limit is fundamental to the hole spins.

<sup>10</sup>With the off-resonant laser, the hole initialization efficiency is 75% [52]. However, the laser also causes spin decoherence lessening the echo visibility by 12% as reported in Sec. 3.5.3.

## 6.2 Experimental Setup

Starting from this section, we examine a series of refinements to the wafer heterostructure, the optical spectroscopic and spin control setups.

### 6.2.1 Wafer Composition

The fabrication steps of the QD wafer have been documented extensively in the supplementary material of Ref. [35]. Here we highlight a few notable differences in the next-generation device.

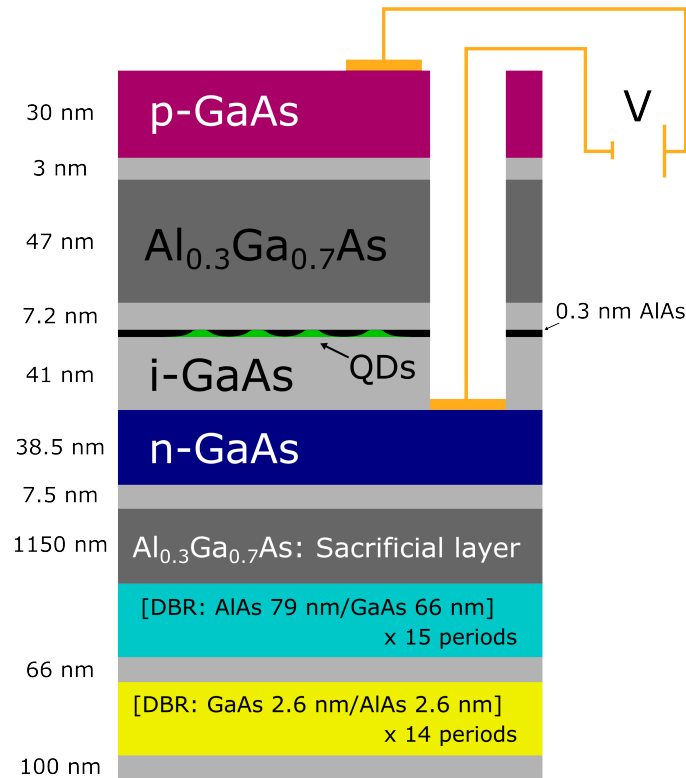


Figure 6.3: **Wafer composition of the  $p$ - $i$ - $n$  diode.** The GaAs membrane is designed to be around 180 nm-thick to support the single waveguide mode [36]. A layer of self-assembled InAs QDs is located at the center of the membrane for maximal coupling to the optical field. Two stacks of DBR layers are grown to increase the brightness of the QD by reflecting downward-scattered field. A 0.3 nm AlAs layer prevents occupation of the electron wetting layer states [152]. Applying a bias voltage  $V$  across the diode deterministically charges the QD with an electron.

Fig. 6.3 outlines the heterostructure of the  $p$ - $i$ - $n$  diode used for this work. A 174 nm-thin GaAs membrane spanning from the hole-rich  $p$ -doped to the electron-rich  $n$ -doped layers is grown on top of the Al<sub>0.3</sub>Ga<sub>0.7</sub>As sacrificial layer. The sacrificial layer is removed using hydrofluoric acid at later stages of fabrication to create suspended nanophotonic waveguides. Underneath this layer is an addition of two stacks of distributed Bragg reflectors (DBR), which can boost the reflection of downward-scattered light by 60% [35]. This is different than the DBR-absent wafer used in Fig. 1.2 and Chapter 3, and is shown to increase the grating coupler efficiency by 20% (from 60% to 80%) [35].

## 6.2.2 Optical and Spin Control Setup

### 6.2.2.1 Voigt Mount

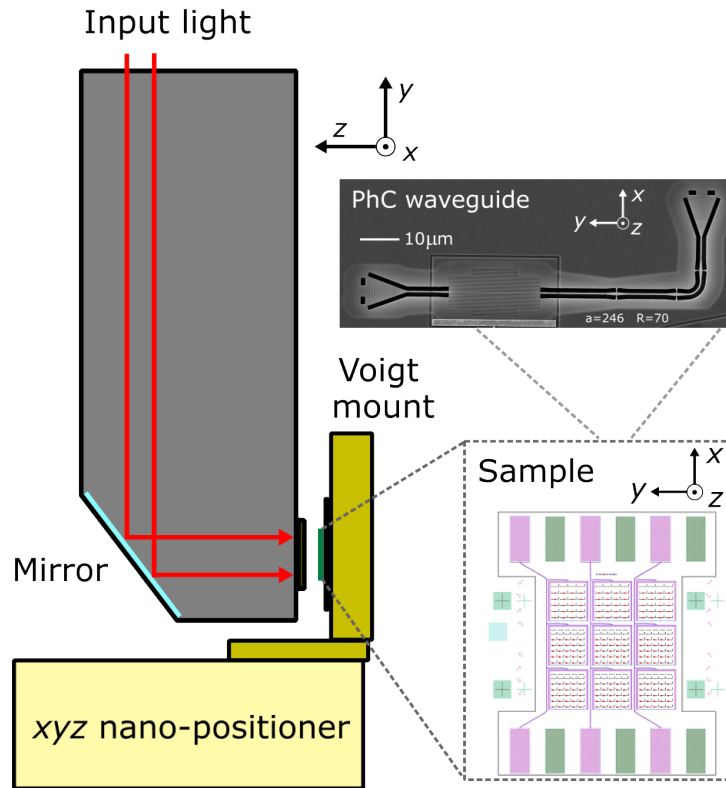


Figure 6.4: **New imaging objective with Voigt mount.** The input beam is reflected by an angled mirror and focused on the sample which is mounted sideways, such that a higher in-plane magnetic field up to 5 T can be applied. The Voigt mount is attached on top of three piezo-stages for positioning. The photonic-crystal waveguide (PCW) device investigated in this chapter has a lattice constant  $a = 246$  and hole radius  $R = 70$  in the slow light region.

As discussed in Sec. 6.1.2, one potential improvement to the spin coherence time is to adopt a higher magnetic field at 4 – 5 T. However, the maximum horizontal magnetic field exerted by the superconducting vector magnet in the cryostat is limited to 3 T, while the vertical magnetic field could reach up to 5 T. This motivates the design of a new sample holder<sup>11</sup> of which we called the “Voigt mount”, where the sample PCB can be mounted on the L-shaped holder (Fig. 6.4), allowing the higher vertical magnetic field to be utilized as the “in-plane” magnetic field relative to the QD growth axis ( $z$ -axis defined in Fig. 6.4).

A 45° angled silver mirror is used to deflect the downward laser beam horizontally. The deflected beam is then focused by an objective lens which has a working distance of 1.61 mm and numerical aperture (NA) of 0.68. It is important to note that the lens is aspheric thus it is not corrected for chromatic aberration<sup>12</sup>. The total loss of the new

<sup>11</sup>This is the cheaper option than replacing the magnet in the cryostat.

<sup>12</sup>One should expect that when switching the frequency of the probe laser, the focus changes. Evidently, the laser spot for an above-band laser could appear wildly out of place on the camera due to chromatic aberration.

imaging objective is estimated to be 4% including 3% loss from the silver mirror and 0.3% loss due to the objective lens. For optical experiments, the sample chip is cooled to 4.2 K inside a closed-cycle cryostat to suppress phonon scattering.

### 6.2.2.2 D-shaped Mirror

Another area of improvement for higher excitation and collection efficiencies is the replacement of a 50:50 beamsplitter (BS) that directs light in and out of the cryostat. Figure 6.5 compares the previous (a) and new (b) optical breadboard setups. In the previous design, the 50:50 BS (enlarged in Fig 6.5a for illustrative purposes) splits both the excitation and signal light by half, which halves not only the QD collection efficiency but also the available excitation power for spin control<sup>13</sup>. This is improved by replacing the BS with a D-shaped mirror<sup>14</sup>, whereby exploiting the 70  $\mu\text{m}$  spatial separation between the QD position and the collection grating coupler, both the excitation and collection efficiencies are enhanced by twofold.

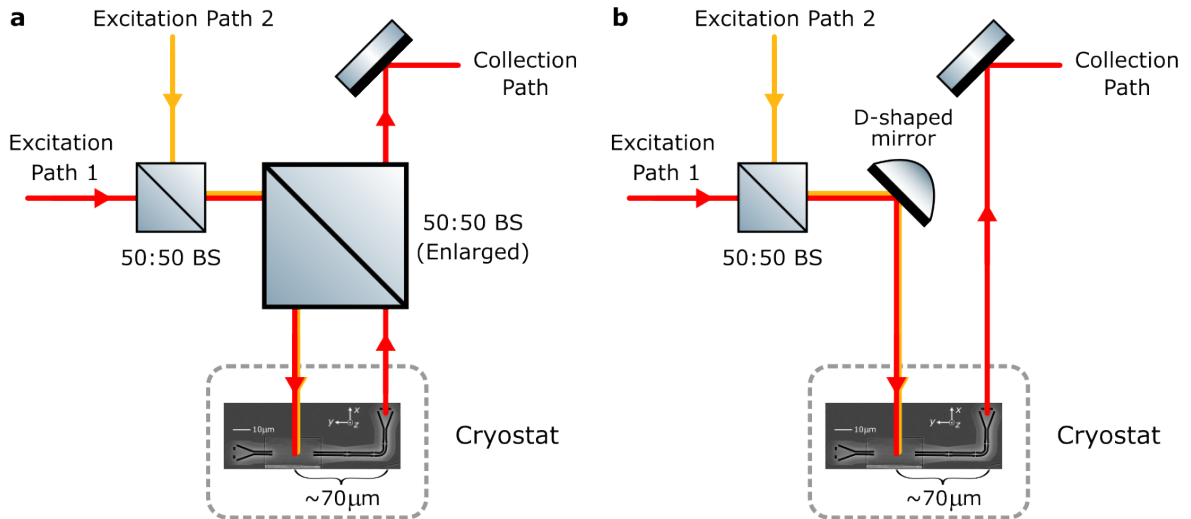


Figure 6.5: **New optical setup with a D-shaped mirror.** (a) Original design where both the excitation and fluorescence are halved by the 50:50 BS (enlarged). (b) The 50:50 BS replaced by a D-shaped mirror.

<sup>13</sup>There was always a shortage of rotation laser power due to the 4.5 dB EOM insertion loss, limiting the maximum spin Rabi frequency.

<sup>14</sup>This specific type of mirror helps separate closely spaced optical beams, as the reflective coating extends to the straight edge of the mirror.

### 6.2.2.3 Electron Spin Control Setup

In Chapter 3 and Ref. [18], microwave pulses required for optical hole spin control is generated by a “Poor man’s” setup<sup>15</sup> consisting of a microwave source, a splitter, a phase shifter and two microwave switches toggled by a custom-made field-programmable gate array (Cyclone V FPGA from Intel). For this setup, the minimum separation between pulses is 8 ns [52] due to non-ideal switches, making composite pulses impossible to apply. Furthermore, it allows only a change in the relative phase between pulses in the same sequence but not with different rotational axes. This means more sophisticated dynamical decoupling schemes like Carr-Purcell-Meiboom-Gill (CPMG) sequence which requires multi-axis spin rotations cannot be implemented without further modifications to the setup.

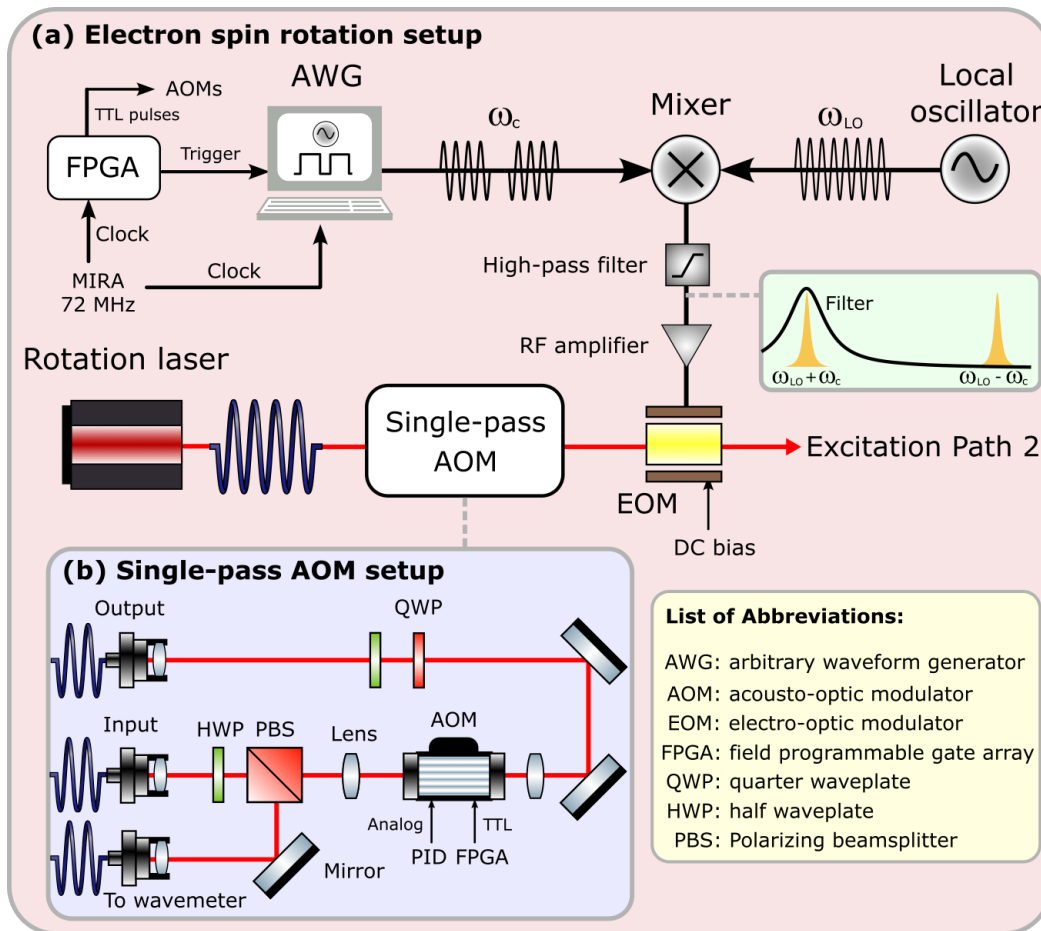


Figure 6.6: **Electron spin control setup.** A continuous-wave laser (Toptica CTL) passes through a single-pass AOM setup for slow power stabilization and wavelength locking, which is then modulated by a fiber-coupled EOM before being directed into the cryostat. The microwave pulses fed into the EOM are generated by an AWG mixed with another microwave source.

Fortunately, these issues are resolved by adopting an arbitrary waveform generator (Active Technologies AWG5064). Since it has a maximum 6 GHz output microwave frequency, the AWG output signal of carrier frequency  $\omega_c$  must be mixed with another microwave source (local oscillator in Fig. 6.6a) of frequency  $\omega_{LO}$  using a frequency mixer

<sup>15</sup>Please refer to Figure 6.4 in Ref. [52].

(Mini-Circuits ZX05-153LH-S+) to match the tens of GHz Zeeman ground-state splitting of the electron spin. The higher-frequency band  $\omega_c + \omega_{LO}$  is transmitted through a high-pass filter (Mini-Circuits ZVBP-10R5G-S+) and amplified (ixBlue DR-PL-20-MO at 15 dBm) to drive a fiber-coupled EOM (ixBlue NIR-MX800-LN-10).

The EOM then modulates the rotation laser to generate two sidebands for driving the two-photon Raman transition as illustrated in Fig. 3.18b. In the current work,  $\omega_c = 2.3$  GHz and  $\omega_{LO} = 8.55$  GHz are set to drive an electron Zeeman ground-state splitting of  $2(\omega_c + \omega_{LO}) = 21.7$  GHz at 4 T. The factor of 2 stems from frequency difference between two sidebands. To compensate for optical loss through the EOM, we modify the original double-pass AOM setup (Fig. 3.6b) to a single-pass configuration (Fig. 6.6b), which improves the maximum optical power available for spin control by 20%.

A clock signal of 72.63 MHz generated by a picosecond Ti:Sapphire laser (Coherent MIRA 900 P) is first divided into two signals via a BNC T-splitter to synchronize with the FPGA and AWG respectively. This enables synchronization between the MIRA optical pulses, spin readout and control pulses in the entanglement pulse sequence.

## 6.3 Electron Spin Spectroscopy

Due to a multitude of reasons listed in Sec. 6.1.2, it is favourable to opt for electron as the QD spin qubit. In the following sections, we perform optical spectroscopy to search for the QD negatively charged exciton state  $X^-$  and characterize its optical properties as well as optical cyclicity under an external in-plane magnetic field.

### 6.3.1 Quantum Dot Search

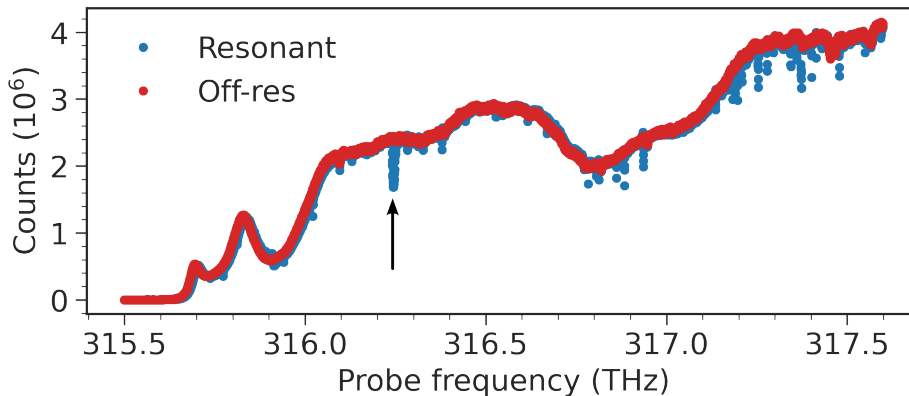


Figure 6.7: **Frequency-dependent waveguide transmission.** Scanning the frequency of a probe laser coupled to the waveguide exposes transmission dips corresponding to resonant frequencies of QDs. This scan is performed on the PCW in Fig. 6.4 at 1.34 V with  $\mathbf{B}_x = 0$  T. The waveguide cut-off frequency (band-edge) is 315.65 THz. Off-resonant voltage is 1 V. Arrow points to a potential  $X^-$  candidate.

QD search typically begins with a coarse waveguide transmission measurement at a chosen bias voltage to identify the waveguide band-edge [119, 52], see Fig. 6.7 for example. A good rule of thumb is to search for large transmission dips that are spectrally close (blue-detuned by  $\sim 1$  THz) to the band-edge. Large transmission dips arise from the destructive interference between the scattered field from a well-coupled QD and the probe field, which could signify a high waveguide-coupling efficiency  $\beta$  as well as a low spectral diffusion rate. A large  $\beta$  does not necessarily guarantee a high optical cyclicity<sup>16</sup> [52], but is nevertheless essential to the light-matter interaction and overall collection efficiency. QDs spectrally close to the band-edge benefit from Purcell enhancement as the group velocity of the guided light approaches zero (slow light regime, Sec. 1.4).

Once such a QD is found, an external in-plane magnetic field of  $\mathbf{B}_x = 4$  T is applied to zeeman-split any charged state to reveal multiple transmission dips in a finer frequency scan. Ideally two transmission dips are expected since the probe laser coupled to the waveguide through the grating couplers is either Y- or X-polarized, corresponding to either the two outermost vertical or inner diagonal transitions<sup>17</sup>. In practice, however,

<sup>16</sup>Since  $\beta = \beta_{\parallel} + \beta_{\perp}$  includes the coupling efficiency of both Y- and X-polarized light, while optical cyclicity is given by their ratios  $C \approx \beta_{\parallel}/\beta_{\perp}$ . For QDs located spatially close to the air holes,  $\beta_{\perp}$  ( $\beta_{\parallel}$ ) is high (low), leading to small cyclicity but decent  $\beta$ . Note that we take  $\beta_{\parallel} = \beta_x$  and  $\beta_{\perp} = \beta_y$  following the orientation in Fig. 1.7.

<sup>17</sup>For a QD located at the center of a photonic-crystal waveguide with the waveguide Y-axis aligned with its Y-dipole [ $1\bar{1}0$ ] (X-dipole [ $110$ ]), we expect to observe two transmission dips in the outermost (inner) transitions.

this is tricky to observe since these dips are only visible at the co-tunneling voltages in which the spin state can be repopulated and continuously driven.

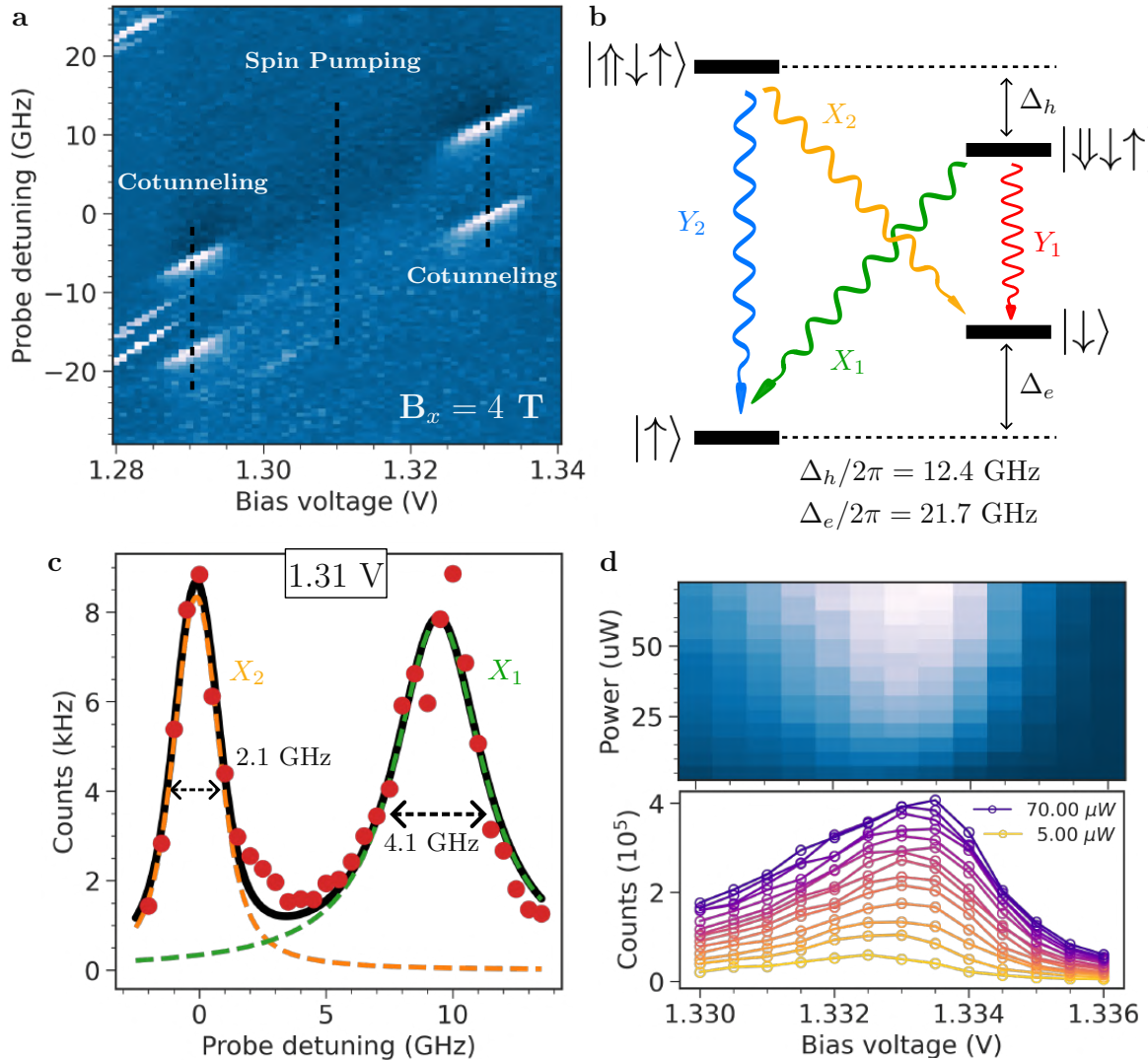


Figure 6.8:  $X^-$  spectroscopy at  $B_x = 4 \text{ T}$ . (a) Frequency and voltage scans revealing the  $X^-$  plateau maps. Measured with APD. Central frequency is 316.2825 THz. (b) Energy levels of  $X^-$ . (c) Fluorescence from the X-polarized transitions at the spin-pumping voltage 1.31 V. Dashed curves are deconvoluted Voigt lineshapes obtained from the fit (black solid line). (d) Fluorescence from  $X_2$  at different probe powers and bias voltages. Only a small amount  $< 2 \text{ mV}$  of resonance shift is observed at 70  $\mu\text{W}$ .

Figure 6.8a shows a fine resonant transmission scan over the probe detuning and bias voltages, which unveils two spectral lines marking two optical transitions of  $X^-$ . A follow-up two-color spin pumping measurement indicates that they are X-polarized. The middle section of both lines appear to be cut off, since the band structure of the diode is tilted at these voltages such that electron co-tunneling is suppressed [42]. This regime of voltages is referred to as the spin pumping region, and has the voltage needed for the entanglement experiment since the electron spin is shielded against tunneling processes which hinders its  $T_1$  time.

From this point onward, we perform two-color spin pumping experiments by exciting the  $X^-$  state on top using two continuous-wave lasers. Exciting on top means the polar-

ization of the probe lasers is not restricted to the grating polarization. Two orthogonally-polarized lasers can then be used to drive  $\Lambda$ -level systems, unfolding all four optical transitions thanks to electron  $\Delta_e$  and hole  $\Delta_h$  Zeeman splittings (Fig. 6.8b). Note that Fig. 6.8b is the level scheme of  $X^-$  expressed in the spin  $x$ -eigenbases under the in-plane magnetic field  $\mathbf{B}_x$ , here for brevity in the rest of the chapter we omitted the subscript.

Figure 6.8c shows the resonance fluorescence spectra of the inner diagonal transitions of  $X^-$  by two-color spin pumping at 1.31 V (corresponds to the spin-pumping voltage denoted in Fig. 6.8a). Fitting the spectra with two Voigt lineshapes with a lifetime of the  $X_2$  transition  $\tau_0 \approx 235$  ps (estimated in Sec. 6.3.2) yields a 2.1 GHz FWHM with an inhomogeneous broadening of  $\sigma_e/2\pi = (532 \pm 91)$  MHz for the  $X_2$  transition.

Additionally, we record the resonance fluorescence spectra of  $X^-$  at  $\mathbf{B}_x = 0$  T at different excitation powers of a continuous-wave probe laser. Here a slight shift in QD resonance ( $< 2$  mV) is observed at 12 times of the excitation power, indicating power tuning is less of an issue compared to the previous sample<sup>18</sup>. This measurement is carried out at zero magnetic field to minimize spin dragging effect<sup>19</sup>.

### 6.3.2 Optical Cyclicity

In this section, we follow the approach in Ref. [20] to extract the optical cyclicity of  $X^-$ . The idea is to first measure both its radiative lifetime  $\tau_o = 1/\Gamma$  as well as the radiative decay rate  $\gamma_Y$  of vertical transitions. From here, the cyclicity  $C \equiv \gamma_X/\gamma_Y = (\Gamma - \gamma_Y)/\gamma_Y$  can be estimated.

The radiative lifetime of  $X^-$  is measured using  $p$ -shell excitation by the MIRA pulsed laser. A resonant peak of  $X^-$  at  $\mathbf{B}_x = 0$  T is first marked on a spectrometer using a continuous-wave narrowband laser. With the narrowband laser turned off, the MIRA laser is used to scan around  $\approx 20$  nm blue-detuned from the resonance to recover the peak. The signal is then maximized with optical alignment. The time-resolved signal can then be measured with APDs<sup>20</sup> (Fig. 6.9). Fitting the fluorescence decay with the formula  $I(t) = I_0 e^{-t/\tau_o} + I_{\text{offset}}$  gives  $\tau_o = (235.1 \pm 0.7)$  ps, indicating a waveguide-induced Purcell enhancement of 4.2 compared to  $\tau \approx 1$  ns in bulk.

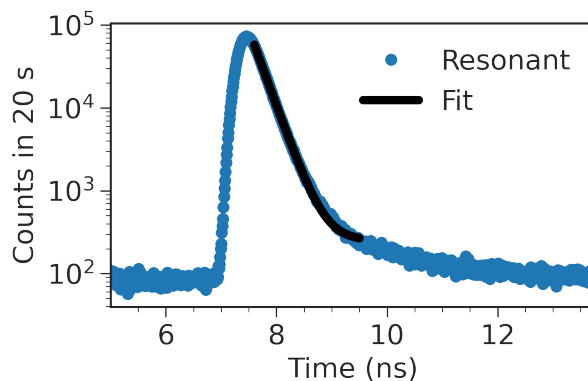


Figure 6.9: **Time-resolved fluorescence decay of  $X^-$  using a picosecond laser.** The trion lifetime is extracted by fitting the decay with a single exponential. Measured by exciting the QD  $p$ -shell at 1.331 V with  $\mathbf{B}_x = 0$  T and APD.

<sup>18</sup>See Fig. 5.5 in Ref. [52].

<sup>19</sup>See Fig. S2 in Ref. [153], for instance.

<sup>20</sup>Ideally with SNSPDs which have a lower timing jitter 260 – 290 ps (APD: 350 ps) [52].

To extract the radiative decay rate  $\gamma_Y$ , we perform a power-dependent two-color spin-pumping measurement, where the optical spin pumping rate  $\gamma_{\text{osp}}$  depends on  $\gamma_Y$  and the driving Rabi frequency  $\Omega_p$  [20]:

$$\gamma_{\text{osp}} = \gamma_Y \int_{-\infty}^{\infty} \frac{\Omega_p^2}{2\Omega_p^2 + \Gamma^2 + 4\delta_e^2} N(\delta_e, \sigma_e) d\delta_e. \quad (6.2)$$

Figure 6.10a shows the histogram of the measurement sequence, which begins by optically pumping  $Y_2$  transition (light blue region) to prepare the state  $|\uparrow\rangle$ . A 400 ns probe pulse (yellow region) is then applied to drive the  $X_2$  transition of optical Rabi frequency  $\Omega_p = \Gamma\sqrt{P/P_{\text{sat}}}$  controlled by the laser power  $P$  and saturation power  $P_{\text{sat}}$ . At each power,  $\gamma_{\text{osp}}$  is extracted by performing a single exponential fit to the fluorescence decay during the probe (black solid line in Fig. 6.10a). Henceforth a list of fitted values of  $\gamma_{\text{osp}}$  is obtained, which is then fitted using Eq. (6.2) to eventually extract  $\gamma_Y$ , with free variable  $P_{\text{sat}}$  and fixed  $\sigma_e/2\pi = (532 \pm 91)$  MHz (estimated in Sec. 6.3.1).  $\Gamma = 1/\tau_o = (4.25 \pm 0.01)$  ns<sup>-1</sup> is the total trion decay rate inferred from its lifetime.

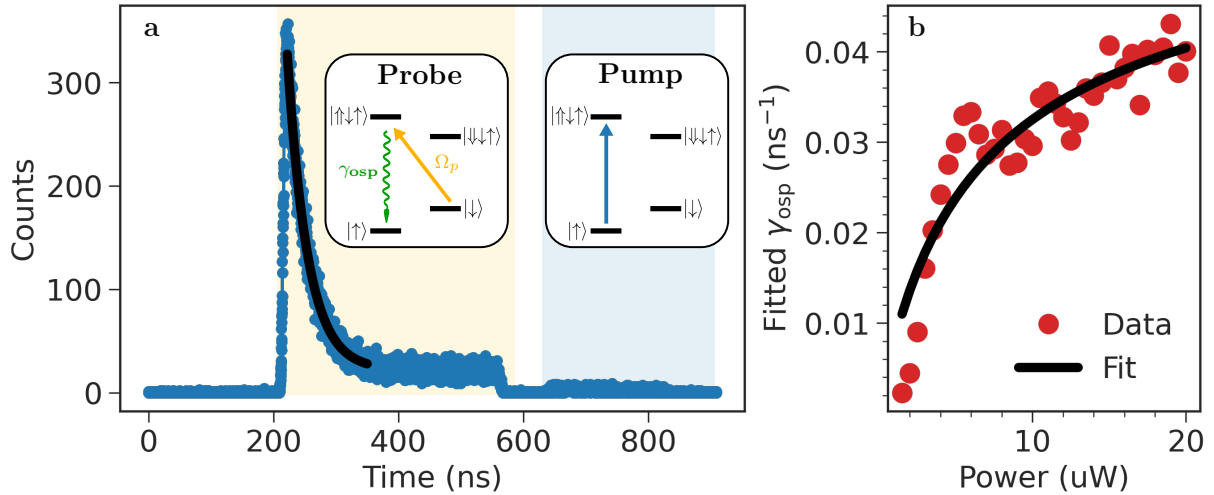


Figure 6.10: **Two-color spin-pumping measurements to extract  $\gamma_Y$ .** (a) Time-resolved histogram of the pulse sequence. The electron is optically pumped to  $|\uparrow\rangle$  (light blue region) and probed with a 400 ns pulse (yellow) at  $6.5 \mu\text{W}$ .  $\gamma_{\text{osp}}$  is estimated by fitting the decay during the probe pulse. (b) Extracted  $\gamma_{\text{osp}}$  at different probe powers. Fitting with Eq. (6.2) yields the radiative decay rate  $\gamma_Y$ .

From the fit in Fig. 6.10b we estimated  $\gamma_Y = (0.114 \pm 0.009)$  ns<sup>-1</sup> yielding an optical cyclicity of

$$C = \frac{\Gamma - \gamma_Y}{\gamma_Y} = 36.3 \pm 2.9, \quad (6.3)$$

which is 2.5 times larger than that of the previous QD reported in Chapter 3. The current QD is likely located in close proximity to the photonic-crystal waveguide center where  $\gamma_Y$  is strongly inhibited [20], while the waveguide mode is aligned with the X-dipole [110] due to the waveguide being 90°-rotated with respect to Fig. 1.7.

## 6.4 Electron Spin Control

Coherent control of the electron spin ground states is implemented optically via two-photon Raman transitions using the same approach introduced in Sec. 3.5. The only difference is in the control pulse sequence where two additional pulses are included to “cool” the nuclear spin ensembles [97] in the vicinity of the electron spin in order to extend its spin dephasing time  $T_2^*$ . In this section, we demonstrate coherent optical spin control with the inclusion of nuclear spin cooling techniques.

### 6.4.1 Spin Rabi Oscillations

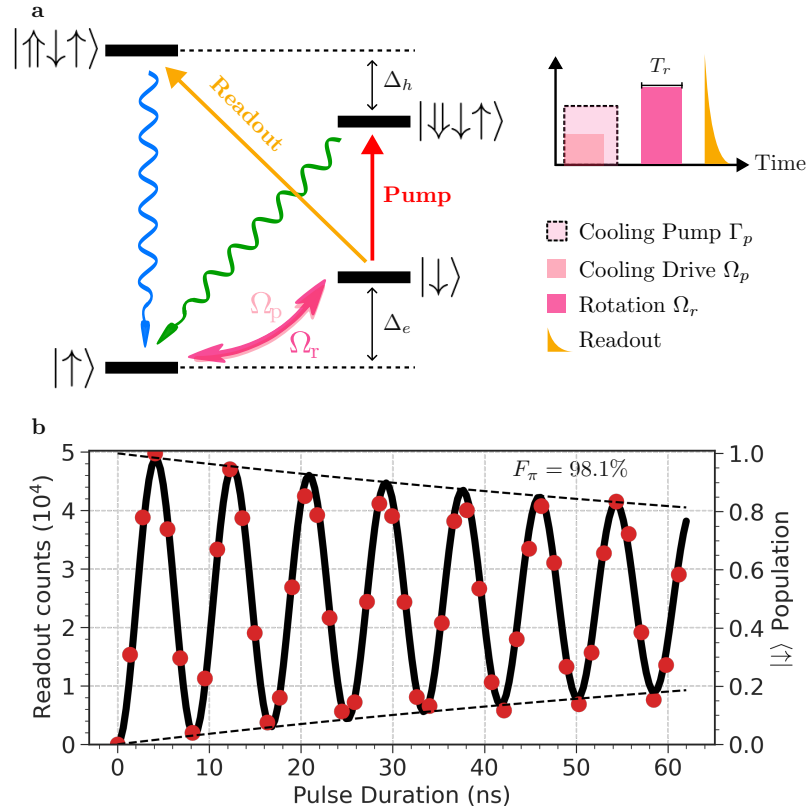


Figure 6.11: **Electron spin Rabi oscillations.** (a) Energy levels of  $X^-$  under the Voigt magnetic field with nuclear cooling. A  $1.2 \mu\text{s}$  pulse drives  $|\downarrow\rangle \rightarrow |\downarrow\uparrow\rangle$  with optical spin pumping rate of  $\Gamma_p$  into  $|\uparrow\rangle$ . When applied together with a  $1.1 \mu\text{s}$  rotation pulse  $\Omega_p$ , the nuclear spins gradually flip and converge to a steady-state, narrowing the Overhauser field fluctuations  $\sigma_{\text{OH}}$ . (b) After nuclear cooling, a spin control pulse of varying duration  $T_r$  is applied to exhibit coherent Rabi oscillations between the electron ground states, with  $\pi$ -fidelity of  $F_\pi = 98.1\%$  at  $T_r \approx 4 \text{ ns}$ . Curves are explained in the text.

Fig 6.11a shows the level diagram of the QD electron spin under  $\mathbf{B}_x = 4 \text{ T}$ . To observe Rabi flops of the electron ground states, a  $1.2 \mu\text{s}$  long pulse is first applied to resonantly drive the lowest energy transition  $Y_1$ . This pulse has two particular uses: First, it initializes the electron state in  $|\uparrow\rangle$  via optical spin pumping. Second, when it is applied simultaneously with another  $1.1 \mu\text{s}$  rotation pulse of spin Rabi frequency  $\Omega_p$ <sup>21</sup> (“Cooling

<sup>21</sup>In practice  $\Omega_p \neq \Omega_r$  could be different and are individually optimized. The cooling pump is 100 ns longer than the drive to prepare  $|\uparrow\rangle$ .

Drive” in Fig. 6.11a), the nuclear spins are dragged towards the steady state  $I_z$  due to stimulated Raman scattering [97], thus narrowing the nuclear noise spectrum. Once the electron spin is prepared, a rotation pulse of duration  $T_r$  is applied to coherently transfer its population to  $|\downarrow\rangle$  with spin Rabi frequency  $\Omega_r$ . The rotation laser is 650 GHz red-detuned from the readout transition  $X_1$ :  $|\downarrow\rangle \leftrightarrow |\uparrow\downarrow\uparrow\rangle$ , while its polarization is optimized to be circular by maximizing  $X^-$  fluorescence under the Faraday magnetic field  $\mathbf{B}_z$ .

As the X-polarized transitions are now spin-cycling (Sec. 6.3.2), the  $|\downarrow\rangle$  population is probed by driving the  $X_1$  transition via a 200 ns pumping pulse (orange). Here two narrowband 3 GHz FWHM etalon filters are used to detect photons emitted from the cycling transition. The fluorescence signal gated on first 50 ns of the readout pulse at different values of  $T_r$  is recorded in Fig. 6.11b.

The  $\pi$ -rotation fidelity is extracted similarly by numerically fitting the data using Eq. (3.25) with  $\gamma_r = 0$ , as discussed in Sec. 3.5. For the fit we take  $\sigma_{\text{OH}} = \sqrt{2}/T_2^* \approx 2\pi \times 7$  MHz for  $T_2^* = 33$  ns. The recorded Rabi oscillations are tightly bounded by the decay envelopes  $\frac{1}{2}(1 \pm e^{-3\kappa T_r/2})$  (dashed lines) suggesting that  $\Omega_r \gg 1/T_2^*$ <sup>22</sup> and  $\kappa$  is the prevalent damping mechanism. In this limit, the rotation fidelity is described by

$$F_\pi = \frac{1}{2}(1 + e^{-\frac{3\kappa T_\pi}{2}}), \quad (6.4)$$

with  $T_\pi = \pi/\Omega_r$  as the duration of the  $\pi$ -pulse. From the numerical fit, we extracted  $F_\pi = (0.981 \pm 0.006)$  with  $\kappa = (0.005 \pm 0.0007)$  ns<sup>-1</sup><sup>23</sup>. Apart from the rotation fidelity, another useful metric that benchmarks the efficacy of spin control is the quality factor  $Q \equiv T_{1/e}/T_\pi$ <sup>24</sup> [125] which signifies the total number of  $\pi$  pulses the spin system can be driven before the damped spin coherence reaches  $1/e$  of its original value, and  $T_{1/e} \equiv 2/(3\kappa)$  is the time constant for the exponential term in Eq. (6.4) to decay by a factor of  $1/e$ . Eq. (6.4) can then be rewritten as

$$F_\pi = \frac{1}{2}(1 + e^{-\frac{1}{Q}}), \quad (6.5)$$

which recovers the definition in Ref. [125]. From the fitted decay envelope, we extracted  $Q \approx 31.8 \pm 0.3$ <sup>25</sup>. A second approach is to theoretically estimate  $F_\pi$  given  $\kappa$  using Eq. (4.32) derived in Sec. 4.3.5 with  $\gamma_r = 0$  and  $T_2^* = 33.3$  ns. This predicts  $F_\pi = (0.9865 \pm 0.0015)$  which is again consistent with the experimentally estimated value. The demonstrated values for  $F_\pi$  and  $Q$  are comparable to those obtained for electron spins in Ref. [125] at a similar spin Rabi frequency with a bulk sample, which suggests that embedding the QD in a nanophotonic waveguide might not influence the power-dependent spin-flip rate  $\kappa$ . Instead, this could indicate the spin-flip mechanism is associated with optical control on the wafer heterostructure (See Appendix C for a possible origin of the spin-flip process).

## 6.4.2 Ramsey Interferometry

When numerically fitting the Rabi oscillations, an inhomogeneous spin dephasing time of  $T_2^* = 33$  ns was adopted for Gaussian averaging of the Overhauser field fluctuations.

<sup>22</sup>This condition implies the rotation axis  $\hat{n}$  is not tilted away from  $\hat{y}$ .

<sup>23</sup>This corresponds to a laser-induced  $T_1$  time of 200 ns.

<sup>24</sup>Note that the definition for  $T_\pi$  we used here is different from Refs. [125, 154] as a different fitting formula  $a \cos(2\pi\Omega_r t)e^{-t/T_{1/e}}$  for Rabi oscillations was used.

<sup>25</sup>As a comparison,  $Q = 7.1 \pm 0.5$  for the hole spin investigated in Sec. 3.5, when the readout gating is delayed by 50 ns.

This parameter is experimentally measured by performing Ramsey interferometry, which is investigated in this section.

The general idea of a Ramsey sequence is to project the electron spin on a superposition state under an external magnetic field and observe how its coherence decays over time. The pulse sequence reads as:  $\pi/2 - \tau - \pi/2$  where  $\tau$  is the time allowed for the spin to precess. The  $\pi/2$ -pulses shuffle the spin between the superposition states and the poles. The time taken for the spin coherence to fall to  $1/e$  of its original value is defined as the spin dephasing time  $T_2^*$ , which originates from slow noises in the effective magnetic field exerted by nearby nuclear spins (Overhauser field).

Using the formalism of the two-photon Raman scheme (Sec. 3.5), the unitary transformation of the Ramsey pulse sequence under a two-photon detuning  $\Delta_{\text{MW}}$  is mathematically expressed by

$$\hat{\mathcal{U}}_{\text{Ramsey}} = \hat{R}_y\left(\frac{\pi}{2}, \Delta_{\text{MW}}\right) \hat{T}(\tau, \Delta_{\text{MW}}) \hat{R}_y\left(\frac{\pi}{2}, \Delta_{\text{MW}}\right). \quad (6.6)$$

Here  $\hat{R}_y\left(\frac{\pi}{2}, \Delta_{\text{MW}}\right)$  performs a  $\pi/2$  rotation on the spin around an axis  $\hat{n}$  which is slightly tilted by  $\Delta_{\text{MW}}$ . Its matrix form is derived from Eq. (3.21) [52]:

$$\begin{aligned} \hat{R}_y(\theta, \Delta_{\text{MW}}) &= e^{-iT_r \hat{H}_s} = \cos(\theta) \hat{\mathcal{I}} - i \sin(\theta) \frac{\Omega_r \hat{\sigma}_y - \Delta_{\text{MW}} \hat{\sigma}_z}{\sqrt{\Omega_r^2 + \Delta_{\text{MW}}^2}}; \\ \hat{n} &= \frac{\Omega_r}{\sqrt{\Omega_r^2 + \Delta_{\text{MW}}^2}} \hat{y} - \frac{\Delta_{\text{MW}}}{\sqrt{\Omega_r^2 + \Delta_{\text{MW}}^2}} \hat{z}, \end{aligned} \quad (6.7)$$

for  $\theta \equiv \frac{1}{2} T_r \sqrt{\Omega_r^2 + \Delta_{\text{MW}}^2} = \frac{1}{2} T_r \tilde{\Omega}_r$  is the pulse area driven by a  $T_r$  long square pulse with an effective spin Rabi frequency  $\tilde{\Omega}_r$ .

After applying the first  $\hat{R}_y\left(\frac{\pi}{2}, \Delta_{\text{MW}}\right)$  pulse on an electron spin initialized in  $|\uparrow\rangle$ , it is allowed to precess around the  $-\Delta_{\text{MW}} \hat{z}$  axis (with  $\Omega_r = 0$  in Eq. (6.7)) described by the time-evolution operator  $\hat{T}(\tau, \Delta_{\text{MW}}) \equiv \exp\left(\frac{1}{2} i \Delta_{\text{MW}} \tau \hat{\sigma}_z\right)$ . For an initial state  $\rho_o = |\uparrow\rangle\langle\uparrow|$ , the population in  $|\downarrow\rangle$  can be approximated by

$$\rho_{|\downarrow\rangle\langle\downarrow|} = |\langle\downarrow|\hat{\mathcal{U}}_{\text{Ramsey}} \rho_o \hat{\mathcal{U}}_{\text{Ramsey}}^\dagger|\downarrow\rangle|^2 = \frac{1}{2} [1 + \cos(\tau \Delta_{\text{MW}})]. \quad (6.8)$$

In deriving Eq. (6.8) we assume  $\Delta_{\text{MW}} = 0$  during the rotational pulses which holds in the limit of  $\Omega_r \gg |\Delta_{\text{MW}}|$ <sup>26</sup>.

When the bi-chromatic laser is on resonance with the two-photon transition, the only contribution to the laser detuning is the parallel component of the Overhauser noise (i.e.,  $\Delta_{\text{MW}} = \Delta_{\text{OH}}^\parallel$ ) resulting from non-zero nuclear quadrupolar fields [151]. Therefore, Eq. (6.8) is averaged over a Gaussian Overhauser distribution  $N(0, \sigma_{\text{OH}})$  as previously discussed, resulting in a Gaussian decay:  $\rho_{|\downarrow\rangle\langle\downarrow|} = \frac{1}{2} (1 + e^{-(\tau/T_2^*)^2})$  wherein the spin dephasing time is inferred from  $T_2^* \equiv \sqrt{2}/\sigma_{\text{OH}}$ . At  $\tau = 0$ , the Ramsey sequence drives an effective  $\pi$ -rotation thus  $\rho_{|\downarrow\rangle\langle\downarrow|} = 1$  as expected.

However, when driven off-resonantly with a fixed laser detuning of  $\Delta_0$ , Eq. (6.6) becomes  $\hat{R}_y\left(\frac{\pi}{2}, 0\right) \hat{T}(\tau, \Delta_0 + \Delta_{\text{OH}}^\parallel) \hat{R}_y\left(\frac{\pi}{2}, 0\right)$ , assuming  $|\Delta_{\text{MW}}| = |\Delta_0 + \Delta_{\text{OH}}^\parallel| \ll \Omega_r$  during the rotation pulses. The average  $|\downarrow\rangle$  population is then

$$\rho_{|\downarrow\rangle\langle\downarrow|} = \frac{1}{2} [1 + \cos(\Delta_0 \tau) e^{-(\tau/T_2^*)^2}], \quad (6.9)$$

<sup>26</sup>Intuitively this means the axis of spin rotation  $\hat{n}$  is only slightly perturbed in  $\hat{z}$  and is mostly aligned with  $\hat{y}$ .

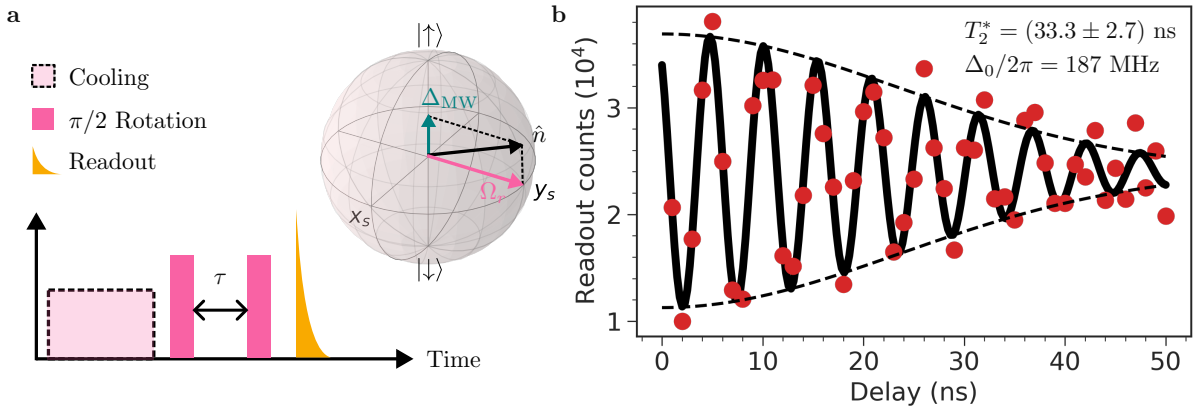


Figure 6.12: **Detuned Ramsey sequence to measure  $T_2^*$ .** (a) Pulse sequence. The electron spin initialized in  $|\uparrow\rangle$  with cooling (pump and drive in Fig. 6.11a) is optically driven by two  $\pi/2$ -pulses that are off-resonant by  $\Delta_{MW} = \Delta_0 + \Delta_{OH}^{\parallel}$  where  $\Delta_{OH}^{\parallel}$  is the drift in electron spin resonance owing to nuclear Overhauser fields. The off-axis  $\pi/2$  rotation on the electron spin causes its precession on the equator with frequency  $\Delta_{MW}$  during time  $\tau$ . (b) Measured counts from reading out  $|\downarrow\rangle$  as a function of pulse delay  $\tau$ . Detuning in the two-photon drive  $\Delta_0$  leads to fast oscillation in the  $|\downarrow\rangle$  population whereas  $\Delta_{OH}^{\parallel}$  results in a slow Gaussian decay in the spin coherence.

which oscillates with frequency  $\Delta_0$  bounded by the  $T_2^*$  decay envelope<sup>27</sup>.

Figure 6.12a depicts the experimental pulse sequence for the off-resonant Ramsey experiment. The electron spin is initially prepared in  $|\downarrow\rangle$  and projected to the equatorial state. The microwave frequency which modulates the optical rotation pulses is set to be detuned from resonance by 100 MHz. Together with random drifts  $\Delta_{OH}^{\parallel}$  from the Overhauser fields, this results in a total two-photon detuning of  $\Delta_{MW}$  which tilts the spin rotational axis  $\hat{n}$ . Before applying the  $\pi/2$  control pulses, the electron spin is cooled and prepared in the  $|\uparrow\rangle$  similar to the Rabi-flop measurement (Sec. 6.4). The cooling drive  $\Omega_p$  is resonant to the two-photon transition such that the spin cooling becomes effective.

By sweeping the delay  $\tau$  between two  $\pi/2$  pulses, we observe damped oscillations as anticipated in Eq. (6.9). Fitting the data with the formula  $A \cos(2\pi\Delta_0\tau)e^{-(\tau/T_2^*)^2} + B$ , we extracted  $T_2^* = (33.3 \pm 2.7) \text{ ns}$  and  $\Delta_0/2\pi = (187 \pm 0.9) \text{ MHz}$ . The small deviation between  $\Delta_0$  and the two-photon detuning due to the modulation frequency  $\Delta_0^{\text{RF}} = 2 \times 100 \text{ MHz}$  could be ascribed to nuclear spin feedback effects [154], which by altering the Overhauser fields the electron precession frequency is changed.

### 6.4.3 Hahn-echo Visibility

As established in Sec. 3.5.3, the Hahn-echo visibility more or less constrains the maximum fidelity measured in the equatorial basis. In this section, we measure and optimize echo visibilities for the  $n = 1$ - and 2-photon entanglement protocols. In general, the number of  $\pi$ -pulses in an  $n$ -photon GHZ state generation protocol is  $2n - 1$ .

<sup>27</sup>The two-photon Raman scheme operates in the rotating frame of the drive. At zero detuning  $\Delta_0 = 0$  there is no Larmor precession since the drive coincides with the rotating frame of the precessing electron. With non-zero detuning  $\Delta_0 \neq 0$ , the drive rotates at a different frequency than the electron, thus the electron state appears to oscillate with  $\Delta_0$  [154].

Figure 6.13 measures the spin-echo visibility for  $n = 1$ - and  $n = 2$ -photon protocols at the pulse delay  $\tau = 29$  ns<sup>28</sup>. To optimize the microwave waveform peak-to-peak voltage  $V_{pp}$ , we run a Hahn-echo sequence where the last  $\pi/2$  pulse is in phase with the previous two pulses (Fig. 6.13a), thus in the ideal case the sequence should drive an effective  $2\pi$  rotation on the spin state initialized in  $|\uparrow\rangle$ . The optimal  $V_{pp}$  is therefore the voltage required to minimize readout counts from  $|\downarrow\rangle$ .

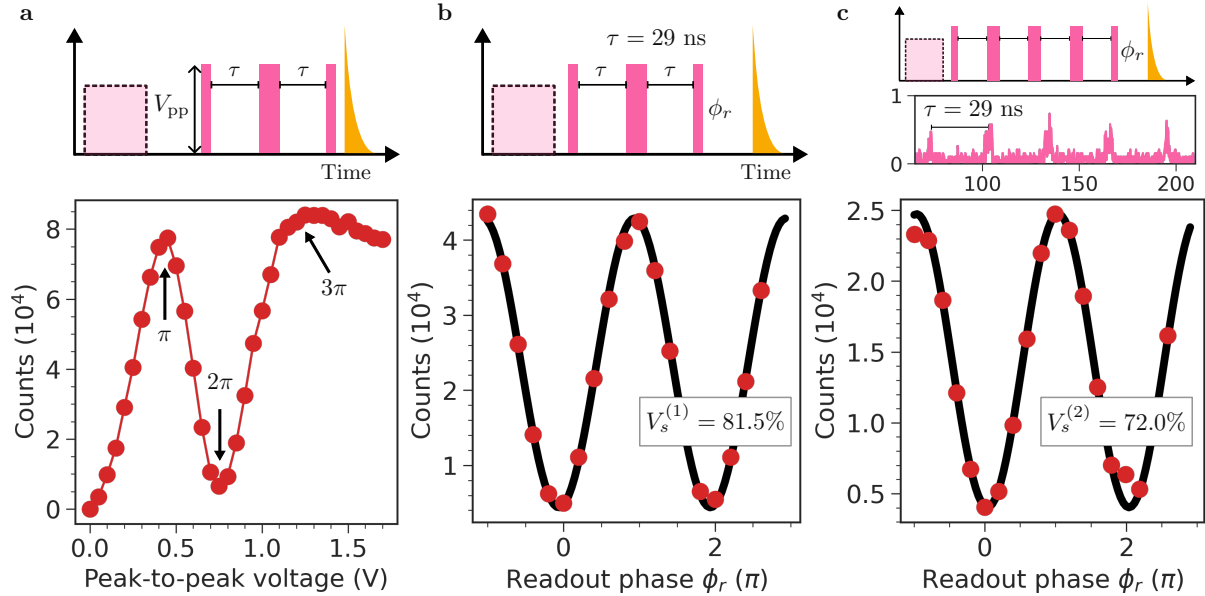


Figure 6.13: **Spin-Echo at fixed delay  $\tau = 29$  ns.** (a) Increasing the peak-to-peak voltage of the microwave waveform for the rotational pulses changes the total pulse area of the echo sequence, revealing Rabi-like oscillations. All pulses are in-phase thus the optimal  $V_{pp}$  corresponds to the voltage for a  $2\pi$  rotation. (b) Hahn-echo visibility measurement by varying the relative phase  $\phi_r$  of the last  $\pi/2$  pulse for  $n = 1$ -photon entanglement protocol. Data fitted using  $A\sin^2(B\phi_r + \phi_0) + C$  with free parameters  $A, B, C$  and  $\phi_0$ . (c) Visibility measurement for  $n = 2$  in which two additional  $\pi$ -pulses are included.

With set values for  $V_{pp}$  and  $\tau$ , we perform the same echo sequence but vary the relative phase of the last  $\pi/2$  pulse  $\phi_r$ <sup>29</sup> to project the equatorial spin state into either the optically dark state  $|\uparrow\rangle$  (with  $\phi_r = 2n\pi$  corresponding to an effective  $2n\pi$ -rotation for  $n \in \mathbb{Z}$ ) or bright state  $|\downarrow\rangle$  (with  $\phi_r = (2n - 1)\pi$  for an effective  $(2n - 1)\pi$ -rotation). From fitting the data in Figs. 6.13b-c we find high echo visibilities of  $V_s^{(1)} = (81.5 \pm 1.5)\%$  and  $V_s^{(2)} = (72.0 \pm 1.6)\%$  for the 1-photon and 2-photon experiments, respectively. In particular,  $V_s^{(1)}$  is comparable to the value obtained in Ref. [151] at the same magnetic field (4 T in Voigt geometry) and echo delay ( $\tau_{\text{echo}} = 2\tau \approx 58$  ns).

Theoretically, the maximum attainable visibility  $V_{s,\text{max}}^{(n)}$  for a spin-echo with  $(2n - 1)$  middle  $\pi$ -pulses can be inferred from the spin Rabi oscillations alone, as the echo sequence can be thought of as splitting the singular pulse in a Rabi-flop measurement into three pulses which are distant in equal time intervals. The visibility of the Rabi-flop curve is an upper bound for  $V_s$  since errors from imperfect pulse shaping and finite homogeneous

<sup>28</sup>The choice of this particular value for  $\tau$  will be shortly discussed in the next figure.

<sup>29</sup>The azimuthal angle of the  $\pi/2$  pulse is  $\phi_s = \phi_r + \frac{\pi}{2}$  where  $\phi_r$  is defined as the relative phase shift from previous rotational pulses, with  $\pi/2$  the azimuthal angle for previous rotations along the  $+y$  axis, see Eq. (3.21).

dephasing time  $T_2$  have little impact on the Rabi oscillations. For instance, as  $V_s^{(1)}$  measures the contrast in readout counts of  $|\downarrow\rangle$  between driving an effective  $\pi$ - and  $2\pi$ -pulses, an upper bound  $V_{s,\max}^{(1)}$  is found to be

$$V_{s,\max}^{(1)} = \frac{\rho_{|\downarrow\rangle\langle\downarrow|}(T_\pi) - \rho_{|\downarrow\rangle\langle\downarrow|}(T_{2\pi})}{\rho_{|\downarrow\rangle\langle\downarrow|}(T_\pi) + \rho_{|\downarrow\rangle\langle\downarrow|}(T_{2\pi})} = \frac{e^{-\frac{1}{Q}} + e^{-\frac{2}{Q}}}{2 + e^{-\frac{1}{Q}} - e^{-\frac{2}{Q}}} = 94.2\%, \quad (6.10)$$

where the readout counts from driving pulses of durations  $T_\pi$  and  $T_{2\pi}$  are expressed by the Rabi decay envelopes, as in Eq. (6.4):

$$\begin{aligned} \rho_{|\downarrow\rangle\langle\downarrow|}(T_\pi) &= \frac{1}{2}(1 + e^{-\frac{3\kappa T_\pi}{2}}) = \frac{1}{2}(1 + e^{-\frac{1}{Q}}); \\ \rho_{|\downarrow\rangle\langle\downarrow|}(T_{2\pi}) &= \frac{1}{2}(1 - e^{-\frac{3\kappa T_{2\pi}}{2}}) = \frac{1}{2}(1 - e^{-\frac{2}{Q}}). \end{aligned} \quad (6.11)$$

Likewise, for  $n$ -photon GHZ state generation, an upper bound on the corresponding  $n$ -photon echo visibility  $V_{s,\max}^{(n)}$  can be expressed in terms of the  $Q$ -factor:

$$V_{s,\max}^{(n)} = \frac{e^{-\frac{(2n-1)}{Q}} + e^{-\frac{2n}{Q}}}{2 + e^{-\frac{(2n-1)}{Q}} - e^{-\frac{2n}{Q}}}. \quad (6.12)$$

Eq. (6.12) is useful in benchmarking the minimum bound on the spin coherence and  $Q$ -factor required for scaling up the time-bin multi-photon entanglement approach.

The aberration between  $V_{s,\max}^{(1)}$  and measured  $V_s^{(1)}$  might be attributed to pulse errors<sup>30</sup>, limited bandwidth in the microwave setup to switch phase<sup>31</sup>, finite  $T_2$  from a non-zero echo delay and detuning errors<sup>32</sup> during spin control. The echo sequence in the entanglement protocol is in principle a Carr-Purcell sequence where the rotational pulses evolve around the same axis. As such, pulse errors gradually accumulate leading to diminished spin rephasing. One feasible solution could be to implement the Carr-Purcell-Meiboom-Gill version [155] of the echo by setting the axis of rotation on the middle  $\pi$  pulses (i.e., to  $+x$  axis) to be orthogonal to those of the  $\pi/2$  pulses ( $+y$  axis), which ‘‘pins’’ the equatorial spin state in place since it is an  $x$ -eigenstate after the first  $\pi/2$  pulse.

<sup>30</sup>In the supplementary material of Ref. [155] the authors also considered possibility of the miscalibration of  $\pi/2$  pulses by fixing its duration to be exactly halved of the  $\pi$  pulse. This should in principle be circumvented in our case as we optimized  $V_{\text{pp}}$  of the echo sequence based on the characterization in Fig. 6.13a.

<sup>31</sup>See Sec. 4.8.2 of Ref. [154].

<sup>32</sup>See the last section in the Supplementary Material of Ref. [151].

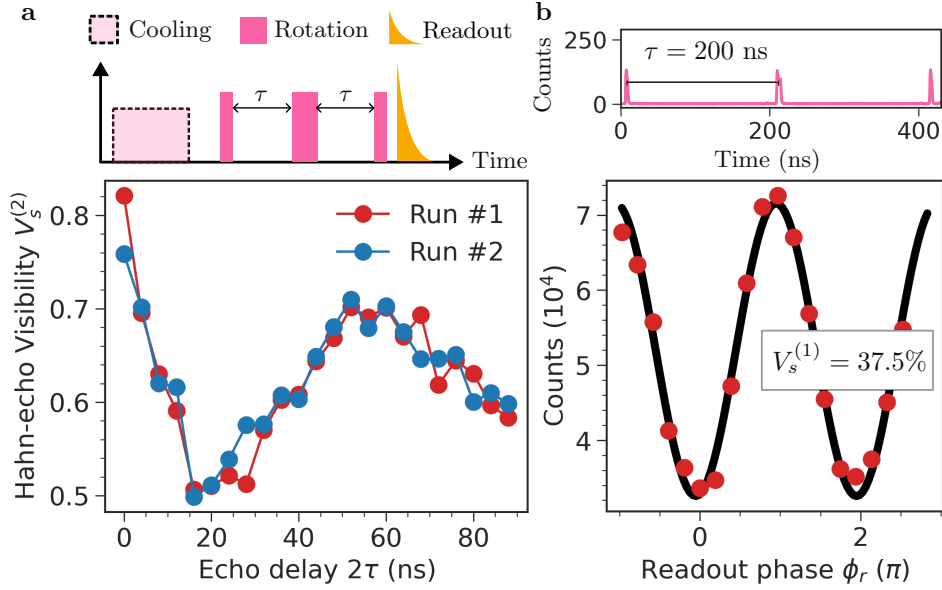


Figure 6.14: **Echo visibility at different pulse delays..** (a) Increasing the echo delay  $\tau_{\text{echo}} = 2\tau$  reveals a reproducible collapse and revival of the visibility  $V_s^{(1)}$ . Peak observed at  $\tau_{\text{echo}} \approx 58$  ns. (b) Visibility measurement at  $\tau_{\text{echo}} = 400$  ns by varying the readout phase  $\phi_r$ . A fit with the formula  $0.375 = 0.82 e^{-(400/T_2)^a}$  assuming the compression factor [156]  $a = 1$ <sup>33</sup> gives a rough estimate of  $T_2 \approx 511$  ns. The visibility recorded at  $\tau_{\text{echo}} \approx 58$  ns is lower than in Fig. 6.13 as the pulse settings are not optimized.

Now we justify the choice of a pulse delay  $\tau = 29$  ns for both echo sequences. This is supported by a measurement of the echo visibility with a varied echo delay  $\tau_{\text{echo}} = 2\tau$  (Fig. 6.14a), where a modulation of the echo amplitude at short delays is clearly visible. Specifically, a revival of the echo signal occurs at  $\tau_{\text{echo}} = 2\tau \approx 58$  ns which is consistent with previous measurements on electron spins at the same magnetic field [151]. This can be attributed to the interplay of parallel Overhauser field noises between different nuclei species [129, 154]. When  $\tau_{\text{echo}}$  is tuned to multiples of the relative nuclear Larmor periods, the accumulated phase induced between the electronic ground states averages out during the echo [158, 159], leading to revival of spin coherence. Based on this observation, we could maximize the echo visibility for  $n$ -photon entanglement protocols by selecting the optimal  $\tau$ <sup>34</sup>, as demonstrated previously.

<sup>33</sup>Note that it is only true when the noise autocorrelation time is much shorter than  $T_2$  [157], but does not hold for slow  $1/f$  noise.

<sup>34</sup>While the effect of parallel Overhauser noises due to nuclear quadrupolar fields could be made negligible by increasing the external magnetic field [151], this also washes out the visibility modulation, which leads to a lower visibility at the same delay.

## 6.5 Optical Pulsed Excitations

Single-photon emission from the QD is achieved by optically driving the cycling transition  $|\downarrow\rangle \rightarrow |\uparrow\downarrow\uparrow\rangle$  with a picosecond pulsed laser. Due to the spectrally close X-polarized transitions, we red-detune the laser by 2 GHz such that only the tail of the laser pulse can weakly excite the undesired  $X_1$  transition (Fig. 6.15b). In contrast to the single-photon scattering approach, here the FWHM duration of the laser excitation pulse ( $\tau_{\text{MIRA}} = 29.6$  ps) needs to be much shorter than the QD lifetime ( $\tau_o = 235$  ps, see Sec. 6.3.2), such that there is a single excitation within the pulse. As the laser is now spectrally broad  $\sigma_o = 2\pi \times 6.33$  GHz  $\gg \Gamma = 2\pi \times 0.677$  GHz, the excitation process is inefficient<sup>35</sup>, thus the system needs to be driven with a large optical Rabi frequency<sup>36</sup> to reach population inversion (i.e., an optical  $\pi$  pulse).

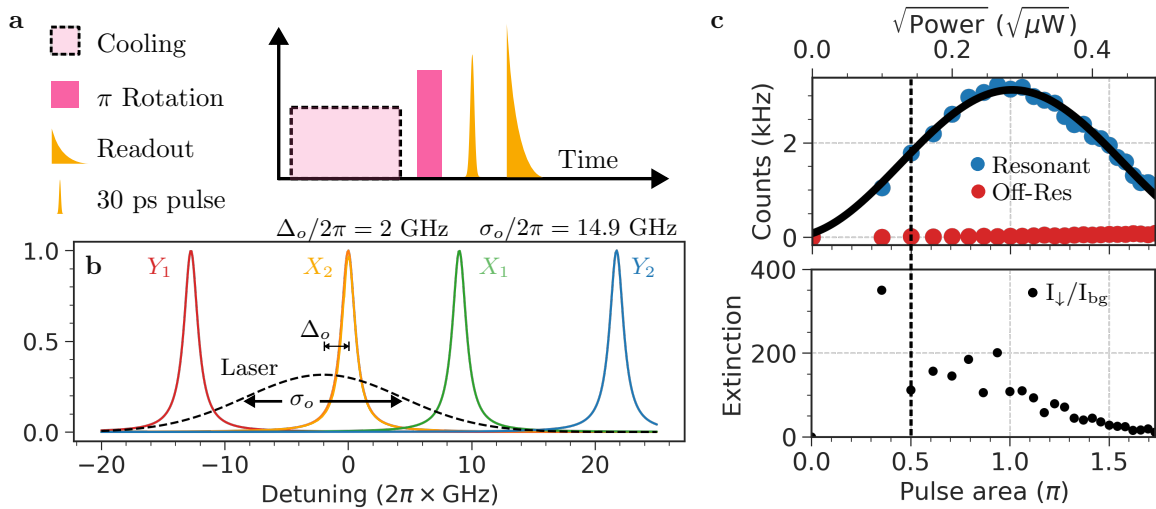


Figure 6.15: **Pulsed excitations of the QD.** (a) Pulse sequence for nuclear spin cooling, a spin  $\pi$ -rotation to prepare  $|\downarrow\rangle$  and the excitation laser pulse. (b) Power spectrum of the excitation laser relative to the QD optical transitions. For simplicity the linewidths for all transitions are assumed identical, taken to be the transformed-limited linewidth  $\Gamma/2\pi = 677$  MHz. The laser is 2 GHz red-detuned from the main transition  $X_2$  (centered at 316.2825 THz) to avoid driving  $X_1$ . (c) Optical Rabi oscillation between  $|\downarrow\rangle$  and  $|\uparrow\downarrow\uparrow\rangle$ . Laser extinction is given by the ratio between intensities of photons emitted on resonant 1.3155 V and off-resonant 0.4 V bias voltages. Dashed vertical line corresponds to the laser power used in the  $g^{(2)}$  and Hong-Ou-Mandel experiments.

Experimentally, the excitation pulses are produced using the same optical setup described in Sec. 3.2 of Ref. [52]. The mode-locked Ti:Sapphire laser (Coherent MIRA 900 P) outputs 4 ps (FWHM in duration) pulses every  $T_{\text{MIRA}} = 13.77$  ns, which are then reflected by a volume Bragg grating (VBG from OptiGrate). The VBG reflects different frequency components of the input pulse with different time delays [160], thus broadening the pulse to around  $\tau_{\text{MIRA}} = 29.6$  ps (FWHM bandwidth of 14.9 GHz). The stretched pulses are directed through a double-pass AOM setup (Fig. 3.6b) to extract excitation pulses that align in time with other pulses (i.e., cooling, spin control and readout) in the

<sup>35</sup>It is inefficient when compared to single-photon scattering, where the excitation pulse is narrowband, and close to resonance of the QD, see Sec. 1.5.

<sup>36</sup>Also, in order to excite the QD on top of the planar structure, more optical power is required for enough light to couple into the waveguide.

measurement sequence. A fast photodiode is used to detect the unaltered MIRA pulses of repetition frequency  $f_{\text{MIRA}} = 72.63$  MHz serving as the main clock for the FPGA and AWG (Sec. 6.2.2.3).

Figure 6.15c presents power-dependent optical Rabi oscillations between the effective two-level system  $|\downarrow\rangle \leftrightarrow |\uparrow\downarrow\uparrow\rangle$ , where the optical power for driving a  $\pi$ -pulse is extracted by fitting the background-subtracted counts with the formula  $A \sin^2(BP_{\text{in}} + \phi_0)$  for an input power  $P_{\text{in}}$ <sup>37</sup> and free variables  $A$ ,  $B$  and  $\phi_0$ . Dashed line corresponds to the power used for pulsed excitations in the entanglement protocol, which is at around 10% of the  $\pi$ -pulse power to suppress excitation of  $X_1$ . Counts are recorded with SNSPDs and two etalon filters. Excitation of  $Y_1$  is mitigated by running the pulse sequence in Fig. 6.15a without the spin  $\pi$ -pulse, and optimizing the laser polarization to minimize fluorescence from  $X_1$  via the transition path  $|\uparrow\rangle \rightarrow |\uparrow\downarrow\uparrow\rangle \rightarrow |\downarrow\rangle$ .

### 6.5.1 Purity and Indistinguishability

For benchmarking the QD as a source of entangled photons, one could quantify the quality of emitted photons by their purity and indistinguishability. Experimentally this is probed measuring the second-order correlation function at zero time delay  $g^{(2)}(\tau = 0)$  and the Hong-Ou-Mandel (HOM) visibility  $V_{\text{HOM}}$ <sup>38</sup>, respectively. Both experiments can be simultaneously conducted [18] using the time-bin interferometer shown in Fig. 3.7.

The general idea is to excite the QD initialized in the  $|\downarrow\rangle$  state (by applying a spin  $\pi$ -rotation pulse on  $|\uparrow\rangle$ ) with two picosecond pulses separated by the interferometric delay  $\tau_{\text{int}}$ . The emitted photons in the early and late time-bins are guided into the detection path of the time-bin interferometer with narrow frequency filters, leading to three time-resolved fluorescence peaks on the detectors. Heralding the photon detection window in the side (middle) peak constitutes a  $g^{(2)}$  (HOM) experiment (Fig. 6.16a).

The purity  $g^{(2)}(0)$  of the emitted photons is measured by time-gating the detection on the side peaks, and recording coincidences between two detectors at different time delays. At zero time delay, photons arriving at the side peaks are ideally anti-bunched since they correspond to events in which a single photon is emitted in the early (late) time-bin propagating through the short (long) path of the detection interferometer. The single photons recorded in these detection windows are incident on a 50:50 beamsplitter, resembling a Hanbury-Brown and Twiss (HBT) setup. Coincidence clicks can thus be observed at time delays corresponding to repetitions of the sequence duration  $\Delta n_{\text{rep}}$ , as plotted in Figs. 6.16b-d. Each measurement sequence takes  $\tau_{\text{seq}} = 1.8 \mu\text{s}$  to generate a single photon in each side peak.

Figure 6.16b shows the un-normalized histogram of photon coincidences recorded within the Early-short (blue) and Late-long (red) detection windows. The coincidences in the latter detection window is 87% of those in the former window, owing to a combined effect of finite cyclicity (leading to coincidence reduction of  $(C/(C+1))^2 \approx 93.6\%$ ) and cross-excitation error from the MIRA laser. To estimate  $g^{(2)}(0)$ , we normalize the histogram according to average coincidence counts taken between  $50 < |\Delta n_{\text{rep}}| < 100$  and find  $g^{(2)}(0) = 8.4\%$  ( $g^{(2)}(0) = 11.5\%$ ) for early (late) time-bin. By fitting the coincidences at long delays with an exponential  $g^{(2)}(\Delta n_{\text{rep}}) = Ae^{-\Delta n_{\text{rep}}/\tau_{\text{decay}}}$  [52], we extracted a decay time constant of  $\tau_{\text{decay}} = (17.7 \pm 0.2)$  ms averaged over two time-bins, with a

<sup>37</sup>Measured free space at a power meter on the optical breadboard, before entering the cryostat.

<sup>38</sup>As discussed in Chapter 5, the photon indistinguishability can be more directly estimated by power-dependent photon visibility measurement.

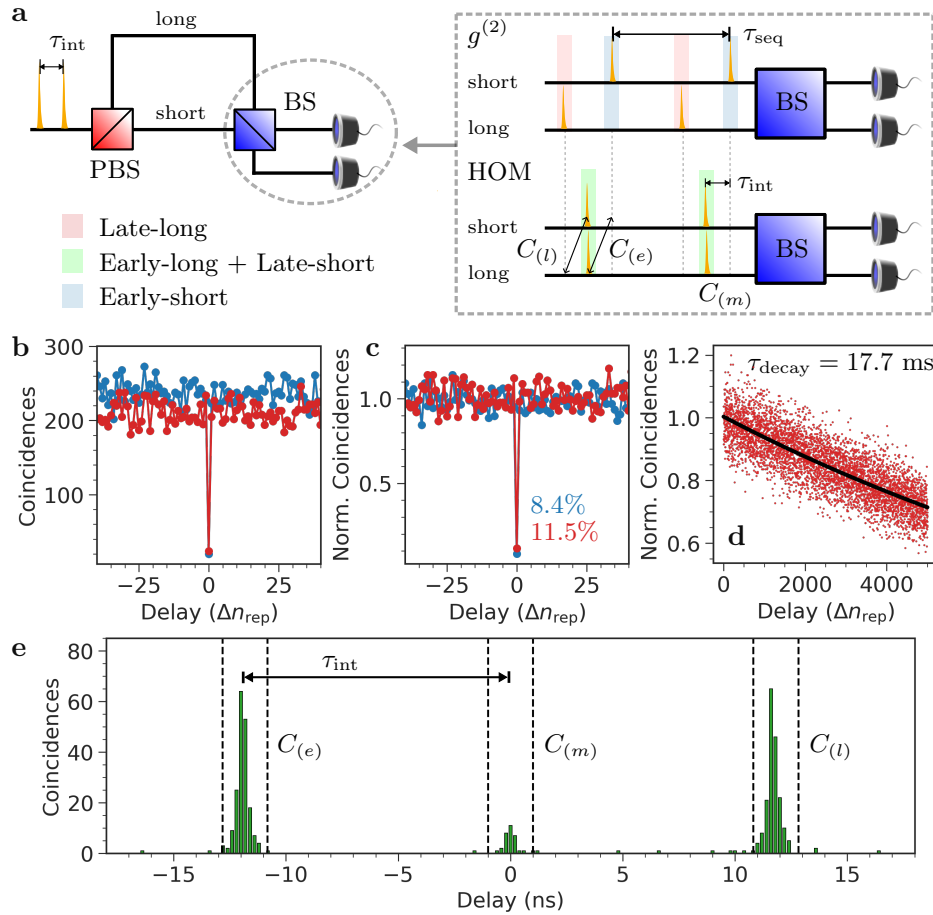


Figure 6.16:  $g^{(2)}$  and HOM measurements using the time-bin interferometer. **(a)** Schematics of photon streams before the 50:50 beamsplitter.  $g^{(2)}$  is measured by time-gating on the red or blue peaks and sweeping the detector delay across different repetitions  $\tau_{\text{seq}}$ . HOM is time-gated on the middle time window (green) where early and late photons interfere. Normalization is done by measuring coincidences of early or late photons passing between short and long paths. **(b)** Coincidences between photons separated in units of number of repetitions  $\Delta n_{\text{rep}}$ . Each point is the total summed counts integrated for 1 s. **(c)** Normalized coincidences in (b). **(d)** Fit of the blinking of  $g^{(2)}$  in long delays. **(e)** Coincidences between photons separated by  $\tau_{\text{int}}$  within the repetition.

varying amplitude of 20%, which is likely to be a result of slow spectral diffusion noises<sup>39</sup> occurring on a similar timescale [136].

The observed  $g^{(2)}(0)$  is higher than previously measured values on a hole spin in Ref. [18]. A portion of the multi-photon component can be explained by residual leakage from the excitation laser. The light arriving at the detectors is modelled as a statistical mixture of single-photon emission from the QD and background photons from the laser obeying Poissonian statistics [161]. This contribution is estimated to be  $g_{\xi}^{(2)} = 2\xi - \xi^2 \approx 2\%$  for  $\xi = I_{\text{bg}}/(I_{\downarrow} - I_{\text{bg}})$  [52] is the ratio between the background photons and single-photons from the QD extracted in Fig. 6.15c. The remaining contribution to  $g^{(2)}(0)$  most likely originates from re-excitation error during the laser pulse.

<sup>39</sup>This is much slower than the  $2.2 \mu\text{s}$  decay time constant extracted in Ref. [52] for hole spins, which is measured without nuclear cooling. The ms decay time might indicate that nuclear noises for the electron spin investigated here are suppressed by nuclear cooling.

The photon indistinguishability is estimated by time-gating the detection on the middle peak, where emitted photons in the early and late time-bin temporally overlap at the 50:50 beamsplitter and interfere. When both photons are indistinguishable, they exhibit HOM interference [5] and always bunch up in the same output port. At zero time delay between detectors at each port, ideally no coincidence click is expected when the early and late photons are indistinguishable. At delays  $\pm\tau_{\text{int}}$ , however, coincidence clicks occur between photons splitting through the short and long paths as they do not interfere due to temporal separation.

Following Refs. [52, 118, 161], the raw HOM visibility measured with the time-bin interferometer setup can be estimated using

$$V_{\text{HOM}}^{\text{raw}} = 1 - \frac{C_{(m)}(\tau = 0)}{\frac{1}{2}[C_{(e)}(\tau = -\tau_{\text{int}}) + C_{(l)}(\tau = +\tau_{\text{int}})]}, \quad (6.13)$$

where  $C_{(m)}(\tau = 0)$  is the number of coincidences between detectors when gated on the middle time window. It is normalized by the average number of coincidences between photons recorded during the time windows separated by  $\tau_{\text{int}}$ , e.g., the coincidences  $C_{(e)}(-\tau_{\text{int}})$  of early photons traversing between the short and long paths. These photons do not show HOM interference but result in coincidence clicks when the detector time delay is  $\pm\tau_{\text{int}}$ .

Figure 6.16e shows the histogram of three coincidence peaks. A raw visibility  $V_{\text{HOM}}^{\text{raw}} = 87.2\%$  is obtained using Eq. (6.13), by normalizing the middle peak by total counts from two side peaks with a 2 ns integration window.

## 6.6 Parameter Summary

In Table 6.1 we summarize the measured parameters governing the quality of the spin-photon interface.

Parameter	Value
QD qubit	Electron spin $X^-$
Emission wavelength	949.8 nm
External magnetic field $\mathbf{B}_x$	4 T
Total decay rate of the QD $\Gamma$	$(4.25 \pm 0.01) \text{ ns}^{-1}$ (Sec. 6.3.2)
Ground-state Zeeman splitting $\Delta_e$	$2\pi \times 21.7 \text{ GHz}$ (Sec. 6.3.1)
Electron in-plane $g$ -factor $g_{e,x}$	0.388
Excited-state Zeeman splitting $\Delta_h$	$2\pi \times 12.4 \text{ GHz}$ (Sec. 6.3.1)
Hole in-plane $g$ -factor $g_{h,x}$	0.228
Optical cyclicity $C = \gamma_X/\gamma_Y$	$36.3 \pm 2.9$ (Sec. 6.3.2)
Standard deviation in spectral diffusion fluctuation $\sigma_e$	$2\pi \times (532 \pm 91) \text{ MHz}$ (Sec. 6.3.1)
Standard deviation in pulse spectral width $\sigma_o$	$39.7 \text{ ns}^{-1}$ (Sec. 6.5)
Spin-echo visibility $V_s^{(1)}$ for $n = 1$ -photon at pulse delay 29 ns	$(81.5 \pm 1.5)\%$ (Sec. 6.4.3)
Spin-echo visibility $V_s^{(2)}$ for $n = 2$ -photon at pulse delay 29 ns	$(72.0 \pm 1.6)\%$ (Sec. 6.4.3)
Spin $\pi$ -rotation fidelity $F_\pi$	$(98.1 \pm 0.6)\%$ (Sec. 6.4)
Spin dephasing time $T_2^*$	$(33.3 \pm 2.7) \text{ ns}$ (Sec. 6.4.2)
Spin coherence time $T_2^{\text{echo}}$	511 ns (Rough estimate, Sec. 6.4.3)
Purity $1 - g^{(2)}(0)$	90.1% (Sec. 6.5.1)
Raw HOM visibility $V_{\text{HOM}}$	87.2% (Sec. 6.5.1)
Sequence duration $\tau_{\text{seq}}$	1.8 $\mu\text{s}$

Table 6.1: Key properties characterizing the QD electron spin and the waveguide device. Electron (hole) in-plane  $g$ -factors are estimated using  $g_{e,x} = \frac{\hbar\Delta_e}{\mu_B|\mathbf{B}_x|}$  ( $g_{h,x} = \frac{\hbar\Delta_h}{\mu_B|\mathbf{B}_x|}$ ) where  $\mu_B$  is the Bohr magneton.

## 6.7 Two-Qubit Entanglement

With the optical and spin properties of the QD understood, we implement the protocol detailed in Sec. 6.1.2 for  $n = 1$  and measure spin-photon entanglement.

### 6.7.1 Measurement Results

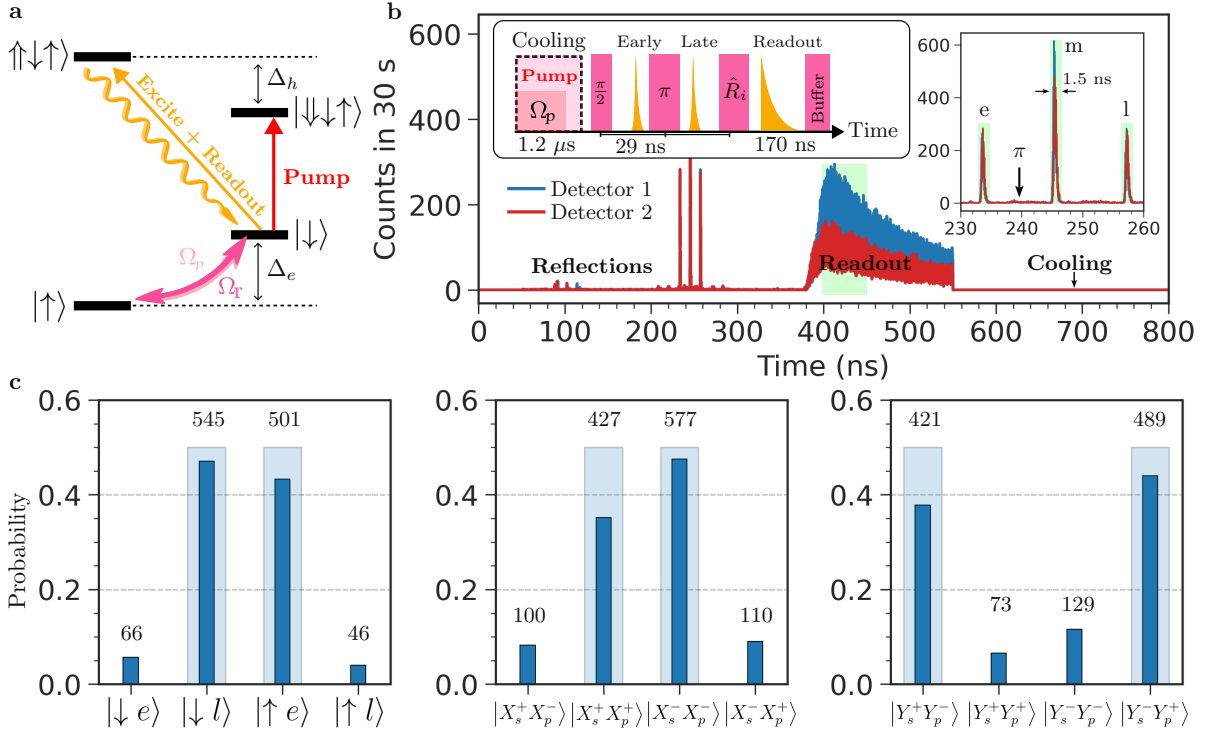


Figure 6.17: **Generation and verification of Bell state.** (a) Energy levels of  $X^-$ . Note that as opposed to Fig. 6.2a, here the X-polarized transitions are cycling. (b) Histogram of the entanglement sequence shown up to 800 ns. The right inset is a close-up view on optical excitation pulses. The buffer pulse duration varies in different measurement settings to maintain constant average rotation power. Green shaded region is the integration window for photon and spin readout. (c) Measured probability of each spin-photon basis state, normalized by a total sum of all coincidences in the same basis. Raw coincidence counts are provided. Shaded bars are ideal probabilities.

The entanglement between the QD electron spin and  $n = 1$  photon is realized by implementing the pulse sequence depicted in Figs. 6.17a-b. The electron spin is prepared in  $|\uparrow\rangle$  with reduced nuclear noises from a  $1.2 \mu\text{s}$  cooling pump and  $1.1 \mu\text{s}$  cooling drive. A spin control sequence of  $\pi/2 - \pi - \hat{R}_i$  interleaved with excitation pulses in the early and late time-bin is then applied. The pulse delay 29 ns is the optimal delay which gives rise to optimal echo visibility (Sec. 6.4.3). The last control pulse  $\hat{R}_i = 0, \pi, \pm\pi/2$  projects the spin state into  $\pm Z$ -,  $\pm X$ - and  $\pm Y$ -basis states, allowing for further spin readout. Both the spin readout and optical excitation pulses drive the same cycling transition  $X_2$ :  $|\downarrow\rangle \leftrightarrow |\uparrow\uparrow\rangle$  (Sec. 6.3.2). The excitation laser is 2 GHz red-detuned from  $X_2$  and attenuated to reduce the probability of driving  $X_1$  (Sec. 6.5).

Following Eq. (6.1), the ideal Bell state has the form  $|\psi_{\text{ideal}}\rangle = (|\uparrow e\rangle - |\downarrow l\rangle)/\sqrt{2}$  written in the Z-basis<sup>40</sup>. The Bell-state fidelity can be estimated exactly using Eq. (3.26) as explained in Sec. 3.7, by measuring the emitted photons (through the time-bin interferometer) and time-averaged readout of the electron spin state. From coincidence counts between photonic and spin readout, we recorded raw spin-photon correlations of

$$\begin{cases} \langle \hat{\mathcal{P}}_z \rangle = (90.3 \pm 0.9)\%; \\ \langle \hat{\mathcal{M}}_x \rangle = (65.4 \pm 2.2)\%; \\ \langle \hat{\mathcal{M}}_y \rangle = (-63.7 \pm 2.3)\%, \end{cases} \quad (6.14)$$

which gives a raw fidelity of  $\mathcal{F}_{\text{raw}}^{\text{Bell}} = (77.4 \pm 0.9)\%$ , without any background subtraction. Strikingly, the temporal overlap of fluorescences between the rotational pulses and optical excitations documented in Sec. 3.7.0.1 vanishes thanks to the fast 4 ns  $\pi$ -rotation pulse (Sec. 6.4), as evidenced in the inset of Fig. 6.17b.

## 6.7.2 Preliminary Infidelity Analysis

Based on our current understanding of the system and the associated error mechanisms, one could theoretically evaluate the contribution from individual error components that limit the Bell-state fidelity. Consequently, an overall fidelity estimate including all relevant errors can be obtained and compared with the experimental data.

### 6.7.2.1 Cross-excitation Error

As covered in Sec. 4.3.4, expectation values in equatorial bases  $|\langle \hat{\mathcal{M}}_x \rangle|, |\langle \hat{\mathcal{M}}_y \rangle| \approx 64.5\%$  should ideally approach the echo visibility  $V_s^{(1)} = 81.5\%$ , as their measurements share the same spin control and readout sequence. The discrepancy (17%) between two values thus can be solely ascribed to spectral overlap between the  $X_1$  transition and the excitation laser (Fig. 6.15b). For the spin initialized in a superposition state, by driving both  $X_2$  and  $X_1$  during optical excitations, the spin ground states are entangled with the frequencies of the emitted photons and are effectively mixed<sup>41</sup>. This cross-excitation error thus acts as a phase-damping channel [162]. Its infidelity contribution is estimated to be

$$1 - \mathcal{F}_{\text{cross}}^{\text{Bell}} = \frac{1}{2} \left[ V_s^{(1)} - \frac{|\langle \hat{\mathcal{M}}_x \rangle| + |\langle \hat{\mathcal{M}}_y \rangle|}{2} \right] \approx 8.5\%. \quad (6.15)$$

### 6.7.2.2 Echo Rephasing Error

Another major infidelity originates from rephasing errors during the Hahn-echo sequence, resulting in non-unity echo visibility  $V_s^{(1)}$ . These include incoherent spin-flip error (finite  $\kappa$ ), pulse shaping errors, finite  $T_2$  and imperfect spin inversion from non-equatorial rotational axis during spin control [151]. To separate the infidelity owing to finite  $\kappa$  from the rest, we subtract  $V_s^{(1)}$  from the maximum attainable echo visibility  $V_{s,\text{max}}^{(1)} = 94.2\%$  (obtained from the Rabi oscillation fit, see Sec. 6.4). This guarantees that the contribution

<sup>40</sup>To express the ideal state in the X-basis, take  $|\downarrow\rangle \equiv |X_s^+\rangle + |X_s^-\rangle$ ,  $|\uparrow\rangle \equiv |X_s^+\rangle - |X_s^-\rangle$ ,  $|e\rangle \equiv |X_p^+\rangle + |X_p^-\rangle$  and  $|l\rangle \equiv |X_p^+\rangle - |X_p^-\rangle$ .

<sup>41</sup>To understand this, one could imagine exciting both diagonal transitions with equal strengths. The resulting state is a maximally entangled state between the spin states and the frequency-encoded photons. This entanglement is unwanted since the spin state behaves like an incoherent mixture.

from  $\kappa$  is removed and we can consider this error independently in the next section. Here we estimate

$$1 - \mathcal{F}_{\text{Rephasing}}^{\text{Bell}} = \frac{1}{2}(V_{s,\text{max}}^{(1)} - V_s^{(1)}) \approx 6.4\%. \quad (6.16)$$

### 6.7.2.3 Incoherent Spin-flip Error during Rotation

One notable infidelity stems from incoherent spin-flip error induced by the Raman rotation laser (Appendix C), which by following the formalism developed in Sec. 4.3.5, can be estimated as

$$1 - \mathcal{F}_{\kappa}^{\text{Bell}} = 1 - \frac{1}{2} \left[ 1 + (1 - p_{\pi})(1 - p_{\pi/2}) \right] \approx 1.5\%, \quad (6.17)$$

where  $p_{\pi} = 1 - e^{-\kappa T_{\pi}}$  ( $p_{\pi/2} = 1 - e^{-\kappa T_{\pi/2}}$ ) is the probability of introducing a random spin-flip depolarizing error during a  $\pi$ - ( $\pi/2$ -) rotation pulse (Eq. (4.29)). We use  $\kappa \approx 0.005 \text{ ns}^{-1}$  fitted in Sec. 6.4 with a  $T_{\pi} = 4 \text{ ns}$  duration of spin  $\pi$ -rotation pulse used in the entanglement experiment. Eq. (6.17) is derived by extending the analysis in Sec. 4.3.5 to describe the infidelity contribution for an emission-based  $n$ -photon GHZ state. The detailed derivation is documented in Appendix D.

### 6.7.2.4 Imperfect Readout and Initialization

Following Eq. (10.4) in Ref. [52], the entanglement infidelity due to imperfect readout  $F_r$  and initialization  $F_i$  fidelities is given by:

$$1 - \mathcal{F}_{\text{R,I}}^{\text{Bell}} = 1 - \left( \frac{1}{2} + 2F_r F_i - \frac{F_r}{2} - F_i \right) \approx 4.9\%, \quad (6.18)$$

which we take  $F_i, F_r \approx 98\%$ .  $F_i$  is given by the spin pumping fidelity during the  $1.2 \mu\text{s}$  cooling pulse, while  $F_r$  is limited by the spin  $\pi$ -rotation fidelity  $F_{\pi} \approx 98.1\%$ .

### 6.7.2.5 Photon Distinguishability

Pure dephasing as a result of elastic phonon scattering leads to fast time jittering (compared to the QD lifetime) between two emitted photons, giving rise to a random relative phase between the early and late time-bins in the Bell state, which in turn diminishes  $|\langle \hat{\mathcal{M}}_x \rangle|$  and  $|\langle \hat{\mathcal{M}}_y \rangle|$  but has no effect on  $\langle \hat{\mathcal{P}}_z \rangle$ . From Ref. [149], the corresponding infidelity is expressed in terms of the photon indistinguishability  $I$ :

$$1 - \mathcal{F}_{\gamma_d}^{\text{Bell}} = 1 - \frac{1 + I}{2}, \quad (6.19)$$

where  $I \equiv \Gamma/(\Gamma + 2\gamma_d)$  has the same exact form as the intrinsic photon visibility  $V^{(0)} = V_p^0$  derived in Chapter 5. As previously established in the chapter, it is challenging to extract  $V^{(0)}$  directly from HOM and  $g^{(2)}(0)$  measurements without determining the slope  $F$ . A reasonable estimate would be to use the photon visibility  $V_p^0 \approx 92.6\%$  extrapolated from power-dependent measurements in Sec. 3.4.5, as similar samples at the same cryogenic temperatures 4 K are used. Substituting  $I = V_p^0$  into Eq. (6.19), we estimate  $1 - \mathcal{F}_{\gamma_d}^{\text{Bell}} \approx 3.7\%$ .

### 6.7.2.6 Theoretical Overall Fidelity

Combining all considered infidelity contributions, the overall entanglement fidelity is

$$\mathcal{F}_{\text{theory}}^{\text{Bell}} = \mathcal{F}_{\text{cross}}^{\text{Bell}} \times \mathcal{F}_{\text{Rephasing}}^{\text{Bell}} \times \mathcal{F}_{\kappa}^{\text{Bell}} \times \mathcal{F}_{\text{R,I}}^{\text{Bell}} \times \mathcal{F}_{\gamma_d}^{\text{Bell}} \approx 77.3\%, \quad (6.20)$$

which shows excellent agreement with the experimentally measured  $\mathcal{F}_{\text{raw}}^{\text{Bell}} = (77.4 \pm 0.9)\%$ . However, a more careful examination of the entanglement fidelity simultaneously accounting for all errors, for example, by Monte Carlo simulation [18] and following Ref. [149], is much preferred, since the interplay between errors grows increasingly complex with more errors considered. Infidelity due to finite optical cyclicity is not considered separately as it is included in cross-excitation and spin readout errors. Alternatively, using Eq. (54) in Ref. [149] one could estimate 0.7% infidelity from this error alone. Table 6.2 summarizes the considered errors and their individual impact on the entanglement fidelity.

<b>Error</b>	<b>Parameter Value</b>	<b>Infidelity</b>
Cross excitation	-	8.5%
Echo rephasing	$V_s^{(1)} = 81.5\%$	6.4%
Incoherent spin-flip	$\kappa = 0.005 \text{ ns}^{-1}$	1.5%
Readout and initialization	$F_i, F_r = 98\%$	4.9%
Phonon dephasing	$I = V_p^0 = 92.6\%$	3.7%
Finite cyclicity	$C = 36.3$	0.7%
	<b>Measured</b>	<b>Theory</b>
<b>Entanglement fidelity</b>	$(77.4 \pm 0.9)\%$	77.3%

Table 6.2: Summary of most relevant errors with their respective parameters, for  $n = 1$ -photon entanglement protocol with the QD electron spin.

## 6.8 Three-Qubit Entanglement

The extension of the experimental pulse sequence to  $n = 2$ -photon entanglement protocol involves the addition of two optical excitation pulses as well as two  $\pi$ -pulses. While this is conceptually simple, the timing between different control pulses needs to be carefully considered to avoid pulse overlap.

### 6.8.1 Timing Restrictions

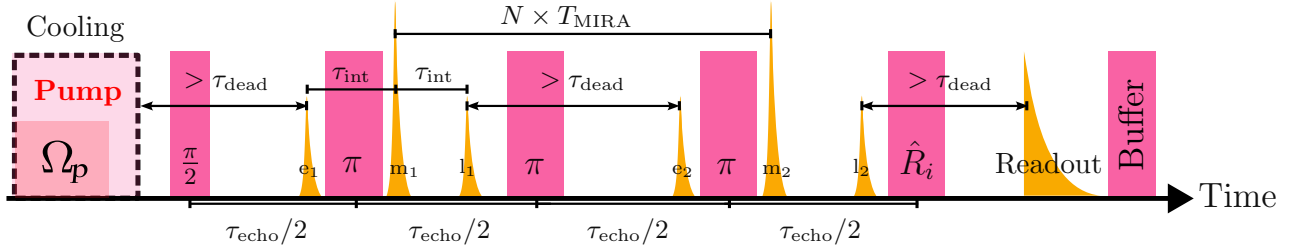


Figure 6.18: **Histogram of the ideal pulse sequence for 2-photon entanglement protocol.** See the main text for timing considerations when designing the sequence.

Due to the fixed repetition period  $T_{\text{MIRA}} = 13.77$  ns of the MIRA pulses and finite detector dead-time, there are several timing constraints when designing the pulse sequence. For instance, the delay between the first photon detected in the late-long window (labelled as  $l_1$  in Fig. 6.18) and the second photon in the early-short window ( $e_2$ ) should ideally be longer than the detector dead-time  $\tau_{\text{dead}} \approx 55$  ns. In Ref. [52], a second excitation pulse is picked from the MIRA pulse train after  $N \times T_{\text{MIRA}} = 6 \times T_{\text{MIRA}} \approx 82.6$  ns for the second photon, to ensure the delay between  $l_1$  and  $e_2$  is 59 ns, slightly longer than  $\tau_{\text{dead}}$ . However,  $N \times T_{\text{MIRA}}$  is also bounded by  $\tau_{\text{echo}} + \tau_{\text{int}}$  as there must be a  $\pi$ -rotation pulse sandwiched between two optical excitations<sup>42</sup>. From here a set of timing restrictions is deduced:

$$\begin{cases} N \times T_{\text{MIRA}} > \tau_{\text{dead}} + 2\tau_{\text{int}}; \\ \tau_{\text{echo}} + \tau_{\text{int}} > N \times T_{\text{MIRA}}; \\ N \times T_{\text{MIRA}} + \tau_{\text{int}} > \tau_{\text{echo}}. \end{cases} \quad (6.21)$$

The first inequality in Eq. (6.21) originates from finite detector dead-time, while the second is governed by the echo delay as discussed above. The last inequality states that both sandwiched  $\pi$ -pulses must be confined between  $e_1$  and  $m_2$ . Since  $\tau_{\text{dead}}$ ,  $T_{\text{MIRA}}$  and  $\tau_{\text{int}} = 11.83$  ns are fixed, from the first inequality we find the lowest integer  $N = 6$ . Hence, combining the second and third inequalities we obtain a bound on  $\tau_{\text{echo}}$ :

$$\frac{N \times T_{\text{MIRA}} + \tau_{\text{int}}}{2} = 47.2 > \frac{\tau_{\text{echo}}}{2} > \frac{N \times T_{\text{MIRA}} - \tau_{\text{int}}}{2} = 35.4, \quad (6.22)$$

which is unfortunately not satisfied with the measured  $\tau_{\text{echo}}/2 = 29$  ns pulse delay that gives the optimal echo visibility (Sec. 6.4.3). To circumvent this, for the second photon we pick the MIRA pulse after  $5 \times T_{\text{MIRA}} \approx 68.9$  ns of the first pulse, with the delay between

<sup>42</sup>This means both  $m_1$  and  $e_2$  need to be confined between the first and third  $\pi$ -pulses, since  $e_2$  must be applied before the third  $\pi$ -pulse. Therefore, the time delay between  $m_1$  and  $e_2$  is shorter than  $\tau_{\text{echo}}$ .

$l_1$  and  $e_2$  now being 45.2 ns, thereby sacrificing counts from the second photon to the detector dead-time (inset of Fig. 6.19b). Moreover, due to finite rise and fall times, the third  $\pi$ -pulse is delayed by an additional 5 ns to avoid overlapping with  $e_2$  (Fig. 6.19a).

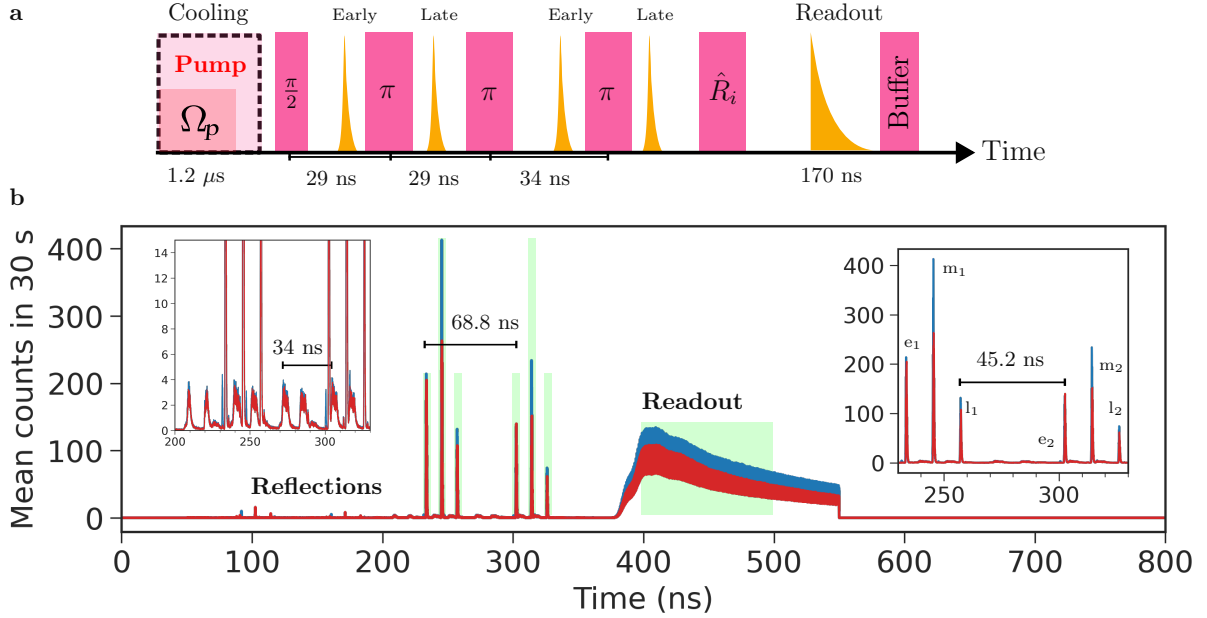


Figure 6.19: **Realistic measurement sequence for 2-photon entanglement.** (a) Implemented pulse sequence. (b) Histogram of the pulse sequence. Left inset shows the third  $\pi$ -pulse is delayed by 34 ns instead of 29 ns to avoid timing overlap with early excitation pulse of the second photon. The rotation pulses appear in pairs due to two paths of the detection interferometer. The reduced fluorescence for the second photon is attributed to detector dead-time. Cooling past 800 ns is not shown. The time-gating for spin readout is 100 ns to collect more counts.

## 6.8.2 Measurement Settings

Following the  $n = 2$ -photon entanglement protocol in Sec. 6.1.2, the state evolves as

$$\begin{aligned}
 |\psi\rangle = \frac{|\uparrow\rangle + |\downarrow\rangle}{\sqrt{2}} & \xrightarrow{\hat{O}_1^{\text{ideal}}} \frac{|l_1\rangle|\downarrow\rangle - |e_1\rangle|\uparrow\rangle}{\sqrt{2}} \\
 & \xrightarrow{\hat{O}_2^{\text{ideal}}} \frac{-|l_1\rangle|l_2\rangle|\downarrow\rangle + |e_1\rangle|e_2\rangle|\uparrow\rangle}{\sqrt{2}}, \quad (6.23)
 \end{aligned}$$

which is a 3-qubit GHZ state  $|\Psi_{\text{GHZ}}^3\rangle$ .  $\hat{O}_i^{\text{ideal}}$  is the operator applying a single round of the ideal protocol to append the  $i$ -photon to the state [149]. In general, the fidelity of an  $N$ -qubit GHZ state  $|\Psi_{\text{GHZ}}^N\rangle$  is obtained by measuring expectation values of  $N + 1$  measurement operators in the output state  $\rho_{\text{out}}$  [137]:

$$\mathcal{F}_{\text{GHZ}}^N \equiv \text{Tr}(\rho_{\text{out}}|\Psi_{\text{GHZ}}^N\rangle\langle\Psi_{\text{GHZ}}^N|) = \text{Tr}[\rho_{\text{out}}(\frac{\hat{\mathcal{P}}_z + \hat{\chi}}{2})] = \frac{1}{2}[\langle\hat{\mathcal{P}}_z\rangle + \langle\hat{\chi}\rangle], \quad (6.24)$$

where the projection operators for a qubit encoded in  $\{|0\rangle, |1\rangle\}$  basis are

$$\begin{aligned}\hat{\mathcal{P}}_z &= |0\rangle\langle 0|^{\otimes N} + |1\rangle\langle 1|^{\otimes N}; \\ \hat{\chi} &= |0\rangle\langle 1|^{\otimes N} + |1\rangle\langle 0|^{\otimes N} = \frac{1}{N} \sum_{k+1}^N (-1)^k \hat{\mathcal{M}}_k; \\ \hat{\mathcal{M}}_k &= \left( \cos \frac{k\pi}{N} \hat{\sigma}_x + \sin \frac{k\pi}{N} \hat{\sigma}_y \right)^{\otimes N}.\end{aligned}\tag{6.25}$$

Here  $\langle \hat{\mathcal{P}}_z \rangle$  measures the expectation value of  $\rho_{\text{out}}$  along the  $z$ -axis (poles of the qubit Bloch sphere), while  $\langle \hat{\mathcal{M}}_k \rangle$  measures the correlations between  $|0\rangle$  and  $|1\rangle$  projected at different symmetry axes that divide the equator into equal sectors, see Fig. 6.20a, for example.

Experimentally, 2 projective measurements are required to characterize each basis since we only read out the spin state in  $|\downarrow\rangle$ . This means for  $N + 1$  projective operators (i.e.,  $\langle \hat{\mathcal{P}}_z \rangle$  and  $N$  operators  $\langle \hat{\mathcal{M}}_k \rangle$ ), a total of  $2(N + 1)$  measurement settings needs to be implemented [52]. As discussed in Sec. 3.7 the photonic state readout in  $\hat{\sigma}_z^{(p)}$  basis is carried out by detecting the presence of photons in the side peaks with the time-bin interferometer, whereas spin projections in  $\hat{\sigma}_z^{(s)}$  are done by applying an extra control pulse  $\hat{R}_i = 0, \pi$  followed by spin readout. For the equatorial state projections  $\langle \hat{\mathcal{M}}_k \rangle$  with  $N = 3$  qubits, 6 different measurement sequences are applied. Table 6.3 shows the experimental settings for measuring photonic and spin states in the equatorial bases.

	$\hat{\mathcal{M}}_1$		$\hat{\mathcal{M}}_2$		$\hat{\mathcal{M}}_3$	
	$ +\rangle$	$ -\rangle$	$ +\rangle$	$ -\rangle$	$ +\rangle$	$ -\rangle$
$k\pi/N$	0	$\pi$	$\frac{\pi}{3}$	$-\frac{2\pi}{3}$	$-\frac{\pi}{3}$	$\frac{2\pi}{3}$
$\phi_{\text{MW}}$	0	$\frac{\pi}{2}$	$\frac{\pi}{6}$	$-\frac{\pi}{3}$	$-\frac{\pi}{6}$	$\frac{\pi}{3}$
$\theta_p$	$\theta_0$	$\theta_0$	$\theta_0 + \frac{\pi}{3}$	$\theta_0 + \frac{\pi}{3}$	$\theta_0 + \frac{2\pi}{3}$	$\theta_0 + \frac{2\pi}{3}$
$\theta_{\text{pol}}$	$\frac{\theta_0}{2}$	$\frac{\theta_0}{2}$	$\frac{\theta_0}{2} + \frac{\pi}{6}$	$\frac{\theta_0}{2} + \frac{\pi}{6}$	$\frac{\theta_0}{2} + \frac{\pi}{3}$	$\frac{\theta_0}{2} + \frac{\pi}{3}$

Table 6.3: Measurement settings of equatorial projection operators  $\hat{\mathcal{M}}_k$  for  $N = 3$ .  $k\pi/N$  ( $\theta_p$ ) corresponds to the azimuthal angle on the Bloch sphere of a spin (photonic) qubit (Fig. 6.20a), while  $\phi_{\text{MW}}$  ( $\theta_{\text{pol}}$ ) is the corresponding AWG microwave phase (linear polarizer angle) in the actual implementation.  $\theta_0 \approx 2\pi$  is the azimuthal angle corresponding to maximum or minimum counts in one of the detectors. The factor of two between  $k\pi/N$  and  $\phi_{\text{MW}}$  comes from the relative phase shift between two sidebands [52].

### 6.8.3 Measurement Results

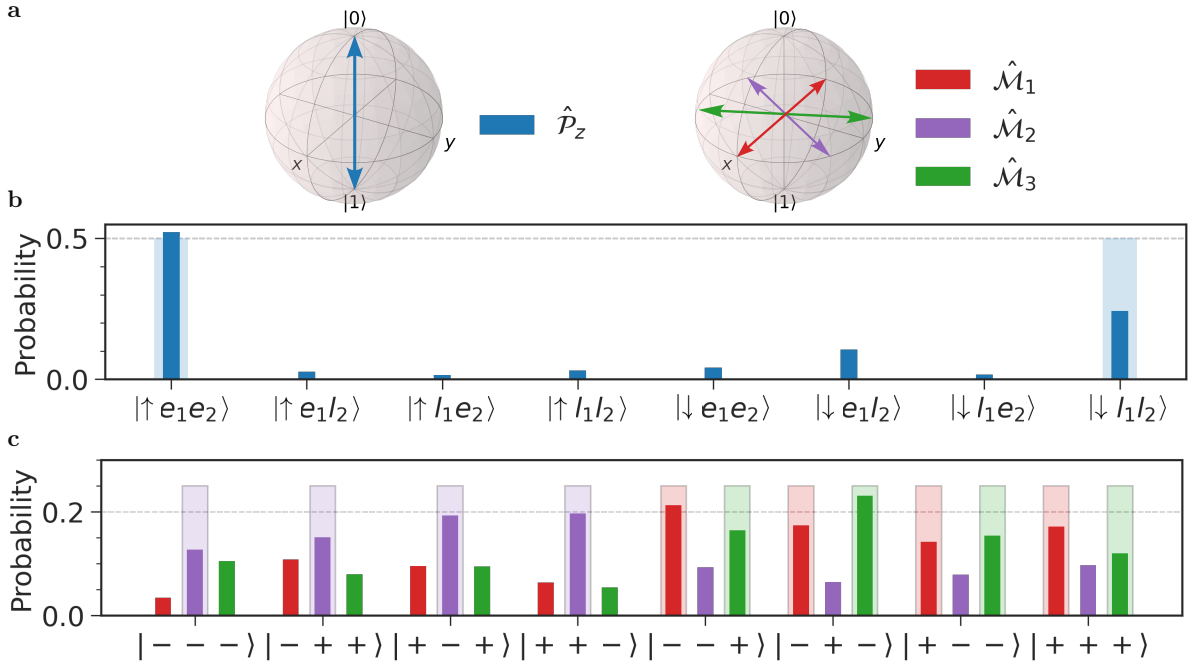


Figure 6.20: **Verification of 3-qubit GHZ state.** (a) Visualization of 4 projective operators on the qubit Bloch sphere for characterizing 3-qubit entanglement. (b) Normalized probabilities of projecting the output state in different measurement basis. Shaded bars are ideal probabilities. Data acquisition time is 37 hours.

Fig. 6.20b lists the normalized probabilities of measuring the output state in 4 different bases, obtained from three-fold coincidences (i.e., two time-bin photons and at least one photon from spin readout). Here we measured raw spin-photon-photon correlations of

$$\begin{cases} \langle \hat{\mathcal{P}}_z \rangle = (76.4 \pm 0.2)\%; \\ \langle \hat{\mathcal{M}}_1 \rangle = (-39.9 \pm 4.5)\%; \\ \langle \hat{\mathcal{M}}_2 \rangle = (33.6 \pm 4.2)\%; \\ \langle \hat{\mathcal{M}}_3 \rangle = (-33.8 \pm 4.4)\%, \end{cases} \quad (6.26)$$

with a raw fidelity of  $\mathcal{F}_{\text{GHZ}}^3 = (56.1 \pm 1.6)\%$  using Eqs. (6.24)-(6.25), which exceeds the classical threshold by 3.8 standard deviations, validating a genuine 3-qubit entanglement. Compared to the two-qubit case, the 14% reduction in  $\langle \hat{\mathcal{P}}_z \rangle$  cannot be wholly explained by the non-unity fidelity  $98.1\% \times 98.1\%$  of two spin  $\pi$ -pulses. Apart from these two control pulses, the difference between the  $n = 1$ - and 2-photon measurement sequences is the addition of a second pair of excitation pulses. Therefore, it appears these excitation pulses might be inducing additional spin errors<sup>43</sup>. Furthermore, the equatorial

<sup>43</sup>Note that this is different from cross-excitation error. For  $\langle \hat{\mathcal{P}}_z \rangle$ , cross-excitation error affects both time-bin equally thus should only contribute to an overall phase shift. Cyclicity also plays a role here, but is expected to be minor (2% in total infidelity from Ref. [149]). One possible explanation for this error is the excitation pulses lower the cooling efficiency by driving the anti-dragging optical transitions via  $|\downarrow\rangle \rightarrow |\uparrow\rangle$ . We also observed reduced Rabi and spin-echo visibilities with more optical excitation pulses.

correlations  $|\langle \hat{\mathcal{M}}_k \rangle|$  are overall 36%<sup>44</sup> lower compared to the echo visibility  $V_s^{(2)} = 72\%$  in which only the excitation pulses are absent, which again suggests cross-excitation error (Sec. 6.7.2).

## 6.9 Summary and Outlook

The time-bin entanglement protocol experimentally demonstrated in Ref. [18] has paved an important route towards the scalable generation of entangled photons. As a continuation of this, we have managed to push for one additional photon, creating a genuine 3-qubit GHZ state between the QD electron spin and 2 photons. This is accomplished by improvements across most aspects of the experiment (Table 6.4). Notably, the spin  $\pi$ -rotation fidelity exceeds 98% with a  $Q$ -factor of 31.8, which lifts off the most notorious photo-induced spin-flip error in the previous work, enabling high spin-echo visibilities of  $V_s^{(1)} = 81.5\%$  and  $V_s^{(2)} = 72.0\%$ . The measured high optical cyclicity of  $C = 36.3$  in the Voigt geometry is unprecedented on the QD platform, boosting both the entanglement and readout fidelities.

	Ref. [18]	Current work
QD spin state	Hole	Electron
Magnetic field $\mathbf{B}_x$	2 T	4 T with Voigt mount (Sec. 6.2.2.1)
Optical setup	Excite and collect via 50:50 beam-splitter	Replaced by D-shaped mirror (Sec. 6.2.2.2)
Spin control setup	FPGA with phase shifter and switches	Replaced by AWG with mixer (Sec. 6.2.2.3)
Rotation fidelity $F_\pi$	88.1% (Sec. 3.5)	98.1% (Sec. 6.4)
Spin dephasing time $T_2^*$	23.2 ns	33.3 ns with nuclear cooling (Sec. 6.4.2)
Echo visibility $V_s^{(1)}$	57% (Sec. 3.5.3)	81.5% (Sec. 6.4.3)
Cyclicity $C$	14.7	36.3 (Sec. 6.3.2)
Lifetime-duration ratio $\tau_o/\tau_{\text{MIRA}}$	$\frac{403 \text{ ps}}{35.6 \text{ ps}} \approx 11.3$	$\frac{235 \text{ ps}}{29.6 \text{ ps}} \approx 7.94$

Table 6.4: Summary of changes in the present work compared to Ref. [18].

Despite significant improvements in spin control and cyclicity, the optical excitation suffers from cross-excitation errors. In the current work, the X-polarized optical transitions are enhanced, where their spectral separation  $\Delta_e - \Delta_h = 2\pi \times 9.3$  GHz is less than the excitation laser FWHM bandwidth  $\sigma_o = 2\pi \times 14.9$  GHz, leading to serious cross-excitation error. In addition, there exists a fundamental trade-off between cross-excitation and re-excitation errors [18]. The excitation laser cannot be stretched longer for narrower pulse width since the QD might get re-excited during its lifetime, leading to multi-photon emission  $g^{(2)}(0) \neq 0$ .

<sup>44</sup>There is of course the infidelity from not fulfilling echo conditions due to the third  $\pi$ -pulse having 5 ns extra pulse delay.

It is, however, possible to bypass this trade-off by simply having Y-polarized cycling transitions. For the ideal protocol (Fig. 6.2a), the outer Y-polarized optical transitions are assumed to be cycling since this minimizes spectral overlap between two equally-polarized transitions given their energy splitting  $\Delta_e + \Delta_h = 2\pi \times 34.1$  GHz. To reach the same lifetime-duration ratio (which dictates the probability of re-excitation) as in Ref. [18], the MIRA pulse length needs to be stretched to 20.8 ps<sup>45</sup>, corresponding to  $\sigma_o/2\pi = 21.2$  GHz  $<$  34.1 GHz. Therefore, the same level of  $g^{(2)}(0)$  could be reached, while the probability of cross-excitation is substantially reduced.

### 6.9.1 Outlook

There are several improvements that push the entanglement fidelity and the number of entangled photons further. Table 6.5 summarizes the current experimental limitations and possible solutions to overcome them.

Current limitations	Future improvements
Cross-excitation error	- Larger splitting (with 90°-rotated waveguides), for reduced spectral overlap with $X_1$ .
Finite $g^{(2)}(0)$ and $V_{\text{HOM}}$	- Pulse stretcher [52] for tunable excitation pulse length. - Larger splitting (with 90°-rotated waveguides).
Echo rephasing error	- Understand limitations at echo delay $\tau_{\text{echo}} = 0$ . - Tune $ \mathbf{B}_x $ to change optimal delay for echo revival. - Algorithmic cooling [163] to increase echo revival amplitude.
Low entanglement rates	- Separate nuclear cooling from the main measurement sequence. - Switch to one-sided waveguides. - Larger splitting (with 90°-rotated waveguides), for full optical $\pi$ -pulse. - Active switching of time-bin measurement bases [52].

Table 6.5: Experimental limitations in the present work and potential solutions.

One idea as to why the X-polarized transitions are cycling in the current sample is, the orientation of the fabricated photonic-crystal waveguide is 90° rotated with respect to the previous sample in Ref. [18]. The sheer strain during self-assembly growth of InAs QDs defines the linear dipoles of the QD transitions (see Sec. 1.3). When the QD is located at the waveguide center with its X-dipoles (which we define to be along the crystal axis [110]) aligned with the fundamental waveguide mode M0 (oriented along  $y$ , defined by the white axes), the coupling of M0 to the X-dipole is maximized and the X-polarized transitions are selectively enhanced (Fig. 6.21a) and cycling. On the other hand, if the waveguide is rotated by 90° with respect to the crystallographic axes (Fig. 6.21b, equivalent to Fig. 1.7), such that the Y-dipoles (defined as  $[1\bar{1}0]$ ) experience Purcell enhancement, Y-polarized transitions therefore become spin-cycling.

<sup>45</sup>In theory it can be stretched further for lower  $g^{(2)}$ , but there might be shortage in excitation power.

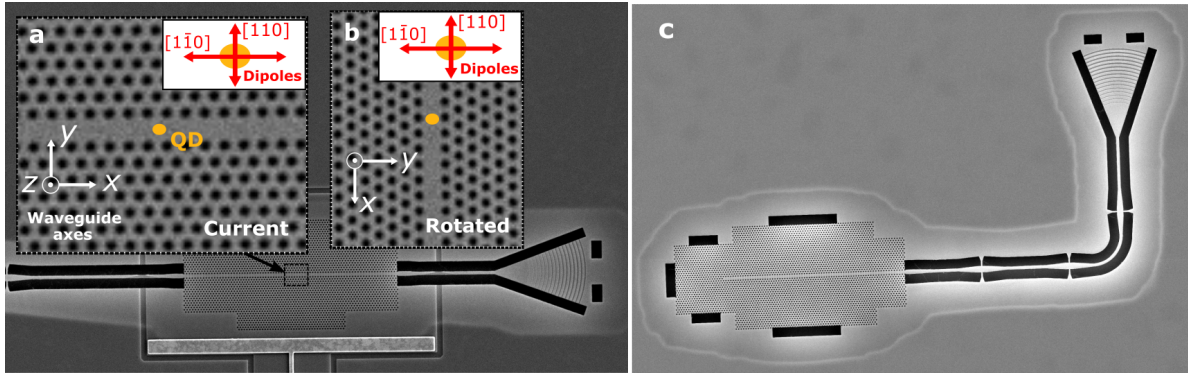


Figure 6.21: **Solutions to ease issues with cross-excitation and low efficiency.** (a) The present QD (orange) is conjectured to be close to the waveguide center with its X-dipoles aligned with the waveguide mode, leading to X-polarized cycling transitions. The QD crystallographic axes (red) are assumed to be perfectly aligned with the waveguide axes (white). (b) Proposed solution to achieve Y-polarized cycling transitions, by fabricating the 90°-rotated waveguide. (c) Scanning Electron Micrograph (SEM) of an one-sided waveguide that in theory enhances QD emission by two-fold, increasing the entanglement rate.

This motivates the fabrication of next-generation waveguide samples with marked orientations along the correct crystallographic axis, to engineer QDs with optically cycling Y-polarized transitions. Such design would help suppress cross-excitation error and multi-photon emission by having a sufficiently wide frequency splitting as previously discussed. Consequently, the entanglement rate would benefit greatly from having driven a full optical  $\pi$  pulse without detuning, since in the current work the QD is excited by a 2 GHz red-detuned optical  $0.1\pi$ -pulse to lower the cross-excitation probability.

Apart from migrating to one-sided waveguides (Fig. 6.21c), the 123 mHz<sup>46</sup> 3-qubit entanglement rate can also be boosted by separating the  $\sim 1 \mu\text{s}$  nuclear cooling pulses from the entanglement measurement sequence. After nuclear cooling, the nuclear spin distribution gradually relaxes back to its “thermal” equilibrium in a timescale governed by the nuclear spin diffusion rate  $\Gamma_{\text{em}}$ . The relaxation time of this decoherence process is measured<sup>47</sup> to be  $1/\Gamma_{\text{em}} = 41.7 \text{ ms}$  at 3 T in Ref. [97]. After each round of nuclear cooling, the  $\sim 600 \text{ ns}$  entanglement sequence can therefore be implemented 60,000 times before starting the next cooling cycle.

With regards to the echo rephasing error, further investigations into the limitations of sub-unity Hahn-echo visibility  $V_s^{(1)}(\tau)$  at pulse delay  $\tau = 0$  (Sec. 6.4.3) are crucial, since  $V_s^{(1)}(0)$  in principle sets an upper bound to the amplitude of echo revival at 29 ns pulse delay, which ultimately curbs the maximum visibility of equatorial correlations  $|\langle \hat{\mathcal{M}}_k \rangle|$ . Algorithmic cooling sequence [163] can also be implemented to further extend the spin dephasing time  $T_2^*$  to beyond 100 ns, whereby narrowing the nuclear spin distribution, the nuclear noises can be better filtered out by the spin-echo<sup>48</sup>, leading to higher echo revival amplitude<sup>49</sup>. Finally, as an interesting thought, to ensure the timing restriction

<sup>46</sup>Estimated by counting the total number of three-fold coincidences per integration time.

<sup>47</sup>Probed by performing Ramsey measurements at increasing pulse delays from the cooling pulses.

<sup>48</sup>The echo filter function works best when the nuclear noise spectrum is effectively a delta function.

<sup>49</sup>Ideally, in the absence of nuclear noises, the echo visibility or amplitude of revived echo at 29 ns pulse delay  $V_s^{(1)}(\tau = 29)$  should approach  $V_s^{(1)}(0)$ .

in Eq. (6.22) is fulfilled by the optimal echo delay, the external magnetic field could be used to finely tune the optimum by controlling nuclear precession frequencies.

# Chapter 7

## Proposal for Deterministic Bell state Analyzers

Based on the photon-scattering scheme demonstrated in Chapter 3, in this chapter we propose an experimentally friendly protocol for implementing a deterministic Bell state analyzer (BSA), which is a two-photon quantum operation that distinguishes between 4 orthonormal photonic Bell states. This is important for performing Bell-state measurements, for deterministic fusion of photonic graph states and entanglement swapping in quantum repeaters [24]. While this has been experimentally demonstrated for polarization-encoded photons by pure optical means [164], we are interested in the solid-state approach using quantum emitters like a quantum dot (QD) to mediate the two-photon interaction, since this easily integrates with the spin-photon interface developed in Chapters 3 and 6 which demonstrate its prowess in generating spin-photon and photon-photon entanglement.

The protocol is built with the current QD-waveguide platform in mind, and is catered towards time-bin encoded photons. We first illustrate the working principle of the BSA by considering its input-output relation in the ideal case. We follow up by verifying each individual case to showcase some of the design rationales behind. At last, we analyze the protocol performance and discuss some hardware requirements for its experimental demonstration on the QD-waveguide platform.

## 7.1 Basic Principle of Bell State Analyzers

Before presenting the BSA protocol, it is instructive to consider the simplest case where the qubit is encoded in the plain  $|0\rangle$  and  $|1\rangle$  bases. The idea of a BSA is that it outputs a unique outcome for a given input Bell state between two photonic qubits, allowing all four Bell states to be distinguishable [24]. This could be achieved by coupling an ancillary qubit to the input photonic states, followed by projective measurements to reveal correlations in the system. Simply put, for a given initial Bell state  $|\Phi^\pm\rangle$  or  $|\Psi^\pm\rangle$ , the input-output relation of the BSA is described by

$$\begin{aligned} |\Phi^\pm\rangle \otimes |0\rangle_a &= \frac{|00\rangle \pm |11\rangle}{\sqrt{2}} \otimes |0\rangle_a \xrightarrow{\text{BSA}} \begin{cases} \frac{|00\rangle + |11\rangle}{\sqrt{2}} \otimes |0\rangle_a \\ \frac{|01\rangle + |10\rangle}{\sqrt{2}} \otimes |0\rangle_a \end{cases} ; \\ |\Psi^\pm\rangle \otimes |0\rangle_a &= \frac{|01\rangle \pm |10\rangle}{\sqrt{2}} \otimes |0\rangle_a \xrightarrow{\text{BSA}} \begin{cases} \frac{|00\rangle - |11\rangle}{\sqrt{2}} \otimes |1\rangle_a \\ \frac{|01\rangle - |10\rangle}{\sqrt{2}} \otimes |1\rangle_a \end{cases}, \end{aligned} \quad (7.1)$$

with the corresponding circuit diagram illustrated in Fig. 7.1, which is similar to the scheme in Ref. [165]. From Eq. (7.1) we see that  $|\Phi\rangle$  and  $|\Psi\rangle$  can first be discerned by reading out the ancillary qubit. An outcome of 0 (1) means the two-photon state is in  $|\Phi^\pm\rangle$  ( $|\Psi^\pm\rangle$ ). In addition, upon detecting the ancilla in the  $|0\rangle_a$  ( $|1\rangle_a$ ) state, the resulting photonic Bell states can be distinguished by parity measurements on the photons, i.e., odd number of 0 or 1 corresponds to the Bell state with negative parity. Since this process involves projective measurement of the qubits, this is also referred to as a destructive Bell-state measurement.

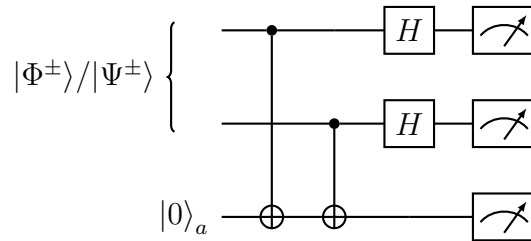
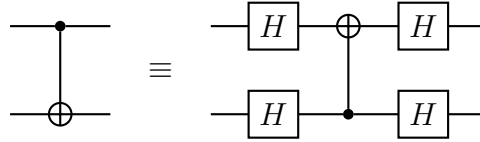


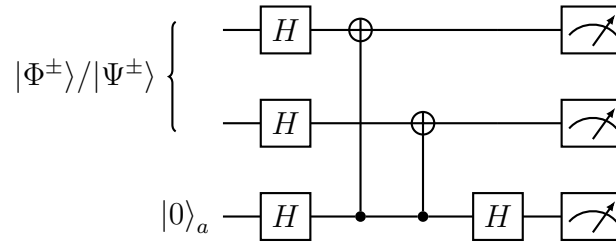
Figure 7.1: **Circuit diagram of a Bell state analyzer.** Eq. (7.1) describes the output states without projective measurements. Figure produced using the Quantikz package [166].

## 7.2 Gate Sequence tailored to Time-bin Photons

Now, to tailor the above circuit (Fig. 7.1) to the time-bin encoding as well as the QD-waveguide platform, we map each CNOT gate into a photon-scattering gate, with the QD spin qubit as the ancilla. One requirement with this approach is that gate operations could only be applied to the spin qubit during the protocol (i.e., no photonic Hadamard gates in between scattering pulses). To perform the mapping, we first invoke the circuit identity:



to simplify the circuit in Fig. 7.1 into



where the QD spin (ancilla) now becomes the control qubit of both CNOT gates. This implies we could directly substitute the CNOT gates by the pulse sequence introduced in Sec. 3.2.1, which consists of sequential scattering of a time-bin qubit interleaved with Hadamard gates. Additionally, to combat against spin dephasing, it is vital to incorporate a spin-echo refusing  $\pi$ -pulse into the protocol [87]. Taking these into considerations, the simplified protocol for BSA is depicted in Fig. 7.2.

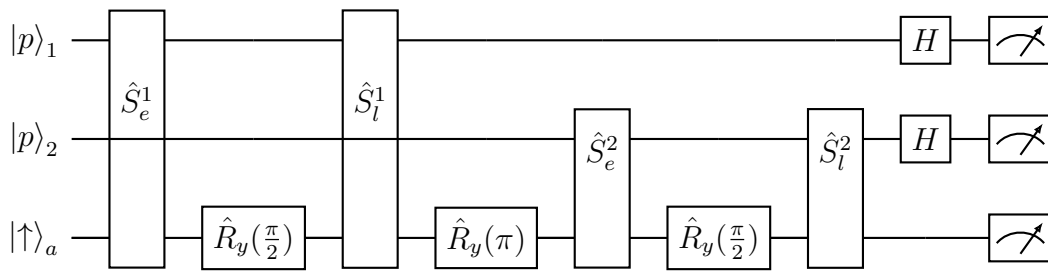


Figure 7.2: Circuit diagram for BSA applicable to time-bin photons. The protocol has been simplified to reduce the number of spin rotations, while keeping the spin-echo intact.  $\hat{S}_j^i$  refers to single-photon scattering interaction between the QD and the  $i$ -th photon in the  $|j\rangle$  basis,  $j \in \{e, l\}$ . The ancilla is assumed to be an electron spin initialized in  $|\uparrow\rangle$ .

### 7.3 Verification of Bell states

To validate the protocol presented in Fig. 7.2, we now compute the output state for each input Bell state. It is pedagogical to consider state propagation of the basis states through the circuit in Fig. 7.1:

$$\begin{cases} |00\rangle \otimes |0\rangle_a & \xrightarrow{\text{BSA}} & |++\rangle \otimes |0\rangle_a; \\ |01\rangle \otimes |0\rangle_a & \xrightarrow{\text{BSA}} & |+-\rangle \otimes |1\rangle_a; \\ |10\rangle \otimes |0\rangle_a & \xrightarrow{\text{BSA}} & |-+\rangle \otimes |1\rangle_a; \\ |11\rangle \otimes |0\rangle_a & \xrightarrow{\text{BSA}} & |--\rangle \otimes |0\rangle_a. \end{cases} \quad (7.2)$$

Here one realizes that due to the two CNOT gates, even (odd) numbers of 0 or 1 in the input state result in  $|0\rangle_a$  ( $|1\rangle_a$ ) for the ancilla, allowing half of the Bell states to be distinguishable. Likewise, for time-bin photons, the corresponding relation can be derived from Fig. 7.2 assuming full single-photon reflection ( $r \rightarrow -1$ ) for the QD spin to be on resonance, and transmission ( $t \rightarrow 1$ ) when it is off-resonant:

$$\begin{cases} |e_1 e_2\rangle \otimes |\uparrow\rangle_a & \xrightarrow{\text{BSA}} & |--\rangle \otimes |\downarrow\rangle_a; \\ |e_1 l_2\rangle \otimes |\uparrow\rangle_a & \xrightarrow{\text{BSA}} & -|+-\rangle \otimes |\uparrow\rangle_a; \\ |l_1 e_2\rangle \otimes |\uparrow\rangle_a & \xrightarrow{\text{BSA}} & |-+\rangle \otimes |\uparrow\rangle_a; \\ |l_1 l_2\rangle \otimes |\uparrow\rangle_a & \xrightarrow{\text{BSA}} & |++\rangle \otimes |\downarrow\rangle_a. \end{cases} \quad (7.3)$$

Using Eq. (7.3), we can then construct the input-output relation for a given Bell state:

$$\begin{aligned} |\Phi^\pm\rangle \otimes |\uparrow\rangle_a &= \frac{|e_1 e_2\rangle \pm |l_1 l_2\rangle}{\sqrt{2}} \otimes |\uparrow\rangle_a \xrightarrow{\text{BSA}} \begin{cases} \frac{|e_1 e_2\rangle + |l_1 l_2\rangle}{\sqrt{2}} \otimes |\downarrow\rangle_a \\ -\frac{|l_1 e_2\rangle + |e_1 l_2\rangle}{\sqrt{2}} \otimes |\downarrow\rangle_a \end{cases} ; \\ |\Psi^\pm\rangle \otimes |\uparrow\rangle_a &= \frac{|e_1 l_2\rangle \pm |l_1 e_2\rangle}{\sqrt{2}} \otimes |\uparrow\rangle_a \xrightarrow{\text{BSA}} \begin{cases} \frac{|l_1 e_2\rangle - |e_1 l_2\rangle}{\sqrt{2}} \otimes |\uparrow\rangle_a \\ -\frac{|e_1 e_2\rangle + |l_1 l_2\rangle}{\sqrt{2}} \otimes |\uparrow\rangle_a \end{cases}, \end{aligned} \quad (7.4)$$

where half of the four Bell states can again be differentiated by projective measurement of the QD spin state. The parity of the Bell state is then determined by checking the coincidence clicks in different time-bins between the first and second photons.

## 7.4 Protocol Analysis

In this section, we present a preliminary analysis of the protocol in Fig. 7.2 based on the spin-photon interface previously characterized in Chapter 6. It is therefore recommended for readers to first skim through the chapter and familiarize with the relevant terminologies. The ancilla qubit we have in mind is an electron spin with a four-level scheme depicted in Fig. 6.8, which has a highly cycling ( $C = 36.3$ ) optical transition  $|\downarrow\rangle \leftrightarrow |\uparrow\downarrow\uparrow\rangle$  and can be coherently controlled with  $F_\pi = 98.1\%$  fidelity under an external magnetic field of  $\mathbf{B}_x = 4$  T.

### 7.4.1 Input-Output Relation for Photon-Scattering

To implement the BSA protocol, we need an atom with a  $\Lambda$ -level scheme in an one-sided waveguide. Although the electron spin qubit characterized in Chapter 6 resides in a two-sided waveguide, for simplicity we here assume such a QD can be found in a single-sided device. In this configuration, the input-output relation for an even mode input field operator  $\hat{a}_{\text{in},e}$  can be written in a similar form as Eq. (3.1):

$$\hat{a}_{\text{out},e} = \left(1 - \frac{2\Gamma_1}{\Gamma + 2i\delta_1}\right) \hat{a}_{\text{in},e}, \quad (7.5)$$

where  $\delta_1$  is the laser detuning with the QD optical transition  $|\downarrow\rangle \leftrightarrow |\uparrow\downarrow\uparrow\rangle$  and  $\Gamma_1 = \frac{C}{C+1}\beta\Gamma$  is the decay rate of the cycling transition with cyclicity  $C$  and waveguide-coupling efficiency  $\beta$  (Sec. 4.3.2).  $\Gamma$  is the total decay rate of the trion  $|\uparrow\downarrow\uparrow\rangle$ . Eq. (7.5) is derived from the first two terms<sup>1</sup> in Eq. (2.5) which holds for one-sided waveguides. In the ideal case with infinite cyclicity and zero coupling loss,  $\Gamma_1 \rightarrow \Gamma$  thus the  $|\downarrow\rangle$  state resonantly reflects the incident field with a reflection coefficient  $r$  given by

$$r = 1 - \frac{2\Gamma_1}{\Gamma + 2i\delta_1} \rightarrow -1; \quad (7.6)$$

and for the electron initialized in  $|\uparrow\rangle$  with a ground-state splitting of  $\Delta_e \gg \Gamma$ , the incident field does not interact with the QD and gets reflected by the bare waveguide without a phase shift. We call this transmission with a coefficient  $t$ :

$$t = 1 - \frac{2\Gamma_1}{\Gamma + 2i(\delta_1 + \Delta_e)} \rightarrow 1. \quad (7.7)$$

Both Eqs. (7.6)-(7.7) underlie the working principle of the single-photon scattering matrix for Eq. (7.3). In the next few sections, we use Eq. (7.5) and some of the theoretical results in Chapter 4 to analyze imperfections in the BSA protocol.

---

<sup>1</sup>For time-bin encoding we are interested in Rayleigh scattering where the frequency of scattered photons is preserved. The third term corresponds to single-photon Raman transition which outputs photons of a different frequency and therefore is undesired.

### 7.4.2 Fidelity for Bell state Analyzer

We quantify the performance of the BSA protocol by the fidelity of each generated photon-photon Bell state given by Eq. (7.4). For each input, we apply the protocol in Fig. 7.2 given a general scattering matrix with scattering operators  $r$  and  $t$ , and compute the inner product between the output and ideal states. For example, for the input Bell state  $|\Phi^+\rangle \otimes |\uparrow\rangle_a$ , the BSA outputs

$$\begin{aligned} |\psi_{\text{out}}\rangle = & \frac{-r(r+t)}{2\sqrt{2}}|e_1e_2 \uparrow\rangle + \frac{(r-t)^2}{4\sqrt{2}}|e_1e_2 \downarrow\rangle + \frac{-r^2+t^2}{4\sqrt{2}}|l_1e_2 \downarrow\rangle \\ & + \frac{-r^2+t^2}{4\sqrt{2}}|e_1l_2 \downarrow\rangle + \frac{-r(r+t)}{2\sqrt{2}}|l_1l_2 \uparrow\rangle + \frac{(r-t)^2}{4\sqrt{2}}|l_1l_2 \downarrow\rangle. \end{aligned} \quad (7.8)$$

As a sanity check, one could verify that when  $r \rightarrow -1$  and  $t \rightarrow 1$ , Eq. (7.8) reduces to  $(|e_1e_2\rangle + |l_1l_2\rangle)/\sqrt{2} \otimes |\downarrow\rangle_a \equiv |\Phi_{\text{ideal}}^+\rangle$ . The corresponding fidelity is therefore

$$F_{\Phi^+} \equiv |\langle \psi_{\text{out}} | \Phi_{\text{ideal}}^+ \rangle|^2 = \int_{-\infty}^{\infty} \left[ \frac{1}{16} |r(\delta_1) - t(\delta_1)|^4 \right] N(0, \sigma_o) d\delta_1, \quad (7.9)$$

which is averaged over the spectral Gaussian wavepacket  $N(0, \sigma_o)$  of two scattering pulses with spectral width  $\sigma_o$  following Eq. (2.6). Note that a more proper way should be to perform different Gaussian averaging for each photon; however, since we expect the infidelity from finite pulse width is low, we assume the consecutive scattering pulses have full spectral overlap.

From this point onward, it is clear that the theoretical formalisms developed in Chapters 2 and 4 can be directly applied to analyze Eq. (7.9). The fidelities for other output states are found similarly

$$\left\{ \begin{array}{l} F_{\Phi^-} = F_{\Phi^+}; \\ F_{\Psi^\pm} = |\langle \psi_{\text{out}} | \Phi_{\text{ideal}}^+ \rangle|^2 = \int_{-\infty}^{\infty} \left[ \frac{1}{4} |r(\delta_1)[r(\delta_1) - t(\delta_1)]|^2 \right] N(0, \sigma_o) d\delta_1. \end{array} \right. \quad (7.10)$$

### 7.4.3 Spin Control Errors

When designing the circuit in Fig. 7.2, the total number of spin rotation pulses is greatly reduced to minimize detrimental effects of laser-induced spin-flip processes (Sec. 4.3.5). First and foremost, the protocol requires only rotation pulses amounting to a total of  $2\pi$ , which is the minimum number of rotations needed for spin-echo. The BSA infidelity (averaged over the four output states) due to finite spin-flip rate  $\kappa$  therefore has the same linear scaling as described in Eq. (4.35), and is estimated to be

$$\mathcal{F}_\kappa^{\text{theory}} \approx 1 - \frac{5\pi}{4} \frac{\kappa}{\Omega_r} - \frac{3}{2} \frac{1}{\Omega_r^2 T_2^{*2}} \approx 99.0\%, \quad (7.11)$$

with an incoherent spin-flip rate  $\kappa = 0.005 \text{ ns}^{-1}$  and spin dephasing time  $T_2^* = 33.3 \text{ ns}$ , for a  $T_r = \pi/\Omega_r = 4 \text{ ns}$   $\pi$ -rotation pulse (Sec. 6.4).

Additionally, the minimum time delay between the  $\hat{R}_y(\frac{\pi}{2})$  and  $\hat{R}_y(\pi)$  pulses, or half of the echo delay  $\tau_{\text{echo}}/2$ , is only bounded by the pulse duration of the scattering pulses  $\hat{S}_l^1$  and  $\hat{S}_e^2$ . Unlike the deterministic gate (Fig. 3.3b) in which the scattering pulses are separated by the interferometric delay, here the time delay between  $\hat{S}_l^1$  and  $\hat{S}_e^2$  can be arbitrarily adjusted. In other words, this allows flexibility for adjusting the echo delay<sup>2</sup> to reach the optimal Hahn-echo visibility  $V_s^{(1)}$  (Sec. 6.4.3).

### 7.4.4 Excitation Errors

#### 7.4.4.1 Cross-excitation Error

Our BSA protocol relies on sequential scattering of two time-bin encoded photonic qubits. In the single-photon scattering regime, the scattering pulse width  $T_{\text{pulse}} = 1/\sigma_o$  is ideally long compared to the QD lifetime  $\tau_o = 1/\Gamma$ . This means with narrowband pulses  $\sigma_o \ll \Gamma$  and a large splitting  $\Delta_e - \Delta_h \gg \Gamma$ , the probability of exciting another X-polarized transition  $|\uparrow\rangle \leftrightarrow |\downarrow\downarrow\uparrow\rangle$  is negligible.

#### 7.4.4.2 Spectral Mismatch Error

The detuning from QD resonance owing to finite spectral width of the scattering pulse reduces the infidelity only to the second order<sup>3</sup>, as discussed in Sec. 2.3.1.1. For the protocol we use  $T_{\text{pulse}} = 4 \text{ ns}$  scattering pulses which is a trade-off between the spectral mismatch error and pulse overlap due to the short interferometric delay  $\tau_{\text{delay}} = 11.8 \text{ ns}$ .

#### 7.4.4.3 Driving-induced Dephasing

Driving-induced decoherence due to remanent multi-photon component in the pulse (Sec. 4.3.7) remains to be a fundamental imperfection for photon-scattering schemes which use weak coherent states. Since the number of scattering pulses in the BSA protocol is doubled compared to the one qubit case, we expect the respective infidelity to be two times higher:

$$\mathcal{F}_{\bar{n}}^{\text{theory}} \approx 1 - 2\bar{n}(P_{\omega_1} + P_{\omega_2}), \quad (7.12)$$

<sup>2</sup>For example, when increasing  $\tau_{\text{echo}}$  to match the echo revival delay, both  $\hat{S}_e^1 - \hat{R}_y(\frac{\pi}{2}) - \hat{S}_l^1$  and  $\hat{S}_e^2 - \hat{R}_y(\frac{\pi}{2}) - \hat{S}_l^2$  pulses can be displaced further away from the  $\hat{R}_y(\pi)$  pulse, so there is no timing restriction similar to Sec. 6.8.1.

<sup>3</sup>This is analyzed for a Gaussian photon wavepacket.

where  $\bar{n}$  is the mean photon number per pulse, and  $P_{\omega_1} + P_{\omega_2}$  is the success probability of single-photon scattering.

### 7.4.5 Systematic Errors

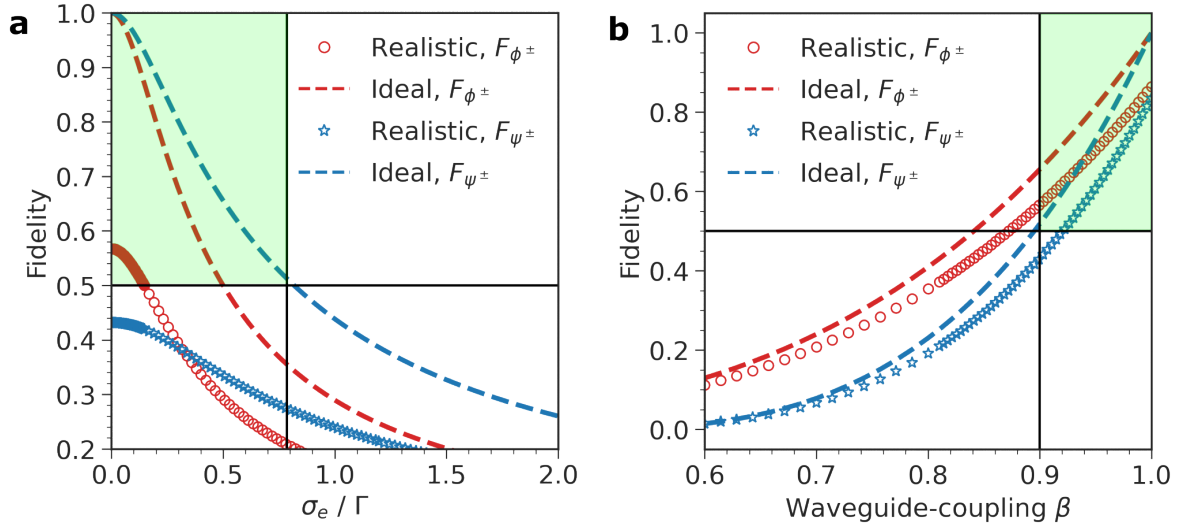


Figure 7.3: **Fidelity of distinguishing Bell states using the BSA, without heralding.** Shaded green regions indicate fidelities of  $> 0.5$  that are reachable with improvements. Vertical line marks the realistic value of the relevant parameter. Computed using Eqs. (7.9)-(7.10). **(a)** Plots of the Bell-state fidelity as a function of spectral diffusion noise  $\sigma_e$  in units of  $\Gamma$ . At  $\sigma_e = 0$  the difference between ideal and realistic curves is given by coupling loss and cyclicity error. **(b)** Fidelity plotted against the waveguide-coupling efficiency  $\beta$ .  $\sigma_e = 0$  is assumed.

#### 7.4.5.1 Cyclicity Error and Coupling Loss

For implementations on one-sided waveguide or cavities, both resonantly and off-resonantly reflected fields are collected, meaning that cyclicity error and waveguide-coupling loss  $1 - \beta \neq 0$  will lead to an imbalance between the two fields, thus in turn lowering the BSA fidelity (to the first order). However, both imperfections can be reduced by using a frequency filter and heralding the protocol on the presence of resonant photons (Sec. 2.1). Fig. 7.3b plots the (unheralded) fidelities of four output Bell state versus the waveguide-coupling efficiency  $\beta$ , under ideal and realistic values of parameters. For the realistic case, we take  $\Gamma_1 = \frac{C}{C+1}\beta\Gamma$  where  $C = 36.3$  is fixed, and assume a pulse duration of  $T_{\text{pulse}} = \sqrt{2 \ln 2} / \sigma_o = 4$  ns. The gap between ideal and realistic curves is therefore mostly given by cyclicity error. Here we observe that without heralding,  $> 80\%$  fidelity is possible when  $\beta > 0.96$  and  $C = 36.3$ .

#### 7.4.5.2 Phonon-induced Pure dephasing

Similar to driving-induced error, fast (compared to QD lifetime) pure dephasing processes by elastic phonon scattering (Sec. 4.3.3) affect single-photon coherence between interfering time-bins, specifically when the scattered photons are measured in the equatorial bases. We expect this infidelity scales linearly with the pure dephasing rate  $\gamma_d$ .

### 7.4.6 Spectral Diffusion

Slow spectral wandering noise has adverse effect on the BSA fidelity via reduction of the resonantly reflected photons (as described by the second term in Eq. (7.5)). When the QD resonance is considerably broadened by spectral diffusion noise (i.e.,  $\sigma_e \approx \Gamma$ ), the output state is dominated by incident photons reflected from the bare waveguide without a phase shift. Although the infidelity is only to the second order in the perturbative regime (Sec. 2.3.1.1), this error currently prevents the protocol (or any deterministic schemes using one-sided waveguides) from being experimentally feasible, since the spectral diffusion noise measured in both QDs is particularly significant:  $\sigma_e/\Gamma \approx 0.7 - 0.84$  (see Secs. 3.6 and 6.6).

To estimate the infidelity from slow spectral diffusion noise, we follow the approach in Sec. 4.3.1 to average Eq. (7.9) over the Gaussian spectral diffusion profile  $N(0, \sigma_e)$ . Figure 7.3a shows the unheralded Bell-state fidelities at different values of  $\sigma_e/\Gamma$ . Vertical line corresponds to  $\sigma_e = 2\pi \times 532$  MHz with  $\Gamma = 4.25$  ns<sup>-1</sup>. At  $\sigma_e = 0$ , the 45%-55% deviation in fidelities between ideal and realistic estimates is due to both cyclicity  $C = 36.3$  and coupling loss  $1 - \beta = 0.1$ . It is therefore absolutely crucial to improve  $\sigma_e$ ,  $C$  and  $\beta$  further to push above the 50%-fidelity limit.

Fortunately, negatively charged excitons  $X^-$  with transform-limited linewidths have been observed [167] in charge-tunable QD devices. Furthermore, there might be an indication that the spectral diffusion noise in the current QD is reduced by nuclear spin cooling.

In Sec. 6.5.1 we measured the second-order correlation function  $g^{(2)}$  at long detector delays using resonant pulsed excitations, and observed a decay time constant of 17.7 ms with a 20% drift in normalized coincidences (Fig. 6.16d). For pulsed  $g^{(2)}$  measurements with narrow (3 GHz FWHM each) frequency filters, the long-delay behaviour should reveal both blinking and spectral diffusion noises: The amplitude indicates the amount of drifts from the noises, while the time constant gives their timescales. The ms timescale for spectral diffusion recorded here might be limited by only charge noise [136] and indicative of a cooled nuclear spin bath.

To verify this, a followed-up experiment would be to repeat the measurement without filters, and observe if the decay time has changed. Without filters, spectral diffusion should not affect  $g^{(2)}$  at long delays provided the drift  $\sigma_e$  is smaller than the broadband pulse width. Additionally, a direct verification of this hypothesis is to perform power-dependent resonance-fluorescence or resonant-transmission measurements with nuclear cooling, to extract the  $X^-$  linewidth.

## 7.5 Experimental Hardware

In this section, we discuss requirements on the experimental hardware to implement a proof-of-principle demonstration of BSA.

For the BSA to work, the two photonic qubits should ideally couple to the grating coupler of the single-sided waveguide and scatter on the QD (Fig. 7.4). To collect the resonantly reflected photons, the cross-polarized excitation scheme introduced in Sec. 3.3.3 could only reject laser backscatter (i.e., from reflections inside the cryostat), but is unable to suppress off-resonant photons reflected by the terminated end of the waveguide. Therefore, it might not be practical to use the QD bias voltage to define a signal-to-noise ratio<sup>4</sup>. A clever polarization alignment procedure [168] might help improve the extinction in this case.

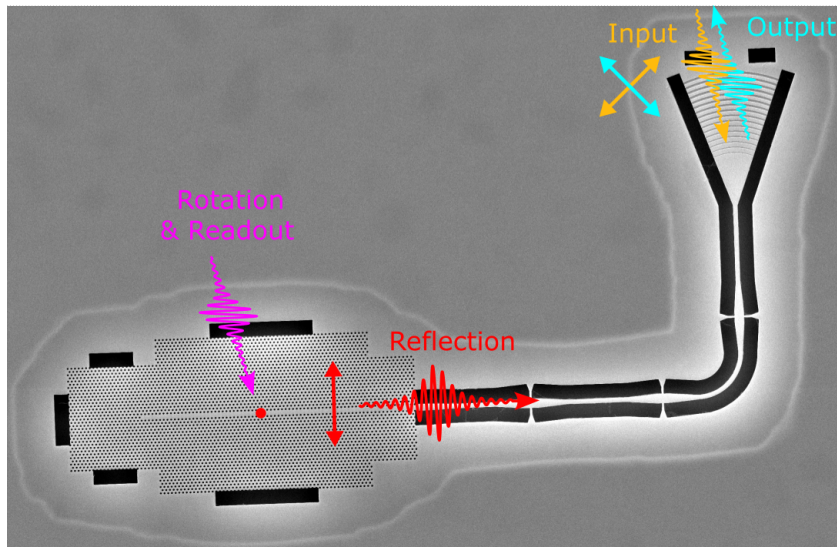


Figure 7.4: **Excitations for implementing BSA.** The spin rotation and readout pulses are implemented in the same manner discussed in Chapter 6.

Regarding the optical setup, the D-shaped mirror added in Sec. 6.2.2.2 needs to be replaced by a 50:50 beamsplitter, as both the qubit laser and collection paths on the optical breadboard need to couple to the same spot. In addition, to verify the protocol, an additional optical interferometric setup might be required to prepare four input photonic Bell states. This means the excitation and detection paths of the time-bin interferometer are separated, thus both interferometers need to be actively stabilized.

In principle the BSA protocol works also with the electron initialized in the opposite spin state  $|\downarrow\rangle$ . Here we assume it is prepared in  $|\uparrow\rangle$ , to be compatible with the experiment in Chapter 6 where we optically pump the transition  $|\downarrow\rangle \rightarrow |\downarrow\downarrow\uparrow\rangle$  to prepare  $|\uparrow\rangle$  during nuclear spin cooling.

<sup>4</sup>Typically we define the signal-to-noise ratio to be  $\text{SNR} = (I_{\text{res}} - I_{\text{off}})/I_{\text{off}}$ , where  $I_{\text{res}}$  ( $I_{\text{off}}$ ) is the intensity measured at resonant (off-resonant) bias voltage.

## 7.6 Conclusion

In this chapter we propose an experimentally accessible protocol to realize a Bell state analyzer. Our protocol is customized for the quantum dot (QD) spin-photon interface developed in this thesis and is able to distinguish between time-bin encoded photonic Bell pairs. A further analysis of the protocol performance suggests that the spectral diffusion noise is currently a dominant error source limiting its fidelity, though there are some experimental evidences already showing transform-limited  $X^-$  QDs, which points to an optimistic outlook.



# Chapter 8

## Summary with Outlook

The central results reported in this thesis are categorized into three pieces: (1) theoretical analysis of quantum state transfer between a frequency-encoded photon and a quantum-dot spin, (2) experimental demonstration of spin-photon entanglement via photon-scattering, supported by theoretical analysis of the entanglement fidelity, and; (3) experimental realization of spin-photon-photon entanglement by single-photon emission of a quantum dot. All three pieces of work are built upon a waveguide-mediated coherent spin-photon interface, and cater to specific applications crucial for quantum information processing.

In **Chapters 2** we proposed and investigated the feasibility of a photon-scattering protocol to deterministically transfer the state of a flying photon to a local quantum-dot spin embedded in a nanophotonic waveguide. We found that it is robust to most of the current experimental imperfections with fidelity comparable to the atomic platform, and can in principle operate passively without active pulse control. Moreover, we laid out a detailed guide for realistic implementation of the protocol, which we hope to motivate future experiments.

In **Chapter 3**, we experimentally generated a Bell state between a time-bin encoded photon and a quantum-dot hole spin in a photonic-crystal waveguide. We benchmarked the quality of the light-matter interface required for entanglement generation, by measuring the optical coherence of the single-photon scattering process and fidelity of spin control. A coherent spin-photon interface with optical cyclicity of  $C = 14.7$  and hole spin-control fidelity of  $F_\pi = 88.1\%$  is sufficient to generate an entanglement fidelity of  $\mathcal{F}_{\text{Bell}} = 74.3\%$ , which is comparable to other solid-state systems, while the entanglement speed is improved by two orders of magnitude.

To understand the contribution from various imperfections that limit  $\mathcal{F}_{\text{Bell}}$ , in **Chapter 4** we followed the theoretical tools developed in Chapter 2 and analyzed the entanglement protocol under known experimental errors such as phonon-induced pure dephasing, spin control errors, spectral diffusion and waveguide-coupling loss. From the theory, we obtained a reliable estimate of the fidelity which shows full agreement with the measured  $\mathcal{F}_{\text{Bell}}$ . The convergence between theoretical and experimental estimates has demonstrated not only a good understanding of our quantum system, but also validity of the theory.

An interesting short study sprang from Chapter 3 is the direct measurement of pure dephasing rate in the waveguide platform, by interfering two resonantly scattered single photons on a beamsplitter and measuring the detector contrast at different photon numbers. To unravel intriguing physics in the measurement, in **Chapter 5** we considered nonlinear scattering dynamics with two-photon states, and found a neat expression of the

detector intensity contrast, or termed photon visibility. We noticed a salient resemblance between the photon visibility and the Hong-Ou-Mandel visibility. Consequently, given complexity of measuring the latter, the photon visibility measurement could potentially be a more accurate and accessible way to extract the pure dephasing rate.

The agreement between theory and experiment demonstrated in Chapter 4 gives us confidence in applying the scattering theory to analyze other related schemes. Besides, the photon-scattering approach enables a plenitude of exciting applications within quantum information processing. For these reasons, **Chapter 7** showcased one of such applications by presenting a simple protocol for deterministic Bell-state analyzers (BSA). The protocol is constructed based on our waveguide-induced spin-photon interface, and is greatly simplified to suit the current experimental needs. We performed a rudimentary theoretical analysis of its fidelity, and highlighted some experimental challenges that future entrants need to overcome for a proof-of-principle experiment.

Finally, as an extension of the time-bin entanglement scheme in Ref. [18], we experimentally realized entanglement between a quantum-dot electron spin and two photons in **Chapter 6**. This experiment relies on spontaneous single-photon emission of the negatively charged exciton, which is fundamentally different from the photon-scattering scheme in the previous chapters. Both approaches are connected by time reversal symmetry, but can both mediate light-matter entanglement.

Several modifications in the experimental setup and quantum-dot device have smoothed the way for an improved spin-photon interface, with a higher cyclicity  $C = 36.3$  and near-unity electron spin-rotation fidelity  $F_\pi = 98.1\%$ . With these, we measured a spin-photon Bell-state fidelity of  $\mathcal{F}_{\text{Bell}} = 77.4\%$  and 3-qubit GHZ-state fidelity of  $\mathcal{F}_{\text{GHZ}}^3 = 56.1\%$ . The fidelities are primarily reduced by cross-excitation error owing to the broadband excitation laser exciting unwanted transitions, but can be mitigated by fabricating waveguides  $90^\circ$  relative to the quantum-dot crystallographic axes in the current sample. Therefore, the path towards a higher number of entangled photons is clear, and the generation of 4-qubit entanglement should be within experimental reach.

# Appendix A

## Formula of the Average Gate Fidelity in Heralded Operations

In this Appendix we derive the linear relation between the Choi-Jamiolkowski fidelity  $\mathcal{F}^{\text{CJ}}$  and the weighted average conditional fidelity  $\bar{\mathcal{F}}^{(c)}$  used in Chapter 2:

$$\bar{\mathcal{F}}^{(c)} = \frac{2}{3}\mathcal{F}^{\text{CJ}} + \frac{1}{3}. \quad (\text{A.1})$$

The proof is made by deriving an expression for each fidelity and comparing their results.

Proof:

**(1) Choi-Jamiolkowski fidelity  $\mathcal{F}^{\text{CJ}}$ .** The starting point for the Choi-Jamiolkowski fidelity is to consider a (fictitious) input state, which is a Bell-state between two subsystems A and S:

$$|\psi_{\text{in}}\rangle = \frac{1}{\sqrt{2}}\left(|0_A 0_S\rangle + |1_A 1_S\rangle\right). \quad (\text{A.2})$$

The Choi-Jamiolkowski fidelity corresponds to the fidelity of the state when we apply our map  $\mathcal{I}_A \otimes \mathcal{E}_S$  to the ideal EPR-pair in the bipartite system. If the Choi-Jamiolkowski fidelity is above 50% this guarantees that the fictitious state would remain entangled after the (conditional) operation on qubit S, and thus signifies that the map is entanglement-preserving.

The quantum gate process in general is modelled by the superoperator  $\mathcal{E}$  acting on an outer product  $|i\rangle\langle j|$ . Requiring the density matrix to be normalized after a non-trace preserving map, i.e., by conditioning on a photon in the output, the density matrix of the output state is

$$\begin{aligned} \rho_{\text{out}} &= \frac{|\psi_{\text{out}}\rangle\langle\psi_{\text{out}}|}{\text{Tr}(|\psi_{\text{out}}\rangle\langle\psi_{\text{out}}|)} \\ &= \frac{|\psi_{\text{out}}\rangle\langle\psi_{\text{out}}|}{\sum_{i,j \in \{0,1\}} \langle i_A j_S | (|\psi_{\text{out}}\rangle\langle\psi_{\text{out}}|) | i_A j_S \rangle} \\ &= \frac{|0_A\rangle\mathcal{E}(|0_S\rangle\langle 0_S|)\langle 0_A| + |0_A\rangle\mathcal{E}(|0_S\rangle\langle 1_S|)\langle 1_A| + |1_A\rangle\mathcal{E}(|1_S\rangle\langle 0_S|)\langle 0_A| + |1_A\rangle\mathcal{E}(|1_S\rangle\langle 1_S|)\langle 1_A|}{\sum_{j,m \in \{0,1\}} \mathcal{M}_{j,m,m,j}}, \end{aligned} \quad (\text{A.3})$$

where  $\mathcal{M}_{k,l,l,k} = \langle k_S | \mathcal{E}(|l_S\rangle\langle l_S|) |k_S\rangle$  can be interpreted as the probability for subsystem S to be in state  $|k\rangle$  after the operation  $\mathcal{E}$  when starting in state  $|l\rangle$ .

For a perfect gate operation denoted by the unitary operator  $\mathcal{U}_{\text{ideal}}$ , we have

$$\frac{1}{\sqrt{2}} \left( |0_A 0_S\rangle + |1_A 1_S\rangle \right) \rightarrow \frac{1}{\sqrt{2}} \left[ |0_A\rangle \otimes \mathcal{U}_{\text{ideal}} |0_S\rangle + |1_A\rangle \otimes \mathcal{U}_{\text{ideal}} |1_S\rangle \right] = |\psi_{\text{ideal}}\rangle. \quad (\text{A.4})$$

Therefore, the Choi-Jamiolkowski fidelity of the mapping is

$$\mathcal{F}^{\text{CJ}} = \langle \psi_{\text{ideal}} | \rho_{\text{out}} | \psi_{\text{ideal}} \rangle = \frac{\sum_{j,m=\{0,1\}} \mathcal{M}'_{j,j,m,m}}{2 \sum_{j,m=\{0,1\}} \mathcal{M}_{j,m,m,j}}, \quad (\text{A.5})$$

where  $\mathcal{M}'_{k,l,i,j} = \langle k_S | \mathcal{U}_{\text{ideal}}^\dagger \mathcal{E}(|l_S\rangle\langle i_S|) \mathcal{U}_{\text{ideal}} |j_S\rangle$  computes the overlap with the ideal state.

**(2) Weighted average of the conditional fidelity  $\bar{\mathcal{F}}^{(c)}$ .** To evaluate the weighted average we need to consider the evolution of specific states.

The input-output relation for applying a unitary operator  $\mathcal{U}$  on an arbitrary input qubit S on the Bloch sphere is

$$|\psi_{\text{in}}\rangle = \cos \frac{\theta}{2} |0_S\rangle + \sin \frac{\theta}{2} e^{i\phi} |1_S\rangle \xrightarrow{\mathcal{U}} \cos \frac{\theta}{2} \mathcal{U} |0_S\rangle + \sin \frac{\theta}{2} e^{i\phi} \mathcal{U} |1_S\rangle = |\psi_{\text{out}}\rangle, \quad (\text{A.6})$$

which can be generalized to a non-unitary operation  $\mathcal{E}$  via  $\mathcal{U}|i\rangle\langle j|\mathcal{U}^\dagger \rightarrow \mathcal{E}(|i\rangle\langle j|)$ . The normalized density matrix of the output state then becomes

$$\begin{aligned} \rho_{\text{out}} &= \frac{|\psi_{\text{out}}\rangle\langle\psi_{\text{out}}|}{\text{Tr}(|\psi_{\text{out}}\rangle\langle\psi_{\text{out}}|)} \\ &= \frac{\cos^2(\frac{\theta}{2})\mathcal{E}(|0_S\rangle\langle 0_S|) + \sin^2(\frac{\theta}{2})\mathcal{E}(|1_S\rangle\langle 1_S|) + \sin(\frac{\theta}{2})\cos(\frac{\theta}{2})e^{i\phi}\mathcal{E}(|1_S\rangle\langle 0_S|) + \text{H.c.}}{\sum_{i=\{0,1\}} \langle i_S | \left( \cos^2(\frac{\theta}{2})\mathcal{E}(|0_S\rangle\langle 0_S|) + \sin^2(\frac{\theta}{2})\mathcal{E}(|1_S\rangle\langle 1_S|) + \sin(\frac{\theta}{2})\cos(\frac{\theta}{2})e^{i\phi}\mathcal{E}(|1_S\rangle\langle 0_S|) + \text{H.c.} \right) |i_S\rangle}, \end{aligned} \quad (\text{A.7})$$

where the denominator is the success probability  $P_i^s$  of the map for the specific input qubit state. The fidelity for each cardinal input state can then be computed using  $\mathcal{F}_i^{(c)} = \langle \psi_{\text{ideal}} | \rho_{\text{out}} | \psi_{\text{ideal}} \rangle$  at 6 different sets of values for  $\theta$  and  $\phi$ .

When evaluating the weighted average  $\bar{\mathcal{F}}^{(c)}$ , the weighted sum  $\sum_i P_i^s \mathcal{F}_i^{(c)}$  and  $\sum_i P_i^s$  will contain the sum of phases  $e^{\pm i\phi}$  over 4 different sets of azimuthal angle  $\phi$ , thus the phases will eventually be cancelled out according to the table below:

The weighted average conditional fidelity is therefore

$$\bar{\mathcal{F}}^{(c)} = \frac{\sum_i P_i^s \mathcal{F}_i^{(c)}}{\sum_i P_i^s} = \frac{1}{3} \frac{\sum_{j,m=\{0,1\}} \left( \mathcal{M}'_{j,j,m,m} + \mathcal{M}'_{j,m,m,j} \right)}{\sum_{j,m=\{0,1\}} \mathcal{M}_{j,m,m,j}}. \quad (\text{A.8})$$

Index $i$	$\theta$	$\phi$	$e^{i\phi}$	$e^{2i\phi}$	$e^{-i\phi}$	$e^{-2i\phi}$	Fidelity
1	0	-	-	-	-	-	$\mathcal{F}_1^{(c)}$
2	$\pi$	-	-	-	-	-	$\mathcal{F}_2^{(c)}$
3	$\pi/2$	0	1	1	1	1	$\mathcal{F}_3^{(c)}$
4	$\pi/2$	$\pi$	-1	1	-1	1	$\mathcal{F}_4^{(c)}$
5	$\pi/2$	$\pi/2$	$i$	-1	$-i$	-1	$\mathcal{F}_5^{(c)}$
6	$\pi/2$	$3\pi/2$	$-i$	-1	$i$	-1	$\mathcal{F}_6^{(c)}$

**(3) Comparing two fidelities.** Comparing (A.5) with (A.8) we find a relation between the two expressions

$$\bar{\mathcal{F}}^{(c)} = \frac{2}{3}\mathcal{F}^{\text{CJ}} + \frac{1}{3} \frac{\sum_{j,m=\{0,1\}} \mathcal{M}'_{j,m,m,j}}{\sum_{j,m=\{0,1\}} \mathcal{M}_{j,m,m,j}}, \quad (\text{A.9})$$

Using the property that the trace of a matrix is invariant under the unitary transformation  $\mathcal{U}_{\text{ideal}}$ , we arrive at

$$\bar{\mathcal{F}}^{(c)} = \frac{2}{3}\mathcal{F}^{\text{CJ}} + \frac{1}{3}. \quad (\text{A.10})$$

Eq. (A.10) thus establishes a linear relation between two fidelity definitions, which allows us to extract the Choi-Jamiolkowski fidelity for the heralded state-transfer protocol.



# Appendix B

## Normalization of the Two-photon Output State

Here we show that the analytical forms in Eq. (5.8) satisfy the normalization condition for the two-photon output state. The computation code is documented in the Mathematica notebook “AnalyticalPhotonVisibility.nb” [26]. A two-photon input state with a Gaussian spectral profile  $\Phi$  for each photon is expressed as

$$|2\rangle_{\text{in}} = \int d\omega_a d\omega_b \Phi(\omega_a) \Phi(\omega_b) \hat{a}^\dagger(\omega_a) \hat{a}^\dagger(\omega_b) |\emptyset\rangle, \quad \text{with } \Phi(\omega_i) \equiv (2\pi\sigma_o^2)^{-\frac{1}{4}} \exp\left(-\frac{(\omega_i - \omega_0)^2}{4\sigma_o^2}\right), \quad (\text{B.1})$$

where  $\omega_0$  is the resonant frequency of the quantum dot (QD).  $\sigma_o$  is the spectral width of the Gaussian input pulse centered at  $\omega_0$ . After scattering, both photons can be transmitted or reflected, or either one is transmitted while another is reflected, see Fig. 5.1. In general, the two-photon output state in either of the above cases is written as

$$\begin{aligned} |2\rangle_{\text{out}} &= \int d\omega_a d\omega_b \Phi(\omega_a) \Phi(\omega_b) F(\omega_a, \omega_b) \hat{a}^\dagger(\omega_a) \hat{a}^\dagger(\omega_b) |\emptyset\rangle \\ &\quad + \int d\Delta_2 d\omega_a d\omega_b \Phi(\omega_a) \Phi(\omega_b) \mathcal{B}(\omega_a, \omega_b, \Delta_2) \hat{a}^\dagger(v_a) \hat{a}^\dagger(v_b) |\emptyset\rangle \\ &= \underbrace{\int dK d\Delta_1 \Phi(K, \Delta_1) F(K, \Delta_1) |K, \Delta_1\rangle}_{\text{Linear}} + \underbrace{\int dK d\Delta_1 d\Delta_2 \Phi(K, \Delta_1) \mathcal{B}(K, \Delta_1, \Delta_2) |K, \Delta_2\rangle}_{\text{Nonlinear}} \\ &\equiv |\mathcal{L}\rangle + |\mathcal{N}\rangle, \end{aligned} \quad (\text{B.2})$$

where  $\Phi(K, \Delta_1) = \Phi(\omega_a) \Phi(\omega_b)$  and  $\Delta_1 \equiv (\omega_a - \omega_b)/2$ .  $F(\omega_a, \omega_b)$  is the QD response function. For example,  $F(\omega_a, \omega_b) = \mathcal{R}(\omega_a) \mathcal{T}(\omega_b)$  when photon  $a$  is elastically reflected while photon  $b$  is transmitted. We define  $K = \omega_a + \omega_b$  the total energy of the photons which is conserved during scattering, thus with the sum of output frequencies  $v_a + v_b = K$  and their difference  $\Delta_2 \equiv (v_a - v_b)/2$  we express  $v_a = K/2 + \Delta_2$  and  $v_b = K/2 - \Delta_2$ .  $\mathcal{B}$  is the momentum distribution of the two correlated photons given by [120]

$$\mathcal{B}(K, \Delta_1, \Delta_2) = \frac{1}{2} \left( \frac{1}{4} B \right) = \frac{2i\Gamma^2}{\pi} \frac{K - 2\omega_0 + i\Gamma}{[4\Delta_1^2 - (K - 2\omega_0 + i\Gamma)^2][4\Delta_2^2 - (K - 2\omega_0 + i\Gamma)^2]}. \quad (\text{B.3})$$

Here  $K - 2\omega_0$  is the total energy detuning to the QD resonance.  $\Gamma$  is the QD total decay rate. Note that an extra factor of 1/2 is included to account for the symmetric states

of two bosons, as Eqs. (127), (128) and (130) in Ref. [120] describe the total nonlinear contribution from two interchangeable bosons  $k_1$  and  $p_1$  whereas we are only interested in the contribution from one particular pair.

The probability amplitude of each of the output terms is therefore

$$\begin{aligned}
\langle \mathcal{L} | \mathcal{L} \rangle &= \int dK dK' d\Delta_1 d\Delta_1' \Phi(K, \Delta_1) \Phi^*(K', \Delta_1') F(K, \Delta_1) F^*(K', \Delta_1') \delta(K - K') \delta(\Delta_1 - \Delta_1') \\
&= \int dK d\Delta_1 |\Phi(K, \Delta_1)|^2 |F(K, \Delta_1)|^2; \\
\langle \mathcal{N} | \mathcal{N} \rangle &= \int dK dK' d\Delta_1 d\Delta_1' d\Delta_2 d\Delta_2' \Phi(K, \Delta_1) \Phi^*(K', \Delta_1') \\
&\quad \times \mathcal{B}(K, \Delta_1, \Delta_2) \mathcal{B}(K', \Delta_1', \Delta_2') \delta(K - K') \delta(\Delta_2 - \Delta_2') \\
&= \int dK d\Delta_1 d\Delta_1' d\Delta_2 \Phi(K, \Delta_1) \Phi^*(K, \Delta_1') \mathcal{B}(K, \Delta_1, \Delta_2) \mathcal{B}(K, \Delta_1', \Delta_2); \\
\langle \mathcal{L} | \mathcal{N} \rangle &= \int dK dK' d\Delta_1 d\Delta_1' d\Delta_2 \Phi(K, \Delta_1) \Phi^*(K', \Delta_1') F^*(K', \Delta_1') \mathcal{B}(K, \Delta_1, \Delta_2) \delta(K - K') \delta(\Delta_2 - \Delta_1') \\
&= \int dK d\Delta_1 d\Delta_2 \Phi(K, \Delta_1) \Phi^*(K, \Delta_2) F^*(K, \Delta_2) \mathcal{B}(K, \Delta_1, \Delta_2). \tag{B.4}
\end{aligned}$$

As an example we shall compute the cross-term  $\langle \mathcal{L} | \mathcal{N} \rangle$  for one photon transmitted and another reflected. The QD response function is given by

$$\begin{aligned}
F^*(K, \Delta_2) &= \mathcal{T}^*(\omega_a) \mathcal{R}^*(\omega_b) = \left( 1 - \frac{\Gamma}{\Gamma + 2i(\omega_a - \omega_0)} \right) \frac{-\Gamma}{\Gamma + 2i(\omega_b - \omega_0)} \\
&= \left( 1 - \frac{\Gamma}{\Gamma + i(K - 2\omega_0) + 2i\Delta_2} \right) \frac{-\Gamma}{\Gamma + i(K - 2\omega_0) - 2i\Delta_2} \\
&= \frac{i\Gamma(K - 2\omega_0 + 2\Delta_2)}{[(K - 2\omega_0) - i\Gamma]^2 - 4\Delta_2^2}. \tag{B.5}
\end{aligned}$$

Therefore,

$$\begin{aligned}
\langle \mathcal{L} | \mathcal{N} \rangle_{\text{TR}} &= \frac{-\Gamma^2}{\pi^2 \sigma_o^2} \int dK e^{-\frac{(K-2\omega_o)^2}{4\sigma_o^2}} (K - 2\omega_0 + i\Gamma) \\
&\quad \times \int \frac{e^{-\frac{\Delta_2^2}{2\sigma_o^2}} (K - 2\omega_0 + 2\Delta_2)}{[(K - 2\omega_0 - i\Gamma)^2 - 4\Delta_2^2][4\Delta_2^2 - (K - 2\omega_0 + i\Gamma)^2]} d\Delta_2 \\
&\quad \times \int \frac{e^{-\frac{\Delta_1^2}{2\sigma_o^2}}}{[4\Delta_1^2 - (K - 2\omega_0 + i\Gamma)^2]} d\Delta_1, \tag{B.6}
\end{aligned}$$

where the integrals with  $\Delta_1$  and  $\Delta_2$  are separable and thus can be straightforwardly computed. The integral with  $K$ , however, has no closed form. Thus the trick is to first apply the perturbative limit where  $\sigma_o \ll \Gamma$  to simplify and expand the integrand to the fourth order (See the attached Mathematica notebook [26]). The corresponding analytical form can therefore be found after integrating with  $K$ :

$$\langle \mathcal{L} | \mathcal{N} \rangle_{\text{TR}} \approx -\frac{8}{\sqrt{\pi}} \frac{\sigma_o^3}{\Gamma^3}, \quad \sigma_o \ll \Gamma. \tag{B.7}$$

Similarly, using the same trick we find

$$\begin{aligned}
\langle \mathcal{L}|\mathcal{N} \rangle_{\text{RT}} &\approx -\frac{8}{\sqrt{\pi}} \frac{\sigma_o^3}{\Gamma^3}; & \langle \mathcal{L}|\mathcal{L} \rangle_{\text{RT}} &\approx \frac{4\sigma_o^2}{\Gamma^2} - \frac{64\sigma_o^4}{\Gamma^4} \\
\langle \mathcal{L}|\mathcal{N} \rangle_{\text{TT}} &\approx -\frac{8}{\sqrt{\pi}} \frac{\sigma_o^3}{\Gamma^3}; & \langle \mathcal{L}|\mathcal{L} \rangle_{\text{TT}} &\approx \frac{16\sigma_o^4}{\Gamma^4} \\
\langle \mathcal{L}|\mathcal{N} \rangle_{\text{RR}} &\approx -\frac{4}{\sqrt{\pi}} \frac{\sigma_o}{\Gamma} + \frac{72}{\sqrt{\pi}} \frac{\sigma_o^3}{\Gamma^3}; & \langle \mathcal{L}|\mathcal{L} \rangle_{\text{RR}} &\approx 1 - \frac{8\sigma_o^2}{\Gamma^2} + \frac{112\sigma_o^4}{\Gamma^4} \\
\langle \mathcal{N}|\mathcal{N} \rangle &\approx \frac{2}{\sqrt{\pi}} \frac{\sigma_o}{\Gamma} - \frac{24}{\sqrt{\pi}} \frac{\sigma_o^3}{\Gamma^3}; & \langle \mathcal{L}|\mathcal{L} \rangle_{\text{TR}} &\approx \frac{4\sigma_o^2}{\Gamma^2} - \frac{64\sigma_o^4}{\Gamma^4}.
\end{aligned} \tag{B.8}$$

One interesting observation is that the terms associated with the nonlinearity scale with odd powers, while the linearities scale with only even powers. The normalization condition is therefore satisfied when  $\sigma_o \ll \Gamma$  as

$$\begin{aligned}
&\sum_i (\langle \mathcal{L}|\mathcal{L} \rangle_i + \langle \mathcal{L}|\mathcal{N} \rangle_i + \langle \mathcal{N}|\mathcal{L} \rangle_i + \langle \mathcal{N}|\mathcal{N} \rangle_i) \\
&= \sum_i \langle \mathcal{L}|\mathcal{L} \rangle_i + 2 \sum_i \langle \mathcal{L}|\mathcal{N} \rangle_i + \sum_i \langle \mathcal{N}|\mathcal{N} \rangle_i \\
&= 1 + 2 \left( \frac{-4}{\sqrt{\pi}} \frac{\sigma_o}{\Gamma} + \frac{48}{\sqrt{\pi}} \frac{\sigma_o^3}{\Gamma^3} \right) + 4 \left( \frac{2}{\sqrt{\pi}} \frac{\sigma_o}{\Gamma} - \frac{24}{\sqrt{\pi}} \frac{\sigma_o^3}{\Gamma^3} \right) = 1.
\end{aligned} \tag{B.9}$$



# Appendix C

## Speculations on the Origin of Power-dependent Spin-flips

One hypothesis on the origin of the power-dependent spin-flips is the Raman laser ejects the quantum-dot (QD) charge when subject to a strong rotation pulse. The charge is removed from the QD confinement, followed by the tunneling of another charge under the presence of an applied bias voltage. The tunnelled charge now has a randomized spin state with its spin coherence scrambled, which manifests in an incoherent spin-flip rate  $\kappa$ . This photoelectric effect may take place when the QD is illuminated by a laser with energy greater than some threshold energy [126].

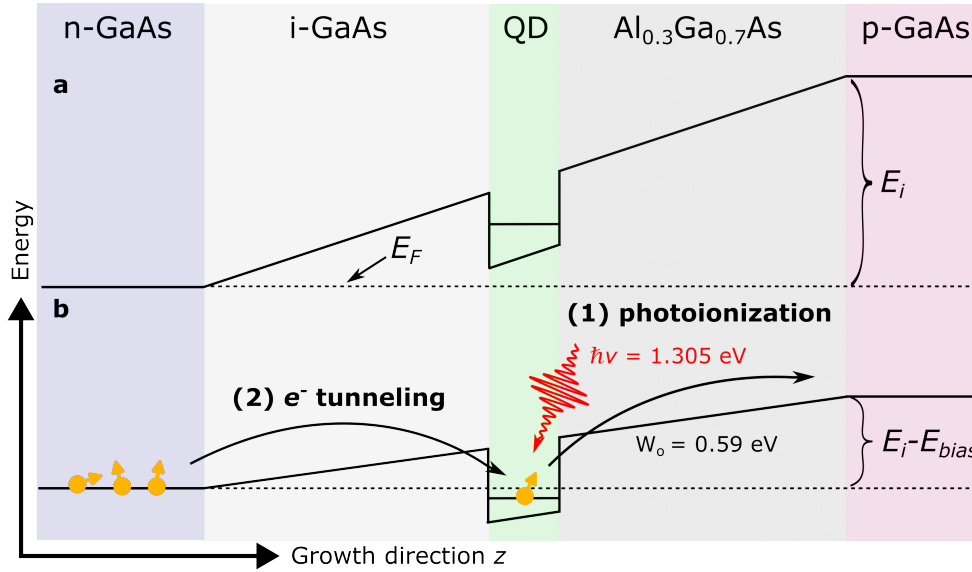


Figure C.1: **Proposed mechanism for laser-induced spin decoherence.** (a) Energy levels of the  $p-i-n$  diode conduction band without applying a bias voltage. The QD energy level is above the Fermi level  $E_F$  thus tunneling from the electron-rich  $n$ -layer is forbidden. (b) At the  $X^-$  bias voltage, the band structure is tilted downwards such that the Fermi level has higher energy than the QD  $s$ -shell. An electron is thus trapped in the QD as the spin qubit. Laser-induced spin-flip is hypothesized to be a two-step process: (1) the confined electron is kicked out by the red-detuned Raman laser (red) with photon energy larger than the work function  $W_0$ . (2) Another electron tunnels into the emptied QD with a random spin state.

Before elaborating further, it is instructive to first recap how an applied bias voltage

prepares the  $X^-$  ground state (Sec. 1.2.2). Fig. C.1a schematically shows the conduction-band energy at different layers of the diode. The electronic potential difference between the doped  $n$ - and  $p$ - layers results in a built-in energy difference  $E_i$ . In the figure, the QD energy level ( $s$ -shell) is shown to be above the Fermi energy  $E_F$  of electrons defined by the  $n$ -doped back contact, which means electron tunneling to the QD is energetically forbidden.

Now, when a constant  $X^-$  bias voltage is applied, which in our case is 1.31 V, the QD level has lower energy than the Fermi sea with resonant frequency of 316.272 THz (1.308 eV), thus an electron is trapped<sup>1</sup> as the QD ground state. The energetic offset (or work function) between the confined state of the electron in the QD and the bandgap energy of the  $\text{Al}_{0.3}\text{Ga}_{0.7}\text{As}$  blocking barrier<sup>2</sup> is given by  $W_o = (1.899 - 1.308) = 0.59$  eV, which is significantly lower than the photon energy from the red-detuned Raman laser (1.305 eV for 315.622 THz). This means the laser has sufficient energy to lift the confined electron far above the  $\text{Al}_{0.3}\text{Ga}_{0.7}\text{As}$  conduction band edge. The photoionization rate also appears to scale linearly with laser power [126], consistent with our observations on  $\kappa$  and  $\gamma_r$  (Sec. 3.5). Once the QD becomes empty, another electron tunnels from the Fermi reservoir to the QD, as it is energetically favourable at the  $X^-$  bias voltage, but its spin state is effectively random<sup>3</sup>.

If the hypothesis is true, this means such a photoelectric effect might be unavoidable for optical spin control of QDs, since the Raman laser frequency is at least 300 THz<sup>4</sup> (corresponding to a photon energy of 1.24 eV still greater than the threshold energy  $W_o$ ).

Additionally, if the photoelectric effect is internal, i.e., the ejected electron/hole jumps to a higher-energy state or charge trap within the diode layers, in which case the transition rate of such process should be described by Fermi's Golden rule, and depends on the wavefunction overlap between initial and final states. This implies modifications on the thickness of different heterostructure layers could suppress the transition rate.

It remains an open question whether the mechanism for power-dependent spin-flips is different between electrons and holes, as our sample size is limited.

<sup>1</sup>More electrons are forbidden by Coulomb blockade [42].

<sup>2</sup>The bandgap energy of  $\text{Al}_x\text{Ga}_{1-x}\text{As}$  is given by  $(1.519 + 1.155x + 0.37x^2)$  eV [31].

<sup>3</sup>The spin should in theory be in the thermal state  $0.44|\downarrow\rangle\langle\downarrow| + 0.56|\uparrow\rangle\langle\uparrow|$  described by the Boltzmann distribution at  $T = 4.2$  K,  $\Delta_e/2\pi = 21.7$  GHz and  $\mathbf{B}_x = 4$  T.

<sup>4</sup>In the two-photon Raman scheme, the Raman laser can in principle be more far-detuned from the optical transitions; however, a gigantic amount of optical power would be required to drive the spin with sufficient spin Rabi frequency. Other detrimental photo-created charge effects could arise with more power.

# Appendix D

## Effect of Laser-induced Spin Flips on $n$ -photon GHZ Fidelity

Here we attempt to model the effect of the incoherent spin-flip rate  $\kappa$  on an  $n$ -photon GHZ entanglement fidelity. The idea is to apply the operator  $\hat{\mathcal{O}}_i$  representing a single round of optical excitations and a spin  $\pi$ -rotation pulse on the initial state  $|\Psi_s\rangle \otimes |\emptyset\rangle_p$ , where  $|\Psi_s\rangle$  is the spin superposition state after applying a spin  $\pi/2$ -rotation and  $|\emptyset\rangle_p$  is the  $n$ -photon vacuum state. Note that here we assume a photon is generated conditioned on the spin state  $|\uparrow\rangle$ , while the experiment in Chapter 6 excites  $|\downarrow\rangle$  instead. There is however no difference in the theoretical expression of  $n$ -photon entanglement fidelity.

### D.1 1-photon case: A spin-photon Bell state

The first-round operator has the form [149]

$$\hat{\mathcal{O}}_1^{\text{ideal}} = \hat{R}_y^{(\pi)} (-|\uparrow\rangle\langle\downarrow|\mathcal{A}_{l_1}^\dagger + |\downarrow\rangle\langle\uparrow|\mathcal{A}_{e_1}^\dagger), \quad (\text{D.1})$$

where  $\mathcal{A}_{e_i}^\dagger$  ( $\mathcal{A}_{l_i}^\dagger$ ) denotes the  $i$ -photon creation operator in the early (late) time-bin. Note that Eq. (D.1) includes two perfect  $\pi$ -rotation pulses: One of which is represented by the inner products  $|\uparrow\rangle\langle\downarrow|$  and  $|\downarrow\rangle\langle\uparrow|$  with a phase difference  $\pi$  as  $\hat{R}_y^{(\pi)}|\uparrow\rangle = -|\downarrow\rangle$ . Applying this on the initial state  $\rho_0 \equiv |\Psi_s\rangle\langle\Psi_s| \otimes |\emptyset\rangle_p\langle\emptyset|_p$  results in the Bell state

$$\begin{aligned} \hat{\mathcal{O}}_1^{\text{ideal}} \rho_0 \hat{\mathcal{O}}_1^{\text{ideal}\dagger} &= \hat{R}_y^{(\pi)} [\mathcal{A}_{l_1}^\dagger |\uparrow\rangle\langle\downarrow|\rho_0|\downarrow\rangle\langle\uparrow|\mathcal{A}_{l_1} - \mathcal{A}_{e_1}^\dagger |\downarrow\rangle\langle\uparrow|\rho_0|\downarrow\rangle\langle\uparrow|\mathcal{A}_{l_1} \\ &\quad - \mathcal{A}_{l_1}^\dagger |\uparrow\rangle\langle\downarrow|\rho_0|\uparrow\rangle\langle\downarrow|\mathcal{A}_{e_1} + \mathcal{A}_{e_1}^\dagger |\downarrow\rangle\langle\uparrow|\rho_0|\uparrow\rangle\langle\downarrow|\mathcal{A}_{e_1}] \hat{R}_y^{(\pi)\dagger} \\ &= \frac{1}{2} \hat{R}_y^{(\pi)} [ |l_1 \uparrow\rangle\langle l_1 \uparrow| - |e_1 \downarrow\rangle\langle l_1 \uparrow| - |l_1 \uparrow\rangle\langle e_1 \downarrow| + |e_1 \downarrow\rangle\langle e_1 \downarrow| ] \hat{R}_y^{(\pi)\dagger} \equiv \rho_1^{\text{ideal}}, \end{aligned} \quad (\text{D.2})$$

where we assume spin rotations with unit fidelity. In such a case, the spin superposition state is  $|\Psi_s\rangle = (|\uparrow\rangle + |\downarrow\rangle)/\sqrt{2}$ . Here the second  $\pi$ -rotation is written out separately since it will not be implemented for the experiment. This means when evaluating the  $n$ -photon GHZ fidelity, the final  $\pi$ -rotation is not applied.

Under the presence of the spin-flip depolarizing error, the state evolves as

$$\begin{aligned}
\hat{O}_1 \rho_0 \hat{O}_1^\dagger &= \mathcal{E}_{\text{depol}}^\pi \left( \mathcal{A}_{l_1}^\dagger |\uparrow\rangle\langle\downarrow| \mathcal{E}_{\text{depol}}(\rho_0) |\downarrow\rangle\langle\uparrow| \mathcal{A}_{l_1} - \mathcal{A}_{e_1}^\dagger |\downarrow\rangle\langle\uparrow| \mathcal{E}_{\text{depol}}(\rho_0) |\downarrow\rangle\langle\uparrow| \mathcal{A}_{l_1} \right. \\
&\quad \left. - \mathcal{A}_{l_1}^\dagger |\uparrow\rangle\langle\downarrow| \mathcal{E}_{\text{depol}}(\rho_0) |\uparrow\rangle\langle\downarrow| \mathcal{A}_{e_1} + \mathcal{A}_{e_1}^\dagger |\downarrow\rangle\langle\uparrow| \mathcal{E}_{\text{depol}}(\rho_0) |\uparrow\rangle\langle\downarrow| \mathcal{A}_{e_1} \right) \\
&= \mathcal{E}_{\text{depol}}^\pi \left( \left[ (1-p_\pi)d + \frac{p_\pi}{2} \right] |l_1 \uparrow\rangle\langle l_1 \uparrow| + \left[ (1-p_\pi)a + \frac{p_\pi}{2} \right] |e_1 \downarrow\rangle\langle e_1 \downarrow| \right. \\
&\quad \left. - \left[ (1-p_\pi)b \right] |e_1 \downarrow\rangle\langle l_1 \uparrow| - \left[ (1-p_\pi)c \right] |l_1 \uparrow\rangle\langle e_1 \downarrow| \right) \\
&\equiv \mathcal{E}_{\text{depol}}^\pi \left( \rho_1^{(1)} |l_1 \uparrow\rangle\langle l_1 \uparrow| + \rho_4^{(1)} |e_1 \downarrow\rangle\langle e_1 \downarrow| + \rho_2^{(1)} |e_1 \downarrow\rangle\langle l_1 \uparrow| + \rho_3^{(1)} |l_1 \uparrow\rangle\langle e_1 \downarrow| \right) \equiv \rho_1.
\end{aligned} \tag{D.3}$$

Here we introduced the depolarizing channels  $\mathcal{E}_{\text{depol}}$  and  $\mathcal{E}_{\text{depol}}^\pi$  where  $\mathcal{E}_{\text{depol}}(\rho_s) = (1-p_\pi)\rho_s + p_\pi \mathcal{I}/2$  and  $\mathcal{E}_{\text{depol}}^\pi(\rho_s) = (1-p_\pi)\hat{R}_y^{(\pi)}\rho_s\hat{R}_y^{(\pi)\dagger} + p_\pi \mathcal{I}/2$ , where  $p_\pi$  is the probability of incoherent spin-flips during the  $\pi$ -rotation. To understand why there are two depolarizing channels, as an example,  $|\uparrow\rangle\langle\downarrow|\mathcal{E}_{\text{depol}}(\rho_0)|\downarrow\rangle\langle\uparrow|$  means having a depolarizing error before the  $\pi$ -rotation, which is mathematically equivalent to introducing the error during rotation as the order does not matter. For an arbitrary spin state  $\rho_0$ , both channels transform it into

$$\begin{aligned}
\mathcal{E}_{\text{depol}} \left( \begin{bmatrix} a & b \\ c & d \end{bmatrix} \right) &= \begin{bmatrix} (1-p_\pi)a + \frac{p_\pi}{2} & (1-p_\pi)b \\ (1-p_\pi)c & (1-p_\pi)d + \frac{p_\pi}{2} \end{bmatrix} \\
\mathcal{E}_{\text{depol}}^\pi \left( \begin{bmatrix} a & b \\ c & d \end{bmatrix} \right) &= \begin{bmatrix} (1-p_\pi)d + \frac{p_\pi}{2} & -(1-p_\pi)c \\ -(1-p_\pi)b & (1-p_\pi)a + \frac{p_\pi}{2} \end{bmatrix}.
\end{aligned} \tag{D.4}$$

Eq. (D.4) is useful for evaluating the  $n$ -photon GHZ fidelity.

## D.2 2-photon case: A GHZ state

Applying the second-round operator gives

$$\begin{aligned}
\hat{O}_2 \rho_1 \hat{O}_2^\dagger &= \mathcal{E}_{\text{depol}}^\pi \left( \mathcal{A}_{l_2}^\dagger |\uparrow\rangle\langle\downarrow| \mathcal{E}_{\text{depol}}(\rho_1) |\downarrow\rangle\langle\uparrow| \mathcal{A}_{l_2} - \mathcal{A}_{e_2}^\dagger |\downarrow\rangle\langle\uparrow| \mathcal{E}_{\text{depol}}(\rho_1) |\downarrow\rangle\langle\uparrow| \mathcal{A}_{l_2} \right. \\
&\quad \left. - \mathcal{A}_{l_2}^\dagger |\uparrow\rangle\langle\downarrow| \mathcal{E}_{\text{depol}}(\rho_1) |\uparrow\rangle\langle\downarrow| \mathcal{A}_{e_2} + \mathcal{A}_{e_2}^\dagger |\downarrow\rangle\langle\uparrow| \mathcal{E}_{\text{depol}}(\rho_1) |\uparrow\rangle\langle\downarrow| \mathcal{A}_{e_2} \right) \\
&= \mathcal{E}_{\text{depol}}^\pi \left( \rho_4^{(2)} |l_2 l_1 \uparrow\rangle\langle l_2 l_1 \uparrow| + \rho_1^{(2)} |e_2 e_1 \downarrow\rangle\langle e_2 e_1 \downarrow| + \rho_2^{(2)} |e_2 e_1 \downarrow\rangle\langle l_2 l_1 \uparrow| + \rho_3^{(2)} |l_2 l_1 \uparrow\rangle\langle e_2 e_1 \downarrow| \right),
\end{aligned} \tag{D.5}$$

where  $\rho^{(2)}$  is the 2-photon-spin density matrix before the final  $\pi$ -rotation, evaluated by applying the inner products on  $\mathcal{E}_{\text{depol}}(\rho_1) = \mathcal{E}_{\text{depol}}(\mathcal{E}_{\text{depol}}^\pi(\rho^{(1)}))$ :

$$\begin{cases} \rho_1^{(2)} = (1 - p_\pi)^2 \rho_4^{(1)} + (1 - p_\pi) \frac{p_\pi}{2} + \frac{p_\pi}{2} \\ \rho_2^{(2)} = (-1)^2 (1 - p_\pi)^2 \rho_3^{(1)} \\ \rho_3^{(2)} = (-1)^2 (1 - p_\pi)^2 \rho_2^{(1)} \\ \rho_4^{(2)} = (1 - p_\pi)^2 \rho_1^{(1)} + (1 - p_\pi) \frac{p_\pi}{2} + \frac{p_\pi}{2}. \end{cases} \quad (\text{D.6})$$

### D.3 Induction to $n$ -photon GHZ state

The entanglement fidelity for the  $i$ -photon state is given by the overlap between the ideal and final states

$$\mathcal{F}_i = \frac{\langle \psi_{\text{ideal}} | \rho^{(i)} | \psi_{\text{ideal}} \rangle}{\text{Tr} \rho^{(i)}} = \frac{1}{2} \frac{\sum_k \rho_k^{(i)}}{\rho_1^{(i)} + \rho_4^{(i)}}, \quad (\text{D.7})$$

where the ideal  $i$ -photon GHZ state is  $|\psi_{\text{ideal}}\rangle = (|e_1 e_2 \dots e_i \downarrow\rangle - |l_1 l_2 \dots l_i \uparrow\rangle) / \sqrt{2}$  before applying the last  $\pi$ -rotation. For the 1-photon, 2-photon and (generalizing to)  $n$ -photon state, the corresponding fidelities are

$$\begin{aligned} \mathcal{F}_1 &= \frac{1}{2} \frac{(1 - p_\pi)(a + d) + p_\pi + (1 - p_\pi)(b + c)}{(1 - p_\pi)(a + d) + p_\pi} \xrightarrow{a+d=1} \frac{1}{2} \left[ 1 + (1 - p_\pi)(1 - p_{\pi/2}) \right]; \\ \mathcal{F}_2 &= \frac{1}{2} \frac{(1 - p_\pi)^3(a + d) + 2 \left( \frac{p_\pi}{2}(1 - p_\pi)^2 + \frac{p_\pi}{2}(1 - p_\pi) + \frac{p_\pi}{2} \right) - (-1)^3(1 - p_\pi)^3(b + c)}{(1 - p_\pi)^3(a + d) + 2 \left( \frac{p_\pi}{2}(1 - p_\pi)^2 + \frac{p_\pi}{2}(1 - p_\pi) + \frac{p_\pi}{2} \right)} \\ &\xrightarrow{a+d=1} \frac{1}{2} \left[ 1 + (1 - p_\pi)^3(1 - p_{\pi/2}) \right]; \\ \mathcal{F}_n &= \frac{1}{2} \frac{(1 - p_\pi)^{2n-1}(a + d) + 2 \left( \frac{p_\pi}{2}(1 - p_\pi)^{2n-2} + \dots + \frac{p_\pi}{2} \right) - (-1)^{2n-1}(1 - p_\pi)^{2n-1}(b + c)}{(1 - p_\pi)^{2n-1}(a + d) + 2 \left( \frac{p_\pi}{2}(1 - p_\pi)^{2n-2} + \frac{p_\pi}{2}(1 - p_\pi)^{2n-3} + \dots + \frac{p_\pi}{2} \right)} \\ &= \frac{1}{2} \frac{(1 - p_\pi)^{2n-1}(a + d) + [1 - (1 - p_\pi)^{2n-1}] + (1 - p_\pi)^{2n-1}(b + c)}{(1 - p_\pi)^{2n-1}(a + d) + [1 - (1 - p_\pi)^{2n-1}]} \\ &\xrightarrow{a+d=1} \frac{1}{2} \left[ 1 + (1 - p_\pi)^{2n-1}(1 - p_{\pi/2}) \right], \end{aligned} \quad (\text{D.8})$$

where the exponent  $(2n - 1)$  means  $(2n - 1)$   $\pi$ -rotation pulses are needed to generate an  $n$ -photon GHZ state.  $a, b, c$  and  $d$  are spin matrix elements resulting from applying a  $\pi/2$ -spin rotation on the spin state initialized in  $|\downarrow\rangle$ , with  $p_{\pi/2}$  the probability of incoherent spin-flips and assuming infinite  $T_2^*$ :

$$\mathcal{E}_{\text{depol}}^{\pi/2} \left( \begin{bmatrix} 0 & 0 \\ 0 & 1 \end{bmatrix} \right) = \begin{bmatrix} \frac{1}{2} & \frac{1}{2}(1 - p_{\pi/2}) \\ \frac{1}{2}(1 - p_{\pi/2}) & \frac{1}{2} \end{bmatrix} \equiv \begin{bmatrix} a & b \\ c & d \end{bmatrix}. \quad (\text{D.9})$$



# Bibliography

- [1] Jeremy L. O’Brien, Akira Furusawa, and Jelena Vučković. Photonic quantum technologies. *Nature Photonics*, 3(12):687–695, Dec 2009.
- [2] Emanuele Pelucchi, Giorgos Fagas, Igor Aharonovich, Dirk Englund, Eden Figueroa, Qihuang Gong, Hübel Hannes, Jin Liu, Chao-Yang Lu, Nobuyuki Matsuda, Jian-Wei Pan, Florian Schreck, Fabio Sciarrino, Christine Silberhorn, Jianwei Wang, and Klaus D. Jöns. The potential and global outlook of integrated photonics for quantum technologies. *Nature Reviews Physics*, 4(3):194–208, Mar 2022.
- [3] E. Knill, R. Laflamme, and G. J. Milburn. A scheme for efficient quantum computation with linear optics. *Nature*, 409(6816):46–52, 2001.
- [4] J. Chow, E. Greplová, F. Heijman, C. Kuchkovsky, D. O’Halloran, J. Pointing, G. Shutko, and C. J. Williams, editors. *State of quantum computing: building a quantum economy*. World Economic Forum insight report, 2022.
- [5] C. K. Hong, Z. Y. Ou, and L. Mandel. Measurement of subpicosecond time intervals between two photons by interference. *Phys. Rev. Lett.*, 59:2044–2046, Nov 1987.
- [6] Till Joscha Weinhold. *Stepping stones towards linear optical quantum computing*. PhD thesis, University of Queensland, 2010.
- [7] Peter Lodahl. Quantum-dot based photonic quantum networks. *Quantum Science and Technology*, 3(1):013001, oct 2017.
- [8] Jianwei Wang, Fabio Sciarrino, Anthony Laing, and Mark G. Thompson. Integrated photonic quantum technologies. *Nature Photonics*, 14(5):273–284, May 2020.
- [9] A. Javadi, I. Söllner, M. Arcari, S. Lindskov Hansen, L. Midolo, S. Mahmoodian, G. Kiršanskė, T. Pregolato, E. H. Lee, J. D. Song, S. Stobbe, and P. Lodahl. Single-photon non-linear optics with a quantum dot in a waveguide. *Nature Communications*, 6(1):8655, Oct 2015.
- [10] David P. DiVincenzo. The physical implementation of quantum computation. *Fortschritte der Physik*, 48(9-11):771–783, Sep 2000.
- [11] Ali W. Elshaari, Wolfram Pernice, Kartik Srinivasan, Oliver Benson, and Val Zwiller. Hybrid integrated quantum photonic circuits. *Nature Photonics*, 14(5):285–298, May 2020.
- [12] E. Togan, Y. Chu, A. S. Trifonov, L. Jiang, J. Maze, L. Childress, M. V. G. Dutt, A. S. Sørensen, P. R. Hemmer, A. S. Zibrov, and M. D. Lukin. Quantum entanglement between an optical photon and a solid-state spin qubit. *Nature*, 466(7307):730–734, Aug 2010.

- [13] W. B. Gao, P. Fallahi, E. Togan, J. Miguel-Sanchez, and A. Imamoglu. Observation of entanglement between a quantum dot spin and a single photon. *Nature*, 491(7424):426–430, Nov 2012.
- [14] Kristiaan De Greve, Peter L. McMahon, Leo Yu, Jason S. Pelc, Cody Jones, Chandra M. Natarajan, Na Young Kim, Eisuke Abe, Sebastian Maier, Christian Schneider, Martin Kamp, Sven Höfling, Robert H. Hadfield, Alfred Forchel, M. M. Fejer, and Yoshihisa Yamamoto. Complete tomography of a high-fidelity solid-state entangled spin–photon qubit pair. *Nature Communications*, 4(1):2228, Jul 2013.
- [15] J. R. Schaibley, A. P. Burgers, G. A. McCracken, L.-M. Duan, P. R. Berman, D. G. Steel, A. S. Bracker, D. Gammon, and L. J. Sham. Demonstration of quantum entanglement between a single electron spin confined to an inas quantum dot and a photon. *Phys. Rev. Lett.*, 110:167401, Apr 2013.
- [16] I. Schwartz, D. Cogan, E. R. Schmidgall, Y. Don, L. Gantz, O. Kenneth, N. H. Lindner, and D. Gershoni. Deterministic generation of a cluster state of entangled photons. *Science*, 354(6311):434–437, 2016.
- [17] Yu He, Yu-Ming He, Yu-Jia Wei, Xiao Jiang, Kai Chen, Chao-Yang Lu, Jian-Wei Pan, Christian Schneider, Martin Kamp, and Sven Höfling. Quantum state transfer from a single photon to a distant quantum-dot electron spin. *Phys. Rev. Lett.*, 119:060501, 2017.
- [18] Martin Hayhurst Appel, Alexey Tiranov, Simon Pabst, Ming Lai Chan, Christian Starup, Ying Wang, Leonardo Midolo, Konstantin Tiurev, Sven Scholz, Andreas D. Wieck, Arne Ludwig, Anders Søndberg Sørensen, and Peter Lodahl. Entangling a hole spin with a time-bin photon: A waveguide approach for quantum dot sources of multiphoton entanglement. *Phys. Rev. Lett.*, 128:233602, Jun 2022.
- [19] Stephanie Wehner, David Elkouss, and Ronald Hanson. Quantum internet: A vision for the road ahead. *Science*, 362(6412):eaam9288, 2018.
- [20] Martin Hayhurst Appel, Alexey Tiranov, Alisa Javadi, Matthias C. Löbl, Ying Wang, Sven Scholz, Andreas D. Wieck, Arne Ludwig, Richard J. Warburton, and Peter Lodahl. Coherent spin-photon interface with waveguide induced cycling transitions. *Phys. Rev. Lett.*, 126:013602, Jan 2021.
- [21] Dapeng Ding, Martin Hayhurst Appel, Alisa Javadi, Xiaoyan Zhou, Matthias Christian Löbl, Immo Söllner, Rüdiger Schott, Camille Papon, Tommaso Pregnolato, Leonardo Midolo, Andreas Dirk Wieck, Arne Ludwig, Richard John Warburton, Tim Schröder, and Peter Lodahl. Coherent optical control of a quantum-dot spin-qubit in a waveguide-based spin-photon interface. *Phys. Rev. Applied*, 11:031002, 2019.
- [22] Johannes Borregaard, Hannes Pichler, Tim Schröder, Mikhail D. Lukin, Peter Lodahl, and Anders S. Sørensen. One-way quantum repeater based on near-deterministic photon-emitter interfaces. *Phys. Rev. X*, 10:021071, Jun 2020.
- [23] D. Witthaut, M. D. Lukin, and A. S. Sørensen. Photon sorters and QND detectors using single photon emitters. *EPL (Europhysics Letters)*, 97(5):50007, mar 2012.

- [24] Johannes Borregaard, Anders Søndberg Sørensen, and Peter Lodahl. Quantum networks with deterministic spin–photon interfaces. *Adv. Quant. Tech.*, 2(5–6):1800091, 2019.
- [25] Robert Raussendorf and H.J. Briegel. A one-way quantum computer. *Phys. Rev. Lett.*, 86:5188–5191, 2001.
- [26] Ming Lai Chan. Research data archive for the PhD thesis Spin-Photon Interface for Quantum Information Processing. <https://doi.org/10.17894/ucph.7c2ebfa2-7db1-414b-986b-4cd4ae0ac6da>, 2023. [Online; accessed 12-June-2023].
- [27] S.M. Sze. *Physics of Semiconductor Devices*. Wiley-Interscience, 2007.
- [28] Peter Lodahl, Sahand Mahmoodian, and Søren Stobbe. Interfacing single photons and single quantum dots with photonic nanostructures. *Rev. Mod. Phys.*, 87:347–400, May 2015.
- [29] J. Márquez, L. Geelhaar, and K. Jacobi. Atomically resolved structure of inas quantum dots. *Applied Physics Letters*, 78(16):2309–2311, Apr 2001.
- [30] Oliver Gywat, Hubert J. Krenner, and Jesse Berezovsky. *Spins in Optically Active Quantum Dots: Concepts and Methods*. Wiley, 2009.
- [31] NSM Archive aluminium gallium arsenide band structure and carrier concentration. <http://www.ioffe.ru/SVA/NSM/Semicond/AlGaAs/bandstr.html>. Accessed: 2023-04-30.
- [32] I. Vurgaftman, J. R. Meyer, and L. R. Ram-Mohan. Band parameters for iii–v compound semiconductors and their alloys. *Journal of Applied Physics*, 89(11):5815–5875, Jun 2001.
- [33] Camille Papon. *Photonic circuits with multiple quantum dots: Towards scalable operation of deterministic single-photon sources*. PhD thesis, University of Copenhagen, 2022.
- [34] S. E. Thomas, M. Billard, N. Coste, S. C. Wein, Priya, H. Ollivier, O. Krebs, L. Tazaïrt, A. Harouri, A. Lemaitre, I. Sagnes, C. Anton, L. Lanco, N. Somaschi, J. C. Loredó, and P. Senellart. Bright polarized single-photon source based on a linear dipole. *Phys. Rev. Lett.*, 126:233601, Jun 2021.
- [35] Ravitej Uppu, Freja T. Pedersen, Ying Wang, Cecilie T. Olesen, Camille Papon, Xiaoyan Zhou, Leonardo Midolo, Sven Scholz, Andreas D. Wieck, Arne Ludwig, and Peter Lodahl. Scalable integrated single-photon source. *Science Advances*, 6(50), 2020.
- [36] Henri Thyrestrup, Gabija Kirsanske, Hanna Le Jeannic, Tommaso Pregnolato, Liang Zhai, Laust Raahauge, Leonardo Midolo, Nir Rotenberg, Alisa Javadi, Rüdiger Schott, Andreas D. Wieck, Arne Ludwig, Matthias C. Löbl, Immo Söllner, Richard J. Warburton, and Peter Lodahl. Quantum optics with near-lifetime-limited quantum-dot transitions in a nanophotonic waveguide. *Nano Letters*, 18(3):1801–1806, 2018.

- [37] Jonathan H. Prechtel, Andreas V. Kuhlmann, Julien Houel, Arne Ludwig, Sascha R. Valentin, Andreas D. Wieck, and Richard J. Warburton. Decoupling a hole spin qubit from the nuclear spins. *Nature Materials*, 15(9):981–986, Sep 2016.
- [38] I. A. Larkin, Sebastian Ujevic, and E. A. Avrutin. Tunneling escape time from a semiconductor quantum well in an electric field. *Journal of Applied Physics*, 106(11):113701, Dec 2009.
- [39] D. A. B. Miller, D. S. Chemla, T. C. Damen, A. C. Gossard, W. Wiegmann, T. H. Wood, and C. A. Burrus. Band-edge electroabsorption in quantum well structures: The quantum-confined stark effect. *Phys. Rev. Lett.*, 53:2173–2176, Nov 1984.
- [40] J. J. Finley, M. Sabathil, P. Vogl, G. Abstreiter, R. Oulton, A. I. Tartakovskii, D. J. Mowbray, M. S. Skolnick, S. L. Liew, A. G. Cullis, and M. Hopkinson. Quantum-confined stark shifts of charged exciton complexes in quantum dots. *Phys. Rev. B*, 70:201308, Nov 2004.
- [41] Anthony J. Bennett, Raj B. Patel, Joanna Skiba-Szymanska, Christine A. Nicoll, Ian Farrer, David A. Ritchie, and Andrew J. Shields. Giant stark effect in the emission of single semiconductor quantum dots. *Applied Physics Letters*, 97(3):031104, Jul 2010.
- [42] Richard J. Warburton. Single spins in self-assembled quantum dots. *Nature Materials*, 12:483 EP –, 05 2013.
- [43] Alexander Rolf Korsch. Manipulating transition rates of self-assembled indium arsenide quantum dots via electronic and optical coupling in semiconductor heterostructures. Master’s thesis, Ruhr-Universität Bochum, 2019. See Sec 3.3.2.
- [44] N. A. J. M. Kleemans, J. van Bree, A. O. Govorov, J. G. Keizer, G. J. Hamhuis, R. Nötzel, A. Yu. Silov, and P. M. Koenraad. Many-body exciton states in self-assembled quantum dots coupled to a fermi sea. *Nature Physics*, 6(7):534–538, Jul 2010.
- [45] Camille Papon, Ying Wang, Ravitej Uppu, Sven Scholz, Andreas Dirk Wieck, Arne Ludwig, Peter Lodahl, and Leonardo Midolo. Independent operation of two waveguide-integrated single-photon sources. *arXiv*, 2210.09826, 2022.
- [46] Alexey Tiranov, Vasiliki Angelopoulou, Cornelis Jacobus van Diepen, Björn Schriniski, Oliver August Dall’Alba Sandberg, Ying Wang, Leonardo Midolo, Sven Scholz, Andreas Dirk Wieck, Arne Ludwig, Anders Søndberg Sørensen, and Peter Lodahl. Collective super- and subradiant dynamics between distant optical quantum emitters. *Science*, 379(6630):389–393, 2023.
- [47] M. Bayer, G. Ortner, O. Stern, A. Kuther, A. A. Gorbunov, A. Forchel, P. Hawrylak, S. Fafard, K. Hinzer, T. L. Reinecke, S. N. Walck, J. P. Reithmaier, F. Klopff, and F. Schäfer. Fine structure of neutral and charged excitons in self-assembled in(ga)as/(al)gaas quantum dots. *Phys. Rev. B*, 65:195315, May 2002.
- [48] Jeppe Johansen, Brian Julsgaard, Søren Stobbe, Jørn M. Hvam, and Peter Lodahl. Probing long-lived dark excitons in self-assembled quantum dots. *Phys. Rev. B*, 81:081304, Feb 2010.

- [49] Eougenious L. Ivchenko and Grigory Pikus. *Superlattices and other heterostructures: symmetry and optical phenomena (Springer Series in Solid-State Sciences, 110) Second edition*. Springer-Verlag, New York, 1996.
- [50] A. V. Koudinov, I. A. Akimov, Yu. G. Kusrayev, and F. Henneberger. Optical and magnetic anisotropies of the hole states in stranski-krastanov quantum dots. *Phys. Rev. B*, 70:241305, Dec 2004.
- [51] N. J. Traynor, R. T. Harley, and R. J. Warburton. Zeeman splitting and g factor of heavy-hole excitons in  $\text{In}_x\text{Ga}_{1-x}\text{As}/\text{GaAs}$  quantum wells. *Phys. Rev. B*, 51:7361–7364, Mar 1995.
- [52] Martin Hayhurst Appel. *A Quantum Dot Source of Time-Bin Multi-Photon Entanglement*. PhD thesis, University of Copenhagen, 2021.
- [53] Yu. G. Kusrayev, A. V. Koudinov, I. G. Aksyanov, B. P. Zakharchenya, T. Wojtowicz, G. Karczewski, and J. Kossut. Extreme in-plane anisotropy of the heavy-hole g factor in (001)-cdte/cdmnte quantum wells. *Phys. Rev. Lett.*, 82:3176–3179, Apr 1999.
- [54] Jonathan H. Prechtel, Franziska Maier, Julien Houel, Andreas V. Kuhlmann, Arne Ludwig, Andreas D. Wieck, Daniel Loss, and Richard J. Warburton. Electrically tunable hole g-factor of an optically active quantum dot for fast spin rotations. *Physical Review B*, 91(16):165304–, 04 2015.
- [55] Liang Zhai, Matthias C. Löbl, Giang N. Nguyen, Julian Ritzmann, Alisa Javadi, Clemens Spinnler, Andreas D. Wieck, Arne Ludwig, and Richard J. Warburton. Low-noise gaas quantum dots for quantum photonics. *Nature Communications*, 11(1):4745, Sep 2020.
- [56] Xiaoyan Zhou, Irina Kulkova, Toke Lund-Hansen, Sofie Lindskov Hansen, Peter Lodahl, and Leonardo Midolo. High-efficiency shallow-etched grating on gaas membranes for quantum photonic applications. *Applied Physics Letters*, 113(25):251103, 2018.
- [57] Ying Wang. *Novel nanofabrication methods and processes for quantum photonic integrated circuits*. PhD thesis, University of Copenhagen, 2021.
- [58] John D. Joannopoulos, Steven G. Johnson, Joshua N. Winn, and Robert D. Meade. *Photonic Crystals: Molding the Flow of Light - Second Edition*. Princeton University Press, 2008.
- [59] M. Arcari, I. Söllner, A. Javadi, S. Lindskov Hansen, S. Mahmoodian, J. Liu, H. Thyrrerstrup, E. H. Lee, J. D. Song, S. Stobbe, and P. Lodahl. Near-unity coupling efficiency of a quantum emitter to a photonic crystal waveguide. *Phys. Rev. Lett.*, 113:093603, Aug 2014.
- [60] Annika Kurzmann, Arne Ludwig, Andreas D. Wieck, Axel Lorke, and Martin Geller. Auger recombination in self-assembled quantum dots: Quenching and broadening of the charged exciton transition. *Nano Letters*, 16(5):3367–3372, May 2016.
- [61] Christopher Gerry and Peter Knight. *Introductory Quantum Optics*. Cambridge University Press, Cambridge, 2004.

- [62] J. T. Shen and Shanhui Fan. Coherent photon transport from spontaneous emission in one-dimensional waveguides. *Opt. Lett.*, 30(15):2001–2003, Aug 2005.
- [63] D Witthaut and A S Sørensen. Photon scattering by a three-level emitter in a one-dimensional waveguide. *New Journal of Physics*, 12(4):043052, apr 2010.
- [64] M. K. Bhaskar, R. Riedinger, B. Machielse, D. S. Levonian, C. T. Nguyen, E. N. Knall, H. Park, D. Englund, M. Lončar, D. D. Sukachev, and M. D. Lukin. Experimental demonstration of memory-enhanced quantum communication. *Nature*, 580(7801):60–64, Apr 2020.
- [65] L.-M. Duan and H. J. Kimble. Scalable photonic quantum computation through cavity-assisted interactions. *Phys. Rev. Lett.*, 92:127902, Mar 2004.
- [66] Dorothea Pinotsi and Atac Imamoglu. Single photon absorption by a single quantum emitter. *Physical review letters*, 100(9):093603, 2008.
- [67] Serge Rosenblum, Adrien Borne, and Barak Dayan. Analysis of deterministic swapping of photonic and atomic states through single-photon raman interaction. *Phys. Rev. A*, 95:033814, Mar 2017.
- [68] Orel Bechler, Adrien Borne, Serge Rosenblum, Gabriel Guendelman, Ori Ezrahi Mor, Moran Netser, Tal Ohana, Ziv Aqua, Niv Drucker, Ran Finkelstein, Yulia Lovsky, Rachel Bruch, Doron Gurovich, Ehud Shafir, and Barak Dayan. A passive photon–atom qubit swap operation. *Nature Physics*, 14(10):996–1000, 2018.
- [69] Itay Shomroni, Serge Rosenblum, Yulia Lovsky, Orel Bechler, Gabriel Guendelman, and Barak Dayan. All-optical routing of single photons by a one-atom switch controlled by a single photon. *Science*, 345(6199):903–906, 2014.
- [70] K Inomata, K Koshino, Z. R. Lin, W. D. Oliver, Jaw Shen Tsai, Y Nakamura, and T Yamamoto. Microwave down-conversion with an impedance-matched  $\lambda$  system in driven circuit qed. *Physical review letters*, 113(6):063604, 2014.
- [71] T. Pregolato, X.-L. Chu, T. Schröder, R. Schott, A. D. Wieck, A. Ludwig, P. Lodahl, and N. Rotenberg. Deterministic positioning of nanophotonic waveguides around single self-assembled quantum dots. *APL Photonics*, 5(8):086101, 2020.
- [72] Alexei Gilchrist, Nathan K. Langford, and Michael A. Nielsen. Distance measures to compare real and ideal quantum processes. *Phys. Rev. A*, 71:062310, Jun 2005.
- [73] Michał Horodecki, Paweł Horodecki, and Ryszard Horodecki. General teleportation channel, singlet fraction, and quasidistillation. *Phys. Rev. A*, 60:1888–1898, Sep 1999.
- [74] Michael A Nielsen. A simple formula for the average gate fidelity of a quantum dynamical operation. *Physics Letters A*, 303(4):249 – 252, May 2002.
- [75] P. Tighineanu, C. L. Dreeßen, C. Flindt, P. Lodahl, and A. S. Sørensen. Phonon decoherence of quantum dots in photonic structures: Broadening of the zero-phonon line and the role of dimensionality. *Phys. Rev. Lett.*, 120:257401, 2018.

- [76] E. A. Muljarov and R. Zimmermann. Dephasing in quantum dots: Quadratic coupling to acoustic phonons. *Phys. Rev. Lett.*, 93:237401, Nov 2004.
- [77] Sumanta Das, Vincent E. Elfving, Florentin Reiter, and Anders S. Sørensen. Photon scattering from a system of multilevel quantum emitters. ii. application to emitters coupled to a one-dimensional waveguide. *Phys. Rev. A*, 97:043838, Apr 2018.
- [78] B. Eble, C. Testelin, P. Desfonds, F. Bernardot, A. Balocchi, T. Amand, A. Miard, A. Lemaître, X. Marie, and M. Chamarro. Hole–nuclear spin interaction in quantum dots. *Phys. Rev. Lett.*, 102:146601, Apr 2009.
- [79] Denis V. Bulaev and Daniel Loss. Spin relaxation and decoherence of holes in quantum dots. *Phys. Rev. Lett.*, 95:076805, Aug 2005.
- [80] Alexander V. Khaetskii, Daniel Loss, and Leonid Glazman. Electron spin decoherence in quantum dots due to interaction with nuclei. *Phys. Rev. Lett.*, 88:186802, Apr 2002.
- [81] J. Houel, A. V. Kuhlmann, L. Greuter, F. Xue, M. Poggio, B. D. Gerardot, P. A. Dalgarno, A. Badolato, P. M. Petroff, A. Ludwig, D. Reuter, A. D. Wieck, and R. J. Warburton. Probing single-charge fluctuations at a GaAs/AlAs interface using laser spectroscopy on a nearby ingaas quantum dot. *Phys. Rev. Lett.*, 108:107401, Mar 2012.
- [82] L. Besombes, K. Kheng, L. Marsal, and H. Mariette. Acoustic phonon broadening mechanism in single quantum dot emission. *Phys. Rev. B*, 63:155307, Mar 2001.
- [83] B. Krummheuer, V. M. Axt, and T. Kuhn. Theory of pure dephasing and the resulting absorption line shape in semiconductor quantum dots. *Phys. Rev. B*, 65:195313, May 2002.
- [84] Jean Dalibard, Yvan Castin, and Klaus Mølmer. Wave-function approach to dissipative processes in quantum optics. *Phys. Rev. Lett.*, 68:580–583, Feb 1992.
- [85] L. I. Childress, J. M. Taylor, A. S. Sørensen, and M. D. Lukin. Fault-tolerant quantum repeaters with minimal physical resources and implementations based on single-photon emitters. *Phys. Rev. A*, 72:052330, Nov 2005.
- [86] I. A. Merkulov, Al. L. Efros, and M. Rosen. Electron spin relaxation by nuclei in semiconductor quantum dots. *Phys. Rev. B*, 65:205309, Apr 2002.
- [87] E. L. Hahn. Spin echoes. *Phys. Rev.*, 80:580–594, Nov 1950.
- [88] F. H. L. Koppens, K. C. Nowack, and L. M. K. Vandersypen. Spin echo of a single electron spin in a quantum dot. *Phys. Rev. Lett.*, 100:236802, Jun 2008.
- [89] Xiaoya Judy Wang, Stefano Chesi, and W. A. Coish. Spin-echo dynamics of a heavy hole in a quantum dot. *Phys. Rev. Lett.*, 109:237601, Dec 2012.
- [90] S. Massar and S. Popescu. Optimal extraction of information from finite quantum ensembles. *Phys. Rev. Lett.*, 74:1259–1263, Feb 1995.
- [91] K. Hammerer, M. M. Wolf, E. S. Polzik, and J. I. Cirac. Quantum benchmark for storage and transmission of coherent states. *Phys. Rev. Lett.*, 94:150503, Apr 2005.

- [92] H. J. Carmichael. Quantum trajectory theory for cascaded open systems. *Physical review letters*, 70(15):2273, 1993.
- [93] Klaus Mølmer, Yvan Castin, and Jean Dalibard. Monte carlo wave-function method in quantum optics. *JOSA B*, 10(3):524–538, 1993.
- [94] Howard Carmichael. Quantum trajectories i. *An Open Systems Approach to Quantum Optics: Lectures Presented at the Université Libre de Bruxelles October 28 to November 4, 1991*, pages 113–125, 1993.
- [95] P. Borri, W. Langbein, U. Woggon, V. Stavarache, D. Reuter, and A. D. Wieck. Exciton dephasing via phonon interactions in inas quantum dots: Dependence on quantum confinement. *Phys. Rev. B*, 71:115328, Mar 2005.
- [96] Jack Hansom, Carsten H. H. Schulte, Claire Le Gall, Clemens Matthiesen, Edmund Clarke, Maxime Hugues, Jacob M. Taylor, and Mete Atatüre. Environment-assisted quantum control of a solid-state spin via coherent dark states. *Nature Physics*, 10(10):725–730, Oct 2014.
- [97] D.A. Gangloff, G. Éthier-Majcher, C. Lang, E. V. Denning, J. H. Bodey, D. M. Jackson, E. Clarke, M. Hugues, C. Le Gall, and M. Atatüre. Quantum interface of an electron and a nuclear ensemble. *Science*, 364(6435):62–66, 2019.
- [98] Xing Ding, Yu He, Z.-C. Duan, Niels Gregersen, M.-C. Chen, S. Unsleber, S. Maier, Christian Schneider, Martin Kamp, Sven Höfling, Chao-Yang Lu, and Jian-Wei Pan. On-demand single photons with high extraction efficiency and near-unity indistinguishability from a resonantly driven quantum dot in a micropillar. *Phys. Rev. Lett.*, 116:020401, 2016.
- [99] Christian Junge, Danny OShea, Jürgen Volz, and Arno Rauschenbeutel. Strong coupling between single atoms and nontransversal photons. *Physical review letters*, 110(21):213604, 2013.
- [100] Andrea Aiello, Peter Banzer, Martin Neugebauer, and Gerd Leuchs. From transverse angular momentum to photonic wheels. *Nature Photonics*, 9(12):789–795, 2015.
- [101] Serge Rosenblum, Orel Bechler, Itay Shomroni, Yulia Lovsky, Gabriel Guendelman, and Barak Dayan. Extraction of a single photon from an optical pulse. *Nature Photonics*, 10(1):19–22, 2016.
- [102] D Reitz, C Sayrin, R Mitsch, P Schneeweiss, and A Rauschenbeutel. Coherence properties of nanofiber-trapped cesium atoms. *Physical review letters*, 110(24):243603, 2013.
- [103] Andreas Reiserer and Gerhard Rempe. Cavity-based quantum networks with single atoms and optical photons. *Rev. Mod. Phys.*, 87:1379–1418, 2015.
- [104] Elisa Will, Luke Masters, Arno Rauschenbeutel, Michael Scheucher, and Jürgen Volz. Coupling a single trapped atom to a whispering-gallery-mode microresonator. *Physical Review Letters*, 126(23):233602, 2021.

- [105] Xinchao Zhou, Hikaru Tamura, Tzu-Han Chang, and Chen-Lung Hung. Coupling single atoms to a nanophotonic whispering-gallery-mode resonator via optical guiding. *Phys. Rev. Lett.*, 130:103601, Mar 2023.
- [106] Christiana Panayi, Mohsen Razavi, Xiongfeng Ma, and Norbert Lütkenhaus. Memory-assisted measurement-device-independent quantum key distribution. *New Journal of Physics*, 16(4):043005, apr 2014.
- [107] K. Boone, J.-P. Bourgoin, E. Meyer-Scott, K. Heshami, T. Jennewein, and C. Simon. Entanglement over global distances via quantum repeaters with satellite links. *Phys. Rev. A*, 91:052325, 2015.
- [108] Anton Lauenborg Andersen. Quantum key distribution and entanglement distribution with satellite links. Master’s thesis, University of Copenhagen, 2020. Introduced in Chapter 2.6.1. Our scheme could be used to herald the mapping of the photon onto the memory at the satellite with near-unity success probability.
- [109] H.J. Briegel, D.E. Browne, W. Dür, R. Raussendorf, and M. Van den Nest. Measurement-based quantum computation. *Nat. Phys.*, 5:19, 2009.
- [110] Ravitej Uppu, Leonardo Midolo, Xiaoyan Zhou, Jacques Carolan, and Peter Lodahl. Quantum-dot-based deterministic photon–emitter interfaces for scalable photonic quantum technology. *Nature Nanotechnology*, Oct 2021.
- [111] Peter Lodahl, Arne Ludwig, and Richard J. Warburton. A deterministic source of single photons. *Physics Today*, 75(3):44–50, 2022.
- [112] Bastian Hacker, Stephan Welte, Gerhard Rempe, and Stephan Ritter. A photon–photon quantum gate based on a single atom in an optical resonator. *Nature*, 536(7615):193–196, Aug 2016.
- [113] Michael A. Nielsen. Cluster-state quantum computation. *Reports on Mathematical Physics*, 57(1):147–161, 2006.
- [114] Jung-Tsung Shen and Shanhui Fan. Theory of single-photon transport in a single-mode waveguide. i. coupling to a cavity containing a two-level atom. *Phys. Rev. A*, 79:023837, Feb 2009.
- [115] Konstantin Tiurev, Martin Hayhurst Appel, Pol Llopart Mirambell, Mikkel Bloch Lauritzen, Alexey Tiranov, Peter Lodahl, and Anders Søndberg Sørensen. High-fidelity multiphoton-entangled cluster state with solid-state quantum emitters in photonic nanostructures. *Phys. Rev. A*, 105:L030601, Mar 2022.
- [116] C. T. Nguyen, D. D. Sukachev, M. K. Bhaskar, B. Machielse, D. S. Levonian, E. N. Knall, P. Stroganov, R. Riedinger, H. Park, M. Lončar, and M. D. Lukin. Quantum network nodes based on diamond qubits with an efficient nanophotonic interface. *Phys. Rev. Lett.*, 123:183602, Oct 2019.
- [117] Lena Bauer, Bernhard Hametner, Christopher Clemens Mayer, and Siegfried Wassertheurer. Mathematical wave fitting models for the quantification of the diurnal profile and variability of pulse wave analysis parameters. *Simulation Notes Europe*, pages 153–160, 2017.

- [118] Simon Refshauge Pabst. Towards spin-multiphoton entanglement from a quantum dot. Master's thesis, University of Copenhagen, 2021. Formulated in Chapter 6.3.
- [119] Freja Thilde Pedersen. *Deterministic Single and Multi-photon Sources with Quantum Dots in Planar Nanostructures*. PhD thesis, University of Copenhagen, 2020.
- [120] Jung-Tsung Shen and Shanhui Fan. Strongly correlated two-photon transport in a one-dimensional waveguide coupled to a two-level system. *Phys. Rev. Lett.*, 98:153003, Apr 2007.
- [121] Hanna Le Jeannic, Tomás Ramos, Signe F. Simonsen, Tommaso Pregnolato, Zhe Liu, Rüdiger Schott, Andreas D. Wieck, Arne Ludwig, Nir Rotenberg, Juan José García-Ripoll, and Peter Lodahl. Experimental reconstruction of the few-photon nonlinear scattering matrix from a single quantum dot in a nanophotonic waveguide. *Phys. Rev. Lett.*, 126:023603, Jan 2021.
- [122] Shanhui Fan, Şükrü Ekin Kocabaş, and Jung-Tsung Shen. Input-output formalism for few-photon transport in one-dimensional nanophotonic waveguides coupled to a qubit. *Phys. Rev. A*, 82:063821, Dec 2010.
- [123] Alisa Javadi, Dapeng Ding, Martin Hayhurst Appel, Sahand Mahmoodian, Matthias Christian Löbl, Immo Söllner, Rüdiger Schott, Camille Papon, Tommaso Pregnolato, Søren Stobbe, Leonardo Midolo, Tim Schröder, Andreas Dirk Wieck, Arne Ludwig, Richard John Warburton, and Peter Lodahl. Spin-photon interface and spin-controlled photon switching in a nanobeam waveguide. *Nat. Nanotech.*, 13(5):398–403, 2018.
- [124] Jan Dreiser, Mete Atatüre, Christophe Galland, Tina Müller, Antonio Badolato, and Ataç Imamoglu. Optical investigations of quantum dot spin dynamics as a function of external electric and magnetic fields. *Phys. Rev. B*, 77:075317, Feb 2008.
- [125] J. H. Bodey, R. Stockill, E. V. Denning, D. A. Gangloff, G. Éthier-Majcher, D. M. Jackson, E. Clarke, M. Hugues, C. Le Gall, and M. Atatüre. Optical spin locking of a solid-state qubit. *npj Quantum Information*, 5(1):95, 2019.
- [126] P. Lochner, J. Kerski, A. Kurzmann, A. D. Wieck, A. Ludwig, M. Geller, and A. Lorke. Internal photoeffect from a single quantum emitter. *Phys. Rev. B*, 103:075426, Feb 2021.
- [127] A. Kurzmann, A. Ludwig, A. D. Wieck, A. Lorke, and M. Geller. Photoelectron generation and capture in the resonance fluorescence of a quantum dot. *Applied Physics Letters*, 108(26):263108, 2016.
- [128] Bernhard Urbaszek, Xavier Marie, Thierry Amand, Olivier Krebs, Paul Voisin, Patrick Maletinsky, Alexander Högele, and Ataç Imamoglu. Nuclear spin physics in quantum dots: An optical investigation. *Rev. Mod. Phys.*, 85:79–133, Jan 2013.
- [129] E. A. Chekhovich, M. N. Makhonin, A. I. Tartakovskii, A. Yacoby, H. Bluhm, K. C. Nowack, and L. M. K. Vandersypen. Nuclear spin effects in semiconductor quantum dots. *Nature Materials*, 12(6):494–504, Jun 2013.

- [130] C. T. Nguyen, D. D. Sukachev, M. K. Bhaskar, B. Machielse, D. S. Levonian, E. N. Knall, P. Stroganov, C. Chia, M. J. Burek, R. Riedinger, H. Park, M. Lončar, and M. D. Lukin. An integrated nanophotonic quantum register based on silicon-vacancy spins in diamond. *Phys. Rev. B*, 100:165428, Oct 2019.
- [131] Norbert Kalb, Andreas Reiserer, Stephan Ritter, and Gerhard Rempe. Heralded storage of a photonic quantum bit in a single atom. *Phys. Rev. Lett.*, 114:220501, Jun 2015.
- [132] Anna Tchebotareva, Sophie L. N. Hermans, Peter C. Humphreys, Dirk Voigt, Peter J. Harmsma, Lun K. Cheng, Ad L. Verlaan, Niels Dijkhuizen, Wim de Jong, Anaïs Dréau, and Ronald Hanson. Entanglement between a diamond spin qubit and a photonic time-bin qubit at telecom wavelength. *Phys. Rev. Lett.*, 123:063601, Aug 2019.
- [133] Nadia Olympia Antoniadis, Mark Richard Hogg, Willy Frederik Stehl, Alisa Javadi, Natasha Tomm, Rüdiger Schott, Sascha René Valentin, Andreas Dirk Wieck, Arne Ludwig, and Richard John Warburton. Cavity-enhanced single-shot readout of a quantum dot spin within 3 nanoseconds. *arXiv*, 2210.13870, 2022.
- [134] Hyochul Kim, Ranojoy Bose, Thomas C. Shen, Glenn S. Solomon, and Edo Waks. A quantum logic gate between a solid-state quantum bit and a photon. *Nature Photonics*, 7(5):373–377, May 2013.
- [135] Stephan Welte, Bastian Hacker, Severin Daiss, Stephan Ritter, and Gerhard Rempe. Cavity carving of atomic bell states. *Phys. Rev. Lett.*, 118:210503, May 2017.
- [136] Andreas V. Kuhlmann, Julien Houel, Arne Ludwig, Lukas Greuter, Dirk Reuter, Andreas D. Wieck, Martino Poggio, and Richard J. Warburton. Charge noise and spin noise in a semiconductor quantum device. *Nature Physics*, 9(9):570–575, Sep 2013.
- [137] Otfried Gühne, Chao-Yang Lu, Wei-Bo Gao, and Jian-Wei Pan. Toolbox for entanglement detection and fidelity estimation. *Phys. Rev. A*, 76:030305, Sep 2007.
- [138] Vincent E. Elfving, Sumanta Das, and Anders S. Sørensen. Enhancing quantum transduction via long-range waveguide-mediated interactions between quantum emitters. *Phys. Rev. A*, 100:053843, Nov 2019.
- [139] Eva M. González-Ruiz. *Single-photon sources as a key resource for developing a global quantum network*. PhD thesis, University of Copenhagen, 2023.
- [140] H. Ollivier, S. E. Thomas, S. C. Wein, I. Maillette de Buy Wenniger, N. Coste, J. C. Loredó, N. Somaschi, A. Harouri, A. Lemaitre, I. Sagnes, L. Lanco, C. Simon, C. Anton, O. Krebs, and P. Senellart. Hong-ou-mandel interference with imperfect single photon sources. *Phys. Rev. Lett.*, 126:063602, Feb 2021.
- [141] Charles Santori, David Fattal, Jelena Vučković, Glenn S. Solomon, and Yoshihisa Yamamoto. Indistinguishable photons from a single-photon device. *Nature*, 419(6907):594–597, Oct 2002.

- [142] Philip Thomas, Leonardo Ruscio, Olivier Morin, and Gerhard Rempe. Efficient generation of entangled multiphoton graph states from a single atom. *Nature*, 608(7924):677–681, Aug 2022.
- [143] Daniel E. Browne and Terry Rudolph. Resource-efficient linear optical quantum computation. *Phys. Rev. Lett.*, 95:010501, Jun 2005.
- [144] Netanel H. Lindner and Terry Rudolph. Proposal for pulsed on-demand sources of photonic cluster state strings. *Phys. Rev. Lett.*, 103:113602, Sep 2009.
- [145] Recorded seminar: Deterministic source of indistinguishable photons in a cluster state. <https://www.youtube.com/watch?v=g-FnQ15edZ8>. Accessed: 2023-05-06.
- [146] Dan Cogan, Zu-En Su, Oded Kenneth, and David Gershoni. Deterministic generation of indistinguishable photons in a cluster state. *Nature Photonics*, 17(4):324–329, Apr 2023.
- [147] N. Coste, D. A. Fioretto, N. Belabas, S. C. Wein, P. Hilaire, R. Frantzeskakis, M. Gundin, B. Goes, N. Somaschi, M. Morassi, A. Lemaître, I. Sagnes, A. Harouri, S. E. Economou, A. Auffeves, O. Krebs, L. Lanco, and P. Senellart. High-rate entanglement between a semiconductor spin and indistinguishable photons. *Nature Photonics*, Apr 2023.
- [148] J P Lee, B Villa, A J Bennett, R M Stevenson, D J P Ellis, I Farrer, D A Ritchie, and A J Shields. A quantum dot as a source of time-bin entangled multi-photon states. *Quantum Science and Technology*, 4(2):025011, mar 2019.
- [149] Konstantin Tiurev, Pol Llopart Mirambell, Mikkel Bloch Lauritzen, Martin Hayhurst Appel, Alexey Tiranov, Peter Lodahl, and Anders Søndberg Sørensen. Fidelity of time-bin-entangled multiphoton states from a quantum emitter. *Phys. Rev. A*, 104:052604, Nov 2021.
- [150] H. Y. Carr and E. M. Purcell. Effects of diffusion on free precession in nuclear magnetic resonance experiments. *Phys. Rev.*, 94:630–638, May 1954.
- [151] R. Stockill, C. Le Gall, C. Matthiesen, L. Huthmacher, E. Clarke, M. Hugues, and M. Atatüre. Quantum dot spin coherence governed by a strained nuclear environment. *Nature Communications*, 7(1):12745, Sep 2016.
- [152] Matthias C. Löbl, Sven Scholz, Immo Söllner, Julian Ritzmann, Thibaud Denneulin, András Kovács, Beata E. Kardynał, Andreas D. Wieck, Arne Ludwig, and Richard J. Warburton. Excitons in ingaas quantum dots without electron wetting layer states. *Communications Physics*, 2(1):93, Aug 2019.
- [153] Dorian A. Gangloff, Leon Zaporski, Jonathan H. Bodey, Clara Bachorz, Daniel M. Jackson, Gabriel Éthier-Majcher, Constantin Lang, Edmund Clarke, Maxime Hugues, Claire Le Gall, and Mete Atatüre. Witnessing quantum correlations in a nuclear ensemble via an electron spin qubit. *Nature Physics*, 17(11):1247–1253, Nov 2021.
- [154] Jonathan Bodey. *A tale of two interfaces: photons and spins linked by a solid-state artificial atom*. PhD thesis, University of Cambridge, 2021.

- [155] Jarryd J. Pla, Kuan Y. Tan, Juan P. Dehollain, Wee H. Lim, John J. L. Morton, Floris A. Zwanenburg, David N. Jamieson, Andrew S. Dzurak, and Andrea Morello. High-fidelity readout and control of a nuclear spin qubit in silicon. *Nature*, 496(7445):334–338, Apr 2013.
- [156] A. M. Waeber, G. Gillard, G. Rangunathan, M. Hopkinson, P. Spencer, D. A. Ritchie, M. S. Skolnick, and E. A. Chekhovich. Pulse control protocols for preserving coherence in dipolar-coupled nuclear spin baths. *Nature Communications*, 10(1):3157, Jul 2019.
- [157] Lukasz Cywiński, Roman M. Lutchyn, Cody P. Nave, and S. Das Sarma. How to enhance dephasing time in superconducting qubits. *Phys. Rev. B*, 77:174509, May 2008.
- [158] Hendrik Bluhm, Sandra Foletti, Izhar Neder, Mark Rudner, Diana Mahalu, Vladimir Umansky, and Amir Yacoby. Dephasing time of gaas electron-spin qubits coupled to a nuclear bath exceeding 200  $\mu$ s. *Nature Physics*, 7(2):109–113, Feb 2011.
- [159] M J Biercuk, A C Doherty, and H Uys. Dynamical decoupling sequence construction as a filter-design problem. *Journal of Physics B: Atomic, Molecular and Optical Physics*, 44(15):154002, jul 2011.
- [160] Leonid B. Glebov, Vadim Smirnov, Eugeniu Rotari, Ion Cohanoschi, Larissa Glebova, Oleg V. Smolski, Julien Lumeau, Christopher Lantigua, and Alexei Glebov. Volume-chirped Bragg gratings: monolithic components for stretching and compression of ultrashort laser pulses. *Optical Engineering*, 53(5):051514, 2014.
- [161] Satoshi Kako, Charles Santori, Katsuyuki Hoshino, Stephan Götzinger, Yoshihisa Yamamoto, and Yasuhiko Arakawa. A gallium nitride single-photon source operating at 200 k. *Nature Materials*, 5(11):887–892, Nov 2006.
- [162] John Preskill. Lecture notes for ph219/cs219: Quantum information chapter 3. [http://theory.caltech.edu/~preskill/ph219/chap3\\_15.pdf](http://theory.caltech.edu/~preskill/ph219/chap3_15.pdf), October 2018. See Sec. 3.4.2.
- [163] Daniel M. Jackson, Urs Haeusler, Leon Zaporski, Jonathan H. Bodey, Noah Shofer, Edmund Clarke, Maxime Hugues, Mete Atatüre, Claire Le Gall, and Dorian A. Gangloff. Optimal purification of a spin ensemble by quantum-algorithmic feedback. *Phys. Rev. X*, 12:031014, Jul 2022.
- [164] Carsten Schuck, Gerhard Huber, Christian Kurtsiefer, and Harald Weinfurter. Complete deterministic linear optics bell state analysis. *Phys. Rev. Lett.*, 96:190501, May 2006.
- [165] Stephan Welte, Philip Thomas, Lukas Hartung, Severin Daiss, Stefan Langenfeld, Olivier Morin, Gerhard Rempe, and Emanuele Distanto. A nondestructive bell-state measurement on two distant atomic qubits. *Nature Photonics*, 15(7):504–509, Jul 2021.
- [166] Alastair Kay. Tutorial on the quantikz package, 2020.

- 
- [167] Andreas V. Kuhlmann, Jonathan H. Prechtel, Julien Houel, Arne Ludwig, Dirk Reuter, Andreas D. Wieck, and Richard J. Warburton. Transform-limited single photons from a single quantum dot. *Nature Communications*, 6(1):8204, Sep 2015.
- [168] Andreas V. Kuhlmann, Julien Houel, Daniel Brunner, Arne Ludwig, Dirk Reuter, Andreas D. Wieck, and Richard J. Warburton. A dark-field microscope for background-free detection of resonance fluorescence from single semiconductor quantum dots operating in a set-and-forget mode. *Review of Scientific Instruments*, 84(7):073905, Jul 2013.